RADAR STUDIES OF ATMOSPHERIC GRAVITY WAVES

by

I.M. Reid, B.Sc. (Hons)

A Thesis presented for the degree of

DOCTOR OF PHILOSOPHY

at the

University of Adelaide

Department of Physics

1984

Contents

Summary

The thesis is concerned with the dynamics of the upper mesosphere and lower thermosphere (i.e. the height region between 60 and 100 km). Two methods of investigation using radio waves at MF have been used. These are the Spaced Antenna (SA) and Doppler Radar Techniques. The Doppler radar technique was the main method of investigation used in this research, and because of this, its reliability as a means of determining winds in the D-region at a frequency of 2 MHz was established by comparison with the much tested and proven SA method. Once this had been done, measurements of mesospheric gravity wave horizontal wavelengths and phase velocities were obtained using a Doppler radar with dual beams and a new analysis technique over a period of two years and over a range of heights, typically 80-94 km. This method also allowed the mesospheric momentum fluxes $\overline{u'w'}$ and $\overline{v'w'}$ to be obtained. From the vertical profile of $\overline{u'w'}$ values of F_u (the zonal wave drag) were computed and compared with the zonal acceleration due to the Coriolis torque acting on the mean meridional circulation. The comparisons show that gravity waves play a major role in determining the mean zonal circulation in the mesosphere. Vertical velocities were also obtained from the same observations. The mean velocities are much larger than those predicted by theory, and appear to be downward for most of the year.

Preface

To the best of the author's knowledge, this thesis contains no material previously published or written by another person, except where due reference is made in the text. It contains no material which has been submitted or accepted for the award of any other degree or diploma in any University.

Iain M Reid

Acknowledgments

The work described in this thesis was carried out under the supervision of Dr R. A. Vincent and Dr B. H. Briggs using the facilities of the Department of Physics, the University of Adelaide. The advice and encouragement of Dr Vincent, his patience and insight into a very wide range of problems in atmospheric physics are very greatly appreciated. Dr Briggs encouragement and advice although of a more general nature, are also appreciated.

Discussions with Dr Wayne Hocking and Sue Ball, and with Ron Craig, Peter May and Laurie Campbell proved very helpful. Alex Didenko provided technical assistance and by way of his happy outlook, encouragement. Lyn Birchby undertook a wide variety of tasks in data analysis, some of which were very tedious and boring, but always enthusiastically and always did excellent work. The typing done by Pattie Owen was excellent, and the typing, proof reading and general assistance provided by my mother, Mabel Reid and my sister, Linda Reid were outstanding. Sam Walker provided the essential knowledge for, and assisted in the survey of the BP field site.

I owe my greatest debt to Holly Walker, my wife, who not only drew the majority of the diagrams, but did countless other important tasks related to this work. Holly's personal support in the course of this work was unfailing.

I also thank my parents for their continued support throughout my academic career.

The author was in receipt of an Australian Commonwealth Postgraduate Award.

This Digital Version of the Thesis

This version of the thesis was scanned in 2015. The font has been changed to Times New Roman, typos have been corrected, some incorrect section numbering corrected, titles added to the references in the reference list, and the structure of some paragraphs has been modified to accommodate the new typeface and to improve the layout of the figures. Apart from this, this is the March 1984 version of the thesis.

Iain Reid, 3 March 2016

1. Introduction and Aim

This work describes observations of internal atmospheric gravity waves in the lower part of the ionosphere known as the D-region. This is generally taken to be that part of the ionosphere in the 60-90 km height range, but later in this thesis we refer to the D-region as the 60-100 km region. This is not strictly correct because the region between 90 and 100 km is usually considered to be part of the E-region of the ionosphere.

Radar observations of wind at MF and HF in the D-region depend upon there being a significant ionized component to backscatter the transmitted radiation. Because the ionized component is relatively small, and the collision frequencies large, a close coupling between the ionized and neutral components is expected, and the ionization is used essentially as a tracer of the movement of the neutral component. In terms of the neutral atmosphere, the D-region corresponds to the mesosphere and lower thermosphere (see below).

The dynamics of this region cannot be considered in isolation from the other parts of the atmosphere because waves excited primarily in the lower atmosphere propagate upward and may transmit characteristics of their region of generation into other parts of the atmosphere. The importance of waves in this region arises from the exponential growth of wave amplitude with height. This is required for conservation of the wave energy density because the mean density of exponentially with height, and in the region above about 80 km, the winds induced by atmospheric waves with periods less than about a day are comparable in magnitude to the mean flow.

1.1 The Formation of the D-region

In the 60-90 km height region, electron densities are small, rising from values of about 10 cm^{-3} at about 60 km to about 10^4 cm^{-3} at 90 km during the day (Vincent, 1980). At night there are few free electrons below about 80 km under quiet conditions, and electron concentrations throughout the region are greatly reduced over daytime values. This is because the D-region formation is dominated by photoionization of minor constituents. Rocket mass spectrometer measurements have shown that such minor constituents as O, O3, CO2, NO, NO2, H2O and OH play an important role in the ion chemistry of the region.

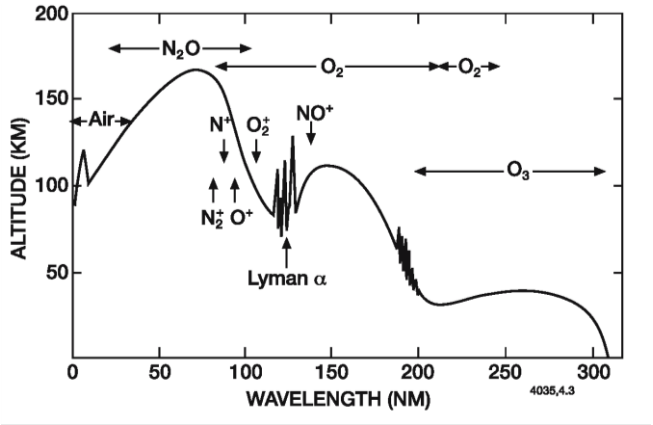

Figure (1-1) The variation of wavelength of the height of unit optical depth for solar radiation incident vertically (after Thomas, 1980).

The ionization is produced primarily by photo-ionization of nitric oxide (NO) by the intense solar Lyman-α radiation (121.6 nm). A high proportion of the incident high energy ionizing solar radiation has been absorbed by the time it reaches D-region heights, but because of the "window" in the ultra-violet (UV) absorption spectrum of 0_2 at 121.6 nm (see Figure (1-1)), Lyman-α radiation penetrates to the 75-90 km height region, where it ionizes NO.

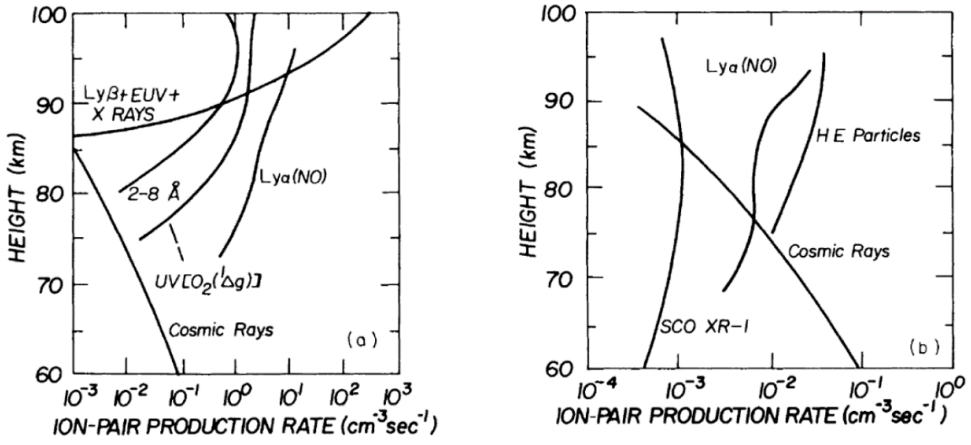

Figure (1-2a) (above left) Daytime and Figure (l-2b) (above right) Nighttime ionization rates (after Arnold and Krankowsky, 1977).

A metastable state of oxygen $O_2('\Delta g)$ produced by the absorption of radiation in the 266-320 nm band by ozone, can be ionized by solar radiation with wavelengths less than 111.8 nm which coincide with "windows" in the absorption spectrum of O_2, and below 90 km at middle latitudes at sunspot minimum, represents the other major source of ions in the D-region.

Above about 85 km, solar extreme ultraviolet (EUV) radiation and soft solar X-rays can ionize most of the dominant constituent neutral gases in the ionosphere, while the Lyman-β line (102.6 nm) can just ionize molecular oxygen. Figure (1-2a) shows the estimated ion pair production rates for undisturbed conditions in the 60-100 km height range for a solar zenith angle of 60°. As we have noted, ion production from NO is dominant. Inspection of this diagram also indicates that cosmic rays become important as a source of ionization below about 70 km. At heights below about 65 km, cosmic rays, which can penetrate deep into the atmosphere, will provide the only source of ionization. This mechanism may explain the existence of the ledge in electron density observed near 60 km and sometimes referred to as the C-layer.

The relative contribution of the galactic cosmic ray flux to ionization in the region below about 70 km increases with geomagnetic latitude and decreases with increasing solar activity. The latter effect results from the screening of the galactic cosmic rays by the increased magnetic fields associated with the solar wind. Short wavelength X-rays can also contribute to ion production and this becomes important when the X-ray flux is highest, that is, during active solar conditions, and its importance is particularly enhanced during solar flare conditions.

The absence of solar radiation at night results in the reduced electron concentrations in the D-region over the daytime values, but D-region ionization is often present at night at concentrations higher than would be expected on the basis of the recombination rates. The absence of significant electron concentrations at night below 80 km is due to the rapid attachment of free electrons to neutrals to form negative ions, and positive and negative ions in proportionately equal concentrations dominate the composition.

During the day the attachment is offset by the photo-disassociation of the negative ions by visible light to produce free electrons. In this region, rapid increases in electron density occur at sunrise, with subsequent decreases at sunset. Above about 80 km, the increase in electron density after sunrise occurs at a relatively slower rate. The ion chemistry of the D-region at night is extremely complicated and not well understood. Figure (1-2b) shows an estimate of the ionization production rates expected in the 60-100 km height range. The ionization of NO by scattered Lyman-a radiation, and the precipitation of high energy electrons from the thermosphere and plasmasphere (which becomes particularly important at higher magnetic latitudes) are indicated as the most important source of ionization.

The D-region as a whole has a complicated ion chemistry and the distribution of the ionizable constituents can vary with time. It to pursue this topic any further but we note that the ion chemistry is strongly temperature dependent. This means that D-region electron densities can be strongly influenced by the dynamics of the mesosphere. This is in turn strongly influenced by the dynamics of lower atmosphere. The best example of this is probably the anomalously large radio wave absorption observed in winter (when compared to summer) at mid to high latitudes (the so called "winter anomaly"). It is now well established that this is at least partly due to coupling between the lower and upper atmospheres by large scale planetary waves (see e.g. Offermann, 1979) The dynamical coupling of the lower and upper parts of the middle atmosphere, and its effect upon the general circulation is of major concern in this thesis.

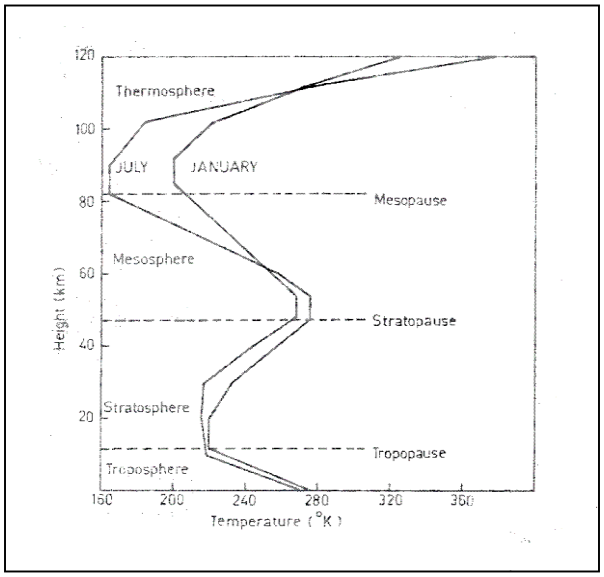

Figure (1-3) Temperature height profile for 45°N, 1966 U.S. Standard Atmosphere

1.2 The Middle Atmosphere and the importance of Gravity Waves

The atmosphere is usually divided into layers on the basis of the variation of the vertical distribution of temperature. Figure (1-3) illustrates the temperature height profile for 45° N for values obtained from the 1966 U.S. Standard Atmosphere and shows the names given to the various regions. The middle atmosphere is generally taken as that part of the atmosphere extending from the tropopause (~10 km) to a height of about 100 km. It includes the stratosphere, mesosphere and the lower thermosphere.

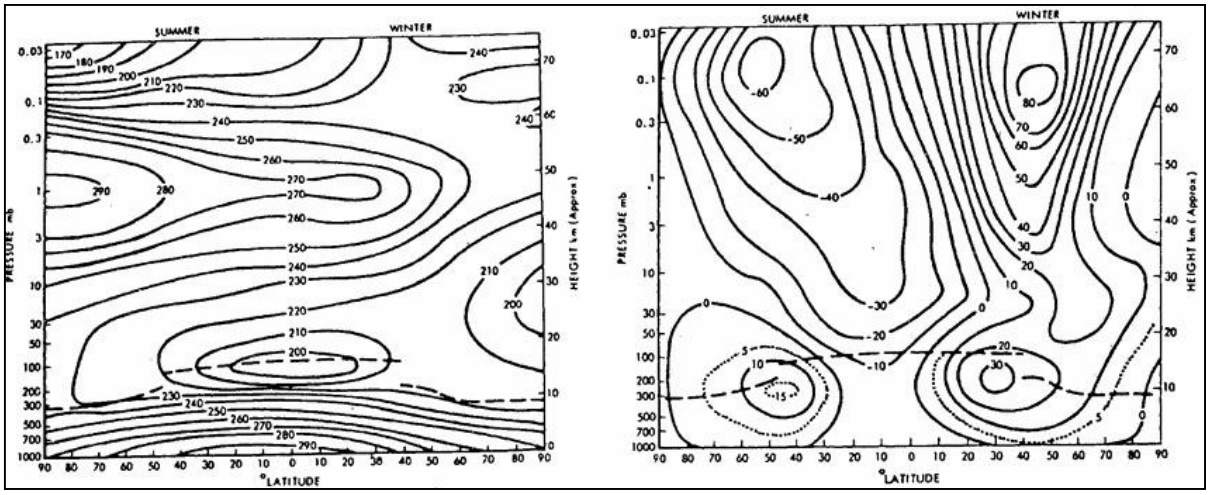

Figure (1-4a.) (Left) Zonally averaged temperature distribution and Figure (l-4b) Zonally averaged· winds (after Murgatroyd, 1969)

Figure (l-4a) shows the zonally averaged temperature distribution for the middle atmosphere based on in situ measurements by radiosonde, rocketsonde and rocket grenade soundings made over a number of years (Murgatroyd, 1969), and is taken from Geller (1983). Inspection of this diagram indicates that the highest temperatures are found in the summer tropics. This is as would be expected on the basis of the geometry of the incoming solar radiation. The summer stratopause temperature is higher than that for the winter stratopause, which is consistent with the larger ozone concentration at the poles, and the absence of solar heating at the winter pole. In the tropics at tropopause heights, a local temperature minimum is noted, and the coldest climatological temperatures are found in the summer polar mesosphere, while the polar winter mesosphere evidences warm temperatures.

The mean zonally averaged winds are shown in Figure (l-4b) and these are in geostrophic and hydrostatic equilibrium with the temperature distribution. Eastward jet streams occur in both summer and winter hemispheres near the tropopause. The winter jet stream magnitude is about twice that of the summer jet stream. In the 60-70 km height region jet streams are noted in both hemispheres, eastward in winter and westward in summer. The winter jet is about 20 ms^{-1} larger in magnitude than the summer jet.

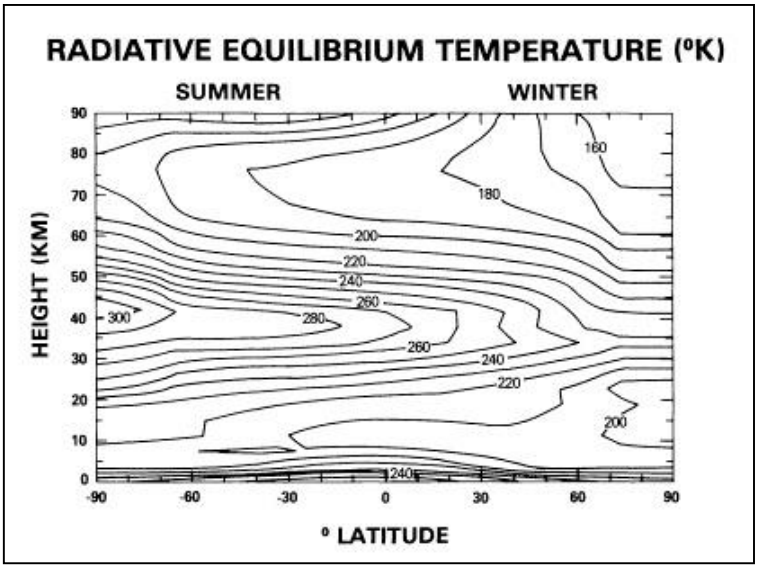

Figure (1-5a) Calculated radiative equilibrium temperature described in text. Units are K (after Geller, l983)

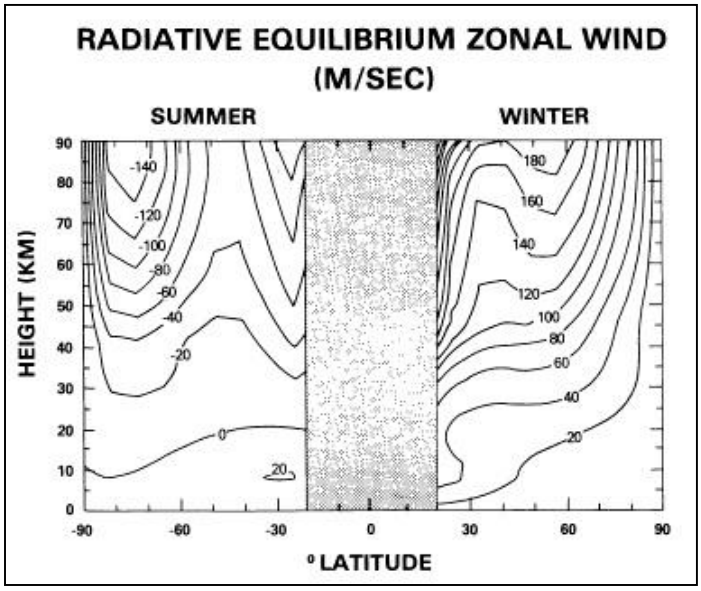

Figure (1-5b) Geostrophic mean zonal winds calculated from the radiative equilibrium temperatures shown in Figure (l-5a). No values are shown near the equator because the geostrophic formula does not apply there. Units are ms^{-1}, and eastward winds are positive.

As Geller (1983) points out, this temperature distribution shown in Figure (l-2b) does not correspond to the radiative equilibrium condition calculated on the basis of the local solar heating and local infra-red cooling. Figure (1-5a and b) is taken from Geller (1983) and compared with Figure (l-4b), the radiative equilibrium state predicts a too warm (cold) summer (winter) stratopause, and too warm (cold) summer (winter) mesosphere.

The mean zonal geostrophic wind calculated from the radiative equilibrium field and shown in Figure (1-5b) shows that the magnitudes of the summer and winter mesospheric jets are too large and they do not close in the mesosphere. Meridional and vertical motions are absent in this model.

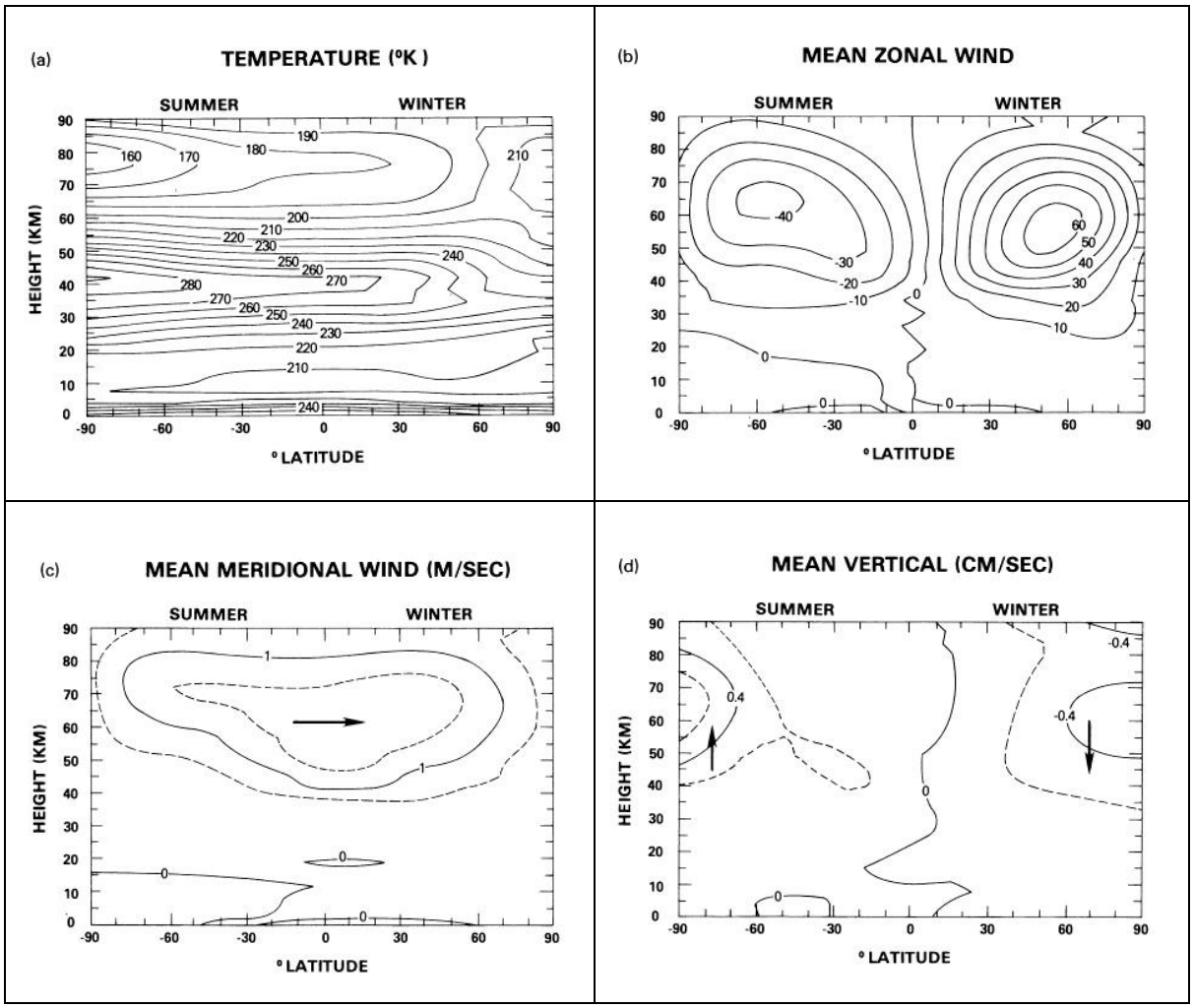

Figure (1-7a) (top left) Model calculated zonally averaged temperature field in K Figure (1-7b) (top right) Zonal wind in ms^{-1}, Figure (1-7c) (bottom left) Mean meridional wind in ms^{-1}, Figure (1-7d) (bottom right) Mean vertical motion in cms^{-1} (after Geller, 1983)

Leovy (1964) first recognized that dynamical processes must account for the departure of the atmosphere from radiative equilibrium, and pointed out that what is lacking in this physical model is a mechanism for zonal momentum dissipation. To simulate this effect mathematically in his model of mesospheric circulation, he hypothesized a linear drag that produces a deceleration proportional to the mean zonal wind speed, a "Rayleigh drag". Leovy used a uniform Rayleigh drag with a damping time of about 15 days. This produced a circulation in qualitative agreement with observations. Later models by Schoeberl and Strobel (1978) and

Holton and Wehrbein (1980) used a Rayleigh drag that increased with height. This resulted in closure of the mesospheric jets and reversal of the mean meridional temperature gradient.

The temperature, mean zonal wind, mean meridional wind and mean vertical wind obtained by Geller (1983), who used a Rayleigh drag profile such that the dissipation time scale increased from about that the dissipation time scale increased from about 10 days throughout the stratosphere to about one day at 90 km, are shown in Figure (1-7a and b). Inspection of these diagrams indicates that the summer stratopause is cooler and the winter stratopause is warmer than in the radiative equilibrium solution. The meridional temperature gradient is reversed so that the winter mesopause is warmer than the summer mesopause.

The mean zonal jet structure closes with height, and the magnitudes are in better agreement with observations. A meridional flow from the summer to the winter flow and upward motion in the summer hemisphere, and a downward motion in the winter hemisphere are evident. The expansion cooling in the summer hemisphere and compression heating in the winter hemisphere associated with the vertical motions are the primary cause of the variations of the temperature field from radiative equilibrium.

Even though a Rayleigh drag does not accurately represent any relevant physical mechanism (Dunkerton 1982), the results of such model calculations indicate that the middle atmosphere temperature and zonal wind strongly depend on zonal momentum drag processes. This momentum is presumed to be transported upward from wave sources in the troposphere. Recent theoretical and observational evidence suggests that of the major wave systems contributing to the dynamics of the mesosphere, namely planetary waves, atmospheric tides and gravity waves, the latter are the most likely candidate for balancing the thermal and momentum budgets of the middle atmosphere.

There is an extensive literature on waves at each of these scales, and it is not our intention to review those for either tides or planetary scale waves. However, no scale of motion can be considered in isolation from the others, and in 1.2.1 and 1.2.2 below we briefly describe these waves, and the observational evidence that suggests that they are not the primary vehicles of momentum transport into the mesosphere.

1.2.1 Planetary waves

Planetary waves are zonally asymmetric disturbances of global scale with periods in excess of a day. They may be divided into two types, stationary modes and transient modes. The former are quasi-permanent features of the circulation in the Northern hemisphere away from the equatorial regions. Any planetary scale waves with periods greater than about 30 days are assumed to be quasi-stationary. Stationary planetary wave activity is observed to be a maximum in the Northern hemisphere winter, while the southern hemisphere is much less disturbed by these waves, and the maximum activity occurs in late spring. They are believed to be forced by flow over topographical features and by differential heating of land masses and the ocean, and this may explain hemispheric variation in activity, because the zonal asymmetries in topography and the land-ocean differences are much smaller in the Southern Hemisphere. Transient or travelling waves occur in both hemispheres with approximately equal strengths. They have time scales of from a few days to four weeks, and are believed to result from hydrodynamic instabilities in the atmosphere.

Both types of planetary waves are primarily excited in the troposphere. Theoretical studies indicate that they may only propagate vertically in the presence of Eastward mean winds, and stationary planetary waves are not observed to propagate through the stratosphere in summer when the mean zonal wind in this region is westward (see Charney and Drazin, 1961). Since the same order of magnitude decelerations are required in both summer and winter hemispheres, but stationary planetary waves do not propagate into the mesosphere in summer, these waves are probably not providing the necessary wave drag to maintain the mean zonal wind and temperature states observed (Geller, 1983).

In addition, Houghton (1978) noted that the summer mesopause temperature, which is particularly sensitive to the strength of the mean meridional circulation, should fluctuate in response to the level of planetary wave activity if planetary waves in either the summer or winter hemisphere were controlling the mean meridional circulation. Since this was not observed in satellite data (Curtis et al., 1974; Hirota 1975, 1976), Houghton argued that planetary waves are not the primary source of momentum transport into the mesosphere, and suggested that gravity waves were the most likely candidate for balancing the thermal and momentum budgets of the middle atmosphere.

1.2.2 Atmospheric Tides

A comprehensive description of these waves may be found in Chapman and Lindzen (1970). The solar tidal motions in the earth's atmosphere have periods of 24, 12 and 8 hours. They are excited by differential solar heating of the earth's atmosphere, and the oscillations are produced as the atmosphere attempts to return to thermodynamic equilibrium. They must propagate westwards with respect to the earth to maintain a fixed phase relationship to their driving force. Excitation is primarily by absorption of solar UV radiation by ozone in the upper stratosphere and by water vapour in the troposphere. UV and EUV absorption in the lower thermosphere is also important.

The 8 and 12 hour oscillations are harmonics of the fundamental period of 24 hours, and are produced because the solar insulation is nearly in the form of a square wave. Elford (1979) examined the role of tidal winds between 80 and 100 km in transporting momentum poleward by using 9 years of meteor radar data obtained at Adelaide. He found an annual variation in momentum flux, and that in summer, the poleward flux was large enough to maintain the mean zonal flow at these heights in middle latitudes, but that the meridional transport of momentum was insufficient to balance that due to the mean flow. On the basis of Elford's (1979) observations, and also theoretical grounds (e.g. Miyahara, 1980) it would appear that at mid-latitudes, atmospheric tides are unlikely to be important contributors to the mesospheric momentum budget. Like Houghton (1978) Elford pointed out that one possible source of momentum flux was short period gravity waves.

1.2.3 Internal Atmospheric Gravity Waves

It is not our intention to review the extensive literature that exists for this class of waves, but rather to provide an indication of some of the salient features related to momentum transport into the mesosphere. Details of these waves may be found in Hines (1960). Mathematical details of their characteristics are described throughout this thesis where appropriate.

Gravity waves are a particular class of internal waves confined to a limited frequency range, the upper limit of which is determined by atmospheric parameters and corresponds to a period of about 5 minutes (the Väisälä -Brunt period). The lower frequency limit is determined by the initial period (about 20.9 h at 35°S), and those waves with periods less than 200 minutes are usually of sufficiently small scale so that Coriolis forces may be ignored. The direction of the oscillation of the medium in which these waves travel is almost transverse to the direction of

phase propagation, and phase and energy propagate orthogonally. Short period gravity waves propagate energy nearly vertically, while those of long period propagate energy nearly horizontally. For a given wave frequency, the horizontal and vertical wavelengths are free to take a range of values which are determined by the dispersion relations for this class of waves.

In the presence of a background wind, the gravity wave frequency is subject to a Doppler shift, Pitteway and Hines (1965). The intrinsic frequency, Ω, that observed in a frame of reference moving with the background wind, is given by the Doppler transformation

$$\Omega = \omega - \boldsymbol{k} \cdot \boldsymbol{u} \tag{1-1}$$

where ω is the angular frequency of the wave observed in a frame of reference stationary with respect to the Earth's surface, $\boldsymbol{k}$ is the wavenumber and $\boldsymbol{u}$ is the background wind.

In the presence of a height varying background wind, the intrinsic frequency may be zero at some height. If this occurs and the Richardson number of the mean flow is large, the wave momentum and energy are transferred to the background flow (e.g. Booker and Bretherton, 1967). The convergence of the gravity wave momentum flux with height leads to an acceleration of the mean flow. Very little wave energy is able to pass a critical level, and a gravity wave spectrum isotropic in azimuth at a lower level may be filtered so that there is a preferred azimuthal direction at higher levels. This preferential orientation makes it possible for momentum to be transferred in a particular direction to the mean flow where the waves are dissipated.

A study by Bretherton (1969a and b) indicated that the mean flow is accelerated generally, whenever gravity waves are dissipated, and later studies indicated the likely importance of this for the mean circulation (Bretherton, 1969c; Hines, 1972; Lindzen, 1973). Examples of dissipative processes are molecular diffusion and radiative cooling, and these operate more or less independently of wave amplitude. Studies by Hines (1960), Hodges (1967) and Lindzen (1967) indicated that both tides and gravity waves would become dynamically and/or convectively unstable above some level due to their exponential growth with height, and that turbulence and smaller scale gravity were likely to be thereby produced.

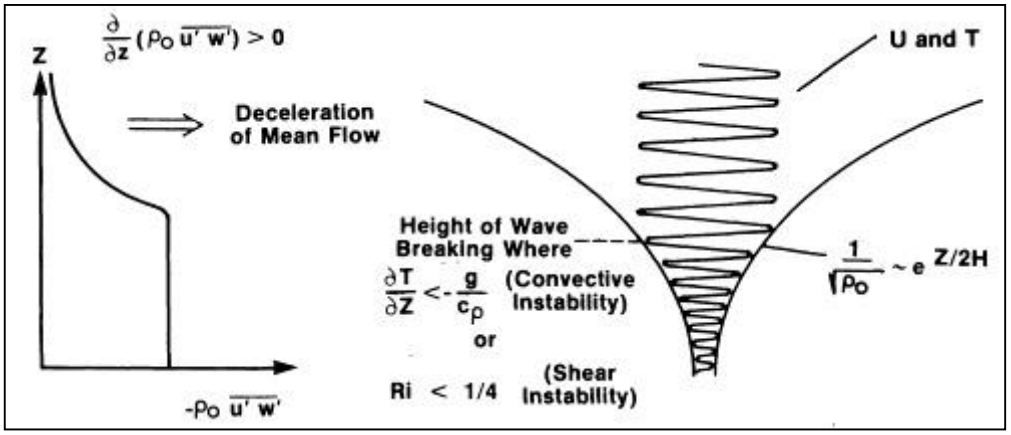

Figure (l-8) Schematic of gravity wave breaking and the resulting vertical flux of zonal momentum (after Geller, 1983)

What happens when this takes place is shown schematically in Figure (1-8) which is taken from Geller (1983). The right hand side of this figure shows the exponential growth with altitude of the horizontal velocity and temperature associated with a monochromatic gravity wave. Above the wave breaking level, the wave amplitude is assumed to be constant. This idea is due to Hodges (1967, 1969) and wave amplitudes are assumed to be limited by the formation of corrective instabilities that produce just that level of turbulent diffusion required to maintain saturation amplitudes.

The left hand side of this diagram illustrates schematically the vertical flux of horizontal momentum in the xz-plane. Above the wave breaking level, the momentum flux decays exponentially. The convergence of the momentum flux with height leads to a deceleration of the mean flow towards the phase velocity of the wave at the wave breaking levels.

Above the wave breaking level, the wave described above is said to be saturated. Gravity wave saturation refers to any process that acts to limit or reduce wave amplitude due to instabilities or interactions arising from large-amplitude motions (Fritts, 1984). It implies that the wave field has reached amplitudes such that secondary instabilities can develop which limit further wave growth (Lindzen, 1981; Dunkerton, 1982). The saturation mechanism thought to be most important in the middle atmosphere, where amplitudes may reach sufficient amplitude to break, is the turbulent breakdown of convectively unstable regions produced by the differential advection of denser air over less dense air by internal gravity wave motions, known as convective overturning or convective instability (Fritts et al., 1984). Another is the Kelvin-Helmholtz (KH) instability (e.g. Fritts, 1979).

Lindzen (1981) proposed a simple scheme by which the effects of gravity wave saturation could be calculated. By generalizing an expression obtained by Hines (1970) to apply to arbitrary mean flows, including critical levels, he obtained an expression for the mean flow accelerations induced by both wave dissipation and momentum flux convergence. The latter effect, the deposition of momentum, is the most important consequence of gravity wave saturation for the middle atmosphere. This is because the mean flow acceleration produced is such that the mean flow is driven towards the phase speed of the wave. The latter quantity has characteristics determined by the forcing mechanism.

Sources of these waves include just about any process which can produce instabilities in the atmosphere with periods greater than the Brunt-Väisälä period. In the mesosphere, possible sources include wind shear, jet streams, and zones of strong shearing and unstable lapse rates produced by tides and other waves. Theory indicates that many locally generated waves are confined to the region of generation, but some modes correspond to waves which could propagate freely away from the region of generation into stable regions of the atmosphere (e.g. Fritts, 1979).

Unlike the mesospheric sources, there are many known tropospheric sources, which include unstable wind shear (Lindzen and Rosenthal, 1976) topography, frontal process (Hines, 1968; Peltier and Ley, 1978; Reed and Hardy, 1972) and convection. Wind shear produces waves with phase velocities characteristic of tropospheric wind speeds, while topography generates gravity waves with a distribution of phase velocities centered about zero. The phase velocity spectrum associated with convective generation is less well understood, but it is reasonable to suppose that the phase distribution is broad and centered about tropospheric wind speeds (Fritts et al., 1984). For a gravity wave spectrum of tropospheric origin, the effect of momentum deposition through wave saturation is a deceleration of the mean flow, as required by the model calculations mentioned earlier.

Following Lindzen's (1981) work, Holton (1982) and Matsuno (1982) examined through modelling the role of gravity wave drag in the middle atmosphere. Holton's work indicated that the saturation of gravity waves with simple phase velocity spectra could produce reasonable profiles of the mean zonal wind. Matsuno (1982) did not use gravity wave saturation explicitly, but incorporated similar effects in that dissipation accelerated the mean flow towards the gravity wave phase speeds, and obtained similar results to those of Holton (1982). Later studies

have examined various other aspects of gravity wave saturation, and a comprehensive review is given by Fritts (1984).

The purpose of this work is to obtain experimental evidence of the role of gravity wave momentum deposition in the mesosphere.

1.3 A Note on Doppler Radar Techniques

The gravity wave observations reported in this work were obtained using Doppler radar techniques at MF. Powerful Doppler radars operating at VHF and UHF have recently become available for mesospheric observations (see e.g. Gage and Balsley, 1978) but meteorological radars operating in the planetary boundary layer have been available for almost two decades. The techniques developed for these devices are often quite general and applicable for Doppler radars observing the mesosphere. A particularly powerful version of the meteorological radar is that using the Velocity Azimuth Display (VAD) technique (see e.g. Wilson and Miller, 1971). In this version of the Doppler radar, a single radar beam is scanned through a range of azimuth angles at a fixed elevation. The theory developed to retrieve information about the mean and fluctuating parts of the wind field for this technique (see e.g. Browning and Wexler, 1968; Wilson, 1970) is particularly useful for a radar capable of directing radar beams at opposite angles to the zenith in a vertical plane.

The most important parameters that can be obtained by a Doppler radar in this configuration are the Reynolds stress terms $\overline{u'w'}$and $\overline{v'w'}$. These terms cannot generally be obtained by a Doppler radar operating with the conventional beam configuration, that is, one beam directed vertically, and one beam offset from the zenith at some angle θ. Their importance arises from the fact that the gravity wave acceleration of the mean flow in the zonal direction is given by

$$F = -\frac{1}{\rho}\frac{\partial}{\partial z}(\rho\overline{u'w'}) \qquad (1\text{-}2)$$

(e.g. Lindzen, 1981), and a similar expression applies for the meridional acceleration due to gravity waves.

The theory to obtain the Reynolds stress terms was developed independently at Adelaide, and is described in Vincent and Reid (1983). It was the development of this theory that enabled the importance of gravity waves in balancing the momentum budget in the mesosphere to be

investigated. Other useful physical parameters that can be obtained using two coplanar beams offset at opposite angles to the zenith in the same vertical plane, and derived from the theory developed for the VAD technique, have also been investigated in this work.

1.4 Summary

On the basis of observational and theoretical studies, gravity waves are thought to play a major role in the momentum and heat budgets of the middle atmosphere. This work attempts to investigate their importance by using Doppler radar techniques to observe the wind field in the D-region of the ionosphere.

2. Equipment and Experimental Procedure

2.1 Introduction

The Buckland Park (BP) aerial array is located on a flat coastal plain about 40 km north of Adelaide at 34° 38'S and 138° 29'E. The individual aerials are half-wave dipoles resonant at 1.98 MHz, but they can be used at the third harmonic of 5.995 MHz. The array is extremely versatile, and individual dipoles, groups of dipoles or the entire array can be used for either transmission or reception. However, the most typical arrangement is that in which a much simpler array situated next to the main array is used for transmission. The transmitting and receiving equipment are situated at the centers of their respective arrays as illustrated in Figure (2.1a). A general, if somewhat dated, description of BP may be found in Briggs et al. (1969).

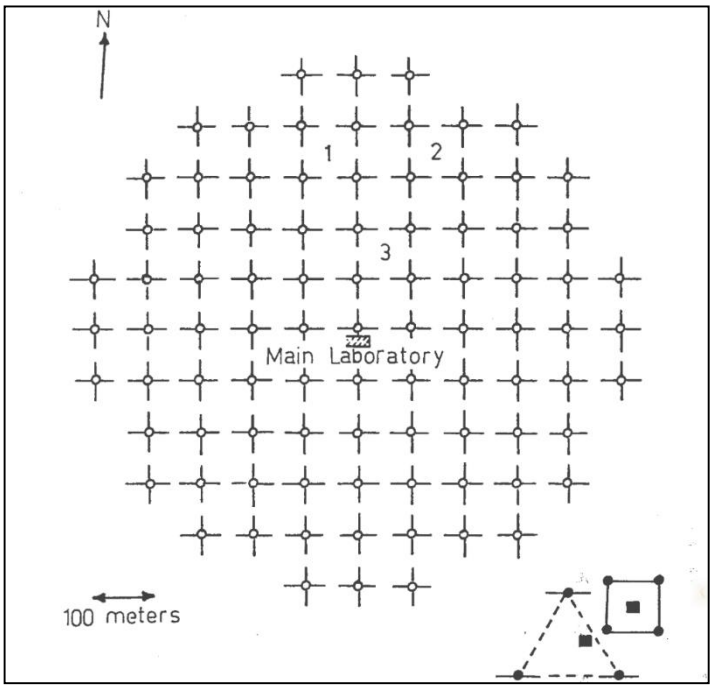

Figure (2-1) Schematic diagram of the BP aerial array. Each cross represents a dipole pair and the spacing between centers is about 91.4 m. The transmitting array is represented by the small square in the lower right hand side of the diagram. The portable SA equipment used in November 1980 is shown as the triangle next to the Rx array. The NS axis of the array is aligned 4° west of true north.

In November 1980 a portable Spaced Antenna (SA) system was operated at the BP site simultaneously with the BP facility, which operated as a dual beam Doppler radar. The SA equipment was in transit from a site near Townsville (19° 40'S, 138° 29'E) to its present

location at Mawson Base, Antarctica (67° 37'S, 62° 52'E). This experiment provided winds from each technique over the range of 80-96 km.

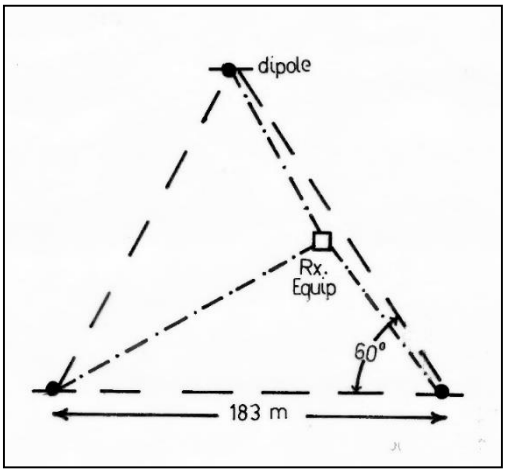

Figure (2.1b). Experimental set-up for the portable SA equipment receiving array used in November 1980 at the BP field site. The dot/dash lines in the diagram represent the coaxial cables connecting the dipoles to the receiving equipment. Excess cable was coiled up and positioned inside the receiving hut. Dipoles were aligned in the EW direction, parallel to the EW dipoles of the main array and the spacing between dipole centers was about 183 m. To position them in the EW direction, they were aligned by eye with the aerial poles in the main array (which have a basic spacing of 91.4 m

2.2 Topography

The site is adjacent to St. Vincent's Gulf about 40 km north of Adelaide and 3 km east of the coast, but the area to the west of the station is used as salt pans. The water table of the site is about 3-5 m below the surface, and the groundwater is quite brackish.

When the aerials are connected up as a broadside array, so that a narrow beam is produced, it is important to know the slope of the ground plane because this will determine the tilt of a nominally "vertical" beam. Since the site is a flat coastal plain, we could reasonably expect the water table, and hence the ground plane, to be parallel to the mean surface level. The results of a survey of the area made with a level and staff are shown in Figure (2.2).

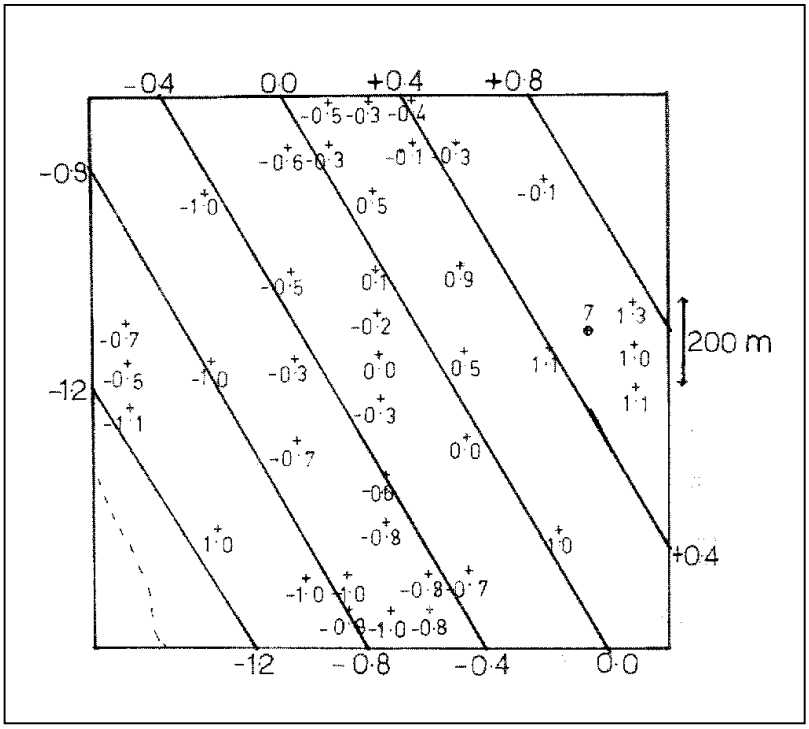

Figure (2.2) Contour plot-of the Buckland Park field site. Spot heights obtained using a level and staff are represented by a cross. The corresponding height relative to the center of the array is written next to each. The crossed circle indicates a spot height relative to sea level. The contours represent a plane fitted to all of the spot heights using a multiple regression analysis.

Figure (2.3) Aerial photograph of BP field site. The scale is about 1:5333. The aerial pole positions are clearly visible and the general outline of the array can be seen. The bright white lines running from the bottom right to the center of the array are roads. Smaller tracks are also visible. Land immediately to the North, East and South is agricultural, while the land to the West is used as salt pans. A number

of dry shallow creek beds can be seen running across the site, including one at the top center of the array.

Thirty-nine spot heights relative to the center of the array were obtained, and these were subjected to a multiple linear regression analysis (Mood and Graybill, 1963) to obtain the mean slope of the ground. Figure (2.2) also shows the contours corresponding to the mean slope, and from these, it is clear that the overall gradient is small, about 1.68×10^{-3} or $0.10°$. The contours fit the data well. The poor fit at the center top of the diagram is due to a local minimum, where a creek bed runs through the site. This was determined by observation of the ground and of an aerial photograph (Figure 2.3) and map.

Also marked on the contour plot are the five-meter contour and a seven-meter spot height taken from an orthocadastral topographical map of the area. The relative heights of the two areas agree well; both show a 2 m difference. The 5 m contour is the only one on the map (apart from a few tiny mounds), but by using the spot heights it appears that the slope of the BP field site is typical of the surrounding area.

It seems reasonable to conclude that a "vertically" pointing beam is about 0.1° from the zenith at an azimuth angle of about 225° measured clockwise from North.

The general expression for the mean radial velocity V_R measured with a Doppler radar at (R, θ, ϕ) where R is the range measured along the beam, θ is the angle from the zenith and ϕ is the azimuth angle measured clockwise from north is (see Chapter 4, Equation (4-3))

$$\overline{V_R}(\phi) = \bar{u}sin\theta sin\phi + \bar{v}sin\theta cos\phi + \bar{w}cos\theta$$

where (u, v, w) are the mean eastward, northward and vertical components of the wind respectively. At BP a beam nominally directed vertically will measure a radial velocity given by

$$\overline{V_R} = \bar{u}(-1.23 \times 10^{-3} + \bar{v}(-1.23 \times 10^{-3}) + \bar{w}$$

where $\theta = 0.10°,\ \phi = 225°$

For values of $(\bar{u}, \bar{v})\ of\ (30, -10)\ ms^{-1}$ we obtain

$$V_R = (-2.5 + \overline{w})\ cms^{-1}$$

so that there will be a bias towards downward vertical velocities of about 3 cm/s in this case.

These values of $(\bar{u}, \bar{v})$ would be typical at Adelaide at 85 km for most of the year. In summer the meridional component will generally be positive at this height so that for $(\bar{u}, \bar{v}) = (30, 10)\ m/s$ we obtain

$$V_R = (-4.9 + \overline{w})\ cms^{-1}.$$

Consequently, vertical velocities measured in summer have a stronger bias towards negative values, but for most of the year the contribution of the horizontal wind to the measured vertical velocity at 85 km is about $3 - 5\ cm/s$. We consider this in a little more detail in Section (2.3.5).

2.3 Buckland Park Equipment

2.3.1 Transmitting Equipment

The transmitter operates at a frequency of 1.98 MHz in a pulsed mode. The pulses are Gaussian in shape and their width may be varied to suit a particular experimental design from about 20-200 μs. The pulse width determines the height resolution of the system; for a full width at half power of 20 μs, the height resolution is 3 km and for 30 μs, 4.5 km, and these widths represent the range for the work described here. The pulse repetition frequency and transmitter array polarization are under computer control, but only one PRF, of 20 Hz, has been used here. The transmitter peak power is about 50 kW, but this may vary from run to run depending on the transmitter tuning and general condition.

The transmitting array consists of four center fed half-wave folded dipoles arranged to form a square. The half-width at half-power of the polar diagram of the transmitting array is approximately 40°. Opposite dipoles are phased together, and by introducing a phase difference of ± 90° between the two pairs, either "ordinary" (0), or "extraordinary" (E or X), circular polarization may be chosen. The ionosphere is birefringent, and circularly polarized EM radiation corresponds to the characteristic wave. Linear polarization may also be obtained, but since this is not a characteristic wavemode, two magnetoionic components result if it is transmitted.

The possibility of mutual interference between these components makes it undesirable, and it has not been used in this work. Of the two characteristic waves, extraordinary mode

polarization is strongly absorbed during the day at heights above about 80 km. For this reason, it is generally used during the night, and ordinary mode is used during the day.

2.3.2 Receiving Array

The receiving array consists of 89 horizontal half-wave dipole pairs arranged on a square grid with a roughly circular perimeter of about 0.9 km diameter. The dipoles that constitute each pair are orthogonal and each dipole is connected to the central receiver building through a buried coaxial cable cut to an integral number of half wavelengths. In this way each of the 178 individual dipoles can be accessed from the central hut where the phase of the signal received at the dipole is reproduced.

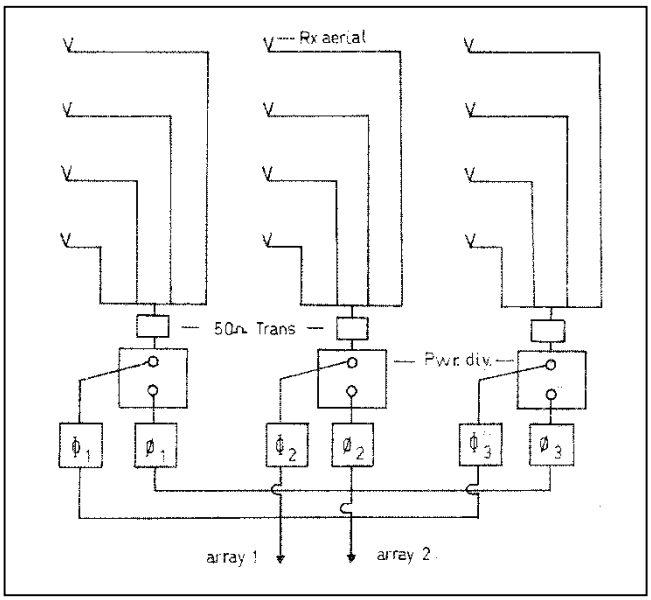

Figure (2.4) Schematic diagram of the array in broadside array configuration. The twelve aerials in this diagram represent one array of dipoles Columns of dipoles are connected to each other and their impedance is transferred to 50 ohms. Each column is then connected to a power divider which provides two identical outputs differing from the original signal only in that their power has been halved. Each output can be treated completely separately by summing the outputs from each column, two circular beams can be obtained. The two beams may be tilted from the zenith by introducing phase delays ϕ_i between the columns before their outputs are summed.

Each cable from the array of dipoles aligned in the north-south direction terminates in a coaxial connector on a "patch board". Here, the array is represented in a plan view with a coaxial connector representing each dipole. Similarly, the dipoles aligned in the east-west direction have cables which terminate in another patch board.

This is an extremely versatile arrangement because any dipole, or any group of dipoles may be used. It allows two completely separate linearly polarized arrays, one polarized EW and one polarized NS, or one (right or left) circularly polarized array- to be utilized. This can be improved on though. Figure (2.4) illustrates schematically the use of phase preserving power dividers to obtain four separate beams, two polarized NS, and two polarized EW. This arrangement halves the power received by each beam, but because the receiving site is relatively low noise and the transmitter is relatively high power, excellent signals are still obtained. The outputs from the power dividers were compared at 1.98 MHz over a range of input voltages using a gain-phase meter, and no significant variation between individual units was detected (a difference of less than 0.5 dB and 1° at 5 mV input).

When a patch board is connected up to produce a broadside array, aerials in a row (or column) are connected in parallel and the impedance is transformed to 50 ohms with a transformer / capacitor combination. The transformers for the EW array were designed for each row by assuming that each aerial was to be included and that each had an impedance of 70 ohms (purely resistive). The individual rows (or columns) are then connected in parallel and the impedance of this combination is in turn transformed to 50 ohms through a coaxial cable transformer / capacitor combination. In this way, the impedance of the array is matched to the input impedance of the receivers. There is a slight difference between the array with dipoles aligned NS and the array with dipoles aligned EW when they are set up as two separate broadside arrays. For the NS array, the transformer/capacitor combination to transform the impedance of the row or column to 50 ohms is inside the connector for each row. On the other hand, those for the EW array are positioned on the back of the patch board. However, this is a trivial difference.

In practice, when setting the aerials up in a broadside array configuration, some aerials must be omitted because they are out of tune or because they have been damaged in some way (e.g. by high winds or corrosion). However, the number of aerials omitted was generally small. Before commencing a run, every aerial was checked using a vector impedance meter. If the impedance differed from the correct value of 70 Ω (purely resistive) by more than about 10%, the aerial was omitted. The capacitor / transformer combination corresponding to the row or column of the omitted aerial was then changed so that an impedance of 50 Ω purely resistive was obtained for that entire row or column. The back scattered signal received by each aerial was also monitored on a CRO to check for noisy operation, a condition not always obvious

from impedance measurements, and omitted if significant noise was present. This involved a subjective judgement.

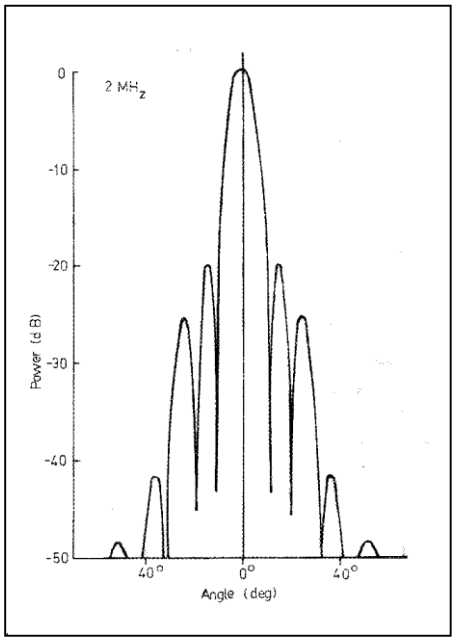

Figure (2.5) Polar diagram of an entire array of dipoles at BP (Re-drawn from Hocking (l983a)).

To tilt the beams away from the zenith, phase shifts were introduced between the rows (or columns) by using appropriate lengths of coaxial cable. This is a simple method for a fixed beam tilt, but involves a lot of coaxial cable (442 m were required to tilt one beam 11.6° and for four beams 1,769 m were required). The cables were accurately measured and cut to the required lengths, and the phasing cables for each of the four beams were checked against each other by using a gain-phase meter. Typical amplitude ratios, for two cables nominally the same length, were 0.1 dB and the largest phase difference was less than 4°.

Only two tilt angles were used for this work, 0° and 11.6°. The latter angle was chosen because it reduces the effects of specular reflections from the vertical (Hocking, 1979), as it corresponds to the first null of the array polar diagram (Figure 2-5).

Twelve aerials of the large array are used in the SA experiment. These are used as three groups of dipoles, each of which consists of four dipoles connected in parallel. This increases the gain, improves the signal to noise ratio and because the beam width is decreased, the effects of off vertical echoes are reduced (Figure 2.6). The impedance of each group of dipoles is transformed to 50 ohms, and they are connected through a 50-ohm cable to a receiver. The spacing between the receiving sites affects the results of the experiment, the so called "Triangle Size Effect"

(Golley and Rossiter, 1970; Rossiter, 1970) and a spacing of about 200 m has been shown to provide reliable results at 1.98 MHz (Stubbs, 1972). The relative aerial positions used for the SA experiment are shown in Figure (2.1a).

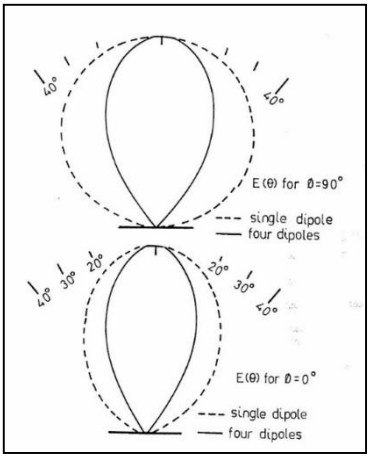

Figure (2.6) The polar diagram of a single horizontal dipole (dashed line), and of a group of four dipoles (solid line).

2.3.3 Receiving equipment

The receiving system is designed to measure complex amplitude information by recording the "in-phase" and "quadrature" components of the received signal. What this means is that the received signal is expressed as

$$E(t) = I(t) + iQ(t)$$

where $I(t) = "in-phase"\ component$ and $Q(t) = "quadrature"\ component$. This is processed so that the phase corresponds to the Doppler shifted frequency of the backscatter signal. Details of this may be found in Ball (1981) and Wilson and Miller (1971).

The amplitude and phase at any time are then simply given as

$$E(t) = (I^2(t) + Q^2(t))^{1/2},$$

$$\phi(t) = arctan(Q(t)/I(t)),$$

respectively.

Obviously, with this system, the phase relation between the in-phase and quadrature components must be such that the latter component leads the former by 90°. A problem arises

here with the BP system because this phase relationship may be changed by the system being turned off. This peculiarity made it necessary to monitor the phase relationship before commencing a data run and after any power failures. The effect of this phase change is to add or subtract 90° to the argument of $arctan(Q(t)/I(t))$. This multiplies the sign of ϕ by minus one, and any radial velocities measured by the Doppler technique are reversed in sign. The system maintained its phase unless it was turned off or the power failed.

In the DW run of July 1982 which extended over 16 days, and perhaps gave more opportunity to detect unusual effects, abrupt changes in radial velocity which could be related to phase changes were found on some occasions. An example of radial velocity time series obtained in this observational period is shown in Figure (2-8). This is in fact the clearest example. This diagram represents periods less than 8 hours only. On the 8th, an abrupt change in radial velocity is evident at the time of the polarization change in both beams above about 90 km, and in the southward beam time series it is evident down to about 82 km.

Since these beams were offset at equal and opposite angles to the zenith in the same vertical plane, this change, if it is real, can only correspond to a vertical motion of sufficient magnitude to dominate the contribution to the radial velocity from horizontal wind motion. At other times this effect was not present at all heights in each beam, and often did not occur in all beams at the same time and height. When it did occur in a number of beams at the same time and height, it often indicated a change in radial velocity of the same sign in each beam.

These effects are difficult to explain only in terms of a phase change because of their inconsistency from beam to beam and height to height, and even if the signs are reversed, the time series are not continuous. Abrupt changes in radial velocity can be found in this and other data sets at times not corresponding to polarization changes, and when the phase was known not to have changed, and consequently, the situation is rather complicated. Abrupt changes in velocity can be observed in SA observations obtained with amplitude only data, thus precluding any possibility of these changes resulting from a phase change (Figure 2-7).

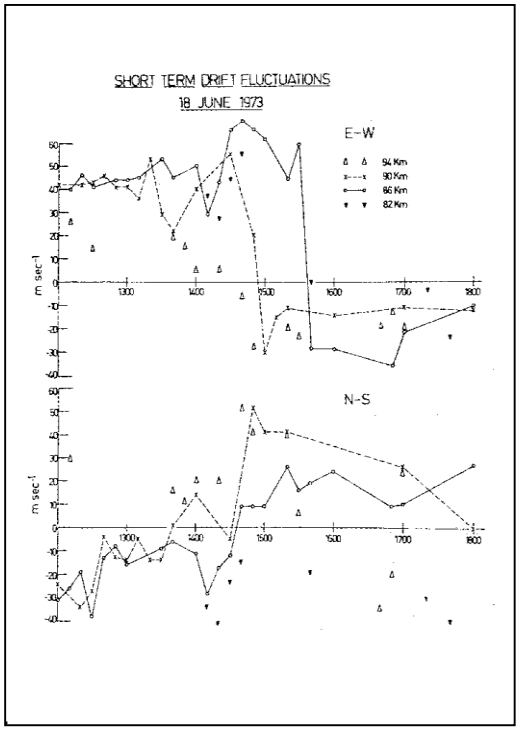

Figure (2.7) SA Wind results for 18th June, l973 from Briggs, Stubbs and Vincent (1974). Individual wind values represent ten minute averages. Note the abrupt changes in the zonal wind components between 1400 and 1500. These results were obtained with amplitude only data.

One possible instrumental explanation for the change in the July 1982 time series is that the transmitter pulse "broke up" occasionally, thus introducing additional frequencies into the phase of the returned signal. However, this is unlikely. Because there is some uncertainty in this particular data set, it has been analyzed somewhat cautiously. The mean square radial velocities are not changed significantly when the Section of the time series showing the abrupt changes is removed, but these data were not considered suitable for cross spectral analysis. Further details may be found in Chapter 6 and 7.

The receiving system was under the control of a 16-bit NOVA 2 minicomputer with three basic peripherals; a dual drive floppy disk system, a nine track read/write tape recorder (seven track, write only in November 1980) and a printer/terminal. The computer itself has 32,000 words of core memory, and whilst real time analysis of data was possible for low data acquisition rates, all of the data presented here has been analyzed off-line.

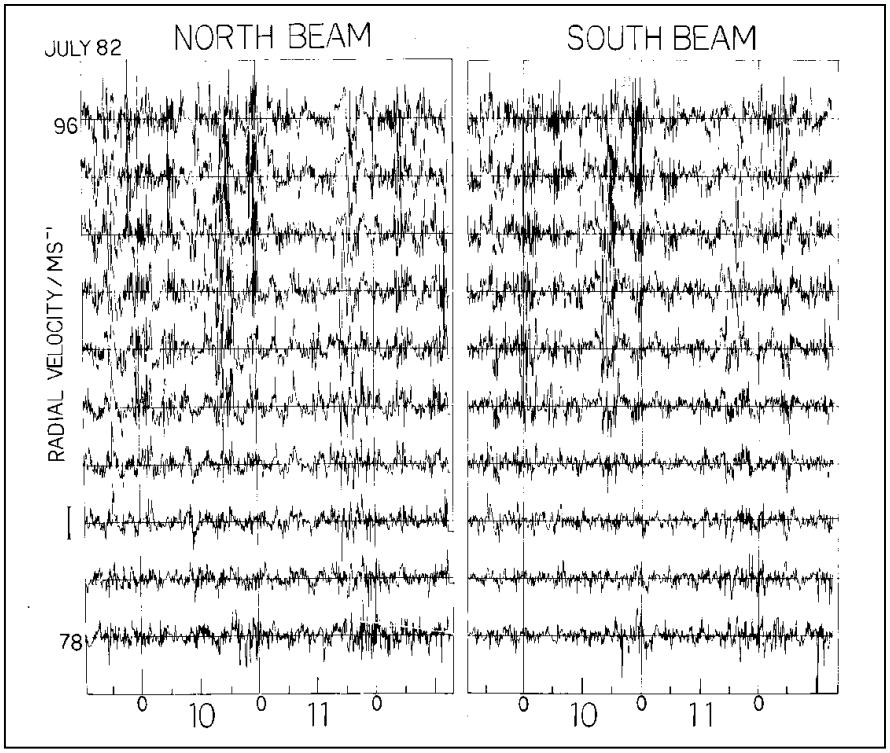

Figure (2.8) Radial velocity time series for motions with periods less than 8 hours. For details see text.

The parameters discussed below can be chosen to suit a particular experimental design. However, unless otherwise stated, those specified below are those that have been used for this work.

Data were sampled simultaneously on from one to four receivers over ten height ranges every 0.05s. Receiver outputs were digitized to levels, and adjacent height ranges were separated by 2 km. Every eight consecutive points from a given receiver and height range were averaged so that the signal to noise ratio was increased by eight times (coherent averaging). Thus data points were obtained every 0.4 s at each receiver and each height. After obtaining 256 such data points, each comprised of a real (in-phase) and imaginary (quadrature) component, data were written on to magnetic tape. This corresponded to a data set of 102.4 s duration, and data could be taken again·17.6 s later. That is, every 120 s, a maximum of 102.4 s of data could be obtained. The receivers were calibrated against each other by feeding a 1.98 MHz signal into a phase preserving power divider, and taking the identical outputs to the separate receivers. The receivers were then compared using a gain-phase meter. The receiver bandwidth is 25 kHz which gives an effective height resolution of 4 km.

2.3.4 Data Acquisition Programs

Two programs were used to obtain data. The first sampled 15 heights with fixed gain, which meant winds could be measured over a range of 30 km with a 2 km height interval. With this set-up, heights from 70-100 km were sampled. The second program was that used to obtain data for the SA experiment, but modified to handle a maximum of four, rather than three channels. This program was more flexible in that two separate 20 km height ranges (2 km interval) could be sampled at alternate times, and that the receiver gains were under computer control. Thus, if the alternate starting heights were 60 km and 80 km, the sampling rate would be one wind measurement every 4 minutes over 40 km.

However, as discussed in Chapter 5, the scatterers below about 80 km are very anisotropic, and this has important consequences for the interpretation of the Doppler spectra. Furthermore, below this height range, few wind values are obtained at night, and the analysis of discontinuous data presents some computational problems. Because of this, later data runs used the second program, starting at a range of 80 km for each two-minute sample. This meant one wind measurement could be obtained every two minutes, with variable receiver gain control, over 20 km with a 2 km height interval.

2.4 Beam Configurations and Nomenclature

The most typical arrangement for the multi-beam Doppler Wind technique is that in which one beam is offset from the vertical in the east-west plane, and another is offset by an approximately equal angle in the north-south plane. If it is assumed that the vertical velocity is essentially zero, at least for the mean wind and for the longer periods, then the radial velocities in these beams can be used to calculate the horizontal wind (see Chapter 4). If the complete wind field is to be measured, a vertical beam is also used. This last arrangement will be referred to as the Triple Orthogonal (Beam) Doppler experiment. The same arrangement without the vertical beam, that is, one beam eastward, one beam northward, will be referred to as the Dual Orthogonal (Beam) Doppler experiment.

These arrangements are commonly used to measure some of the mean and fluctuating components of the wind field. Whilst other arrangements are possible, they are not commonly used because most information of interest can be obtained from these two beam arrangements using the assumption that the wind vector is constant in a horizontal plane.

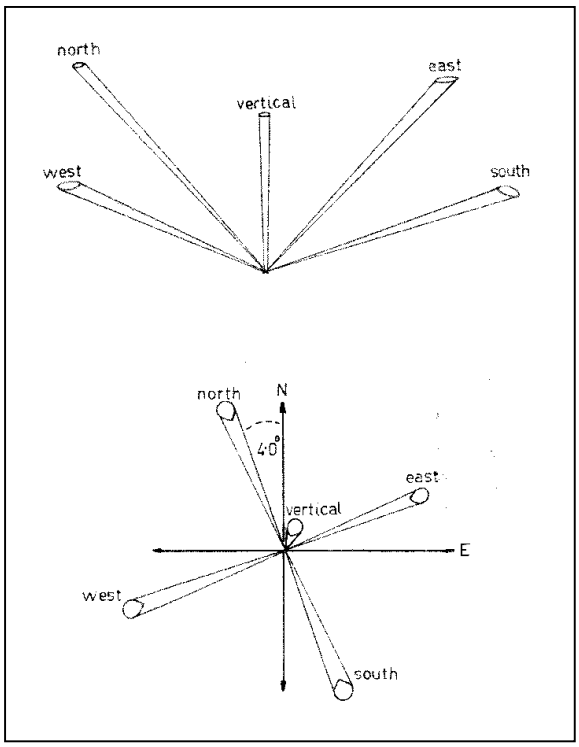

Figure (2.9) The beam positions available when using BP. A maximum of four channels are available at any one time. Note that beams are 4 degrees off cardinal axes.

Since the short scale component of the wind field may consist of turbulence of various scales and many randomly phased gravity waves of different frequency, horizontal and vertical scales, amplitudes, and propagation directions, measurement of many useful parameters related to the small scale motions requires a statistical approach. Since the mean values of the perturbation velocities of these motions will be close to zero, the mean square values are often of more interest. The mean square value of the radial velocity can contain a maximum of six terms depending on the beam pointing direction. By considering one vertical plane the number of beam pointing directions required to solve this Equation is reduced to three. However, with two suitably arranged beams, the variance and covariance terms in the mean square radial velocity Equation can be separated (see Chapter 4).

The beam arrangements used in this work have therefore depended upon the parameters required, and obviously upon the number of beams available. In November 1980 and May 1981 only two beams were available when using the entire array, however with the addition of phase preserving power dividers in mid-1981 this number was increased to three. In late 1981 this was increased to the maximum number of four beams available for this work. As more beams became available, experiments were designed to make full use of them. However, the complete

wind field could not be measured with four beams and so in any one experiment some quantities had to be omitted. The beam positions available are illustrated in Figure (2-9).

We now consider the beam arrangements used.

2.4.1 Dual Complementary Coplanar (DCC) beam arrangement

With this beam arrangement, two beams are offset from the zenith at equal and opposite angles in the same plane. Figure (2-10) illustrates this experimental arrangement for a zenith angle of 11.6°. The beam half width at half power is about 4.5° which corresponds to a full width half power of about 14 km at 85 km, and the beam separation between centers at the same height is about 35 km. This width will determine the smallest scale (gravity wave and turbulent) of motion that can be resolved by BP in this mode of operation (see Chapter 4). Note that the beam will be broadened by $sec(11.6°)$ by being pointed off-vertical (Skolnik, 1962). Useful horizontal winds can be obtained between about 80 and 96km, but the upper limit will be' determined by the leading edge of the E-region.

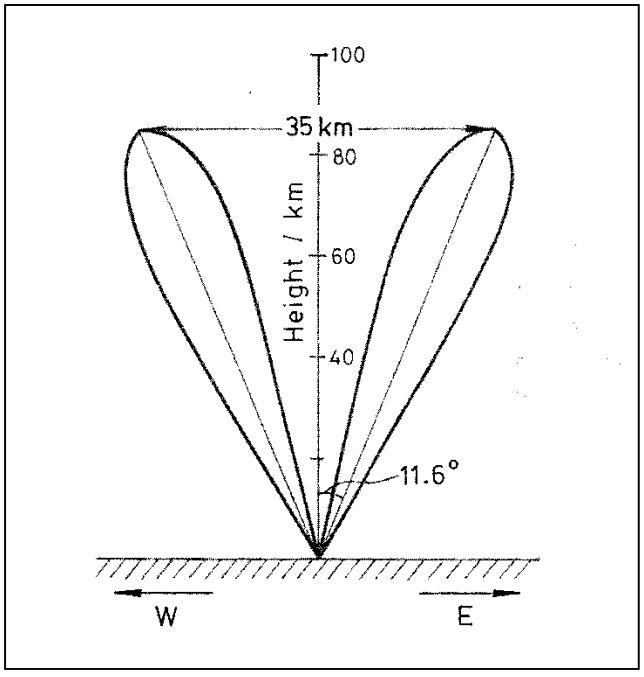

Figure (2.10) Schematic diagram of two beams tilted 11.6° from the zenith, one to the east and the other to the west. Note the separation of the beams and their half power and half width. This is the beam configuration used in May 81 and in the nomenclature out-lined in the text, is the Dual Complementary Coplanar beam arrangement. The beam width at half power is about 14 km.at 85 km.

2.4.2 Dual Coplanar (DC) Beams

This arrangement occurred as a sub-group of other experiments, except in September 1981 and February 1982 (when it was used with more than one beam pointing in the same direction to check for systematic channel differences). One beam is directed vertically and one beam is directed at $+\theta$ to the zenith in the same plane. Because of the relatively wide beams used, the separation of beams is rather small in this arrangement. The separation between half power points will be about 4 km, which together with the beam resolution of l4 km may make the measurement of horizontal scale difficult. Useful horizontal winds may be obtained over the same height range as for the DCC beam arrangement. Vertical winds may be measured above 60 km during the day, and above 80 km at night.

2.4.3 Triple Coplanar (Complementary Pair) TC(CP) Beam Arrangement

This is as in Section (2.4.1) but with vertically directed beam added.

2.4.4 Orthogonal Pair of Dual Coplanar (OPDC) Beams

In this arrangement four beams are used. One pair is aligned in the EW plane and these beams are directed at equal and opposite angles to the zenith. The other pair of beams is aligned in the NS plane and these are directed vertically and at $+\theta$ to the zenith.

2.4.5 Orthogonal Pair of Dual Complementary Coplanar (OPDCC) Beams.

Four beams are arranged so that one pair is directed at equal and opposite angles $\pm\theta$ to the zenith in the EW plane, and the other pair is arranged in the same fashion in the NS plane.

There are of course many other useful arrangements possible when using fixed beam positions. For instance, the "Coplanar Pair Dual CC" (CPDCC) Beam arrangement in which four beams are off-set from the vertical in the same plane, with one pair off set at equal and opposite angles, and the other pair arranged in a similar fashion at a different zenith angle. This would provide redundancy in the measurement of parameters in this plane and if one pair was arranged at 11.6° from the zenith and the other at a somewhat larger angle, the maximum scale measurable would be increased from that of about 200 km available when using $\theta = 11.6°$ (see Chapter 4). However, the maximum off zenith angle will be determined by the scattering polar diagram of the irregularities producing backscatter. Vincent and Belrose (1978) found that above 80 km returns may be received from up to 20° on occasion, and consequently the beam separation

could be increased to a maximum of about 60 km at 85 km. In practice, the optimum angle depends upon the polar diagram of the array as well as that of the scatterers and thus would have to be determined by observation.

The beam arrangements used in this work and the periods of observation are shown in Tables (2-1) and (2-2) respectively. The reasons for choosing a particular beam arrangement are discussed in Chapter 4. In December 1981 a combination of the usual SA aerial arrangement and a vertically directed narrow beam was used to simultaneously obtain horizontal and vertical winds. This has a number of advantages over using the Triple Orthogonal Beam arrangement at 2 MHz at BP although the horizontal scale of the motions cannot be obtained. Because the scatterers in the D- region (60 – 100 km) are rather anisotropic, backscatter signals are returned only from angles close to the zenith.

NAME	ARRANGEMENT	ACRONYM
Dual Orthogannal	Two beams in orthogannal planes. (All planes referred to are vertical.)	DO
Dual Coplanar	Two beams in same plane	DC
Dual Complementary Coplanar	Two beams in same plane at equal and opposite zenith angles.	DCC
Triple Orthogannal	Triple beams in orthogannal planes.	TO
Triple Coplanar	Three beams in same plane	TC
Triple Coplanar (Complementary Pair)	Three beams in same plane, two of which are at equal and appropriate zenith angles.	TC(CP)
Orthogannal Pair Dual Coplanar	Two pairs of coplanar Beams in orthogannal planes	OPDC
Orthogannal Pair Dual Complementary Coplanar	Two pairs of complementary Coplanar Beams in orthogannal planes.	OPDCC

Table (2.1) Beam configurations used and their acronyms

Date	Data type	Beam Configuration	Remarks
21-30 Nov 80	SA	Standard SA	Townsville Equipment
21-26 Nov 80	Doppler	DO	Equipment failure on 26 Nov 80 BP receiving equipment
11-14 May 81	Doppler	DCC	East-West plane
15-17 Sep 81	Doppler	DC	Two vertical beams, one beam 11.6° Eastward.
6-9 Nov 81	Doppler	TC (CP)	East-west plane
3,5,6 Dec 81	SA/Doppler	Standard SA; vertical beam	Equipment failure 4 Dec 81
7-10 Dec 81	Doppler	OPDC	Complementary Beam EW plane vertical and Northward Beam NS plane
16-19 Feb 82	Doppler	OPDC	As for Dec 81. Equipment failure 19 Feb 82
23-26 Feb 82	Doppler	OPDCC	Complementary beams EW plane Complementary beams NS plane
26-29 Feb 82	Doppler	DC	Two vertical beams Two beams 11.6° westward.
29-31 Feb 82	SA	Standard SA	
21-26 Apr 82	Doppler	OPDC	As for Dec 81
18-20 May 82	Doppler	OPDC	As for Dec 81 Equipment failure 20 May 82
30 Jun - 6 July 82	Doppler	OPDC	As for Dec 81
6-16 Jul 82	Doppler	OPDCC	Complementary Beams EW plane Complementary Beams NS plane
4-8 Oct 82	Doppler	OPDCC	As for 6-16 Jul 82.

Table (2.2) Data observation periods and beam configurations used. Equipment failures during October 1981 and late December 1981 runs made data from these periods unusable and these have been omitted from this table. It is interesting to note that 40 km of magnetic tape were required to store this data and this highlights the need for an efficient real time analysis.

Lindner (1975b) and Hocking (1979) found most returns from angles of less than 2-3° at those heights below about 80 km at 2 MHz when using the BP array. Since the array half-power half-beam width in this mode is about 4.5°, off vertical beams cannot usually be used to obtain

measurements of horizontal winds in this region without correcting for the effective beam direction (see Chapter 5). However, the SA technique is not restricted in the same way because it makes use of the enhanced echoes from the vertical. It does require sufficient ionization to produce backscatter of course, and this is generally present only during the day below about 80 km.

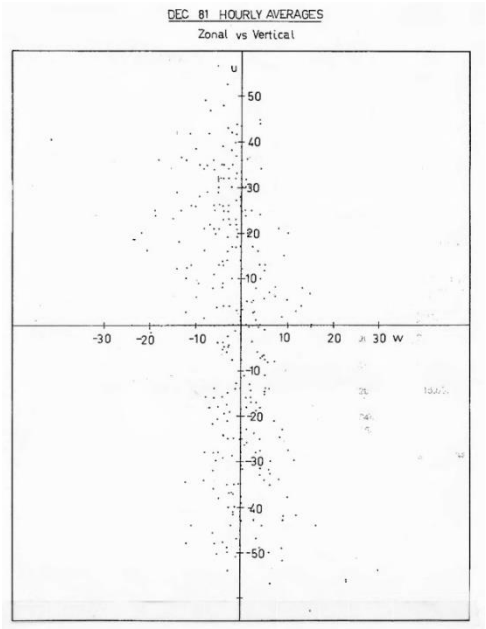

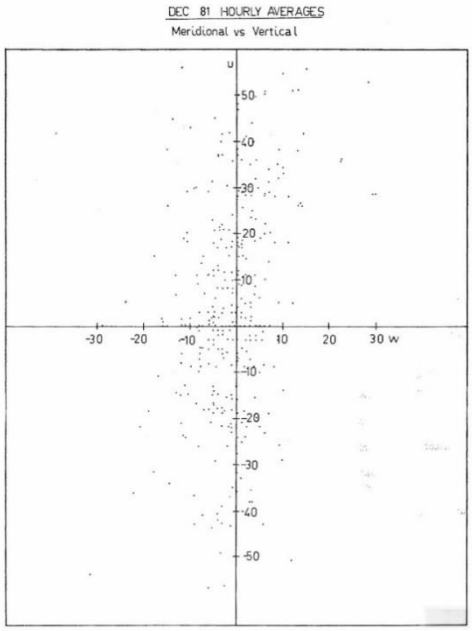

Figure (2.11a) (above left) Scatterplot of SA derived zonal winds (u) and Doppler derived vertical winds (w). Note that the vertical scale is in cms^{-1}. Each point represents a one-hour average, and results from all heights in the range 80-90 km are plotted on the same diagram

Figure (2.11b) (above right) As for Figure (2.11a) but for the meridiona1 component.

This particular experimental arrangement allowed horizontal and vertical components of the wind to be measured down to about 68 km during the day, and above 80 km at night. Thus the Reynolds stress terms $\overline{u'w'}$ and $\overline{v'w'}$ can be obtained in principle in the region below 80 km as long as sufficient data acceptance rates are obtained. It also enabled a comparison of vertical velocities measured with the three wide SA beams to be made with those obtained with the narrow full array beams; the results of which are discussed in Chapter 5. One other comparison was also possible. The vertical and horizontal winds could be compared for consistency to determine the tilt of the vertical beam. Although there is a relation between vertical and horizontal components for each scale of motion, averaging over a few days of observations should leave only the mean wind.

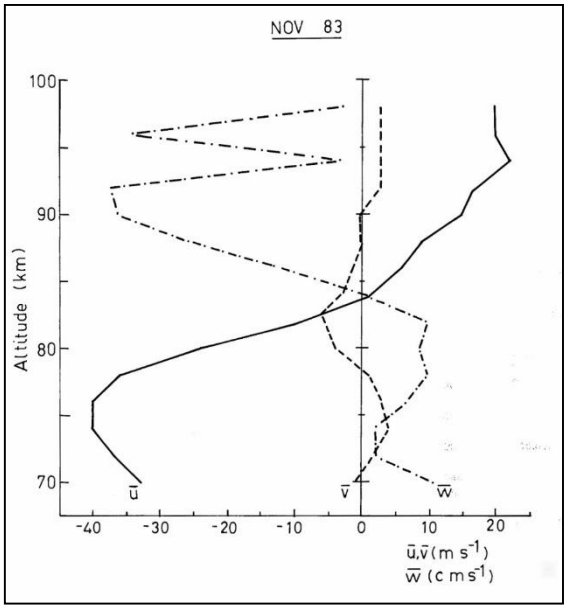

Figure (2.12). The mean zonal (u), meridional (v), and vertical (w) wind velocity for one month of observations obtained in November 1983.

Because these results are pertinent to the effective vertical beam pointing direction we present them here. Figures (2-11a) and (2-11b) show the hourly average zonal and meridional wind values obtained from SA measurements plotted against the measured vertical component for three days of observation for all heights in the range of 80–90 km. No clear correlation is evident. Note that the vertical scale is (cms^{-1}). As further evidence that the vertical beam is directed quite close to the vertical, we present the mean zonal and meridional wind profiles with the vertical wind profile for the month of November 1983 in Figure (2-12), (May and Vincent, private communication). These results are the first obtained at BP using real time analysis.

The measured vertical velocity is consistent in sign with that expected from a tilt towards the south-west, but is somewhat larger over most of the height range. The apparent vertical velocity $\delta\overline{w}$ that would be obtained with a beam tilted at 0.1° towards the South-West and the values of (u, v) for November 1983 are shown in Table (2-3), together with the measured radial velocity for the same period. If we assume that the real vertical velocity is zero, we may calculate the tilt θ required to produce the measured vertical velocity. This is also shown in Table (2-3).

ALT	$\delta\overline{w}$	V_R	θ
70	4.2	10	.24
72	4.3	1	.05
74	4.4	2	.04
76	4.6	7	.21
78	4.3	10	.23
80	3.5	9	.26
82	2.0	10	.51
84	2.5	0	0.0
86	+0.6	-12	1.9
88	-1.1	-26	2.3
90	-1.9	-36	1.9
92	-2.5	-37	1.5
94	-3.1	-3	0.11
96	-3.8	-34	1.2
98	-2.8	-3	0.11

Table (2.3) The contribution of the horizontal wind $\delta\overline{w}$ to the measured vertical velocity, the measured vertical velocity $\overline{V_R}$, and the tilt θ of the vertical beam from the zenith calculated assuming that the mean vertical wind is zero for the monthly mean winds shown in Figure (2-12).

The off-vertical angle of a vertically directed beam is almost certainly less than 1°, because beam swinging experiments on the totally reflecting E-region reproduce the polar diagram of the array to within this amount (Hocking, l98l), so that the vertical velocity above 86 km must contain a significant contribution from the real vertical wind. While the values of V_R and $\delta\overline{w}$ are of the same sign in Table (2-3), this is not the case in general for other observations made during this work. Table (2-4) illustrates similar results for 2 days in May 1982.

ALT	$\delta\overline{w}$	$\overline{V}_R$
80	-3	-28
82	-3	0
84	-3	+11
86	-3	+19
88	-3	+14
90	-2	+11
92	-4	+8
94	-2	+7
96	-.1	+1
98	+3	-4

Table (2.4) As for Table (2.3), but for May 82.

If the measured vertical velocity is produced solely by the horizontal wind component, then these results indicate an off vertical angle opposite to that indicated by those in Table (2-3). While this would be possible if the tilt of the water table changed with the seasons, it seems unlikely.

2.5 Systematic and Random Differences between radar beams

In order to check for systematic differences between separate beams and corresponding receivers, beams were directed to the same direction and radial velocities obtained were compared for systematic and random differences. This was done for three or four hours in May 1981 and for three days in September 1981. However, we will only consider one representative example here. Three days of observations were taken in February 1982. Two beams were directed vertically and two beams were directed westward at 11.6° to the zenith.

Data were acquired at the rate of one record every six minutes between 80 and 90 km and at 1 record every twelve minutes between 70 and 78 km and 92 and 96 km. The data acceptance rates for individual two-minute wind determinations are illustrated in Figure (3-9c). Below 84 km data acceptance rates were less than 50% and below 80 km were considered too low for further analysis. Since the height range of interest for this work is above 80 km, this last fact is of little direct consequence.

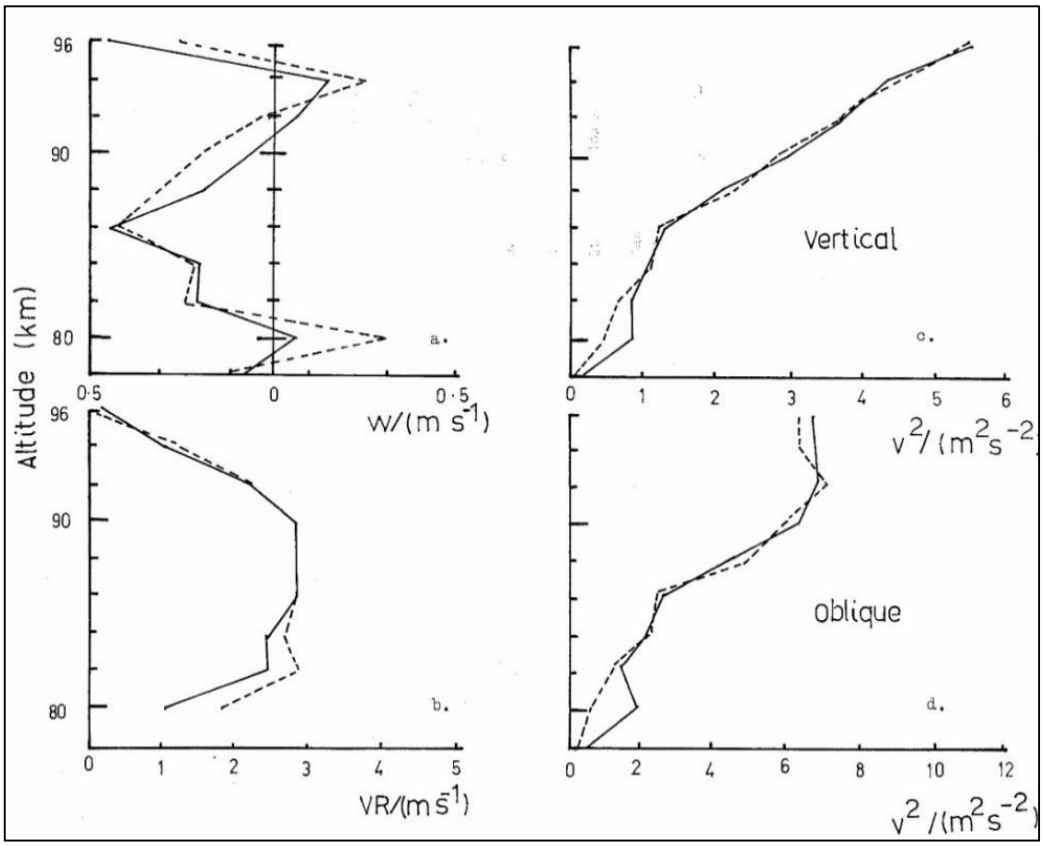

Figure (2.13a) Mean radial velocity for two vertically directed beams. (b) As for (a) but for two beams at $\theta = 11{\cdot}6°$ (c), mean square radial velocity for two vertically directed beams for motions with periods less than 8 hours. (d), as for (c), but for two beams directed at $\theta = 11.6°$.

For the heights above 80 km the data were analyzed to produce separate radial velocity time series corresponding to each of the beams. These were then used to calculate the mean radial velocities for the pair of vertical beams and the pair of off-vertical beams. These are shown as a function of height in Figure (2-13a and b) respectively. The radial velocity from a vertical beam is of course a direct measure of the vertical wind and this is plotted in Figure (2-13a). The weighted mean absolute difference between the two vertical profiles shown in this diagram for heights above 80 km is 0.1 ms^{-1}. The corresponding difference for the off-vertical radial velocities which are positive westward, is also 0.1 ms^{-1}. This is fairly crude measure but can be taken as an indication of the error due to channel differences. The corresponding weighted mean relative errors are 34% and 10% respectively.

The time series were further analyzed using the procedure outlined in Section (3.3) to obtain the mean square radial velocities for periods less than 8 hours and these are shown in Figure (2-13c and d). Above 82 km both show excellent agreement and the mean absolute difference for the mean square radial velocities obtained from both the vertical and off-vertical beams is 0.1 m^2s^{-2} (or 5%).

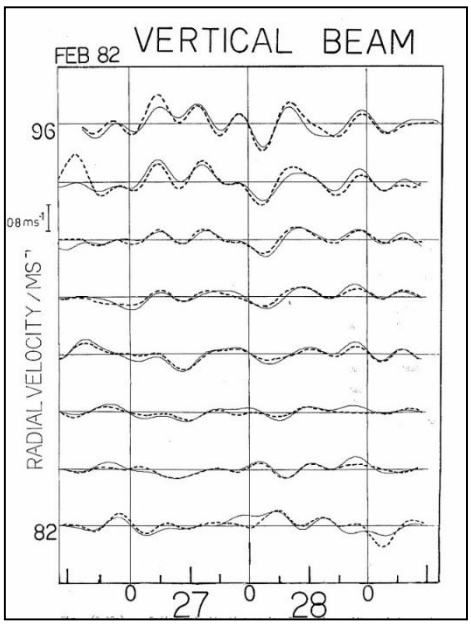

Figure (2-13e) Radial velocity time series for motion swith periods longer than 8 hours measured in two vertically with periods greater directed beams.

These diagrams of $\overline{V_R^2}$ are only meant to indicate the relative values obtained in each pair of beams. No account has been taken of the missing data and some rescaling is necessary if comparisons between heights (especially lower heights) are to be made. However, to convert

these diagrams to $\overline{u'^2}$, $\overline{V_R^2}$ should be x 38 and 37 $\overline{w'^2}$ should be subtracted; this would give about 123 $m^2 s^{-2}$at 90 km or (11 ms^{-1} RMS) (See Chapters 4 and 5).

The agreement between the longer period motions ($> 8\ hours$) measured in the vertically directed beams is also good and Figure (2-13e) illustrates the low pass filtered velocities for a number of heights. There is some variation between these time series, but on the whole, agreement is very good, and harmonic analysis of each time series to obtain the tidal components would produce very similar results. ·

2.6 Portable Spaced Antenna Equipment

The portable SA equipment used in November 1980 is quite similar to that generally used at BP, although a much simpler receiving array is used.

2.6.1 Receiving Array

This array consists of three pairs of crossed half-wave dipoles arranged 1n the form of an equilateral triangle with a spacing of about 165 m between crossed dipole centers. Each dipole is tuned to 1.94 MHz and has the form of an inverted "V", with its center 10 m above the ground, and each end about 2 m above the ground. The impedance of a particular dipole is about 10 ohms because of its proximity to the ground, and this is transformed to 50 ohms by a balance to unbalance transformer. The dipoles are then connected through 50 ohm cables, three half wavelengths long, to the receiving equipment. Signals received by each dipole are fed back to the central receiving site separately, where the appropriate connections and phasings are made. With a phase change of ± 90° between the dipoles of each pair, either O or E modes of polarization can be received. However, only one dipole, which was aligned in the EW direction, was erected at each receiving site at BP for the November 1980 run, and the dipoles were not re-tuned to 1.98 MHz, the BP frequency, because of the limited time for which the equipment was available. Even so, echoes returned from the D-region proved to have satisfactory complex amplitudes. The aerial layout used is shown in Figure (2-1b).

2.6.2 Receiving Equipment

This is essentially the same as the BP equipment. The main differences being that only three receivers are available, the system is controlled by a microprocessor rather than a minicomputer, and the tape recorder is seven track/write only, rather than nine track.

2.7 November 1980 Doppler Wind / Spaced Antenna comparison.

In November 1980 only two channels capable of recording amplitude and phase, and only two narrow beams were available when using the 1 km x 1 km MF array at BP. However, by using the portable SA receiving equipment and aerials which were in transit from Townsville to Mawson Base, it was possible to make a comparison of winds measured by the SA and Doppler techniques.

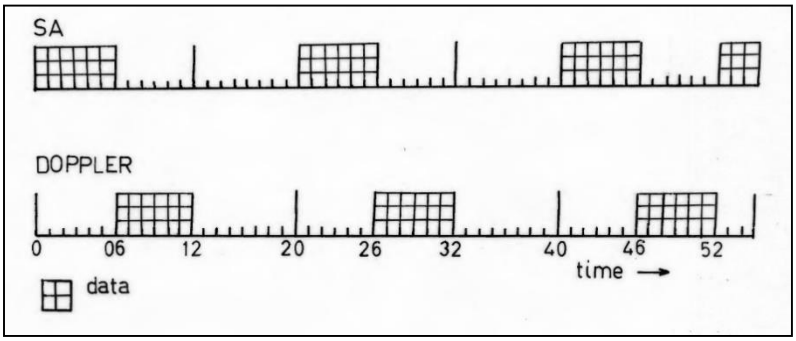

Figure (2.14) Schematic diagram of data acquisition scheme for SA/Doppler wind comparison. The transmitter (Tx) was controlled alternately by each system. The SA system took six minutes' data then remained off for 14 minutes. Doppler system ditto. This gives nine·2-minute samples for each technique per hour. The Tx PRF was 20 Hz, and coherent averaging over 8 Tx pulses was applied. Both systems stored data on magnetic tape. SA height range was 80-100 km in 2 km steps; Doppler, 78-98·km in 2 km steps.

The aerial layout for this experiment is shown in Figure (2-1). The SA receiver rack, containing all of the receiving equipment and microprocessor controller was temporarily installed in a building south of the main array. Single 'droopy dipole' aerials were erected and positioned in the EW direction by aligning them up, by eye, with the aerial poles running along a given NS row of the main array. This simplified the task of laying out the receiving array and gave a spacing between dipole centers of 183 m, a distance about optimum for the D-region SA experiment.

The transmitter was controlled alternately by the BP and SA systems, but the receiving equipment remained completely independent. The BP system triggered the transmitter and recorded data for six minutes, and then waited for fourteen minutes. The SA system started triggering the transmitter and taking data immediately following the BP system and continued for six minutes. It then waited for fourteen minutes. In this way, three two-minute wind determinations were made by each system every twenty minutes (Figure 2-14). The large array

was connected up as two broadside arrays with the beams pointing northwards and westwards 11.6° from the zenith (Figure 2-15). Nine days of SA observations were obtained, but the receiving equipment of the BP facility failed after five days. A summary of the BP and portable SA equipment parameters as used in November 1980 is given in Table (2-5).

SUMMARY OF SYSTEM SPECIFICATIONS

(a) Buckland Park Location 34° 38'S, 138° 29'E.

(1) Transmission

Frequency	1.98 MHz
Wavelength	151.5m
Peak Power Output	50kw
Pulse length	20-30μs
Range resolution	3-4.5km
PRF	20Hz
Tx aerial	Four centre fed half wave folded dipoles arranged in the form of a square. Supported 30m (λ/4) above the ground.
Tx array polar diagram	±40° half power
Tx array polarization	O,X.

(11) Reception

Rx bandwidth	25KHz at half power
Gain	100dB
SA aerials	3 groups of four half wave dipoles connected in parallel. Centre of each group located at the corners of triangles of sides 182m, 204m and 204m.
Width of SA aerial polar diagram	±20°
Broadside array	Each row or column connected in parallel.
Width of array polar diagram	±4.5° half power
Polarization	Linear (circular can be used).

(111) Data Acquisition

Type of data recorded	"In-phase" and "Quadrature"
Number of heights sampled	10, 15, 20
Width of height interval	2km
Number of points coherently averaged	8
Data sampling rate	2.5Hz

Table (2.5) Summary of Buckland Park system specifications

(b) Portable SA Equipment (November 1980 case, reception only).

(i) Reception

Rx bandwidth	30 KHz
Rx aerials	Single droopy half wave dipoles located at corners of triangle of side 183m
Rx array polarization	linear

(ii) Data Acquisition

Type of data recorded	"In phase" and "Quadrature"
Number of heights sampled	10, 20
Width of height interval	2km
Points coherently averaged	8
Data sampling rate	2.5km

Table (2.5) (cont.) summary of portable SA equipment

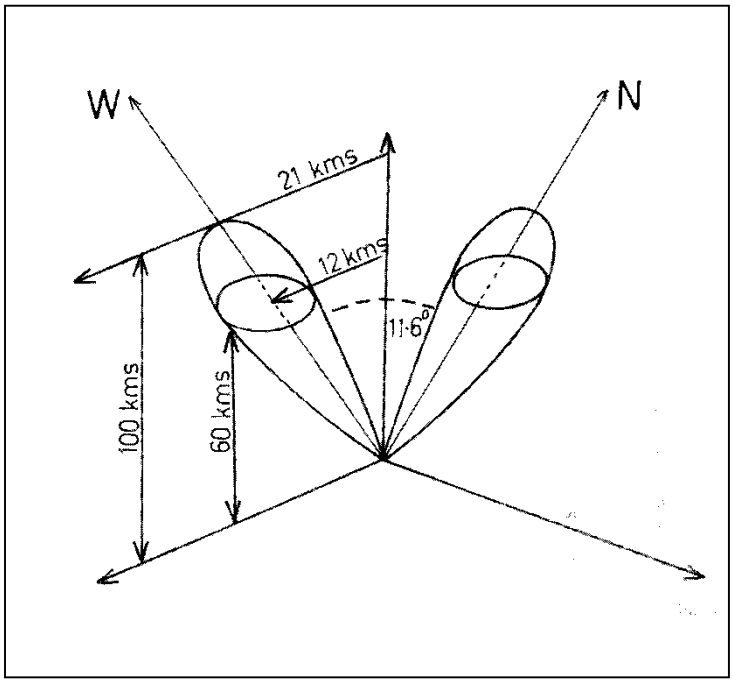

Figure (2.15) Beam configuration used to obtain Nov 80 Doppler data. One beam is offset 11.6° in the EW plane, and the other an equal angle in the NS plane. In the text this beam arrangement is referred to as "Dual Orthogonal".

2.8 Summary and Conclusions

This Chapter has outlined the equipment and experimental procedure as applied in this work. For the most part, it is fairly straightforward. The nomenclature suggested for the various beam configurations is somewhat clumsy and could be improved on, but this is of minor concern. The most important parts of this Chapter are concerned with whether a vertical directed Doppler beam is in fact directed vertically, what is happening to the radial velocities in the July 1982 data set, and the error in the mean square radial velocities.

The survey of the array indicates that the physical ground is very flat and if the electrical ground is similar, then a vertical beam will be directed very close to the zenith. The scatter plots of SA derived winds and Doppler wind derived vertical velocities support the assumption of similar slopes for physical and electrical grounds, as does the data obtained in November 1983. In addition, a comparison of vertical velocities measured in wide (±20°) and narrow (±4.5°) beams indicates good agreement, and since the wide beams are relatively insensitive to the slope of the ground, we feel confident that the evidence indicates that a vertical beam is indeed directed vertically. The results of this particular comparison are presented in Chapter 5.

The abrupt changes in radial velocity in the July 1982 data set, given only cursory treatment in this Chapter, are somewhat harder to come to grips with. The period in which these data were taken was characterized by increased geomagnetic activity and is certainly not typical in this respect of the other observational periods. Detailed analysis exceeds the constraints imposed for this work, and this problem is left for future study. We have however, treated the data in question somewhat cautiously.

The single most important part of this Chapter is concerned with the systematic and random differences in the mean square radial velocity because the error in this quantity will determine the smallest momentum flux that can be resolved. The mean relative error of about 5% means that very accurate measurements of the Reynolds stress and vertical mean square perturbation velocities are possible when observations are averaged over 2-3 days.

In the next Chapter we consider the basic analysis of Doppler spectra and radial velocity time series.

3. Basic Doppler Wind Data Analysis

3.1 Introduction

In this Chapter we are concerned with the basic analysis of the Doppler spectra of backscattered radiation to measure the mean radial velocity of the scattering volume determined by the radar pulse lengths and beamwidth. Here we are only concerned with the accurate retrieval of this information from finite, discrete data lengths, and other considerations are discussed in Chapter 5. General reviews of the analysis of Doppler radar data may be found in Wilson and Miller (1971) and Doviak et al. (1979).

In the next Section we consider some basic ideas related to the measurement of Doppler spectra.

3.2 Basic Ideas

In this Section we consider some basic concepts related to the measurement of the Doppler spectrum produced by radar backscatter. We begin with a n elementary case.

Consider a radar transmitting a plane radio wave of amplitude E_T and frequency ω_0 vertically upward.

The signal transmitted may be expressed as

$$\boldsymbol{E}\,(\boldsymbol{t}) \;=\; \boldsymbol{E_T}\,(\boldsymbol{t})\boldsymbol{e}^{\boldsymbol{i}\omega_0\boldsymbol{t}}. \tag{3-1}$$

A stationary point “target", which in this case may be any fluctuation in refractive index in the volume defined by the radar receiving array beamwidth and the transmitted pulse length, which produces a weak reflection or backscattering of the incident radiation, will return a signal

$$E\,(t) \;=\; E_0\,(t)e^{i(\omega_0 t+\frac{4\pi}{\lambda}R)}, \tag{3-2}$$

where λ = the radar wavelength, R = the instantaneous range of target measured along the radar beam, and E_0 = the voltage of the returned signal.

If the target is moving, the frequency of the returned signal will be Doppler shifted so that its angular frequency ω_R is given by

$$\omega_R = \omega_0(1 + \frac{2V_R}{c}), \tag{3-3}$$

where V_R = radial velocity of target, and c = velocity of light.

For a narrow beam, the radial velocity is the projection of the target velocity on the beam radial direction, that is

$$\boldsymbol{V_R = v \cdot \hat{r},} \tag{3-4}$$

where, for example, 1n this work $\boldsymbol{v} = u\boldsymbol{i} + v\boldsymbol{j} + w\boldsymbol{k}$, and

$$\hat{\boldsymbol{r}} = sin\theta sin\phi\boldsymbol{i} + sin\theta cos\phi\boldsymbol{j} + cos\theta\boldsymbol{k},$$

where (u, v, w) are the zonal, meridional and vertical components of the wind field respectively, and (θ, ϕ) are the angles measured from the zenith and clockwise from north for the co-ordinate aries shown in Figure (4-1).

The returned signal is then

$$E\,(t) = E_0\,(t)e^{i(\omega_R t + \frac{4\pi}{\lambda}R)}. \tag{3-5}$$

This is processed to obtain

$$a(t) = E_0(t)e^{i\omega_d t}, \tag{3-6}$$

where $\omega_d = \omega_R - \omega_0$, so that from (3-3)

$$\omega_d = \frac{4\pi V_R}{\lambda}, \tag{3-7}$$

or

$$f = \frac{4V_R}{\lambda}. \tag{3-7'}$$

That is, the radial velocity may be obtained from the processed signal described by (3-6) as a frequency shift. Equation (3-6) is generally written as the "In-phase", $I(t)$, and "Quadrature", $Q(t)$, components which are defined as

$$I\ (t)\ =\ Re(a(t))\ =\ E_0 o(t)\ cos\ (\omega_d t), \tag{3-8}$$

and,

$$Q\ (\ t)\ =\ Im(a(t))\ =\ E_0(t)\ sin\ (\omega_d t), \tag{3-9}$$

respectively, so that at any time t the amplitude of the returned signal is given by

$$E_0(t)\ =\ (I^2\ (t)\ +\ Q^2\ (t)\ )^{1/2}, \tag{3-10}$$

and its phase is given by

$$\phi\ =\ tan^{-1}(\frac{Q(t)}{I(t)}). \tag{3-11}$$

The entire time series $a(t)$ may be analyzed by one of two essentially equivalent methods, namely power spectral analysis or autocorrelation analysis.

These techniques are equivalent because the Fourier transform of the autocorrelation function is the power spectrum. The former method may be easily illustrated using Equation (3-6). If the Fourier transform of (3-6) is given by

$$A(\omega) = \int_{-\infty}^{\infty} a(t)e^{-\omega t}dt, \tag{3-12}$$

then this represents an impulse of amplitude E_0 at $\omega = \omega_d$ for constant E_0. This represents a target moving with a radial velocity given by (3-7).

Because the scattering volume will not contain a single "target" in general, there will be multiple frequency components and E_0 will vary with time. In this case a spectrum of frequency shifts will result. The square of (3-12) for this case is

$$S(\omega) = |A(\omega)|^2, \tag{3-13}$$

where $S(\omega)$ is called the Doppler spectrum or power density spectrum and represents the backscattered power associated with a particular frequency.

As we have noted, the power spectrum is the Fourier transform of the signal autocorrelation function, that is,

$$S(\omega) = \int_{-\infty}^{\infty} \rho(\tau) e^{-\omega\tau} d\tau, \qquad (3\text{-}13)$$

where τ is the time lag. The autocorrelation function for a signal whose statistics do not change during the time of observation is given by

$$\rho(\tau) = \lim_{T\to\infty} \frac{1}{T} \int_{-T/2}^{T/2} \overline{E^*}(t) E(t+\tau) dt,$$

and the Doppler spectrum of radial velocities $\cdot S(V_R)$ is related to the power spectrum $\cdot S(\omega)$ by

$$S(V_R) = \frac{4\pi S(\omega)}{\lambda}.$$

Apart from the power, there are two other parameters of the Doppler spectrum that provide useful information, and for a Gaussian frequency distribution, completely specify its form. There are the mean frequency shift and the spectral width. In the next Section we briefly consider these quantities in relation to mesospheric backscatter spectra.

3.3 The Doppler Spectrum

The backscattered power is a direct measure of the refractive index variation within the radar pulse volume at a particular frequency shift, or radial velocity, and so the integral of the velocity spectrum is proportional to the total power reflected or scattered from the radar pulse volume.

In the D-region, variations in refractive index result from irregularities in the neutral air but are enhanced by free electrons. At 2 MHz and medium transmitter powers it is the free electrons that are detected and the fluctuations in electron density are taken to be proportional to fluctuations in the index of refraction, because the amount of ionization is small, and the collision frequency is large, so that a close coupling between the ionized and neutral gas components is expected.

The fluctuations themselves are believed to result from turbulence, and the resulting velocity spectrum is the Doppler velocity distribution weighted by the backscattered power. Thus the mean radial velocity is weighted in favour of velocities associated with the largest backscattered power, and the co-existence of scattering and reflection may make interpretation of the spectrum difficult, because individual spectral "spikes" may shift the mean value of the spectrum. The weight given to the radial velocities within the radar pulse volume will depend

upon the antenna pattern, the transmitted pulse-width and the receiver bandwidth in addition to the reflectivity of the scatterers.

If we ignore such effects for the moment, the Doppler spectrum will consist of a mean frequency corresponding to the velocity of the bulk motion of the scattering volume with a range of frequencies distributed about the mean corresponding to the "random" fluctuations of velocity within the scattering volume itself. For no background wind, and a narrow receiving array beamwidth and transmitter pulse-width, the width of the Doppler spectrum is a direct measure of the variance of the fluctuating velocities within this volume. Since backscatter radars are most sensitive to scales equal to half the radar wavelength (corresponding to Bragg scattering), this information is related to a particular scale of motion (about 75m at 2 MHz). The spectral width is exploited to obtain information about these scales (e.g. Gage and Balsley, l978).

In practice, finite beam widths and pulse lengths and the presence of a background wind contribute to the spectral width, and these effects must be considered. Hocking (1983a) has produced a coherent analysis of these effects, and has successfully analyzed spectral width data obtained using a complete array at BP at 2 MHz to measure turbulent energy dissipation rates in the D-region (Hocking, 1983b). The presence of turbulence also reduces the certainty in the measurement of the mean Doppler shift even for an infinitely narrow radar beam, because the spectral "line" corresponding to the mean radial velocity will have a finite width. In practice spectral broadening due to the effects mentioned above will increase this uncertainty.

The time series described by Equation (3-6) is normally only available at discrete time intervals and we now consider the standard results related to the analysis of the discrete Doppler spectrum and auto- correlation function of backscattered radiation.

3.3.1 The Discrete Doppler Spectrum and Auto Correlation Function.

In the following discussion of the discrete Doppler spectrum we follow Wilson and Miller (1971) to obtain Equations (3-14) to (3-21) and consider standard results which require little discussion.

The expression for the discrete Fourier Transform of Equation (3-12) of the estimate based on N time series samples may be written as

$$\hat{A}(k) = \sum_{n=0}^{N-1} a(n) \exp\left(\frac{-2\pi kn}{N}\right), \; -(\frac{N}{2} - 1) \leq k \leq \frac{N}{2}, \tag{3-14}$$

where $a(n)$ is the value of $a(t)$ at $t = t_n$, and the hat on $A(k)$ indicates that it is an estimate. The estimate of power $S(k)$ associated with the frequency interval f_k is given by

$$\hat{S}(k) = \left|\hat{A}(k)\right|^2, \tag{3-15}$$

and the kth frequency interval f_k is given by

$$f_k = \frac{k}{NT}, \tag{3-16}$$

where N = the number of time series samples, and T = the time interval between samples. T may be the radar pulse repetition period or, if coherent averaging is used, nT_R, where n is the number of radar pulses averaged over, and T_R is the radar pulse repetition period.

The finite number of time samples from which the estimate of the power spectrum is calculated limits the velocity resolution and creates a window effect, because the signal time series, which extends to infinity, is multiplied by a "window" of finite length. In the transform domain, the measured spectrum will be the convolution of the square of the Fourier Transform of the window function (the spectral window) with the true spectrum. The spectral window will generally be of the form $\left(\frac{\sin x}{x}\right)^2$, and power in the periphery of the true spectrum may be masked by leakage of power into the side lobes. This effect may be reduced by weighting the signal with a window that shows a more gradual change between data and no data regimes and so reduces the artificial side lobes in the measured spectrum.

In this work we are rather more concerned with the mean Doppler shift, and consequently, the limited resolution in velocity is of more direct concern.

The minimum velocity resolution ΔV_R may be obtained by substituting Equation (3-16) into (3-7'), in which case we obtain

$$\Delta V_R = \frac{\lambda}{2NT}. \tag{3-17}$$

Because the time series samples are only available at discrete intervals, an ambiguity in velocity can be produced if the radial velocity of the scattering medium is such that the phase changes

by more than π between samples T_n, T_{n+1}. This corresponds to the Doppler frequency shift being greater than one half the sampling rate,

$$f_N = \pm\frac{1}{2T}, \tag{3-18}$$

where f_N is the so called "Nyquist" or "aliasing" frequency. Thus the maximum unambiguous ("Nyquist") velocity is obtained by substituting (3-18) into (3-7) and is

$$V_N = V_{Rmax} = \pm\frac{\lambda}{4T}. \tag{3-19}$$

The maximum and minimum unambiguous ranges are easily obtained as

$$R_{max} = \frac{cT}{2}, \tag{3-20}$$

and

$$\Delta R = \frac{c\tau}{2}, \tag{3-21}$$

respectively, where τ = radar pulse length and c is the velocity of light. The parameters described by Equations (3-17) to (3-21) are shown in Table (3-1) for the system at BP as used in this work.

Parameter	**BP system value**
ΔV_R	$0.74\ ms^{-1}$
f_N	$\pm 1.25\ Hz$
V_N	$\pm 95\ ms^{-1}$
R_{max}	$6.00 \times 10^4\ km$
ΔR	$4.5\ km$

Table (3-1) Limiting parameters of the BP system as used in this work

It is clear that the only real limitations due to this choice of parameters are the velocity and minimum range resolutions.

It is worth noting that the velocity resolution can be improved by increasing the number of time series samples at a fixed sampling rate and as is discussed in (3.1.3c) this has other advantages. If the Doppler spectrum is well formed, it may also be reduced by interpolation.

Many researchers do not calculate the Doppler spectrum explicitly but obtain the complex auto correlation function (acf) instead.

This is related to the Doppler spectrum in a simple way as can be easily illustrated. Following Rastogi and Woodman (1974) we note that the j^{th} order derivative of $S(\omega)$ can be evaluated in terms of the j^{th} order derivative of the complex acf $\rho(\tau)$ at $\tau = 0$, where·

$$\rho(\tau) = A(\tau)e^{i\phi(\tau)}, \tag{3-22}$$

and $A(\tau) =$ the amplitude of the acf at lag τ, $\phi(\tau) =$ the phase of the acf at lag τ, and $\tau =$ lag in seconds.

The Doppler shift ω_d is the first moment of the power spectrum $S(\omega)$ so that

$$\omega_d = \int_{-\infty}^{\infty} \omega S(\omega) d\omega, \tag{3-23}$$

and consequently

$$\omega_d = \frac{1}{i}\frac{\rho'(0)}{\rho(0)} = \phi'(0). \tag{3-24}$$

That is, the slope of the phase of the complex auto correlation function at zero lag is equivalent to the Doppler shift in frequency. Using similar arguments, we may obtain the power, P, as

$$P = \rho(0), \tag{3-25}$$

and the spectral width σ^2

$$\sigma^2 = \frac{A''(0)}{\rho(0)}. \tag{3-26}$$

By applying Equations (3-24) to (3-26) these three quantities of the Doppler spectrum may be obtained from the acf. Like the Doppler spectrum this will only be available at discrete intervals, and Woodman and Guillen (1974) demonstrated how Equations (3-24) to (3-26) could be evaluated in this case. Their work indicated that the mean Doppler shift, power and spectral width can be obtained from two points of the acf, those calculated at lags $\tau = \tau_0$ and

τ_1, as long as τ is sufficiently small so that higher order terms of a Taylor expansion of $\phi(\tau)$ and $A(\tau)$ are negligible, and the coherently detected amplitude $E(t)$ forms a discrete complex Gaussian random process in time. The advantage of this particular procedure is that computing time is minimal, something that is particularly important for real time analysis. Woodman and Guillen (1974) showed that if τ is small enough, then

$$\widehat{\omega}_d \approx \frac{\phi(\tau_1)-\phi(0)}{\tau_1}, \tag{3-27}$$

since by definition $\phi(0) = 0$,

$$\hat{f}_d \approx \frac{1}{2\pi}\frac{\phi(\tau_1)}{\tau_1}, \tag{3-28}$$

which may be rearranged to yield

$$\hat{V}_R \approx \frac{\lambda}{4\pi}\frac{\phi(\tau_1)}{\tau_1}. \tag{3-28'}$$

The approximation $\phi(\tau_1) = \phi'(\tau_1)\tau_1$ involves errors of $O(\tau^3)$ due to the truncation of the Taylor expansion.

The estimate of spectral width σ^2 may be obtained from

$$\hat{\sigma}^2 \approx 2\frac{(1-A(\tau_1)/\rho(0)}{{\tau_1}^2}, \tag{3-29}$$

and the power is just

$$\hat{P} = \rho(0). \tag{3-30}$$

The estimate of σ^2 involves errors of $O(\tau^4)$.

Other sources of error in these estimates are the presence of both external and receiver noise in the processed signal, statistical errors in the estimates themselves, finite data lengths, and the finite width of the Doppler spectrum due to finite beam widths and turbulence. This last effect corresponds to an uncertainty in the slope of the phase at $\phi(\tau_1)$.

3.3.2 Noise

Noise in the received backscatter signal will affect all of these estimates. If it is uncorrelated, it will appear only at the zero lag of the amplitude of the acf, and the estimate described by (3-30) will be incorrect. If it is correlated for lags greater than τ_1, Equations (3-27) and (3-28) will also be incorrect. Rastogi and Woodman (1974) point out that for bandwidth limited noise, a suitable choice of τ_1 is $\tau_1 > B^{-1}$, where B is the bandwidth, so that there is an additional constraint on τ_1 in this case.

If a noise spike does appear at the zero lag of the amplitude of the acf, it can be removed in principle by interpolation over this point, and this has the advantage of providing a measure of the signal to noise ratio (SNR).

This is described in more detail in the next Section. In this work, SNR's were generally $\geq 10\ dB$, and when noise spikes were evident, they only appeared at $A(0)$. Because of this, the value of $\tau_1 = 0.4\ s$ appeared to be small enough so that uncorrelated noise in the backscatter time series did not contribute significantly to the error in estimates based on Equations (3-28) and (3-30).

3.3.3 Statistical Errors

Woodman and Guillen (1974) suggested that for their data, the errors in estimates given by (3-27) and (3-28) were comparable to those obtained by calculating the entire Doppler spectrum. The estimate for the error in $\phi(\tau)$ they applied has been given in the Miller and Rochwarger (1972) and Woodman and Hagfors (1969) as

$$\overline{\Delta\phi^2} = \frac{(1-\rho^2)}{2N\rho^2}, \tag{3-31}$$

where N is the number of sample points averaged and ρ is the auto correlation at τ normalized with respect to total power.

The RMS uncertainty in V_R is then

$$\Delta V_R = \frac{1}{(2N)^{1/2}} \frac{c}{2\omega_0} \frac{(1-\rho^2)^{1/2}}{\rho\tau}. \tag{3-32}$$

However, this expression does not seem to take the finite width of the spectrum into account. A review of Doppler weather radar techniques by Doviak et al. (1979) includes a discussion of the statistical errors in moment estimates based on covariance techniques. The discussion is directly applicable to the pulse pair technique, in which there may be two basic pulse spacings and which is a generalization of the work of Woodman and Guillen (1974). They give a maximum likelihood (ML) estimate of the auto covariance $R(\tau)$ as

$$\hat{R}(\tau_s) = \frac{1}{m}\sum_{n=1}^{m} E\big((n+1)\tau_s\big)\, E^*(\mathrm{n}\tau_s), \tag{3-33}$$

where m = the number of echo samples. This assumes a Gaussian spectral density and is strictly true if successive pairs give independent estimates of $R(\tau_s)$. The mean velocity is then

$$\hat{V}_{pp} = \frac{\lambda}{4\pi}\frac{\arg(R(\tau_s))}{\tau_s}, \tag{3-34}$$

and this is an unbiased estimate of the first moment for symmetrical spectra. In our case (3-33) and (3-34) correspond to the auto-covariance evaluated at lag τ_s and to Equation (3-28') respectively. Doviak et al. (1979) then consider the error in $\hat{V}_{pp}$ including correlated pairs and suggest that satisfactory estimation of the mean velocity can be made with an input spectrum width of up to about 0.4 of the Nyquist velocity (Equation (3-19)), and that the uncertainty in the estimate increases rapidly for larger widths. For larger widths the uncertainty increases exponentially and is given by

$$Var\big(\hat{V}_{pp}\big) = \frac{\lambda^2 \exp((4\pi\sigma_v\tau_s)/\lambda^2)}{32\pi^2 m{\tau_s}^2}\Big(\Big(\frac{N}{S}\Big)^2 + 2\Big(\frac{N}{S}\Big)\Big(1 - \exp\Big(-8\Big(\frac{2\pi\sigma_v\tau_s}{\lambda^2}\Big)\Big) + \frac{4\pi^{1.5}}{\lambda}\sigma_v\tau_s\Big), \tag{3-35}$$

where $S/N = SNR$, and the other terms have previously been defined for a Gaussian spectral density and white noise.

σ_v is the input spectral width and for $\sigma_v \sim 5\ m/s$ and $SNR = 10\ dB$ this gives,

$$VAR\,(\hat{V}_{pp}) = 0.52\ m^2\ s^{-2}, \text{ and}$$

$$\Delta\hat{V}_{pp} = \Delta\hat{V}_R \sim 0.72\ ms^{-1},$$

which is approximately the uncertainty in the radial velocity due the sampling interval. Equation (3-35) takes noise and spectral width into account and appears to be more generally applicable than Equation (3-32). It is noteworthy that Doviak et al. (1979) find that at low SNR's, the pp estimator has a lower estimate standard deviation than an FFT evaluated Doppler spectrum.

Given the assumptions of Gaussian spectral density and white noise in Equations (3-32) and (3-35) it seems more appropriate to estimate the uncertainty in radial velocities by analyzing the time series to obtain a measure of the uncertainty. This indicated errors of $0.7\ ms^{-1}$ in individual $102.4\ s$ determinations of radial velocity and since this is rather large when vertical velocities are measured, consecutive $102.4\ s$ estimates of radial velocity were averaged together to reduce the uncertainty.

3.3.4 Finite Data Lengths

The largest likely contribution to the uncertainty in V_R in this work is related to the assumption that $E(t)$ forms a random Gaussian process in time, and hence to the characteristic fading time of the received back scattered radiation. Hocking (1981) used a computer simulation of typical backscatter fading observed at BP, formed from a known Doppler spectrum, to show that if data lengths of 1-2 minutes of such data are Fourier transformed to produce a Doppler spectrum, then this does not necessarily correspond to the true spectrum. These spectra often contained strong spectral peaks that were not related to any components of the true spectrum, and consequently, would not be related to any real motion in the scattering volume.

Hocking estimated that minimum data lengths of (80-100)$T_{\frac{1}{2}}$, where $T_{\frac{1}{2}}$ is the fading time (the width of the auto correlation function, or the inverse width of the Doppler spectrum) are required to produce the true spectrum. Lindner (1975b) found that for observations made at BP, $T_{\frac{1}{2}} \sim 2 - 5\ s$ at 80-90 km, and so data lengths of 160-500 s may be required. Since computer limitations at the field site restricted the data lengths to 102.4s, some care was taken to ensure that acfs were Gaussian.

It is interesting to note that some experimenters select the peak and a few other spectral points from the spectrum of weak signals and use this as an ML estimator for the mean radial velocity (see e.g. Strauch, 1983). Whilst weak returns are rather different from short data lengths, the principle is still valid as long as data lengths are not too short relative to the characteristic

fading time, because the strongest backscatter returns are expected near the mean Doppler shift. In terms of acf analysis, this ML approach would correspond to taking the slope of the phase at the first lag as an estimate of the radial velocity regardless of the form of the acf.

However, some discretion must be used, because if specular reflections are present with frequency shifts significantly different from the mean frequency shift, the estimate may be poor. It is interesting to note that Röttger (1980) suggests that such specular contributions may form a Gaussian random process if sufficiently long data lengths are obtained. Consequently, a good estimate may be obtained by averaging sufficient spectra. Obviously, if a ML estimate of mean radial velocity is made, the width of the measured Doppler spectrum will not have any practical use, except perhaps to put rough upper and lower limits on the mean Doppler shift.

With such an estimate, another kind of ML approach can be applied by checking for consistency between adjacent radial velocities in time and height. This method has been used by Larsen et al. (1982), who checked radial velocity time series for abrupt changes in velocity, and rejected values that differed by more than about 6 ms^{-1} from adjacent values. However, some discretion must be applied in this case as well, because abrupt changes in measured velocity are observed which appear to correspond to real changes in the atmosphere. We have already given an example of this in Chapter 2, and Röttger (1982) has also given an example from simultaneous observations made with the SOUSY VHF radar and rawindsonde information.

The strong spikes observed in Hocking's (1981) short time series spectra would correspond to an oscillatory acf (Awe, 1964), and a radial velocity obtained by applying Equation (3-28') would be erroneous. Rastogi and Woodman (1974) noted that an oscillatory acf may also be formed if two or more scatterers are present in the radar pulse volume, and these are moving with significantly different velocities and backscattering similar amounts of power. For two such scatterers, the phase of the acf will oscillate with a beat frequency corresponding to the difference between the mean frequency shifts associated with the respective radial velocities, and an amplitude that depends upon the relative backscattered powers (see e.g. Rastogi and Bowhill, 1976; Hocking 1981).

In principle, this information could be exploited to determine the radial velocities, but this leaves the problem of which velocity is correct, and ignores the fact that short data lengths could also produce an oscillatory acf. Hocking (1983c) has pointed out that another effect that

could produce oscillatory acfs is related to returns obtained from specular reflection points on a tilted or corrugated reflector. Since such structures are known to be spatially and temporally intermittent in the D-region, this may occur in a sporadic fashion producing a Doppler spectrum with strong spectral spikes that may be related to the true bulk motion of the scattering volume. Again, a representative radial velocity may be hard to obtain.

Because a representative phase could not be determined from oscillatory acfs, they have been rejected in this work. No attempt has been made to determine why they were oscillatory. The possibility of large errors occurring by relying on one point of the acf has encouraged some researchers to use more points to measure the mean radial velocity. For instance, Rastogi and Woodman (1974) noted the strong dependence of ΔV_R on $\rho^2(\tau_1)$ Equation (3-31) and formed an estimate of the radial velocity from

$$V = \frac{V_1 A(\tau_1) + V_2 A(\tau_2)}{A(\tau_1) + A(\tau_2)}, \tag{3-36}$$

where V_1 and V_2 are the radial velocities calculated at $\tau = \tau_1$ and τ_2 respectively using (3-28'). Salah and Holt (1974) Fourier transformed power spectra obtained using the Millstone Hill incoherent scatter radar to obtain the complex acf, and then used a weighted least squares fit of the form $A^2(\tau)$ to the phase before measuring the phase of zero lag.

In this work, after the rejection criteria outlined in the next Section were applied, the phase of the acf at the first lag was generally representative of the phase up to a total shift of 10% of the data length, the maximum length usually considered suitable for acf analysis (Blackman and Tukey, 1959). However, as noted in Section 3.3.3, 102.4s estimates of radial velocity were averaged to give an overall sampling rate of one record every four minutes.

3.4 Rejection Criteria

The information written onto magnetic tape and subsequently analyzed consisted of 256 values of the "in-phase" and "quadrature" components for each 102.4s of data for each beam and for each height. Data values in each 102.4s block were 0.4s apart, and each consisted of eight coherently averaged data points. These data were analyzed off-line using a program based on an auto correlation analysis, and each block was subjected to the following procedure.

The mean and standard deviation were calculated, and if the mean was too high (receivers saturated for a significant time) or too low (little or no signal) or if the standard deviation was

low (low power) the sample was rejected. Data taken in May 1981, September 1981 and November 1981 used receivers with fixed gains, whilst later data were obtained with the receiver gains under computer control. In these latter runs, few data blocks were rejected because of low or high signals in the height range of 80-96 km. Two obvious exceptions to this were during HF fade outs, and when sporadic E was present.

The auto correlation functions of the remaining data blocks were calculated to 20 lags (8 seconds) and by interpolation over the first three points of the amplitude either side of $A(0)$, omitting $A(0)$, the signal to noise ratio (SNR) was calculated. This can be done for noise that is uncorrelated or correlated only for lags less than τ_1, since its contribution to the acf will appear at $A(0)$. The ratio of $\rho(0)$ to the interpolated value $\rho^*(0)$, therefore gives a measure of the SNR. If this was less than l dB the sample was rejected. However, a SNR of -6 dB also appeared to produce reliable results. Comparison of the results of this method of calculating the noise component agree well with results obtained from measurements of the noise signal made with the transmitter off (Hocking and Vincent, 1982).

It was found that the interpolation procedure used to calculate $\rho^*(0)$ occasionally broke down and gave spurious results. Further examinations revealed that these records had an irregular acf, which was actually very oscillatory, and were unreliable. Consequently, they were rejected. The acf was then checked for a significant oscillatory nature and rejected if this were so. As mentioned in the last Section, oscillatory phase can result from statistical effects due to the finite data length or from two or more scatterers moving through the radar pulse volume at different velocities. Both of these effects bias the phase. The number of records rejected for this reason was generally relatively small, a result which is in agreement with comparisons of velocities determined from backscatter spectra and other methods which show that the former method does measure the neutral air motion on average.

For the remaining records the parameters output were then:

(a) The mean and standard deviation of the signal

(b) Signal to noise ratio

(c) Measured half width of the acf

(d) Half width calculated from (3-29)

(e) Radial velocity

(f) Power calculated from (3-22) or from the standard deviation of the signal taking the SNR into account.

Since the array was not calibrated only relative powers were obtained.

Although the half-width of the acfs were calculated they have not been used in this work. However, examination of measured half widths and widths calculated from Equation (3-29) indicates general agreement for accepted records, which can perhaps be taken to indicate that the power spectra were sufficiently Gaussian, and τ_1 sufficiently small, so that (3-28') was valid. Observation of numerous acfs and power spectra corresponding to accepted records indicated that most were well behaved and that the first lag phase of the acf was representative of the phase up to lags of 8 seconds.

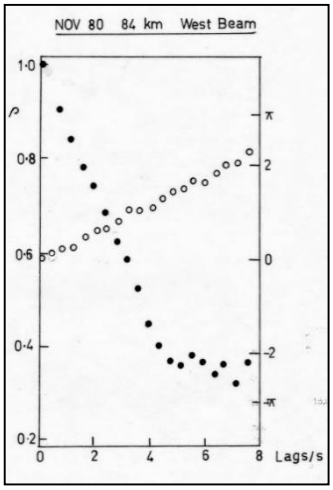

Figure 3.1 Example of an acf from an accepted 102.4s record chosen at random from the NOV 80 data set. The phase is clearly well behaved, although a slight oscillation is evident.

An example chosen at random is shown in Figure (3-1). Some oscillation is evident in the phase, but the slope at the first lag is clearly a good estimate. Two examples of rejected acfs are shown in Figures (3-2) and (3-3). These were chosen at random from the rejected records and illustrate oscillatory and irregular auto-correlations respectively. An example of an accepted 102.4s record is presented as a velocity spectrum in Figure (3-4). A Gaussian form is beginning to appear but records of this length do appear to be marginal. A fit by eye indicates $V_R \sim 11 m/s$ and from the first lag of the phase V_R is found to be $\sim 10\ m/s$. The long tail of the spectrum extending into negative values of V_R may be biasing the result, but this example

indicates statistical errors of ~10% between estimates based on acf and spectral analysis may be possible for some data.

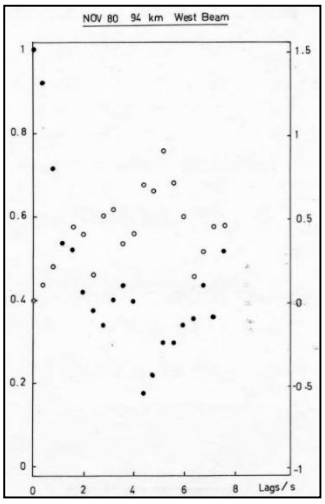

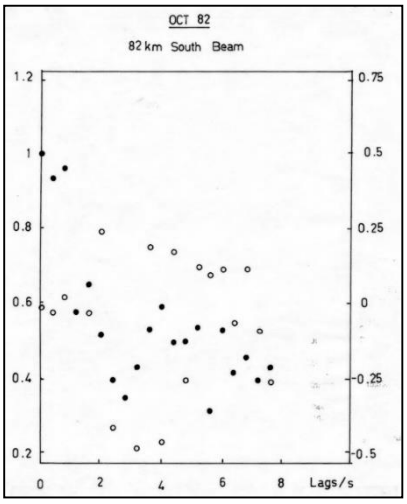

Figure 3.2 (left) Example of an oscillatory acf selected at random from the NOV 80 data set, and Fig 3.3 (right) An example of an irregular acf selected at random from the OCT 82 data set.

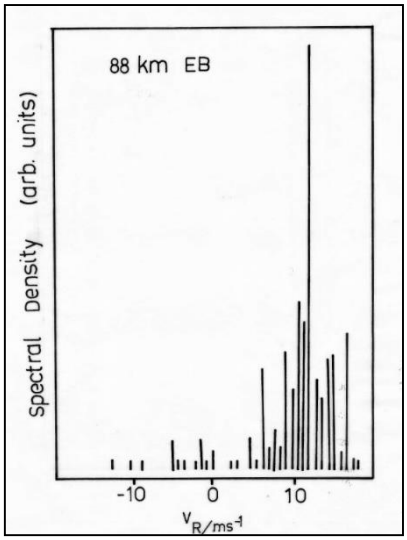

Figure 3.4 An example of the Doppler velocity spectrum corresponding to an accepted 102.4s data record. Note the long tail extending into negative values of radial velocity, and the 'spikey' nature of the spectrum. A Gaussian form is apparent with a peak at about 11 ms^{-1}.

Acf analysis is limited when compared to spectral analysis in one regard. Strong spectral components, which may bias the mean Doppler shift, are harder to detect. These are observed in spectra obtained in both vertical and off-vertical beams (e.g. Röttger, 1981; Hocking, 1983b), and when Gaussian forms are fitted to obtain the various spectral moments, are

generally discriminated out. Because reflectors in the D-region are generally horizontal, these components are rather more important for spectra measured in vertical beams.

In an attempt to determine the presence of a specular component in the acfs obtained from backscattered records in oblique beams, a somewhat arbitrary condition was set upon the amplitude of the auto correlation function for one analysis of May 1981 data. If the width of acf at 8 seconds had not fallen to 0.5 it was tagged “slow fading” and the number of such records was monitored. The rationale for this was that a specular and random component produce a characteristic form of acf as shown in Figure (3-6a), (Ratcliffe, 1956), and the "wings" on the acf can be used to monitor the specular component.

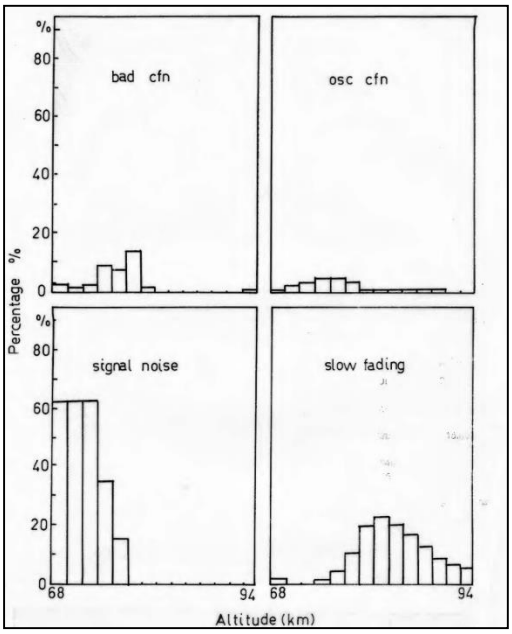

Fig 3.5a The reasons for data rejection and the occurrence of acfs with half widths greater than 8 s (that is, “slow fading” records) for three days of observation in May 81. “Bad cfn” are irregular acfs.

Ratcliffe’s (1956) work refers to spatial rather than temporal auto correlation functions, but appears to be applicable. Gage et al. (1981) have investigated specular returns from the troposphere at VHF obtained in a vertically pointing Doppler beam. They found specular returns were characterized by high power and low spectral width. More isotropic scattering produced spectra which were characterized by rather broader spectral widths and lower signal powers. Since the half width of the auto correlation function is inversely proportional to the half width of the power spectrum, we expect specular returns to have broader auto correlation functions. The superposition of specular and isotropic type scattering is therefore expected to produce a characteristic form of acf.

The results of this analysis are shown in Figure (3-5a and b), there is a clear peak at about 82-84 km, a height which is known to have a strong specular component (Hocking and Vincent, 1982). The velocities determined from these records were consistent with adjacent records and it appears that in this case, correct velocities were obtained. Also shown on this diagram are the reasons for data rejection for May 1981. Below about 78km most records are rejected on the basis of SNR as is expected, because of the highly anisotropic nature of the scatterers. At these heights irregular and oscillatory acfs also account for a small percentage of rejected records. For 80-94 km the few records that are rejected are because of oscillatory acfs.

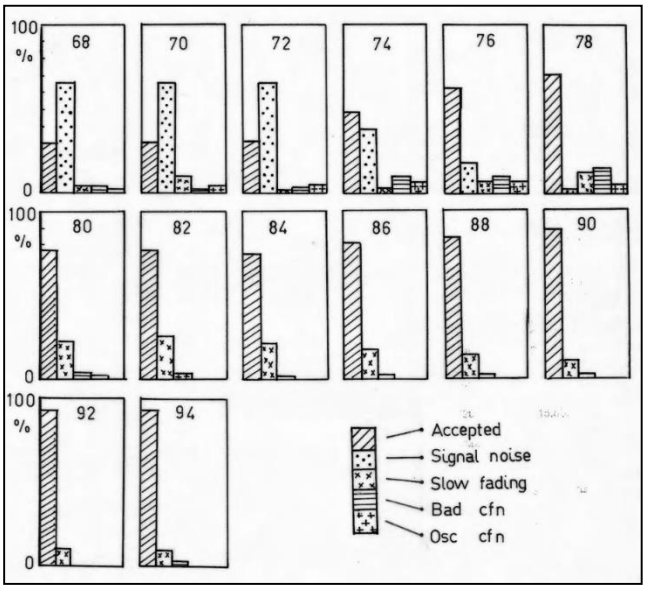

Figure 3.5b As for Figure 3.5a, but with the results presented for each height. Because of the way these results were analyzed, slow fading records have been separated from the accepted records, but should be included.

Near the "tail" of the E-region strong specular reflection from the vertical can bias velocities measured in oblique beams. To illustrate this, we consider a typical example. The amplitudes of four acfs for l02.4s of data obtained in October 1982 from the same height and time are shown in Figure (3-6a). The beams were directed at 11.6° from the zenith Eastwards, Westwards, Southwards and Northward and are labelled this way in the diagram. With the exception of the eastward acf, these amplitudes are characteristic of the presence of a quasi-random and more steady component in the backscattered signal The eastward amplitude is slightly oscillatory, and when we examine the corresponding phase, Figure (3-6b), we note that it is subject to an abrupt 2π phase change at about 4.4 s.

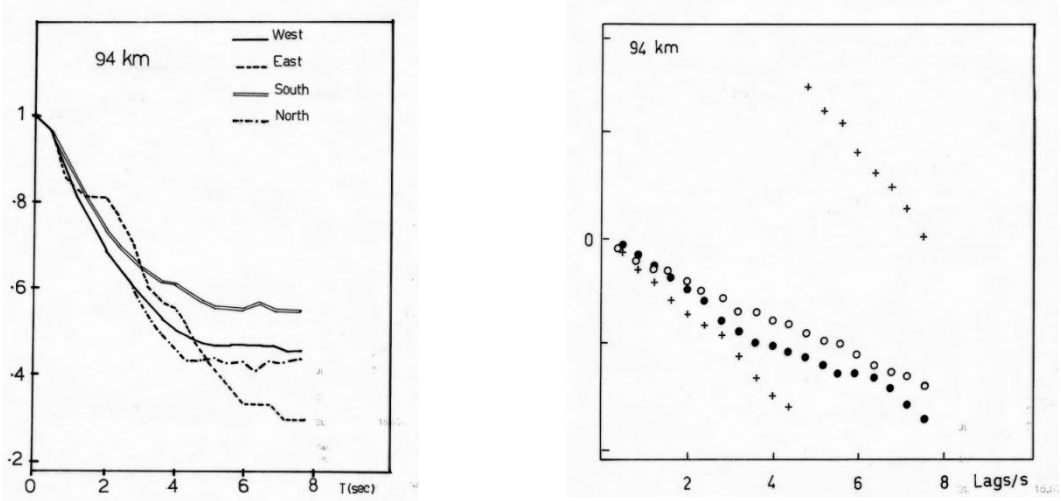

Fig 3.6a (left) Amplitude of four acfs for one 102.4s record from the Oct 82 data set. Note the slight oscillation in the last beam amplitude, and the form of the south beam amplitude, which could be indicative of the superposition of random and more specular components.

Figure 3.6b (right) As for Figure 3.6a, but for the phase of the acfs. The crosses represent the east beam phase. Note the abrupt phase change at 4.4 s and the slight oscillation in the phase of the other two beams. For clarity the phase of the westward beam has been omitted.

This behaviour is typical of an acf corresponding to a backscattered signal in which two or more components are beating. In this case this may be due to specular reflections with different frequency shifts. However, this is uncertain, because the beat frequency does not seem to correspond to the spikes in the power spectrum. The phases of the acfs appear to be well behaved, but when the power spectra are examined Figure (3-6c), it is apparent that they show three well defined peaks which are quite similar for three of the beams. This tends to suggest a specular contribution which is dominating the spectra. The slope of the phase of each acf corresponds to the largest peak in each of the spectra, and since the derived radial velocity is of the same sign for all four of the beams, this suggests a net downward motion of a tilted or corrugated reflector rather than a horizontal motion.

If these strong peaks are real and correspond to different reflection points, then all of the phases should oscillate. However, the peaks correspond to adjacent frequencies and the corresponding beat frequency would be about 100 s, too long to be detected with 102.4 s of data.

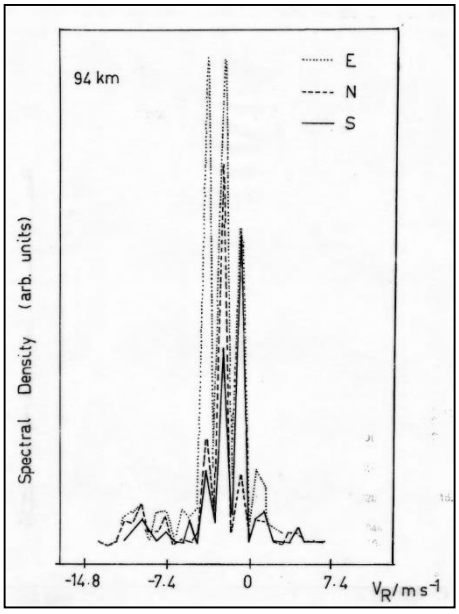

Figure 3.6c As for Figures 3.6a and 3.6b, but now the results are presented as power spectra. Note the narrow spectra and the similarity between the three spectra. For clarity the westward spectrum has been omitted.

This particular record is unsuitable for the simple analysis applied in this work and should be rejected. The fading time criterion could be used because the south beam record exceeds 0.5 at 8 seconds, but this is clearly arbitrary because the Eastward and Northward beam records would not be rejected. The oscillation in the eastward beam records acf could be used because it is evident in both the amplitude and phase but the other records would still remain. The best procedure, and the one followed here, appears to be to analyze and tag such records, and then check the radial velocities for consistency between heights and adjacent data blocks. The fact that at heights near the tail of the E-region radial velocities may not be correct must be borne in mind however. If a vertically directed beam is available, then the half width of the scattering region may be estimated if sufficient averaging in time is possible. Then echoes obtained near the tail of the E-region could be checked and rejected if the angular half width was indicative of a specular return. This would allow an approach based on a rejection algorithm rather than a maximum likelihood method to be applied.

The record we have just discussed is quite typical of records obtained in October 1982 at heights of 90 km and above. Since these were generally unsuitable for analysis, acceptance rates were somewhat lower in October 1982 than in some other months.

The number of accepted records for data taken in some representative observation periods is shown in Figure (3-7) to (3-12). For the height range 80-96 km for May, July and November runs the acceptance rate is clearly very high, while for February and October is more variable.

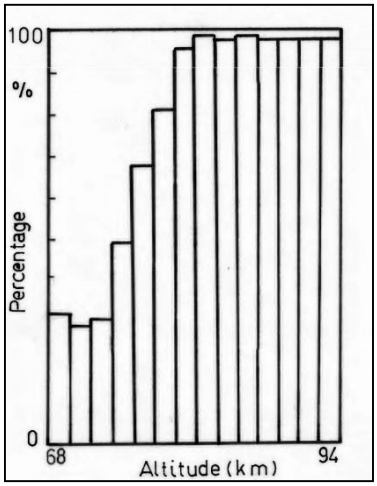

Figure (3.7) The percentage of accepted data for the May 81 data run.

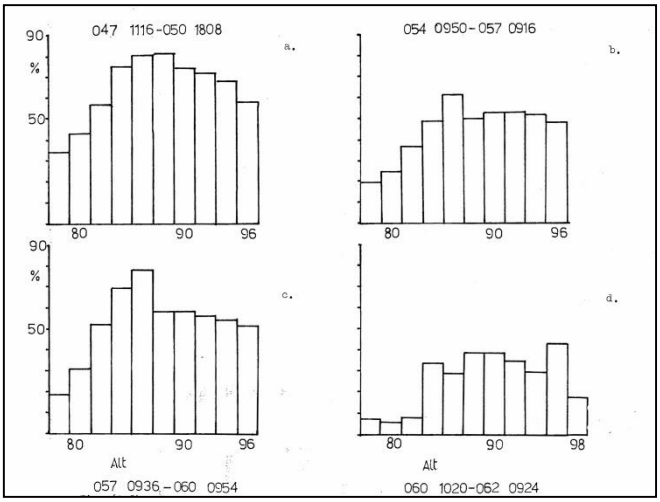

Figure 3.8(a-d). The data acceptance rates for various beam configurations for the February 82 data sets. For details see text.

In February 1982, Figure (3-8), sporadic E was indicated by observation of the CRO at the field site and appeared at heights down to about 90-92km. This reduced the amount of usable data available from the higher heights so much so that data from days 054-057, (Figure (3-8b)) could not be successfully analyzed to obtain momentum flux measurements. Figure (3-8c) is for data obtained using four beams but with two directed vertically, and two directed in the same direction at 11.6° to the zenith, and the data obtained was discussed in Section (2.3.6).

Figure (3-gd) is for SA observations and is fairly typical except for the low acceptances below 84 km.

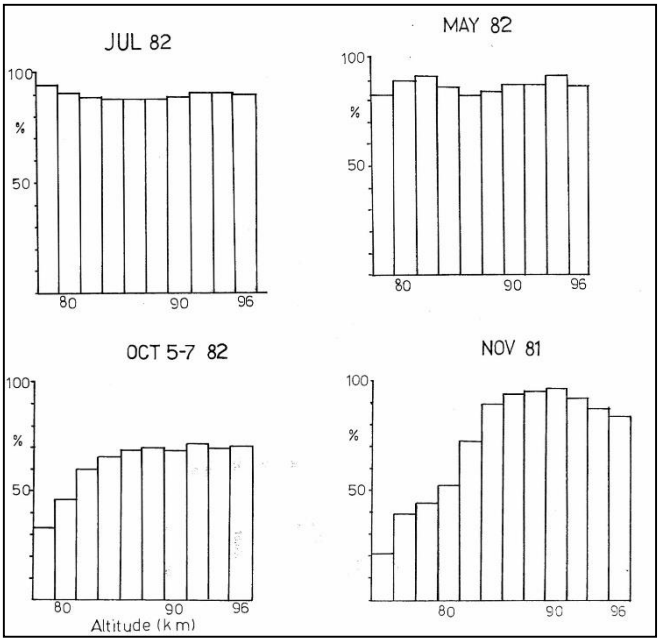

Figures (3.9 to 3.12). The data acceptance rates for various data runs. For details see text.

In October 1982, sporadic E also accounted for the high rejection rate about 88km, and low SNR's for 78-82 km. These data acceptance rates are only intended to give a measure for each run. Because the beam configurations and transmitter power varied from run to run, the array was not calibrated, and receiver gains were controlled in different ways, comparison of data acceptance rates between runs is subject to a number of uncertainties.

The analysis of data acceptance rates will not be pursued here, but there is obviously a great deal of important information that can be derived from such studies. The real importance of these data acceptance rates is in the analysis of the time series to measure $\overline{u'w'}$. Since this quantity may show quite substantial variations in time (Vincent and Reid, 1983), data acceptance rates for various heights must be similar if intercomparisons of $\overline{u'w'}$ measured at various heights are to be valid. We will refer to these acceptance rates in Chapter 6.

3.5 Analysis of Radial Velocity Time Series

The time series of radial velocities from each beam were analyzed with the same basic set of programs used for SA observations. These were modified to cope with the small radial velocities, different data formats and areas of interest but were essentially unchanged. They were generally used in the following way.

The radial velocities for each height range were processed so that consecutive 2 minute determinations of velocity were averaged to produce one observation at each height at half the original record sampling rate. A cubic spline technique was then used to interpolate over small gaps in the data. The resulting time series were then plotted so that the quality of the data could be assessed visually. This was necessary because power failures at the field site at the time of observation and various ionospheric effects (e.g. sporadic E and HF fadeouts) could produce substantial gaps in the data. The interpolation routine could not cope with such data and the following schemes were necessary.

For power failures, which obviously resulted in a loss of all data for their duration, the time series were split into separate computer files, and analyzed as such. For a time series with significant gaps due to ionospheric effects, the interpolation routine was applied to provide a value at the basic sampling rate. These data were then numerically filtered to remove periods less than 8 hours. These low pass values were substituted for the long breaks in the original data and the cubic spline interpolation was then applied again. Periods greater than 8 hours were then removed using a numerical filter and this final form of the data was then suitable to calculate the variance of the time series for periods less than 8 hours. Comparison of variances of data treated in this way with that produced by analysis of separate files showed that the two techniques were equivalent. Since one data file is easier to handle than two, all later data was analyzed in this way. However, great care was taken in setting up the equipment and then ensuring that any breaks due to equipment failures were minimized, and in later observational periods, breaks in the data due to power failures were compensated for by extending the run so that a minimum of three consecutive days of data with no breaks due to equipment failures were obtained.

The filtered time series of radial velocities were cross spectrally analyzed to measure scale and for this complete data sets were required. The time series were split up into consecutive 3, 6 or l2 hour blocks and these were plotted and examined for breaks in the original data. If a data

block had continuous data for its entire length, it was considered suitable for cross spectral analysis. However, if it contained continuous breaks of more than 10% of its entire length it was discarded.

The tidal and mean components of the wind were calculated using a harmonic fit with 12 and 24 hour periods to the hourly values of the horizontal and vertical components derived from the radial velocities for each 24 hours of data. Details of this type of analysis can be found in Ball (1981) and Vincent and Ball (1981).

3.6 Summary and Conclusions

In this Chapter we have considered the analysis of backscatter time series to obtain the various moments of the backscatter Doppler spectrum. The analysis described is quite basic, and nothing new has been reported. However, we would suggest that longer data lengths be obtained (~3 min) and that spectral analysis, although more time consuming, is somewhat more flexible when assessing data quality above 90 km. The real confirmation of the analysis procedure applied is whether the winds derived from it agree with other methods of measurement. The results of a comparison between Doppler and Spaced Antenna derived winds is reported in Chapter 5, and these show quite good agreement.

In the next Chapter we consider the Doppler Wind technique, and the various beam configurations and the parameters that may be obtained are discussed.

4. The Coplanar Doppler Radar Beam Experiment

This Chapter is concerned with the analysis of radial velocity time series measured in multi-beam or beam swinging Doppler radar experiments. Particular reference is made to the Dual Complementary Coplanar Beam Arrangement (see Chapter 2). In the first part we examine the various assumptions made when the Doppler wind technique is applied to the measurement of dynamical parameters of the wind field and their validity for different beam arrangements. In the second part we consider the calculation of the horizontal and vertical scale of gravity wave motion for the same beam arrangements using cross spectral techniques and the gravity wave model of Hines (1960). The measurement of dynamical parameters for scales smaller than the radar pulse volume is considered very briefly in Section 4.4.

4.1 The Measurement of Dynamical Parameters

The basic theory relating to the idealized Dual Complementary Coplanar Beam experiment was introduced by Vincent and Reid (1983). They demonstrated how radial velocities obtained from two narrow Doppler radar beams tilted at $+\theta$ and $-\theta$ to the zenith could be analyzed to obtain a number of useful parameters relating to the mean and fluctuating parts of the wind field, the most important of which was the upward flux of horizontal momentum. In addition, they developed a technique to determine the horizontal scales of gravity wave motions that were present in the wind field.

It appears that the first part of the theory mentioned above described a special case of the VAD radar technique (see Chapter l). In this method a single radar beam is scanned through azimuth angles of from 0° to 360° at a fixed elevation angle. The mean radial velocity, which is a function of the azimuth angle, is then subjected to a Fourier series least squares fit which provides the mean horizontal wind, the horizontal divergence of the wind and the stretching and shearing deformations (Browning and Wexler, 1968). The variance of the radial velocity is similarly processed to obtain the variances and covariances of the components of the wind field (Wilson, 1970). These last two terms are important because they are related to the kinetic energy and momentum transfer and deposition respectively. A description of the VAD method may be found in Wilson and Miller (1971).

The technique does not appear to have been used for investigations outside the troposphere and lower stratosphere, probably because Doppler radars capable of scanning an azimuthal region

in other parts of the atmosphere are quite rare. For instance, for the mesosphere, such a radar relying upon mechanical beam swinging would require a rather large dish antenna and an extremely rapid (prohibitive) rotation rate. A VHF radar with individually phased array elements could do it but the number of phase delays required would be $O(5000)$. The MU radar, presently under construction in Japan, will be capable of this mode of operation (Fukao et al, 1980). One radar that is capable of sampling the wind field of the upper atmosphere in a horizontal plane, which is essentially the same as the information obtained from an azimuthal scan, is Bribie Island (Brownlie et al., 1973). The UHF radar previously at Chatanika, and now at Sondrestrom, is capable of VAD type operation for the lower atmosphere and has been used to obtain mean winds in the troposphere and stratosphere (Peterson and Balsley, 1979; Balsley et al., 1977).

Most of the information that can be obtained from the VAD technique can be obtained from a limited number of beams with a suitable choice of beam geometry. The beam geometry that is required can be obtained from any radar capable of swinging a beam through a range of zenith angles. This type of facility is relatively common because the individual array elements can be connected in parallel to form rows or columns and swinging the beam is then quite simple (see e.g. Section 2.2.2). With real time computer controlled beam swinging it is entirely feasible to relocate a beam in about $1\,ms$, a period during which the atmosphere can be regarded as statistically stationary. If radial velocity time series are obtained from a number of zenith angles, the analysis described in Section (4.1) can be easily applied. In fact, it has some advantages over using fixed beams (Section 4.1.2).

In the following Section we consider the general Equations for the radial velocity measured in a Doppler beam experiment and then consider some specific examples of beam geometry that lead to useful physical parameters of the wind field. We will restrict the analysis to a horizontal slice through the atmosphere because the assumption of a horizontally homogeneous atmosphere (in a statistical sense) is much more general than that of a vertically homogeneous atmosphere. The idealized technique is quite general and can be applied to any part of the atmosphere.

We first consider small scale motions, that is, motions with scales comparable to the spacing between the radar beams. Since both gravity wave and turbulent motions can be viewed as a kind of geophysical “noise" the analysis requires a statistical approach to obtain meaningful results.

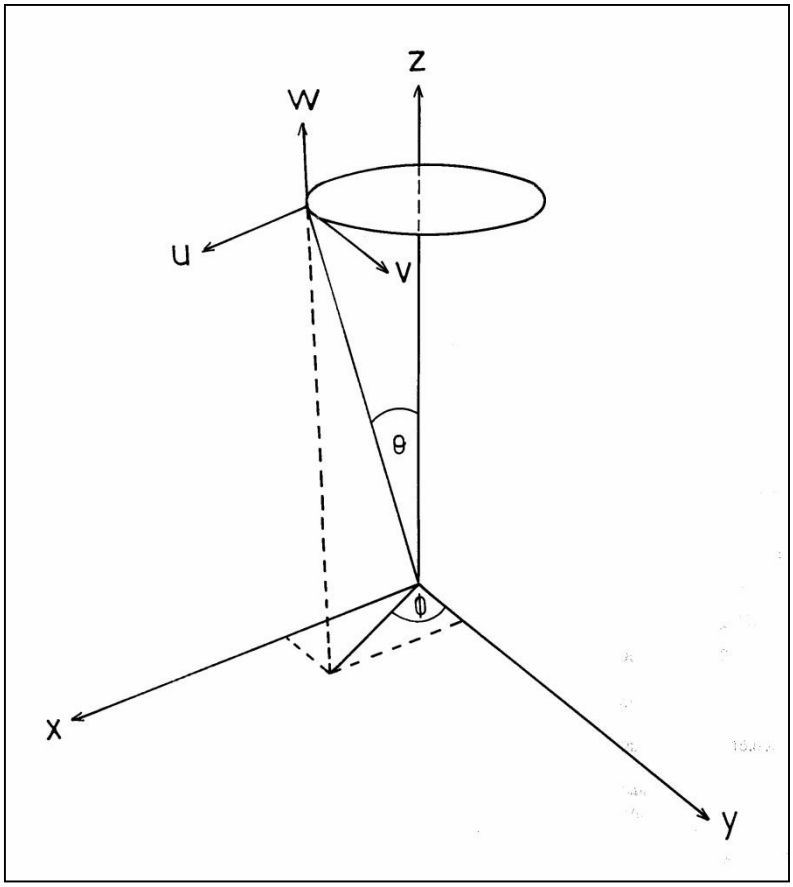

Figure (4-1). The right handed co-ordinate system used in this work. ϕ is the azimuth angle and is measured clockwise from north (+y axis), θ is the zenith angle measured from the vertical (+z axis) and (u,v,w) are the components of the wind in the zonal (+x), meridional (+y) and vertical (+z) directions. In the text we consider a fixed R and θ and the discussion therefore concentrates on radial velocities obtained in radar volumes along the locus indicated.

4.1.1 Small Scale Motions

Consider a radar located at the origin of a right handed co-ordinate system with East as the $+x$-direction and North as the $+y-$direction (Figure 4.1). The instantaneous radial velocity V_R measured by this radar at (R, θ, ϕ) is given by

$$\boldsymbol{V_R}\,(\boldsymbol{R}, \theta, \phi) = \boldsymbol{u}(\boldsymbol{R}, \theta, \phi) sin\theta\ sin\phi + \boldsymbol{v}(\boldsymbol{R}, \theta, \phi) sin\theta\ cos\phi + \boldsymbol{w}(\boldsymbol{R}, \theta, \phi) cos\theta, \qquad (4\text{-}1)$$

where (u, v, w) are the instantaneous zonal, meridional and vertical components of the wind respectively and (R, θ, ϕ) are the range measured along the beam, the beam zenith angle measured from the vertical, and the beam azimuth angle measured clockwise from North, respectively.

We will consider a fixed R and θ (that is, height) and can therefore write

$$\boldsymbol{V_R}\,(\phi) = \boldsymbol{V_R}(\boldsymbol{R}, \theta, \phi),$$

if we keep in mind the fact that this refers to one particular position in space. The mean radial velocity is then

$$\bar{\boldsymbol{V}}_{\boldsymbol{R}}\,(\phi) = \bar{\boldsymbol{u}} sin\theta\, sin\phi + \bar{\boldsymbol{v}} \boldsymbol{s} in\theta\, cos\phi + \bar{\boldsymbol{w}} \boldsymbol{c} os\theta, \tag{4-2}$$

where we have dropped the functional dependence notation for the (u, v, w) and overbars denote a time average. Deviations of V_R from the mean radial velocity $\bar{V}_R$ will result from local velocity variations related to turbulent and gravity wave motion. The easiest way to examine this is to consider the variance of the fluctuations of the instantaneous radial velocity from the mean, that is, the mean square perturbation from the mean.

The mean square radial velocity is

$$\overline{V_R'^2}(\phi) = \overline{\left(V_R(\phi) - \bar{V}_R\,(\phi)\right)},$$

$$= \overline{(u' sin\theta\, sin\phi + v' sin\theta\, cos\phi + w' cos\theta)^2}. \tag{4-3}$$

Where, $u' = (u - \overline{u})$, $v' = (v - \bar{v})$, $w' = (w - \overline{w})$, are the instantaneous velocity fluctuations from the mean.

Expanding Equation (4-3) we obtain

$$\overline{V_R'^2}(\phi) = \overline{(u'^2\, sin^2\phi + \overline{v'^2} sin^2\phi) sin^2\theta + \overline{w'^2} cos^2\theta} + \overline{v'w'} sin\theta\, cos\phi + \overline{u'w'} sin\theta\, cos\phi + \overline{u'v'}\, \sin^2\theta\, sin2\phi. \tag{4-4}$$

which is the general expression for the mean square radial velocity. Lhermitte (1968) derived a similar expression based on Equation (4-1) to investigate turbulence in the boundary layer and Wilson (1970) derived Equation (4-4) for the same purpose.

The $(\overline{u'^2}, \overline{v'^2}, \overline{w'^2})$ are the mean square values of the fluctuating components of the wind field, that is, twice the kinetic energy per unit mass for the zonal, meridional and vertical components respectively.

The covariance terms ($\overline{u'v'}, \overline{u'w'}, \overline{v'w'}$) are the components of the "Reynolds Stress". These correspond to the horizontal momentum flux, the upward flux of zonal momentum and the upward flux of meridional momentum, all per unit mass, respectively.

The most important thing to note about Equation (4-4) is that it contains both variances and covariances. This is obviously a fundamental consideration when using the variance of a radial velocity. Generally, the various quantities in this Equation are only useful if they can be obtained separately.

In order to do this, we must make certain assumptions about the horizontal homogeneity of the wind field and use a sufficient number of beams to obtain the various quantities in Equation (4-4) separately. All Doppler radars must make this assumption because all measure radial velocities in spatially separated parts of the atmosphere. This requires careful consideration and comparison with physically realistic models before it can be applied. However, this is also an advantage, because the spatial variation of the wind field may be measured. With a suitable choice of beam geometry, we can separate the variances from the covariances in Equation (4-4). Equation (4-4) contains six unknowns and so requires six Equations and the assumption that these terms are statistically similar in a horizontal plane to solve. However, by suitable choices of θ and ϕ the number of Equations required (and, of course, the number of parameters obtained) is reduced. For instance, with $\phi = \frac{n\pi}{2},\ n\ integer$, only five Equations or (beam positions) are required to obtain the three components of the kinetic energy and the upward flux of horizontal momentum. The Northward flux of Eastward momentum (or vice versa) cannot be obtained in this case.

Another way of reducing the number of beam positions required is to calculate the individual terms in Equation (4-4) from their components measured in spatially separated volumes. This places a limitation upon the accuracy of the measurement in that only contributions to the terms in Equation (4-4) from scales larger than the spatial separation of the volumes in which the parameters are measured will be correct. The situation is complicated by the differences in the relative magnitudes of (u', v', w') and the variances and covariances calculated from them because some terms will be much larger than others. For instance, $\overline{u'^2}$ and $\overline{v'^2}$ will dominate the other quantities in Equation (4-4) over most of the frequency range between the inertial and Väisälä-Brunt frequencies. Consequently, some spatial covariance estimates are better than others. This is taken up in the next two Sections.

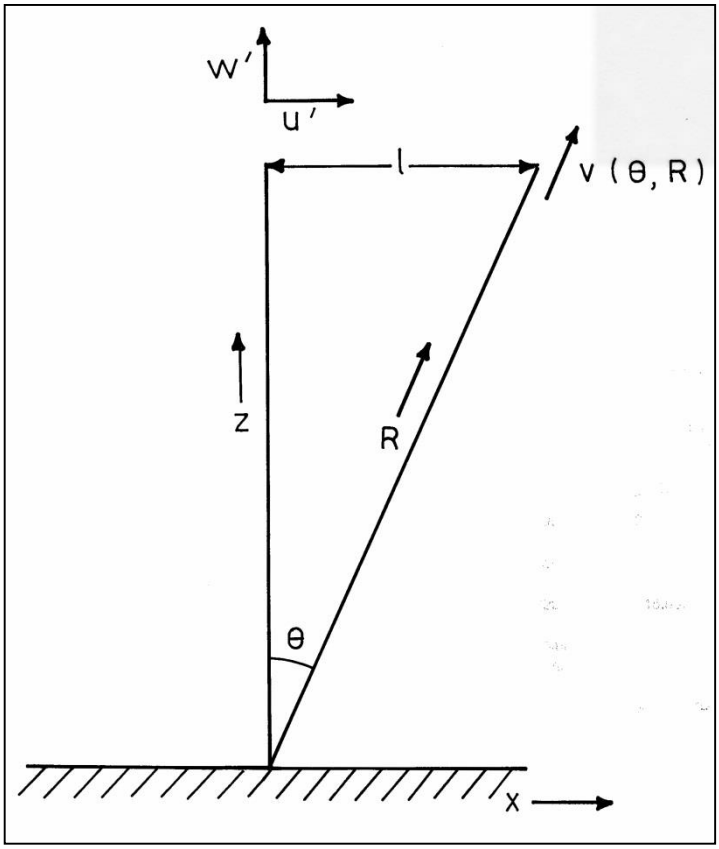

Figure (4.2) Schematic representation of the conventional beam configuration used to measure winds with a Doppler radar. Radial velocities are measured in a horizontal plane $z = R\cos\theta$ *in each beam.* l *is the beam separation and is about l7 km for* $z = 84\ km$, $\theta = 11.6°$, (u', w') *are the horizontal and vertical perturbation velocities and these quantities are a function of position.*

In the next Section we consider the conventional beam configuration used with Doppler radars to obtain the vertical and horizontal components of the wind field. Practical considerations such as finite beam widths and limited height resolution are considered briefly in Section 4.3. The theory discussed in the rest of this Chapter related directly to the beam configurations available when using BP.

4.1.1.1 Vertical and Off-vertical Beams

In this Section we consider the basic beam configuration used to measure winds with a Doppler radar and examine the assumptions used to obtain the mean and fluctuating components of the wind field. This serves as a useful introduction to the complementary coplanar beam technique and highlights the care that must be taken when using such radars.

Consider two radar beams directed at $+\theta$ and $-\theta$ to the zenith in the xz-plane (Figure 4-2). With the instantaneous radial velocities measured in these beams written as

$$V_E = V_R(R, \theta, \phi) \text{ and } V_V = V_R(z),$$

where $z = Rcos\theta$, and $\phi = 90°$, respectively, and the radial velocities are obtained from Equation (4-2) as

$$V_E = (u)_E sin\theta + (w)_E cos\theta, \tag{4-5}$$

$$V_V = (w)_V, \tag{4-6}$$

where the subscript refers to the beam in which the bracketed quantity is measured. These Equations are used to obtain the mean horizontal and vertical components of the wind. Rearranging (4-5) we obtain

$$(\bar{u})_E = \frac{\bar{V}_E - (\bar{w})_E cos\theta}{sin\theta}, \tag{4-5'}$$

(In this Chapter, Equations which are rearrangements of other Equations or are the same basic Equation expressed in a slightly different way are specified with a prime on the Equation number.)

To measure this quantity, it is assumed that

$$V_V = (w)_V = (w)_E, \tag{4-7}$$

so that (4-5') becomes

$$(\bar{u})_{EV} = \frac{\bar{V}_E - \bar{V}_V cos\theta}{sin\theta}, \tag{4-5''}$$

where $(\bar{u})_{EV}$ is defined by (4-5").

Equation (4-7) is equivalent to the assumption that horizontal gradients of the mean wind are negligible. This is reasonable for most of the atmosphere.

The mean square fluctuation of the zonal velocity, the zonal kinetic energy, is calculated from the instantaneous and mean values of Equation (4-5). In this case,

$$\overline{(u'^2)}_E = \overline{(u-\bar{u})^2},$$

$$= \overline{\left(\frac{V'_E - (w')_E cos\theta}{sin\theta}\right)^2}. \quad (4\text{-}8)$$

where $(V')_E = V_E - \bar{V}_E$, and $(w')_E = (w)_E - (\bar{w})_E$ are the instantaneous fluctuations from the mean. Expanding (4-8) we obtain

$$\overline{(u'^2)}_E = \frac{\overline{V_E'^2} + \overline{(w'^2)}_E cos^2\theta - 2\overline{V'_E(w')_V} cos\theta}{sin^2\theta} \quad (4\text{-}9)$$

To measure this quantity, the assumptions made are that

$$\overline{(w'^2)}_E = \overline{(w'^2)}_V \quad (4\text{-}10)$$

and

$$\overline{V'_E(w')}_E = \overline{V'_E(w')}_V \quad (4\text{-}11)$$

in which case (4-9) becomes

$$\overline{(u'^2)}_E = \frac{\overline{V_E'^2} + \overline{(w'^2)}_V cos^2\theta - 2\overline{V'_E(w')_V} cos\theta}{sin^2\theta} \quad (4\text{-}9')$$

Equation (4-10) is straightforward if the statistics of the motions are assumed to be independent of horizontal position, but (4-11) requires further consideration. Expanding the LHS of (4-11) we obtain

$$\overline{V'_E(\mathrm{w'})_E} = \overline{(\mathrm{u'})_E(\mathrm{w'})_E}\sin\theta + \overline{(\mathrm{w'^2})_E}\cos\theta$$

and for the RHS

$$\overline{V'_E(\mathrm{w'})_V} = \overline{(\mathrm{u'})_E(\mathrm{w'})_V}\sin\theta + \overline{(\mathrm{w'})_E(\mathrm{w'})_V}\cos\theta$$

so that implicit in (4-11) is the assumption that

$$\overline{(\mathrm{u'})_E(\mathrm{w'})_E} = \overline{(\mathrm{u'})_E(\mathrm{w'})_V} \quad (4\text{-}11')$$

$$\overline{(\mathrm{w}')_E(\mathrm{w}')_E} = \overline{(\mathrm{w}')_E(\mathrm{w}')_V} \tag{4-11''}$$

Combining (4-10) and (4-11', 4-11") we note that any time $\overline{u'^2}$ is calculated from a vertical and off-vertical beam, the assumptions made are that

$$\overline{u'w'} = \overline{(\mathrm{u}')_E(\mathrm{w}')_V}$$

$$\overline{(\mathrm{w}'^2)_E} = \overline{(\mathrm{w}'^2)_V} = \overline{(\mathrm{w}')_E(\mathrm{w}')_V} \tag{4-12}$$

We may rewrite (4-9') using the terms in (4-12) so that

$$\overline{(u'^2)_{EV}} = \overline{(u'^2)_E} + \left[\overline{(\mathrm{w}'^2)_E} + \overline{(\mathrm{w}'^2)_V} - \overline{(\mathrm{w}')_E(\mathrm{w}')_V}\right]\cot^2\theta$$

$$+2\left[\overline{(u'w')_E} - \overline{(\mathrm{u}')_E(\mathrm{w}')_V}\right]\cot\theta \tag{4-13}$$

If we consider the contribution to $\overline{(u'^2)_{EV}}$ due to a single gravity wave, then Equation (4-13) is dependent on both frequency and scale. The easiest way to consider this is to calculate the ratio of $\overline{(u'^2)_{EV}}$ to the true value $\overline{(u'^2)_E}$ and apply the polarization relations given by Hines (1960) which relate the peak vertical and horizontal perturbation velocities. These are

$$w'_0 = AZ = A\omega_0^2\,(\omega^2 - k_x^2c^2)$$

$$u'_0 = AX = A\omega_0 k_x c^2\left(k_z - i\frac{(2-\gamma)}{(2\gamma H)}\right) \tag{4-14}$$

respectively, where γ is the ratio of specific heats, H the pressure scale height, A an arbitrary amplitude and c is the speed of sound.

The instantaneous perturbation velocities of a single gravity wave of angular frequency ω_0, peak perturbation velocities (u', w') and horizontal and vertical wave numbers (k_x, k_z) can be expressed in terms of R and θ as

$$(u', w') = (u'_0, w'_0)\, e^{i(\omega_0 t - k_x l - k_z z)} \tag{4-15}$$

where $l = R\sin\theta,\ z = R\cos\theta$, and we may include any arbitrary phase variation in the time term.

If the statistics of the motions are homogeneous in a horizontal plane, we may write

$$\overline{(u'^2)}_E = \overline{u'^2}(z)$$

$$\overline{(\mathrm{w}'^2)}_E = \overline{(\mathrm{w}'^2)}_V = \overline{w'^2}(z)$$

$$\overline{(u'w')}_E = \overline{\mathrm{u}'\mathrm{w}'}(\mathrm{z}) \tag{4-16}$$

which are much more general assumptions than those contained in Equation (4-12), because there is no requirement for spatial covariances to be calculated. If (4-16) is valid than we may write Equation (4-13) as

$$\overline{(u'^2)}_{EV} = \overline{u'^2} + 2\left[\overline{w'^2} - \overline{(\mathrm{w}')_E(\mathrm{w}')_V}\right]\cot^2\theta$$

$$+2[\overline{u'w'} - \overline{(\mathrm{u}')_E(\mathrm{w}')_V}]\cot\theta \tag{4-13'}$$

Now

$$\overline{u'^2} = \frac{A^2}{2}\omega_0^2 k_x^2 c^4 (k_z^2 + B^2) \tag{4-17}$$

$$\overline{w'^2} = \frac{A^2}{2}\omega_0^2(\omega_0^2 - k_x^2 c^2)^2 \tag{4-18}$$

$$\overline{u'w'} = \frac{A^2}{2}\omega_0^2 k_x c^2 k_z(\omega_0^2 - k_x^2 c^2) \tag{4-19}$$

where $B = \frac{(2-\gamma)}{2\gamma H}$ and

$$\overline{w'_E w'_V} = \frac{\overline{w'_E w'^*_V}}{2} = \frac{A^2}{2}\omega_0^2(\omega_0^2 - k_x^2 c^2)^2[\cos(k_x l)]$$

$$= \overline{w'^2}[\cos(k_x l)] \tag{4-20}$$

where $*$ = complex conjugate

$$\overline{u'_E w'_V} = \frac{\overline{u'_E w'^*_V}}{2}$$

$$= \frac{A^2}{2}\omega_0^2\, k_x\, c^2 k_z(\omega_0^2 - k_x^2 c^2)[\cos(k_x l)] - \frac{B}{k_z}\sin(k_x l)]$$

$$= \overline{u'w'}[\cos(k_x l)] - \frac{B}{k_z}\sin(k_x l)] \tag{4-21}$$

so that

$$\overline{(u'^2)}_{EV} = \overline{u'^2} + 2\overline{w'^2}[1 - \cos(k_x l)]cot^2\theta + 2\overline{u'w'}\left[1 - \cos(k_x l) + \frac{B}{k_z}\sin(k_x l)\right]cot\theta \tag{4-22}$$

and

$$\frac{\overline{(u'^2)}_{EV}}{\overline{u'^2}} = 1 + \frac{2(\omega_0^2 - k_x^2 c^2)^2}{k_x^2 c^4 (k^2 + B^2)}[1 - \cos(k_x l)]cot^2\theta + \frac{2k_z(\omega_0^2 - k_x^2 c^2)}{k_x c^2}\left[1 - \cos(k_x l) + \frac{B}{k_z}\sin(k_x l)\right]cot\theta \tag{4-23}$$

Equation (4-23) can be evaluated for a given ω_0 and k_x, with k_z, being obtained from the dispersion relation. Figure (4-3a) illustrates this Equation evaluated for a number of wave periods for typical mesospheric values of $B, c, \omega_a \; and \; \omega_g$. The case illustrated corresponds to a range of 86 km. and a zenith angle of 11.6°, and so the height is ~84 km. k_z is negative and k_x positive, but the same results would be obtained for k_z positive and k_x negative. For this range and tilt angle, the horizontal separation of the beams is about 17 km and this corresponds to the minimum in the curves. This is physically reasonable because the perturbation velocities are in phase and the assumptions in Equation (4-12) will be true.

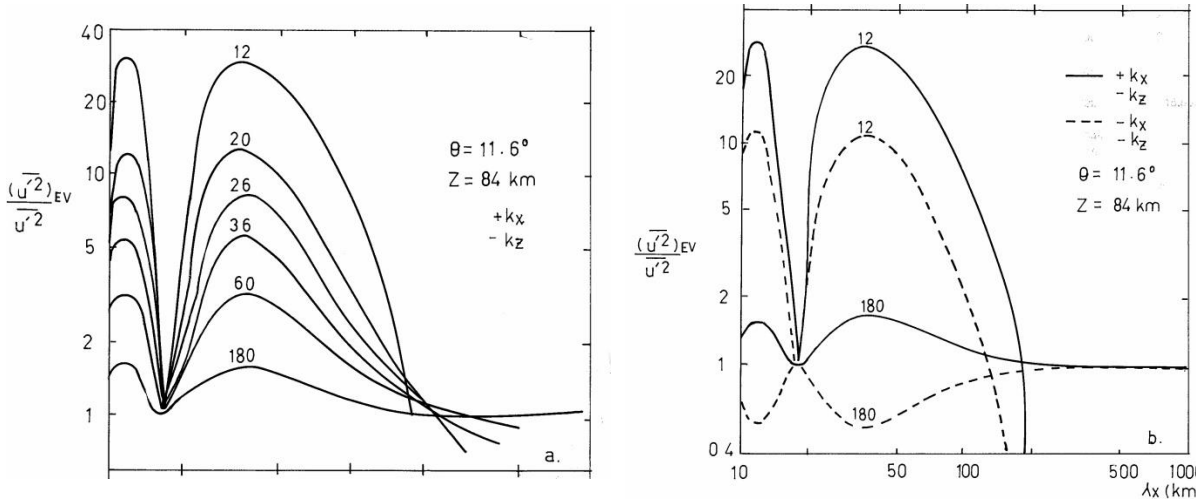

Figure (4.3a) (left) The horizontal kinetic energy calculated using spatial covariance estimates normalized with respect to the correct value for waves propagating in the $+k_x$ direction with downward phase progression. The same result would be obtained for $(-k_x, +k_z)$. The curves are plotted for a height of 84km and an off-vertical angle of 11.6°.

Figure (4.3b) (right) As for 4.3a but two periods are plotted for propagation in the +x and -x directions for downward phase progression.

At twice the beam separation (~35 km.) the measured value of $\overline{(u'^2)}_{EV}$ shows the worst agreement with the expected value $\overline{u'^2}$. This corresponds to the case for which the perturbation velocities are in anti-phase and the spatial covariance estimate terms in Equation (4-12) will be equal and opposite to the true values. For the case of k_z and k_x both negative, we have plotted only two periods, 12 min and 180 min, in Figure (4-3b). Also shown on this diagram are the values of Equation (4-23) for k_x positive and k_z negative. It is clear from this diagram that the 12-minute period wave is quite similar for both directions of horizontal propagation, whilst the plot for the 180-minute period wave exhibits considerable symmetry about $\frac{\overline{(u'^2)}_{EV}}{\overline{u'^2}} = 1$.

Consequently, for a wave field in which the propagation directions are isotropic in the plane of the beams, a motion with a 12-minute period will have its horizontal kinetic energy incorrectly measured, whilst the same quantity measured for a motion with a 180-minute period will be quite close to the correct value. However, if there is a preferred direction of propagation, the horizontal kinetic energy of even this period will be incorrectly measured for scales less than about 100 km (10% error at this wavelength). This is a distinct possibility because some gravity wave may be removed by critical layer interactions (see e.g. Booker and Bretherton, 1967).

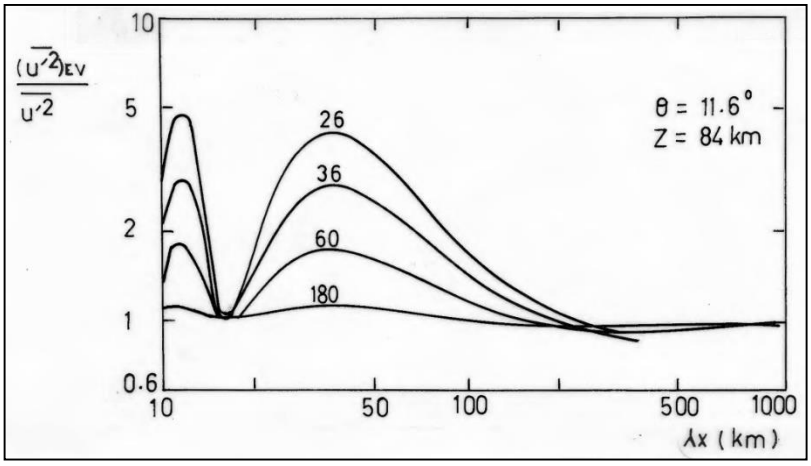

Figure (4.3c) As for (4.3a) but for a wave field in which equal numbers of similar waves are propagating in the +x and -x directions

Figure (4-3c) illustrates the horizontal kinetic energy as measured by this beam arrangement for an isotropic wave field for four periods. It is clear that at $T = 36\,minutes$, there will be substantial errors in $\overline{(u'^2)}_{EV}$ if horizontal scales of less than about l50 km are present. The results for $T = 60\,and\,180\,minutes$ are better, but it is clear than at $T = 60\,min.$, the measured value of $\overline{(u'^2)}_{EV}$ is an overestimate of the correct value $\overline{u'^2}$.

Figure (4-3d) is from Vincent and Reid (1983) and shows the mean zonal wavelength plotted as a function of wave period for three days of observation in May 1981. These results were obtained with the DCC beam arrangement and the analysis described in Section (4-2). If these results are typical, then the spatial covariance estimates of $\overline{u'^2}$ are probably acceptable for an isotropic wave field for periods greater than about 60 minutes.

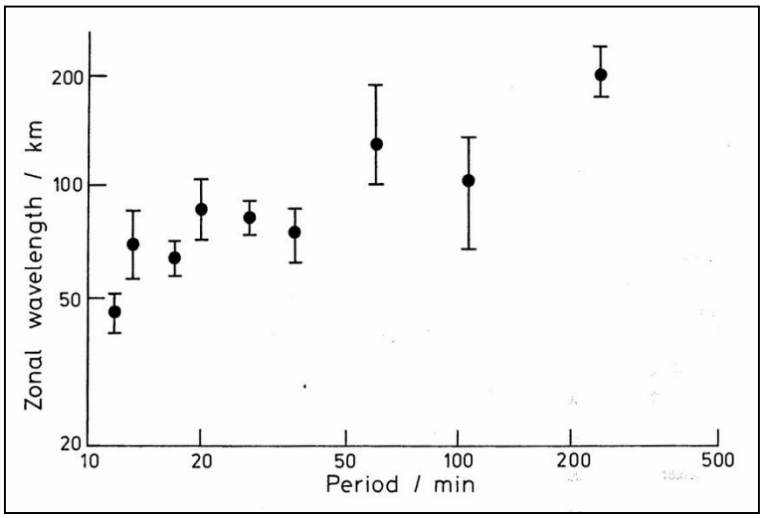

Figure (4-3d) Mean zonal wavelength plotted as a function of wave period for May 1981 results (after Vincent and Reid, 1983)

Inspection of Equation (4-23) indicates that the second term is symmetrical in k_x and k_z, and so is independent of the direction of propagation of the waves that contribute to it. The last term is not, and it is this term that produces the variation in $\overline{(u'^2)}_{EV}$ with the direction of propagation. The relative magnitudes of $\overline{u'^2}$, $\overline{w'^2}$ and $\overline{u'w'}$ are important in this respect, and Figures (4-3e and f) illustrate $\frac{\overline{w'^2}}{\overline{u'^2}}$ and $\frac{\overline{u'w'}}{\overline{u'^2}}$ for a number of wave periods respectively.

It is important to note that $\overline{u'w'}$ is a signed quantity, and if the wave field is isotropic, it will take a value of 0 in this elementary case. $\overline{w'^2}$ is not, and from (4-3e) it is obvious that this quantity is most important for the shortest wave periods and is inconsequential at $T = 180\ minutes$. At this period, the important contribution to $\overline{(u'^2)}_{EV}$ is from the last term in Equation (4-23).

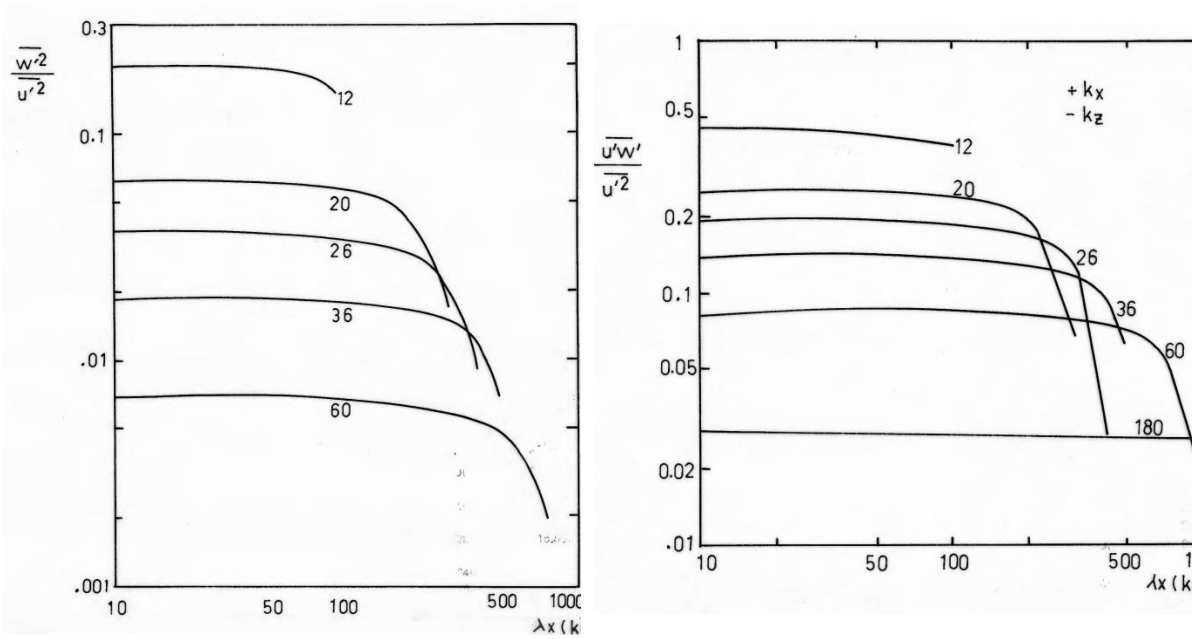

Figure (4.3e) (left) The ratio of the vertical and the horizontal perturbation velocities calculated from the polarization relations for a number of wave periods and horizontal scales.

Figure (4.3f) The ratio of the Reynolds stress to the horizontal kinetic energy for propagation in the +x direction and downward phase progression calculated from the polarization relations. The ratio for propagation in the -x direction and downward phase progression is equal in magnitude to those plotted but opposite in sign for each period and horizontal wavelength.

To illustrate how dependent Equation (4-23) is on θ, Figure (4-3g) shows the results for a gravity wave of 60 minutes' period plotted against horizontal scale for three tilt angles, θ = 5°, 11.6° and 15° at a height of 84 km. It is clear that at any of these tilt angles, the shortest scale that could be correctly measured would be about l50 km. The results for the two largest angles are quite similar and these are somewhat better than those for θ = 5°. It would appear that spatial covariance estimates of the horizontal kinetic energy should be avoided if wave scales of less than 100 km and periods of less than about one hour are of interest, and this can be done by calculating the mean square radial velocities for each beam separately.

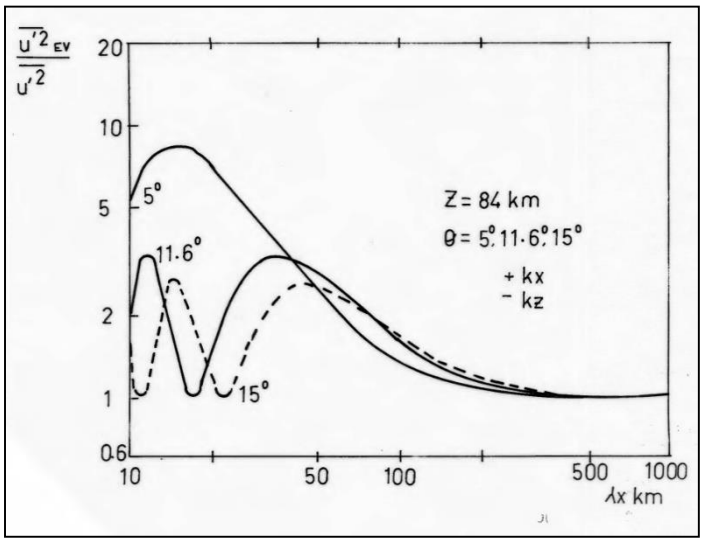

Figure (4.3g) The horizontal kinetic energy calculated using, spatial covariance estimates normalized with respect to the correct value, for three off-vertical beam angles, for propagation in the +x direction with downward phase progression for a wave of period 60 minutes.

This is also of some interest because with some Doppler radars, no measurement of the vertical wind is available and radial velocities are obtained from off-vertical beams only. These are then analyzed using the assumption that the vertical component of the wind is negligible when compared with the horizontal component. For instance, this scheme was used in November 1980 at BP to compare the Doppler radar technique with the SA method. We now consider the validity of estimating the mean square horizontal velocity from the radial velocity measured in an off-vertical beam.

The mean square radial velocity measured in a beam at $+\theta$ to the zenith in the x-z plane is given by

$$\overline{V_E'^2} = \overline{u_E'^2} sin^2\theta + \overline{w_E'^2} cos^2\theta + 2\overline{(u'w')}_E sin\theta cos\theta \tag{4-24}$$

and the estimate of $\overline{u'^2}$ is obtained from

$$\frac{\overline{V_E'^2}}{sin^2\theta} = \overline{u_E'^2} + \overline{w_E'^2} cot^2\theta + 2\overline{u'w'}_E cot\theta \tag{4-24'}$$

It is evident from Equation (4-24') that better estimates of $\overline{u'^2}$ can be obtained from larger values of θ.

With the assumption that

$$\overline{(u'^2)}_E = \overline{u'^2}(z)$$

$$\overline{(w'^2)}_E = \overline{w'^2}(z)$$

$$\overline{(u'w')}_E = \overline{u'w'}(z) \tag{4-25}$$

we obtain after normalizing Equation (4-24') with respect to $\overline{u'^2}$ and applying the polarization relations

$$\frac{\overline{V_E'^2}/sin^2\theta}{\overline{u'^2}} = 1 + \frac{(\omega_0^2 - k_x^2c^2)}{k_x^2c^4(k^2 + B^2)} cot^2\theta + \frac{2k_z(\omega_0^2 - k_x^2c^2)}{k_xc^2(k^2 + B^2)} cot\theta \tag{4-26}$$

This Equation is plotted in Figure (4-4a) for a number of wave periods. However, it is more instructive to consider an isotropic wave field 1n which case the last term will be zero. This is plotted in Figure (4-4b). It is clear from this diagram that the error in the estimate of $\overline{u'^2}$ is about 15% for most scales for T= 60 min, which is probably an acceptable error. At shorter periods the error increases until it is quite substantial T = 12 minutes. One hour would appear to be the minimum time resolution that could be obtained in this case.

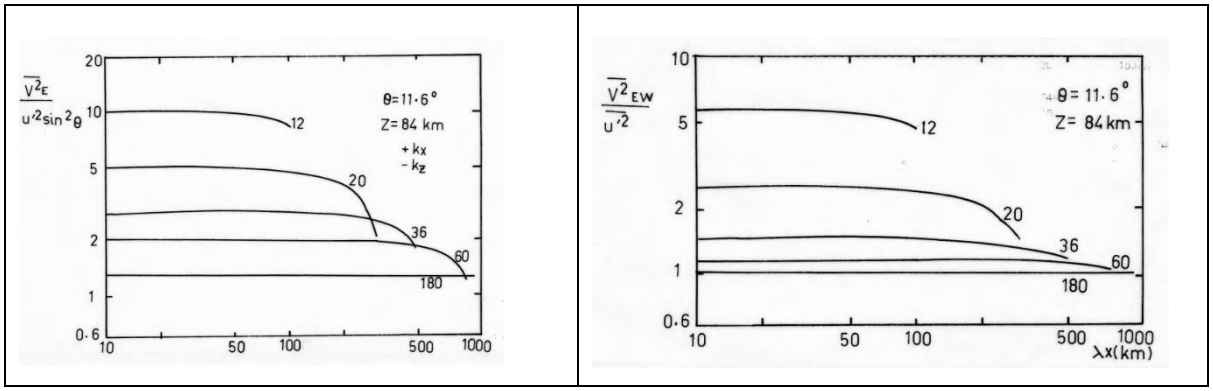

Figure (4.4a) (left) The estimate of horizontal kinetic energy obtained from a single off-vertical beam at a height of 84 km. and tilt angle of 11.6°. The case plotted corresponds to propagation in the -k direction with downward phase progression.

Figure (4.4b) (right) As for 4.4a but for wave field in which equal numbers of similar waves are propagating in the +x and -x directions. In this case, the Reynolds stress is zero.

Note that we have written the LHS of Equation (4-26) as $\frac{\overline{V_{EW}'^2}}{\overline{u'^2}}$ in Figure (4-4b). This is because these results also apply for the DCC beam arrangement in which one beam is directed Eastwards and another Westwards. In this case, however, these results are quite general and the wavefield does not have to be isotropic. We will discuss this arrangement in the next Section and the usefulness of this diagram in Section (4-3-4). If a vertically directed beam is available, then the second term in Equation (4-24') can be removed. In this case, if the wave field is isotropic, the measured value of $\overline{u'^2}$ will be exact. The general expression for the quantity measured when a vertical beam is available is

$$\overline{V_{EV}'^2} = \frac{\overline{V_E'^2} - \overline{V_V'^2}cos^2\theta}{sin^2\theta} \tag{4-27}$$

$$= \overline{u_E'^2} + (\overline{(w'^2)}_E - (\overline{(w'^2)}_V)cot^2\theta + 2(\overline{u'w'})_E cot\theta$$

Where $\overline{V_{EV}'^2}$ is defined by (4-27).

If the wave field is statistically similar in a horizontal plane, then we may apply Equations (4-16) and

$$\overline{V_{EV}'^2} = \overline{u_E'^2} + 2\overline{u'w'}cot\theta \tag{4-27'}$$

Note that without an additional beam at -θ to the zenith, where θ can be any angle such that $0<\theta<\pi/2$ in the same vertical plane, there is no way of separating these terms unless the scale and period of the wave are known (see Section 4.3.4). The accuracy of this expression depends upon the momentum flux term and because $\overline{u'w'}$ is a signed quantity, it is not possible to calculate the contribution of this term to Equation (4-27) from the polarization relations without additional information about the isotropy of the gravity wave field. However, we can obtain a measure of the error in this estimate of $\overline{u'^2}$. Observational evidence indicates that for periods between about 8 hours and the Väisälä-Brunt period (~5 minutes), energy is partitioned approximately equally for periods of 8-2 h and periods 2h-5 min (see e.g. Vincent and Ball, 1981; Vincent, 1984).

Reasonable estimates of momentum flux for 85 km for periods less than about 8 hours are about 1 m^2s^{-2} (Chapter 6) and it can be shown that this will be partitioned so that about 2/3 of the total momentum flux is due to periods less than about 2h (Chapter 6).

The error in Equation (4-27') can then be obtained by normalizing with respect to u'2 such that

$$\frac{\overline{V_{EV}'^2}}{\overline{u'^2}} = 1 + \frac{2\overline{(u'w')}_E cot^2\theta}{\overline{u'^2}} \qquad (4\text{-}28)$$

This will be about 8% for periods between 8 and 2 h, and about 16% for periods less than 2 h, where we have taken $\overline{u'^2}$~ 200 m^2s^{-2} for both of these period ranges for $\theta = 11.6°$. These errors are also probably acceptable. For $\theta = 15°$, the corresponding errors will be about 6% and 12% respectively.

It is apparent that better estimates of $\overline{u'^2}$ can be obtained for periods less than l80 min and scales less than 100 km by calculating the mean square radial velocities and not resorting to the spatial covariance estimates. This is made particularly clear by considering an isotropic wave field, in which case Equation (4-27) is exact, whereas Figure (4-3c) indicates that application of Equation (4-9') may lead to considerable errors for scales less than about 150 km.

Turning now to the Reynolds stress term $\overline{u'w'}$, we can obtain

$$\overline{V_E'^2} = \overline{(u'^2)}_E sin^2\theta + \overline{(w'^2)}_E cos^2\theta + 2\overline{(u'w')}_E sin\theta cos\theta \qquad (4\text{-}24)$$

$$\overline{V_V'^2} = \overline{(w'^2)_V} \tag{4-29}$$

Following a similar scheme to that used to obtain Equation (4-9') w

$$(\overline{u'w'})_{EV} = \frac{\overline{V'_E V'_V} - \overline{V_V'^2} cos\theta}{sin\theta} \tag{4-30}$$

the Reynolds stress. Using Equations (4-5), (4-6) and (4-24) this can be expanded to

$$(\overline{u'w'})_{EV} = \overline{(u')_E (w')_V} + [2(w')_E (w')_V - \overline{(w'^2)_E} - \overline{(w'^2)_V}]\frac{cot\theta}{2} \tag{4-30'}$$

If Equation (4-16) is true then this is

$$(\overline{u'w'})_{EV} = \overline{(u')_E (w')_V} + [(w')_E (w')_V - \overline{w'^2}]cot\theta \tag{4-30'}$$

In Terms of $\overline{u'w'}$ and $\overline{w'^2}$ this becomes

$$(\overline{u'w'})_{EV} = \overline{(u'w')}\left[\cos(k_x l) - \frac{B}{k_z}\sin(k_x l)\right] + \overline{(w'^2}[\cos(k_x l) - 1]cot\theta \tag{4-30''}$$

Writing (4-27) in terms of ω_0, k_x and k_z and normalizing with respect to $(\overline{u'w'})$ we obtain after some rearranging

$$\frac{\overline{(u'w')_{EV}}}{\overline{u'w'}} = \cos(k_x l) + cot\theta \frac{Bk_x c^2 \sin(-k_x l) + (\omega_0 - k_x c^2)[\cos(k_x l) - 1]}{k_x c^2 k_z} \tag{4-30''}$$

Equation (4-31) may be evaluated for a given ω_0, and k_x as before, with k_z being obtained from the dispersion relation.

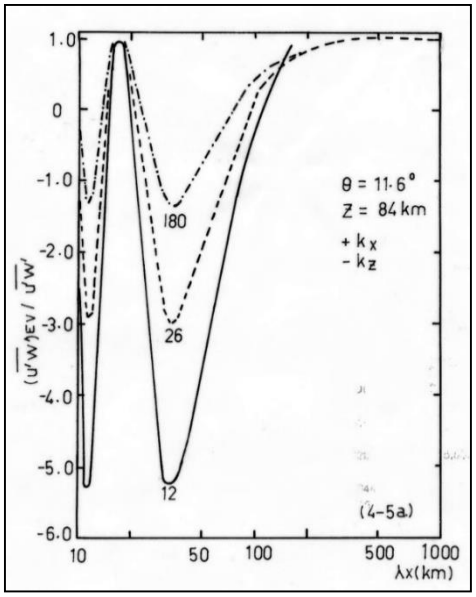

Figure (4.5a) The Reynolds stress measured using spatial covariance estimates normalized with respect to the correct value for a height of 84 km. and an off-vertical beam angle of 11.6°. Propagation is in the +x direction with downward phase progression.

Figure (4-5a) illustrates this Equation evaluated for a number of wave periods for R = 86 km and $\theta = 11.6°$. k_z is negative and k_x positive for this illustration, but the same result would be obtained for k_z positive and k_x neqative.

These results can be interpreted in much the same way as those for $\overline{(u'^2)}_{EV}$. Note that unlike $\overline{u'^2}$ measured using this beam configuration, longer period waves are affected almost as much as shorter period waves so that averaging the data over longer periods will not improve the measurement. In addition, because $cos(k_x\, l)$ is a symmetric function for values of $k_x\, l$ of interest, application of Equation (4-31) in the presence of an isotropic wave field, which should result in $\overline{u'w'} = 0$ in this case, will lead to errors in the measurement for all scales less than about 200 km.

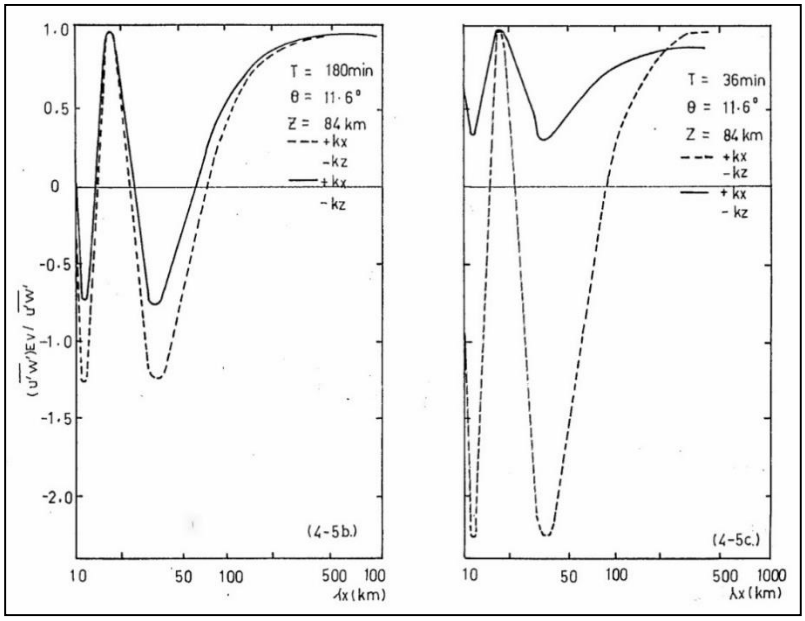

Figure (4.5b) (left) As for Figure 4.5a but for a wave of 180 minutes' period propagating in the +x direction, and another of the same period propagating in the -x direction, and Figure 4.5c (right) As for 4.5b but for a wave of 36-minute period.

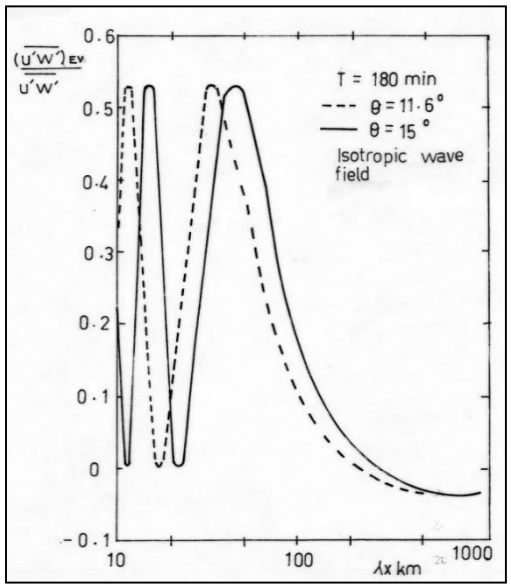

Figure (4.5d) The difference of the normalized estimate of the Reynolds stress from the correct value of zero for a wave field in which equal numbers of similar waves are travelling in the +x and -x directions with downward phase progression for two off-vertical beam angles.

To illustrate this, we have plotted Equation (4-31) for two periods, T = 36 min, and T = l80 min. for (-k_x,- k_z) and (+k_x,- k_z) in Figure (4-5b and c). The difference of $\frac{\overline{(u'w')}_{EV}}{\overline{u'w'}}$ for each of these cases should be zero and in Figure (4-5d) we have plotted the measured value of

$\frac{\overline{(u\prime w\prime)_{EV}}}{\overline{u\prime w\prime}}$ for an isotropic wave field by two tilt angles. It is clear that there will be substantial errors in $\overline{(u'w')}_{EV}$ for scales less than about 150 km, but that T = l80 min will lead to the best measurement of $\overline{(u'w')}_{EV}$.

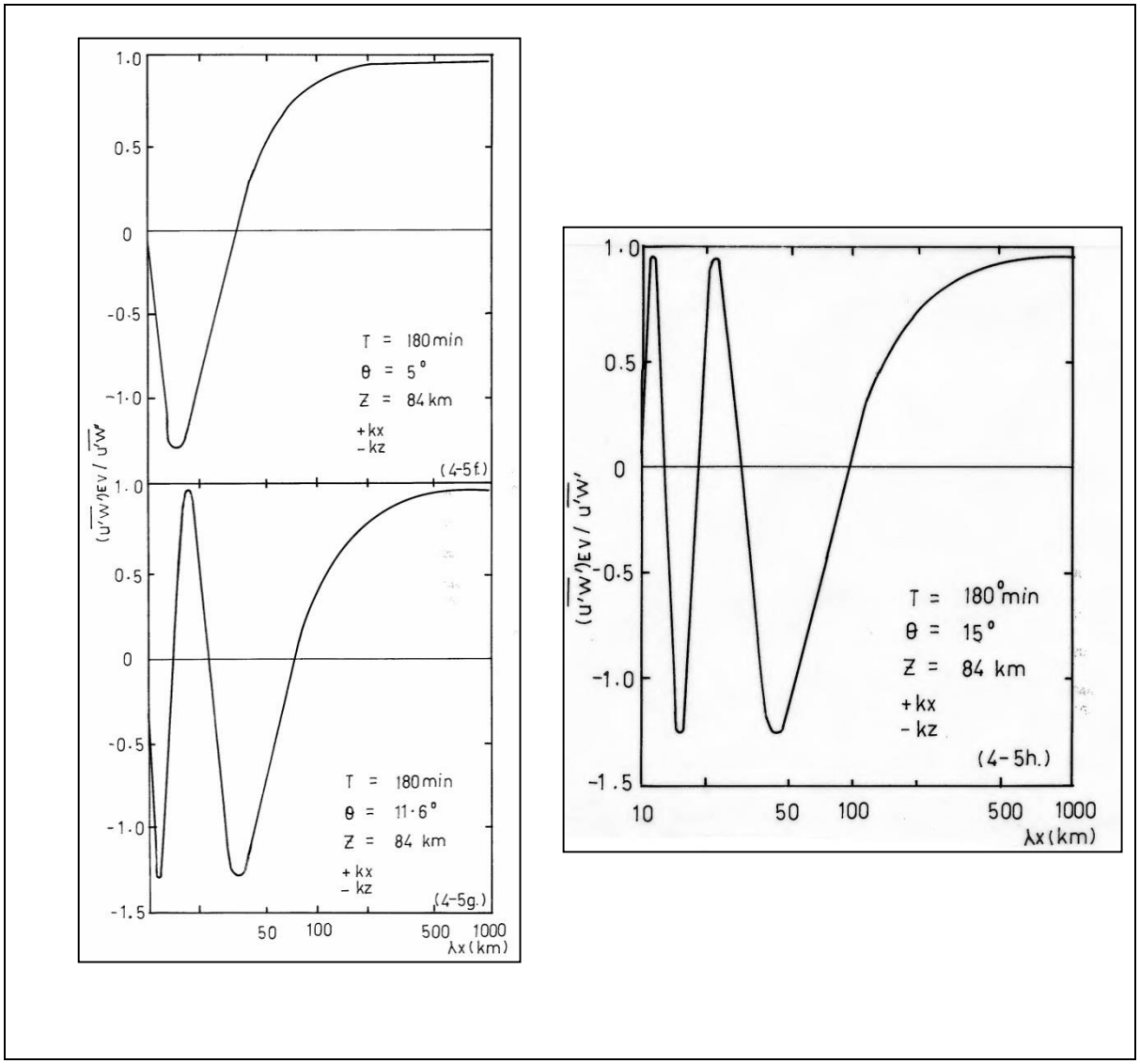

Figure (4.5f) (top left) The estimate of the Reynolds stress normalized with respect to the correct value for a 180-minute period wave and an off-vertical beam angle of 5°. Wave propagation is in the +x-direction with downward phase progression.
Figure(4.5g) (bottom left) As for 4.5f but for an off-vertical angle of 11.6°
Figure(4.5h) (right) As for Figure(4.5g) but for an off-vertical angle of 15°.

Because gravity waves are free to take a range of values of k_x and k_z for a given ω_0, the separation of horizontal scales cannot be achieved by filtering radial velocity time series, unless there is independent evidence for a relation between ω_0, and k_x. This means that if a significant

proportion of the shorter horizontal wavelength waves are contributing to the total Reynolds stress, this beam configuration is of limited use for this value of θ.

Figures (4-5f, g, and h) show Equation (4-31) evaluated for three tilt angles, $\theta = 5, 11.6\ and\ 15°$ for a wave period of 180 minutes. From this diagram it is clear that smaller tilt angles will increase the accuracy of the measurements at shorter scales for this period. Since theory cannot predict which scales contribute most to the total Reynolds stress, the only way to check Equation (4-30) is by comparison with a technique that is not dependent on scale. The complementary coplanar beam method is such a technique. This is considered in the next Section.

4.1.1.2 Two Complementary Coplanar Beams

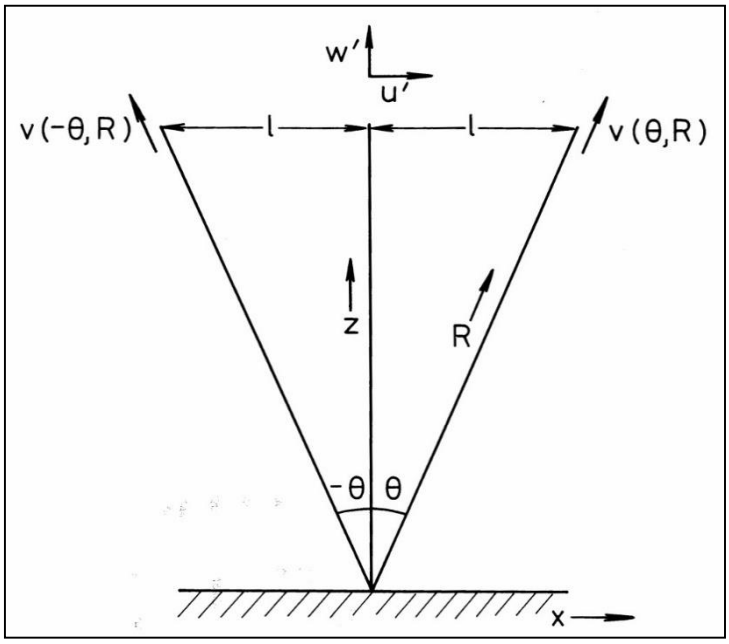

Figure (4.6) Schematic representation of the two dimensional radar situation in which two narrow radar beams are directed at angles $+\theta$ and $-\theta$ to the zenith. In the nomenclature outlined in Chapter 2, this is the DCC-beam arrangement.

We now consider two complementary coplanar beams. This beam arrangement simplifies the statistics considerably, because of its symmetry, and the quantities measured are independent of the scales of the motions present. No assumptions are required about the kind of motion that is present and both turbulent scales larger than the radar pulse volume and gravity wave contributions can be measured, although they cannot be separated unless wave motions are identified, and this can be done 1n principle only for coherent waves. However, the effects of

the Reynolds stress on the mean flow do not depend on the type of motion that produces it. The derivation of Equations (4-33 to 4-37) in this Section follows that of Vincent and Reid (1983).

Consider two radar beams directed at equal and opposite angles θ to the zenith in the xz-plane (Figure 4-6). Then $\phi = 90, 270°$.

Writing

$$\overline{V_E'^2} = \overline{V_R'^2(90)}$$

$$\overline{V_W'^2} = \overline{V_R'^2(270)}$$

where the radial velocities are measured at the same height $z = Rcos\theta$, and substituting into Equation (4-4) we obtain

$$\overline{V_E'^2} = \overline{(u'^2)}_E sin^2\theta + \overline{(w'^2)}_E cos^2\theta + 2\overline{(u'w')}_E sin\theta cos\theta \quad (4\text{-}24)$$

$$\overline{V_W'^2} = \overline{(u'^2)}_W sin^2\theta + \overline{(w'^2)}_W cos^2\theta + 2\overline{(u'w')}_W sin\theta cos\theta \quad (4\text{-}32)$$

where the subscript refers to the beam in which the bracketed quantity is measured. If the statistics of the motions are assumed to be independent of horizontal position, then

$$\overline{(u'^2)}_E = \overline{(u'^2)}_W = \overline{u'^2}(z)$$

$$\overline{(\mathrm{w}'^2)}_E = \overline{(\mathrm{w}'^2)}_W = \overline{w'^2}(z)$$

$$\overline{(u'w')}_E = \overline{(u'w')}_W = \overline{\mathrm{u}'\mathrm{w}'}(\mathrm{z}) \quad (4\text{-}33)$$

These assumptions are rather more general than those described by Equation (4-12). Unlike the latter assumptions, they do not involve any spatial covariance estimates.

Subtracting (4-32) from (4-24) gives

$$\overline{V_E'^2} - \overline{V_W'^2} = 2\overline{u'w'}sin2\theta$$

that is,

$$\overline{u'w'} = \frac{\overline{V_E'^2} - \overline{V_W'^2}}{2sin2\theta} \tag{4-34}$$

Adding (4-19) and (4-17) and rearranging gives

$$\overline{u'^2} + \overline{w'^2}cot^2\theta = \frac{\overline{V_E'^2} + \overline{V_W'^2}}{2sin^2\theta} = \overline{V_{EW}'^2} \tag{4-35}$$

where $\overline{V_{EW}'^2}$ is defined by (4-35). For two beams at +θ and -θ to the zenith in the yz-plane with

$$\overline{V_N'^2} = \overline{V_R'^2(0)}$$

$$\overline{V_S'^2} = \overline{V_R'^2(180)}$$

similar expressions to those of (4-34) and (4-35) apply. In this case

$$\overline{v'w'} = \frac{\overline{V_N'^2} - \overline{V_S'^2}}{2sin2\theta} \tag{4-36}$$

$$\overline{v'^2} + \overline{w'^2}cot^2\theta = \frac{\overline{V_N'^2} + \overline{V_S'^2}}{2sin^2\theta} = \overline{V_{NS}'^2} \tag{4-37}$$

where $\overline{V_{NS}'^2}$ is defined by (4-37). Equations (4-34) and (4-36) indicate that the upward flux of momentum can be obtained from two complementary coplanar beams without a direct measurement of the vertical component of the wind. Since this last parameter is difficult to measure, this beam arrangement has a practical advantage over a vertical and off-vertical beam independent of considerations of scale and frequency dependence. It is interesting to note that Lhermitte (1968) obtained Equation (4-21) to investigate turbulence in the boundary layer and that Vincent and Reid (1983) arrived at it independently.

Equations (4-35) and (4-37) indicate that to obtain the horizontal and vertical kinetic energy separately using the assumptions in Equation (4-33) only, an additional beam is required.

Note that the major assumption made in this derivation is that the statistics of the motions are independent of horizontal position. Fritts (1984) has pointed out that gravity waves with small horizontal scales will influence the mesosphere very near their source, possibly producing substantial spatial inhomogeneity in the momentum flux terms described by Equations (4-34) and (4-36) and the other terms in Equation (4-33). On the other hand, large scale gravity waves

can propagate large distances horizontally before arriving in the mesosphere and can therefore be expected to produce a much more homogeneous flux. This means that there may be some natural limit to the technique. However, this is only likely to become evident when widely separated regions of the atmosphere are observed. For propagating gravity waves and the beam separation we are considering here, the assumptions described by Equation (4-33) are reasonable. It is interesting to note that to measure the horizontal and vertical kinetic energy accurately for all scales a minimum of three coplanar beam positions are required. This is obvious from either (4-24) or 4-32) if each bracketed quantity is treated as a separate parameter, because there are three unknowns, and three Equations, or equivalently, three beam positions, are required to obtain them separately.

Equations (4-35) and (4-37) indicate that we cannot separate the vertical and horizontal kinetic energy. However, if we normalize Equation (4-35) with respect to $\overline{u'^2}$, then we can obtain an indication of those periods for which $\overline{V_{EW}'^2}$ is a good approximation to $\overline{u'^2}$. This ratio has previously been plotted as Figure (4-4b). Inspection of this diagram indicates that at all scales the horizontal kinetic energy for periods greater than about 60 minutes can be obtained with an error of less than 10% and this is acceptable. Consequently, at this beam angle and height (11.6°, 84 km) the momentum flux $\overline{u'w'}$ or $\overline{v'w'}$ can be obtained for any period and horizontal scale and the horizontal kinetic energy $\overline{u'^2}$ or $\overline{v'^2}$ can be obtained for periods greater than about 60 minutes.

To emphasize the problems inherent in using spatial covariance estimates, we can derive an expression for the zonal kinetic energy which involves spatial covariances from two complementary coplanar beams. To do this we anticipate the next Section in which we will consider the larger scale motions.

If we consider the expression for the mean wind in the xz- plane calculated from two beams at $+\theta$ and $-\theta$ respectively, we obtain (see next Section, Equation (4-43))

$$\overline{u_0} = \frac{\overline{V_E} - \overline{V_W}}{2sin\theta}$$

which is rather similar to Equation (4-5'). In principle the zonal kinetic energy can be calculated from this expression in a similar way to that used to calculate this quantity from (4-5'). From the instantaneous and mean values of (4-43) we can obtain

$$\overline{u_0'^2} = \overline{(u_0 - \overline{u_0})^2} \tag{4-38}$$

This can be expanded to obtain (Appendix 4)

$$\begin{aligned}\overline{u_0'^2} = \frac{1}{4}(&\overline{(u'^2)}_E + \overline{(u'^2)}_W + 2\overline{(u')}_E\overline{(u')}_W) \\ &+ \frac{\left(\overline{(w'^2)}_E + \overline{(w'^2)}_W - 2\overline{(w')}_E\overline{(w')}_W\right)}{4tan^2\theta} \\ &+ \frac{(\overline{(u')_E(w')_E} - \overline{(u')_W(w')_W} - \overline{(u')_E(w')_W} + \overline{(u')_W(w')_E}}{2tan\theta}\end{aligned} \tag{4-38'}$$

Equation (4-38') requires the following assumptions to be valid

$$\overline{(u'^2)}_E = \overline{(u'^2)}_W = \overline{(u')_E(u')_W}$$

$$\overline{(\mathrm{w}'^2)}_E = \overline{(\mathrm{w}'^2)}_W = \overline{(w')_E(w')_W}$$

$$\overline{(u'w')}_E = \overline{(u'w')}_W = \overline{(u')_E(w')_W'} = \overline{(u')_W(w')_E} \tag{4-39}$$

The first two terms of these three Equations are just those contained in (4-39). The others are additional assumptions which are scale and frequency dependent. Equation (4-38') may be expressed in terms of the polarization relations for a single gravity wave as before to obtain

$$\begin{aligned}\frac{\overline{u_0'^2}}{\overline{u'^2}} = &\frac{1 + \cos(-2k_x l)}{2} + \frac{(\omega_0^2 - k_x^2c^2)^2}{2k_x^2c^4(k_z^2 + B^2)}[1 - \cos(-2k_x l)]cot\theta \\ &+ \frac{(\omega_0^2 - k_x^2c^2)}{k_xc^2(k_z^2 + B^2)}[Bsin(2k_x l)]cot\theta\end{aligned} \tag{4-40}$$

This expression is symmetrical in k_x and k_z and so is independent of the direction of propagation. It can be evaluated for a given k_x and ω_0 and the results for a number of wave periods are shown in Figure (4-7a). This diagram can be interpreted in much the same way as that for $\frac{\overline{(u'^2)}_{EV}}{\overline{u'^2}}$. At the beam separation (35 km for $R = 86\ km$ and θ = 11.6°) the ratio is one as it is at any value of horizontal wavelengths such that

$$\lambda_x = \frac{2l}{n}, n = 1,2,3, \ldots$$

At $\lambda_x = \frac{4l}{n}, n = 1,3,5,..$ the ratio shows the worst agreement with the expected value of one, because the perturbation velocities are in anti-phase.

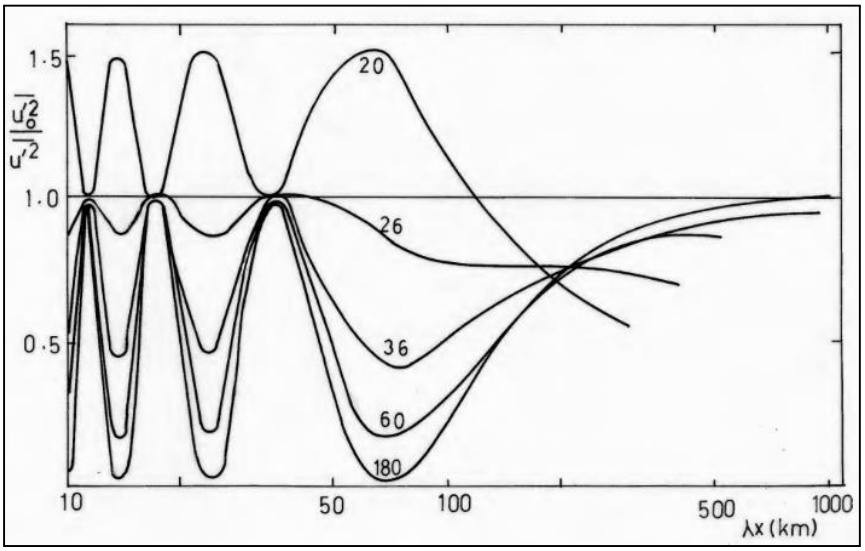

Figure (4.7a). The estimate of the horizontal kinetic energy normalized with respect to the correct value for the DCC beam arrangement. The same results are obtained for any direction of propagation in the xz-plane.

The beam symmetry works against an accurate measurement of the horizontal kinetic energy in this case. Better results can be obtained by reducing θ and Figure (4-7b) illustrates Equation (4-40) evaluated for three tilt angles for a period of 180 minutes. It is apparent from this diagram that $\theta = 5°$ provides the best measurement, but that even this tilt angle produces large errors if scales less than about 100 km are present.

These results are quite reasonable. For two coplanar beams, the best measurement of the horizontal kinetic energy using spatial covariance estimates is obtained using tilt angles of 0 and θ, but this also corresponds to the worst measure of the Reynolds stress term. The best measurement of this is obtained with tilt angles of ±θ, and this corresponds to the worst measurement of the horizontal kinetic energy. This is because a vertical beam is insensitive to variations in the horizontal component of the perturbation velocity. The errors in the estimate of the horizontal kinetic energy arise because of the spatial covariance estimates of the vertical perturbation velocity and Reynolds stress terms.

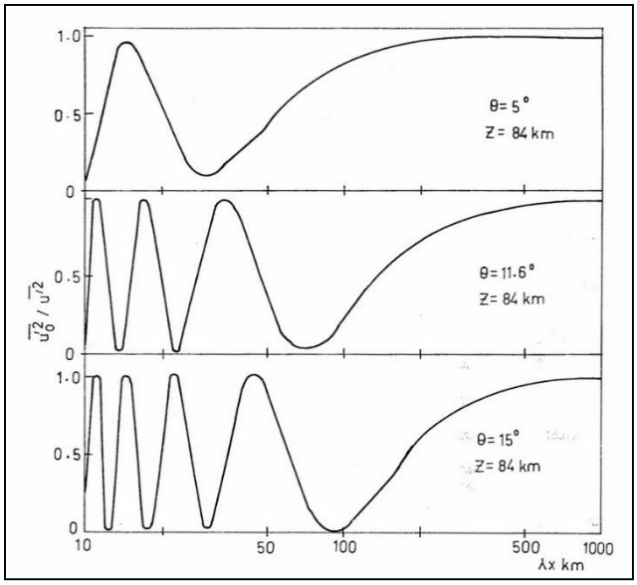

Figure(4.7b) As for (4.7a) for a wave of 180 minutes' period for three off-vertical tilt angles.

Since the horizontal component of the perturbation velocity is in general much larger than either the vertical perturbation velocity or the Reynolds stress, this term tends to dominate in Equation (4-23) for the longer wave periods. The major errors arise for periods shorter than about 60 minutes (10% at 100 km. for an isotropic wave field at this period) associated with shorter scale waves, that is, those waves in which the vertical perturbation velocity the horizontal perturbation velocity. However, there is a strong dependence upon the direction of propagation for the estimate of $\overline{u'^2}$ for longer period waves.

On the other hand, the estimate of the Reynolds stress using Equation (4-30) depends on the spatial covariance estimate of the horizontal and vertical perturbation velocities. This has a $cos(k_x l)$ dependence and this term dominates. The second term on the RHS of (4-30) produces a separation of periods and is dependent upon the direction of propagation, but not sufficiently to provide symmetry in k_x.

With two off-vertical beams, the estimate of the horizontal kinetic energy depends upon the spatial covariance of the horizontal perturbation velocities measured in the two beams. This term has a $cos(2k_x l)$ dependence and is symmetrical, that is, it does not depend upon the direction of propagation. Again, this term dominates the RHS of Equation (4-38). The symmetry of this experimental arrangement produces this dependence. However, this same symmetry allows an accurate determination of the Reynolds stress term because it does not require spatial covariances to be calculated.

It is worth noting that the Reynolds stress term can be measured using the assumption of Equation (4-33) for any two beams as long as neither beam points vertically.

With a suitable choice of beam directions, the error in the measurement of the horizontal kinetic energy using spatial covariance estimates when using two off-vertical coplanar beams can be minimized. We can apply a similar analysis to the mean vertical wind. In this case (Equation (4-45), next Section) the mean wind is

$$\overline{w_0} = \frac{\overline{V_E} + \overline{V_W}}{2cos\theta}$$

The mean square value of the instantaneous value of this Equation may be written as

$$\begin{aligned}
&\overline{w_0'^2} \\
&= (\overline{(u'^2)}_E + \overline{(u'^2)}_W - 2\overline{(u')}_E\overline{(u')}_W \frac{tan^2\theta}{4} \\
&+ \frac{\left(\overline{(w'^2)}_E + \overline{(w'^2)}_W + 2\overline{(w')}_E\overline{(w')}_W\right)}{4} \\
&+ \frac{(\overline{(u')_E(w')_E} - \overline{(u')_W(w')_W} + \overline{(u')_E(w')_W} - \overline{(u')_W(w')_E})}{2} tan\theta
\end{aligned} \tag{4-41}$$

$$\begin{aligned}
\frac{\overline{w_0'^2}}{\overline{w'^2}} = \frac{[1+\cos(-2k_x l)]tan^2\theta}{2} \frac{{k_x}^2 c^4(k_z^2 + B^2)}{2(\omega_0^2 - k_x^2c^2)^2} + \frac{1}{2}[1-\cos(-2k_x l)] \\
+ \frac{k_x c^2}{(\omega_0^2 - k_x^2c^2)}[Bsin(-2k_x l)]tan\theta
\end{aligned} \tag{4-42}$$

Because the vertical perturbation velocity is much smaller than the horizontal perturbation velocity, the first term in Equation (4-42) tends to dominate. This becomes clear when this Equation is plotted (Figure 4-8). From this diagram it is apparent that except at the beam separation and for scales larger than about 1000 km. there is a gross error in this measurement for the longer periods. In general, shorter period waves can be measured more accurately than the longer period waves, because of the relative magnitudes of $\overline{u'^2}$ and $\overline{w'^2}$, but it is clear this this particular spatial covariance estimate is rather poor.

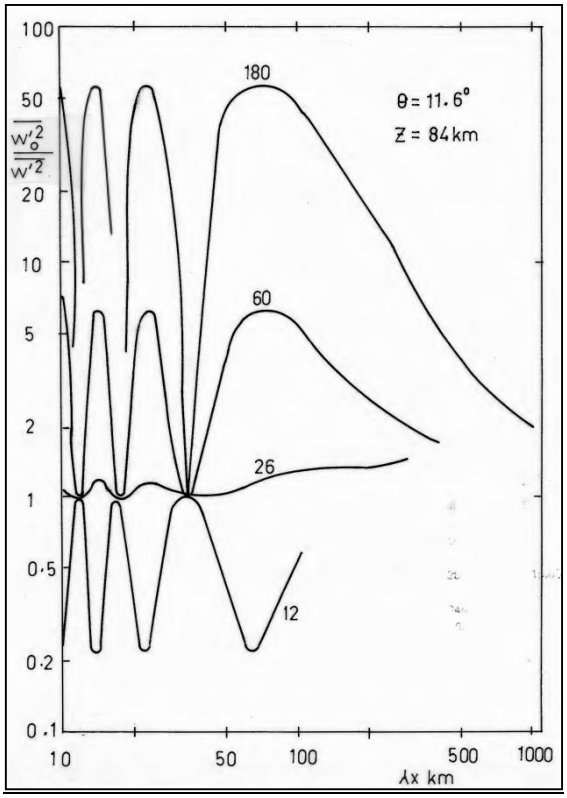

Figure (4.8) The estimate of the vertical kinetic energy obtained using spatial covariance estimates in the DCC beam configuration normalized with respect to the correct value.

4.1.2 Larger Scale Motions

In this Section we consider longer period motions. The analysis of these time scales is relatively simple but as for the shorter scale motions, the spatial variation of the wind field must be considered.

The mean radial velocity as given in Equation (4-2) is

$$\overline{\boldsymbol{V}}_{\boldsymbol{R}}\,(\phi) = \overline{\boldsymbol{u}} sin\theta\, sin\phi + \overline{\boldsymbol{v}} sin\theta\, cos\phi + \overline{\boldsymbol{w}} cos\theta. \qquad (4\text{-}2)$$

If this is calculated over a suitably long interval, the longer period winds and tidal components may be obtained. In this case, we can obtain the various wind components by simple vector decomposition. If we consider the situation as illustrated in Figure (4-6) with one beam.at $+\theta$ to the zenith and one at $-\theta$ in the xz-plane, then $\phi = 90, 270°$ respectively and with

$$\overline{V_E} = \overline{V_R}(90)$$

and

$$\overline{V_W} = \overline{V_R}(270)$$

the zonal component of the mean wind is given by

$$\overline{u_0} = \frac{\overline{V_E} - \overline{V_W}}{2sin\theta} \tag{4-43}$$

Similarly, for the yz-plane, the meridional component is

$$\overline{v_0} = \frac{\overline{V_N} - \overline{V_S}}{2sin\theta} \tag{4-44}$$

Where

$$\overline{V_N} = \overline{V_R}(0)$$

and

$$\overline{V_S} = \overline{V_R}(180)$$

The mean vertical component is

$$\overline{w_0} = \frac{\overline{V_E} + \overline{V_W}}{2cos\theta} = \frac{\overline{V_N} + \overline{V_S}}{2cos\theta} \tag{4-45}$$

These Equations have previously been derived by Vincent and Reid (1983) and similar expressions were derived by Lhermitte (1966).

However, if a gradient exists in the mean wind the situation is slightly more complicated. Lhermitte (1966) realized this and Browning and Wexler (1968) gave a simple technique to determine the effects of a gradient in the horizontal wind field. Following Browning and Wexler we expand the mean horizontal components of the wind field as a truncated Taylor series so that,

$$\bar{u} = \bar{u}_0 + \mathrm{x}\frac{\partial \bar{u}}{\partial x} + \mathrm{y}\frac{\partial \bar{u}}{\partial y}$$

$$\bar{v} = \bar{v}_0 + \mathrm{x}\frac{\partial \bar{v}}{\partial x} + \mathrm{y}\frac{\partial \bar{v}}{\partial y} \tag{4-46}$$

where the higher order terms have been neglected, the zero subscript refers to the velocity between a coplanar pair of beams, we have assumed that horizontal gradients of $\bar{w}$ can be neglected, and (x, y, z) are defined by the coordinate transformation relations for the axes in Figure (4-1). These are,

$$x = Rsin\theta sin\phi$$

$$y = Rsin\theta cos\phi$$

$$z = Rcos\theta \tag{4-47}$$

where R is the range, θ is the angle from the zenith and ϕ is the angle from North. These assumptions seem to be reasonable for the expected magnitudes of the mean winds and gradients in the mesosphere (and most of the atmosphere). Note that the assumption that the horizontal gradients of the mean vertical wind can be neglected is one of the assumptions used to calculate the mean horizontal wind from vertical and off-vertical beams. Substituting (4-46) into (4-2) and applying (4-47) we obtain, after some rearranging,

$$\bar{V}_R(\phi) = \overline{u_0} sin\theta\, sin\phi + \overline{v_0} sin\theta\, cos\phi + \overline{w_0} cos\theta + \left(\frac{\partial \bar{u}}{\partial x} + \frac{\partial v}{\partial y}\right)\frac{R^2 sin^2\theta}{2} + \left(\frac{\partial \bar{v}}{\partial y} - \frac{\partial \bar{u}}{\partial x}\right)\cos 2\phi \frac{Rsin^2\theta}{2} + \left(\frac{\partial \bar{u}}{\partial y} + \frac{\partial \bar{v}}{\partial x}\right)\sin 2\phi \frac{Rsin^2\theta}{2} \tag{4-48}$$

which is the general expression for a mean Doppler radial velocity measured in a beam at (R, θ, ϕ). This is the form of the Equation for the mean radial velocity that is used for VAD radar data analysis (see e.g. Wilson and Miller, 1971). The terms in brackets in Equation (4-48) are,

the horizontal divergence

$$\left(\frac{\partial \bar{u}}{\partial x} + \frac{\partial v}{\partial y}\right)$$

the stretching deformation

$$\left(\frac{\partial \bar{v}}{\partial y} - \frac{\partial \bar{u}}{\partial x}\right)$$

and the shearing deformation

$$\left(\frac{\partial \bar{u}}{\partial y}+\frac{\partial \bar{v}}{\partial x}\right)$$

As was the case for the fluctuating velocities, the various parameters in Equation (4-48) may be obtained from a suitable choice of beam geometry. For the pair of beams in the xz-plane (Figure 4-5) we obtain,

$$\bar{V}_E = \overline{u_0} sin\theta\, sin\phi + \overline{w_0} cos\theta + \frac{\partial \bar{u}}{\partial x} R sin^2\theta \tag{4-49}$$

$$\bar{V}_W = -\overline{u_0} sin\theta + \overline{w_0} cos\theta + \frac{\partial \bar{u}}{\partial x} R sin^2\theta \tag{4-50}$$

From (4-49) and (4-50) it is clear that (4-43) is still valid. This is an obvious result because $\frac{\partial \bar{u}}{\partial x}$ is by definition constant from beam to beam. However, adding (4-49) and (4-50) gives,

$$\overline{w_u^*} = \frac{\overline{V_E} + \overline{V_W}}{2cos\theta} = \overline{w_0} + \frac{\partial \bar{u}}{\partial x} z tan^2\theta \tag{4-51}$$

where z = Rcos8 and $\overline{w_u^*}$ is defined by (4-51).

For the yz-plane,

$$\overline{w_v^*} = \frac{\overline{V_N} + \overline{V_S}}{2cos\theta} = \overline{w_0} + \frac{\partial \bar{v}}{\partial y} z tan\theta \tag{4-52}$$

where $\overline{w_v^*}$ is defined by (4-52). These two Equations indicate that if a gradient exists in the mean horizontal wind the vertical component cannot be obtained from two off-vertical coplanar beams.

If we consider the height range for this work, we note that since $z tan^2\theta$ takes values of from 3 to 4 km over 80 to 96 km with θ = 11.6°, horizontal gradients of ~0.1 $ms^{-1}km^{-1}$ will make a significant contribution to the RHSs of (4-51) and (4-52).

Adding (4-51 and (4-52) we obtain,

$$\frac{\overline{w_u^*} + \overline{w_v^*}}{2} = \overline{w_0} + (\frac{\partial \bar{u}}{\partial x} + \frac{\partial \bar{v}}{\partial y}) z tan^2\theta \tag{4-53}$$

where the term in brackets is the horizontal divergence.

Subtracting (4-52) from (4-51) gives,

$$\frac{\overline{w_u^*} - \overline{w_v^*}}{2} = (\frac{\partial \bar{u}}{\partial x} - \frac{\partial \bar{v}}{\partial y}) z tan^2\theta \qquad (4\text{-}54)$$

where the term in brackets is the stretching deformation. Equations (4-53) and (4-54) apply when four beams are used so that one pair is arranged at $+\theta$ and $-\theta$ to the zenith in the xz-plane, and one pair is arranged in a similar fashion in the yz-plane. It is clear that whilst we can obtain the stretching deformation from (4-54) we cannot obtain the horizontal divergence from (4-53) unless another, vertically directed, beam is available. This is the same situation that occurs for a VAD radar. With the typically large zenith angles used with this method and small vertical velocities 1n the lower atmosphere, an estimate of the divergence is made by neglecting the contribution of the vertical velocity.

A slightly different form of this technique, Stepped Elevation VAD, can incorporate a measurement of the vertical wind. Alternately, a measurement of the vertical wind is made between azimuthal scans (Caton, 1963). Similarly, a single beam scanned through a range of zenith angles with two fixed beams in the orthogonal plane allows a measurement of $\bar{w}$ to be made, enabling $\frac{\partial \bar{u}}{\partial x}$ and $\frac{\partial \bar{v}}{\partial y}$ to be obtained for the xz- and yz-planes respectively. This technique therefore has a definite advantage over using fixed beam pointing directions.

The relative magnitudes of $\bar{w}$, $\frac{\partial \bar{u}}{\partial x}$, and $\frac{\partial \bar{v}}{\partial y}$, and hence the error in taking the sum of the mean velocities from two coplanar beams as the mean vertical velocity, are discussed elsewhere in this thesis. However, it should be noted that the accuracy of the mean vertical velocity, divergence and deformation measurements depends strongly upon the assumption of a uniform mean vertical velocity and that the measured radial velocities are correct. Radial velocities can be in error because they are sensitive to the distribution of scatterers within the radar pulse volume (see e.g. Chapter 5). Note that the shearing deformation $\left(\frac{\partial \bar{u}}{\partial y} + \frac{\partial \bar{v}}{\partial x}\right)$ cannot be obtained from the beam configurations described in this Section. To measure this parameter additional beams at other azimuth angles are required.

It is interesting to note that the continuity Equation can be used in this context to provide some useful information. This Equation is,

$$\frac{\partial \rho}{\partial t} + \frac{\partial (\rho \bar{u})}{\partial x} + \frac{\partial (\rho \bar{v})}{\partial y} + \frac{\partial (\rho \bar{w})}{\partial z} = 0 \tag{4-55}$$

If $\frac{\partial \rho}{\partial t} = 0$ and the atmosphere is horizontally stratified we may write,

$$-\left(\frac{\partial \bar{u}}{\partial x} + \frac{\partial \bar{v}}{\partial y}\right) = \frac{\partial \bar{w}}{\partial z} + \frac{\bar{w}}{\rho}\frac{\partial \rho}{\partial z}$$

and since $\rho = \rho_0 e^{-z/H}$,

$$-\left(\frac{\partial \bar{u}}{\partial x} + \frac{\partial \bar{v}}{\partial y}\right) = \left(\frac{\partial \bar{w}}{\partial z} - \frac{\bar{w}}{H}\right) \tag{4-56}$$

where H is the pressure scale height. Equation (4-56) indicates that if the vertical profile of $\bar{w}$ and the pressure scale height H are known, then so is the horizontal divergence.

The means that if $\frac{\partial \bar{w}}{\partial z}$ is measured along with $\frac{\partial \bar{u}}{\partial x}$ say, then $\frac{\partial \bar{v}}{\partial y}$ may be obtained in principle. In a similar fashion, the mean vertical velocity through a layer may be obtained if the horizontal divergence and the vertical velocity at the top or bottom of the layer is known. This last technique is used for meteorological VAD radars operating in the boundary layer, in which case the values obtained are within 10% of the true values (Wilson and Miller, 1971). This may have some application for ST radars where the assumption that $\bar{w}(0) = 0$ may be applied.

4.1.3 Sensitivity of the Complementary Coplanar Beam Technique

In Section (4.1.1.2) it was stated that when the dual complementary coplanar beam technique is used to measure $\overline{u'w'}$ and $\overline{v'w'}$, the only assumption made about the wind field is that the statistics of the motion at a given height are independent of horizontal position for the beam separation used. However, because we are using a finite beam separation we might expect some natural limit to sensitivity to be inherent in the technique.

For instance, we might expect the longest period waves, which have essentially horizontal perturbation velocities, and contribute approximately equally to the mean square velocities in each beam, to be discriminated against. However, this does not seem to be so from a consideration of some simple examples. Consider a single gravity wave with linearly polarized

perturbation velocities propagating at an angle β to the horizontal plane in the +x-direction as illustrated in Figure (4-9). The radial velocity measured by a beam at +θ to the zenith will be,

$$V'_E = v'_0 \cos(\omega_0 t) sin(\theta + \beta) \tag{4-57}$$

where v'_0 is the peak perturbation velocity, ω_0 is the wave angular frequency and V'_E is defined by (4-57). The mean square radial velocity will be,

$$\overline{V'^2_E} = \overline{v'^2_0}\,\overline{\cos^2(\omega_0 t)} sin^2(\theta + \beta) \tag{4-58}$$

Similarly, for a beam at -θ,

$$\overline{V'^2_W} = \overline{v'^2_0}\,\overline{\cos^2(\omega_0 t)} sin^2(\theta - \beta) \tag{4-58}$$

Subtracting (4-59) from (4-58) we obtain,

$$\overline{V'^2_E} - \overline{V'^2_W} = \frac{\overline{v'^2_0}}{2}[\sin^2(\theta + \beta) - sin^2(\theta - \beta)]$$

$$= \frac{\overline{v'^2_0}}{2} sin2\theta sin2\beta$$

That is,

$$\Delta\overline{V'^2_{EW}} = \frac{\overline{(V'^2_E} - \overline{V'^2_W})}{2sin2\theta} = \frac{\overline{v'^2_0}}{4} sin2\beta \tag{4-60}$$

where $\Delta\overline{V'^2_{EW}}$ is defined by (4-60).

If we consider the momentum flux due to the gravity wave where

$$u'_0 = v'_0 cos\beta$$

$$w'_0 = v'_0 cos\beta$$

Then we can obtain,

$$\overline{u'w'} = \overline{v'^2_0}\,\overline{cos^2\omega t} sin\beta cos\beta = \frac{\overline{v'^2_0}}{4} sin2\beta \tag{4-61}$$

So that,

$$\Delta\overline{V_{EW}'^2} = \overline{u'w'}$$

exactly. We can generalize this result for N waves of frequency ω_n propagating at various angles β_n to the horizontal. In this case,

$$V'_E = v_1' \cos(\omega_1 t)\sin(\theta+\beta_1)+\ldots$$

$$\ldots+v_N' \cos(\omega_N t)\, sin(\theta+\beta_N)$$

$$= \sum_{n=1}^{N} v_n' cos\omega_n t sin(\theta+\beta_n) \tag{4-62}$$

$$\overline{V_E'^2} = \sum_{n=1}^{N} \overline{v_n'^2 cos^2\omega_n t} sin^2(\theta+\beta_n) + \sum_{n=1}^{N}\sum_{\substack{m=1\\m\neq n}}^{M} \overline{v'_m v'_n}\sin(\theta + \beta_m)\sin(\theta+\beta_n)[\cos(\omega_m+\omega_n)\,t + \cos(\omega_m-\omega_n)\,t)] \tag{4-62}$$

Since $\overline{cos\omega t} = 0$, the second term vanishes and

$$\overline{V_E'^2} = \frac{1}{2}\sum_{n=1}^{N} \overline{v_n'^2 cos^2\omega_n t} sin^2(\theta+\beta_n) \tag{4-63}$$

Similarly, for the beam at -θ,

$$\overline{V_W'^2} = \frac{1}{2}\sum_{n=1}^{N} \overline{v_n'^2 cos^2\omega_n t} sin^2(\theta-\beta_n) \tag{4-64}$$

Subtracting (4-52) from (4-51) gives

$$\overline{V_E'^2} - \overline{V_E'^2} = \frac{1}{2}\sum_{n=1}^{N} \overline{v_n'^2} sin2\theta sin2\beta_n \tag{4-64}$$

so that

$$\overline{\Delta V_{EW}'^2} = \frac{1}{4}\sum_{n=1}^{N} \overline{v_n'^2} sin2\theta sin2\beta_n \tag{4-65}$$

Now,

$$u'_n = v'_n cos\beta_n cos\omega_n t$$

$$w'_n = v'_n sin\beta_n cos\omega_n t$$

so that

$$\overline{u'w'} = \sum_{n=1}^{N} \overline{u'_n w'_n} = \frac{1}{4}\sum_{n=1}^{N} v_n'^2 sin2\beta_n \tag{4-66}$$

And

$$\Delta\overline{V_{EW}'^2} = \overline{u'w'}$$

exactly.

If there is a phase difference between the horizontal and vertical perturbation velocities so that the wave has arbitrary polarization it can easily be shown that,

$$\Delta\overline{V_{EW}'^2} = \frac{\overline{u'_0 w'_0}}{2} cos\alpha$$

where a is the phase difference between the vertical and horizontal perturbation velocities, and that,

$$\overline{u'w'} = \frac{\overline{u'_0 w'_0}}{2} cos\alpha$$

so that,

$$\Delta\overline{V_{EW}'^2} = \overline{u'w'}$$

exactly.

These results can be generalized to any linear combination of any number of waves with arbitrary polarization and directions of propagation. It should be noted that if the gravity wave is saturated the above arguments apply, and if the wave actually breaks down into turbulence and this statistically similar in the horizontal, the technique will still measure $\overline{u'w'}$.

4.2 Summary of Parameters

This Section summarizes the parameters that can be obtained directly, in principle, from various beam arrangements using the Equations in Sections (4.1.1.2) and (4.1.1.1). It is not meant to be exhaustive and concentrates mainly on those beam configurations used in this work (for which a maximum of four beams were available). The measurement of horizontal and vertical scales of motion is taken up in Section (4.2) and the parameters that can be obtained from this aspect of the experiment are presented there. Equations that are scale and frequency dependent are marked with an asterisk. Acronyms describing the beam configuration as given in Chapter 2 are indicated in brackets. We begin with a vertical and an off-vertical beam.

4.2.1 Vertical and Off-vertical Beams (DC)

With two beams arranged at 0 and θ to the zenith in the xz-plane, the following parameters may be obtained.

$$(\bar{u})_{EV} = \frac{\bar{V}_E - \bar{V}_V cos\theta}{sin\theta} \qquad (4\text{-}5'')^*$$

$$V_V = (w)_V = (w)_E, \qquad (4\text{-}7)$$

$$\overline{(u'^2)}_{EV} = \overline{((\mathrm{u})_{EV} - (\bar{\mathrm{u}})_{EV})^2} \qquad (4\text{-}9'')^*$$

$$\overline{V_V'^2} = \overline{(w'^2)}_V \qquad (4\text{-}29)$$

$$(\overline{u'w'})_{EV} = \frac{\overline{V'_E V'_V} - \overline{V_V'^2} cos\theta}{sin\theta} \qquad (4\text{-}30)^*$$

$$\frac{\partial \overline{w}}{\partial z} = \frac{\partial \overline{V_V}}{\partial z} \qquad (4\text{-}67)$$

$$\overline{V_{EV}'^2} = \overline{u_E'^2} + 2\overline{u'w'}cot\theta = \frac{\overline{V_E'^2} - \overline{V_V'^2} cos\theta}{sin^2\theta} \qquad (4\text{-}27')$$

Note that Equation (4-5") actually provides a measure of $\bar{u}_0 + \mathrm{x}\frac{\partial \bar{u}}{\partial x}$. As was noted in the derivation of this Equation, this is unlikely to be of any consequence because of the relative magnitudes of these two quantities, but the point is raised to show the similarity of this Equation to Equation (4-9'), in that this beam arrangement does depend, although not strongly, upon the spatial variation of the horizontal wind. To be completely consistent in labelling Equations as scale dependent Equation (4-5") is marked with an asterisk.

4.2.2 Two Complementary Coplanar Beams (DCC)

With two beams arranged at +θ and -θ to the zenith in the xz-plane, the basic parameters that may be obtained are

$$\overline{u_0} = \frac{\overline{V_E} - \overline{V_W}}{2sin\theta} \tag{4-43}$$

$$\overline{w_u^*} = \frac{\overline{V_E} + \overline{V_W}}{2cos\theta} = \overline{w_0} + \frac{\partial \bar{u}}{\partial x} z tan^2\theta \tag{4-51}$$

$$\overline{u_0'^2} = \overline{(u_0 - \overline{u_0})^2} \tag{4-38}*$$

$$\overline{w_0'^2} = \overline{(w_0 - \overline{w_0})^2} \tag{4-41}*$$

$$\overline{u'w'} = \frac{\overline{V_E'^2} - \overline{V_W'^2}}{2sin2\theta} \tag{4-34}$$

$$\overline{u'^2} + \overline{w'^2} cot^2\theta = \frac{\overline{V_E'^2} + \overline{V_W'^2}}{2sin^2\theta} = \overline{V_{EW}'^2} \tag{4-35}$$

Equation (4-51) is similar in form to (4-5") that is,

$$(\bar{u})_{EV} = \overline{u_0} + \frac{\partial \bar{u}}{\partial x} z tan^2\theta = \frac{\bar{V}_E - \bar{V}_V cos\theta}{sin\theta} \tag{4-5''}$$

However, the RHS of (4-51) contains two quantities which are similar in magnitude and the horizontal gradient of the horizontal wind cannot be ignored.

4.2.3 Three Coplanar Beams TC(CP)

For three beams arranged at $-\theta,\ 0\ and\ +\theta$ to the zenith in the xz-plane, we can obtain the following parameters in addition to those of 4.2.2.

$$\bar{w} = \overline{V_V} \tag{4-7}$$

$$\overline{(w'^2)_V} = \overline{V_V'^2} \tag{4-29}$$

$$\frac{\partial \bar{w}}{\partial z} = \frac{\partial \overline{V_V}}{\partial z} \tag{4-67}$$

$$\frac{\partial \bar{u}}{\partial x} = \frac{\overline{w*_u} - \bar{V}_V}{z tan^2\theta} \tag{4-51'}$$

$$\overline{u'^2} = \overline{V_{EW}'^2} - \overline{V_V'^2} cot^2\theta \tag{4-35'}$$

Equations (4-7), (4-29) and (4-67) are trivial and (4-50') is a straightforward rearrangement of (4-51). Equation (4-35') allows the horizontal kinetic energy in this plane to be calculated using the assumptions of (4-33) only, and so is independent of scale.

4.2.4 Three Coplanar Beams + One Orthogonal Beam (OPDC)

If the beams are arranged at $+\theta,\ 0\ and\ -\theta$ to the zenith in the xz-plane, and at $+\theta$ to the zenith in the yz-plane, we can obtain the following parameters in addition· to those of 4.2.2 and 4.2.3.

$$(\bar{v})_{NV} = \frac{\bar{V}_N - \bar{V}_V cos\theta}{sin\theta} \tag{4-68}*$$

$$\overline{(v'^2)_{NV}} = \overline{((\mathrm{v})_{NV} - (\bar{\mathrm{v}})_{NV})^2} \tag{4-69}*$$

$$(\overline{v'w'})_{NV} = \frac{\overline{V'_N V'_V} - \overline{V_V'^2} cos\theta}{sin\theta} \tag{4-70}*$$

$$\overline{V_{NV}'^2} = \overline{v'^2} + 2\overline{v'w'} cot\theta = \frac{\overline{V_N'^2} - \overline{V_V'^2} cos\theta}{sin^2\theta} \tag{4-71}$$

The assumptions made in deriving these Equations have already been discussed in Section (4.1.1.1) for the zonal component, and of course, these can be generalized to the meridional component.

The Equations for the experiments described in Sections (4.2.1) to (4.2.4) for the orthogonal plane are very similar, and they will not be produced here. However, a summary of parameters is presented in Table (4-1).

4.2.5 Dual Coplanar Beams in Orthogonal Planes (OPDCC)

If four beams are arranged at $+\theta and\ -\theta$ to the zenith in the xz-plane, and $+\theta and\ -\theta$ to the zenith in the yz-plane, the following parameters are obtained

$$\overline{u_0} = \frac{\overline{V_E} - \overline{V_W}}{2sin\theta} \tag{4-43}$$

$$\overline{v_0} = \frac{\overline{V_N} - \overline{V_S}}{2sin\theta} \tag{4-44}$$

$$\overline{w_0} + \left(\frac{\partial \bar{u}}{\partial x} + \frac{\partial \bar{v}}{\partial y}\right) z tan^2\theta = \frac{\overline{w_u^*} + \overline{w_v^*}}{2} \tag{4-53}$$

$$\left(\frac{\partial \bar{u}}{\partial x} - \frac{\partial \bar{v}}{\partial y}\right) = \frac{\overline{w_u^*} - \overline{w_v^*}}{2z tan^2\theta} \tag{4-54'}$$

$$\overline{u_0'^2} = \overline{(u_0 - \overline{u_0})^2} \tag{4-38}*$$

$$\overline{v_0'^2} = \overline{(v_0 - \overline{v_0})^2} \tag{4-72}*$$

$$\overline{w_0'^2} = \overline{(w_0 - \overline{w_0})^2} \tag{4-41}*$$

$$\overline{u'^2} + \overline{v'^2} + \overline{w'^2} cot^2\theta = \overline{V_{EW}'^2} + \overline{V_{NS}'^2} \tag{4-73}$$

$$\overline{u'^2} - \overline{v'^2} = \frac{\overline{V_{EW}'^2} - \overline{V_{NS}'^2}}{2} \tag{4-74}$$

$$\overline{u'w'} = \frac{\overline{V_E'^2} - \overline{V_W'^2}}{2sin2\theta} \tag{4-34}$$

$$\overline{v'w'} = \frac{\overline{V_N'^2} - \overline{V_S'^2}}{2sin2\theta} \tag{4-36}$$

These Equations require little further comment, except for (4-41), which can be obtained from both pairs of beams and (4-74) which is a measure of the difference of the kinetic energy of the zonal and meridional components of the horizontal wind and hence of the horizontal isotropy of the wave field.

If a measurement of the vertical wind is made we can obtain Equations (4-7), (4-29) and (4-67) and so separate the terms in Equations (4-53) and (4-73). In addition, all of the parameters

contained in Sections (4.2.1) and (4.2.4) may be obtained. This measurement can be obtained by adding a fifth vertically directed beam, or as was noted earlier, by scanning one beam through a range of zenith angles with two complementary beams fixed in the orthogonal plane. This last arrangement would allow all of the parameters mentioned in this summary to be obtained.

4.2.6 Reference

For reference, the terms we have discussed in this Chapter that depend upon spatial covariance estimates are summarized below.

$$\overline{(u'^2)}_{EV} = \overline{u'^2} + 2\overline{w'^2}[1-\cos(k_x l)]cot^2\theta + 2\overline{u'w'}\left[1-\cos(k_x l)+\frac{B}{k_z}\sin(k_x l)\right]cot\theta \tag{4-22}$$

$$(\overline{u'w'})_{EV} = \overline{(u'w')}\left[\cos(k_x l)-\frac{B}{k_z}\sin(k_x l)\right] + \overline{(w'^2}[\cos(k_x l)-1]cot\theta \tag{4-30''}$$

$$\overline{u_0'^2} = \frac{\overline{u'^2}[1+\cos(2k_x l)]}{2} + \overline{w'^2}[1-\cos(2k_x l)]cot^2\theta + \overline{u'w'}\left[\frac{B}{k_z}sin(2k_x l)\right]cot\theta \tag{4-38''}$$

$$\overline{w_0'^2} = \frac{\overline{u'^2}[1-\cos(2k_x l)]tan^2\theta}{2} + \overline{w'^2}[1+\cos(2k_x l)]cot^2\theta + \overline{u'w'}\left[\frac{B}{k_z}sin(2k_x l)\right]cot\theta \tag{4-41''}$$

The corresponding terms obtained from mean square radial velocities obtained with one or two beams are

$$\overline{u_E'^2} + 2\overline{u'w'}cot\theta = \frac{\overline{V_E'^2} - \overline{V_V'^2}cos\theta}{sin^2\theta} = \overline{V_{EV}'^2} \tag{4-27'}$$

$$\overline{u'w'} = \frac{\overline{V_E'^2} - \overline{V_W'^2}}{2sin2\theta} \tag{4-34}$$

$$\overline{u'^2} + \overline{w'^2}cot^2\theta = \frac{\overline{V_E'^2} + \overline{V_W'^2}}{2sin^2\theta} = \overline{V_{EW}'^2} \tag{4-35}$$

$$\overline{u_E'^2} + \overline{w_E'^2}cot^2\theta + 2\overline{u'w'}_E cot\theta = \frac{\overline{V_E'^2}}{sin^2\theta} \tag{4-24'}$$

$$\overline{(w'^2)}_V = \overline{V_V'^2} \tag{4-29}$$

Table (4-1a)

Mean Wind Component

	$\bar{u}_o$	$\bar{v}_o$	$\bar{u}_{EV}$	$\bar{v}_{NV}$	$\bar{w}$	$\overline{w_u^*}$	$\overline{w_v^*}$	$\frac{\partial \bar{u}}{\partial x}$	$\frac{\partial \bar{v}}{\partial y}$	$\frac{\partial \bar{w}}{\partial z}$	$\frac{\partial \bar{u}}{\partial x} - \frac{\partial \bar{v}}{\partial y}$
DCVE			X		X					X	
DCCEW	X					X					
DCCNS		X					X				
TC(CP)EW	X		X		X	X		X		X	
TC(CP)NS		X		X			X		X	X	
OPDCC	X	X				X	X				X
OPDC(EW)	X		X	X	X	X		X		X	
OPDC(NS)		X		X	X		X		X	X	
Q*OB	X	X	X	X	X	X	X	X	X	X	X

Table (4-1b)

Fluctuating Component

	$u_o'^2$	$v_o'^2$	$w_o'^2$	u'^2	v'^2	w'^2	v_{EW}^2	v_{NS}^2	$u'w'$	vw	$u_{EV}'^2$	$v_{NV}'^2$	$u'w'_{EV}$	$v'w'_{NV}$	V_{EV}^2	V_{NV}^2
DCVE						X				*		*		X		
DCCEW	*		*				X		X							
DCCNS		*	*					X		X						X
TC(CP)EW	*		*	X		X	X		X		*		*		X	
TC(CP)NS		*	*		X	X		X		X		*		*		X
OPDCC	*	*	*				X	X	X	X						
OPDCEW	*		*	X		X	X		X		*	*	*	*	X	
OPDCNS		*	*		X	X		X		X			*	*		X
Q*OB	X	X	X	X	X	X	X	X	X	X	X	X	*	*	X	X

For details of beam configuration nomenclature see chapter 2.
DC = Dual Coplanar Beam
Subscript indicates beam directions, e.g. E≡+θ°Eastwards
V≡ 0°
TC(CP) = Triple Coplanar Beam (Complementary Pair.)
For four beam arrangements, subscript indicates complementary pair.
* indicates scale dependent quantity.
For definition of parameters, see text.

4.3 The Measurement of Horizontal and Vertical Scales of Motion

Extensive use of cross spectral techniques has been made to investigate waves of a wide range of scales in many parts of the atmosphere. For example, Maeda and Handa (1980) used f_0F2 data from widely spaced ionosondes to investigate large scale travelling ionospheric disturbances in the F2-region, Metcalf (1975) used wind and temperature data obtained from aircraft and meteorological radar observations to investigate sub-kilometer scale gravity waves in the lower kilometer of the atmosphere, and Wallace and Chang (1969) have applied cross spectral analysis techniques to investigate large scale travelling tropospheric wave disturbances in the tropics.

Cross correlation techniques have also been applied to Doppler radar data in an attempt to determine the horizontal and vertical scales of wind motion. For instance, Rastogi and Bowhill (1976) did this for radial velocities obtained from three beams of the Jicamarca radar for mesospheric observations. However, because the radial velocity measured in an off-vertical beam contains both horizontal and vertical wind components, the cross correlation functions

obtained between beams are rather difficult to interpret, especially for shorter scales, without additional information.

For gravity wave motion there is a well-defined relation between the vertical and horizontal components. The polarization relations derived by Hines (1960) give this relation in a simple form for a simplified model of the atmosphere, and these may be easily applied to radial velocity time series. The accuracy of this approach depends upon the original assumptions of Hines (1960) and this must be borne in mind as a limitation. Without this kind of additional information other more restricting assumptions must be invoked. For example, Rastogi and Bowhill (1976) assumed that to be significant, cross correlation had to reach values of one, and that cross correlations calculated between off-vertical beams were only useful if either the mean vertical or horizontal components were zero, and this limited the interpretation of their data.

This Section of the Chapter describes the use of the polarization relations and cross spectral analysis to measure horizontal and vertical scales using a single station. Cross spectral techniques lead naturally to a separation of variance according to frequency, and allow the significance of cross spectral phases to be estimated by use of the "coherence squared" of the cross spectrum. The technique described in Smith and Fritts (1983) to measure horizontal scale is discussed in Chapter 7.

4.3.1 Complementary Coplanar Beams

We begin this Section by considering the general expression for the radial velocity due to a single gravity wave of angular frequency ω_0, peak perturbation velocities (u'_0, v'_0, w'_0) and wave numbers (k_x, k_y, k_z) measured at (R, θ, ϕ, t). This is

$$V'_R(R,\theta,\phi,t) = (u'_0 sin\theta sin\phi + v'_0 sin\theta cos\phi + w'_0 cos\theta) \times e^{i(\omega_0 t - k_x l - k_y m - k_z z)} \quad (4\text{-}75)$$

Where

$$l = Rsin\theta sin\phi$$

$$m = Rsin\theta cos\phi$$

$$z = Rcos\theta$$

The following analysis follows that of Vincent and Reid (1983).

If we consider two beams which are arranged at $+\theta and\ -\theta$to the zenith in the xz-plane (Figure 4-6) then according to (4-75) the radial velocity measured in the beam at $+\theta$ (i.e. $\phi = 90°$) will be

$$V'_E = (w'_0 cos\theta + u'_0 sin\theta)e^{i(\omega_0 t - k_x l - k_z z)} \tag{4-76}$$

where $V'_E = V'_R(R, \theta, \phi = 90, t)$

Similarly, the radial velocity measured in the beam at $\phi = 270°$ will be

$$V'_W = (w'_0 cos\theta - u'_0 sin\theta)e^{i(\omega_0 t + k_x l - k_z z)} \tag{4-77}$$

where $V'_W = V'_R(R, \theta, \phi = 270, t)$

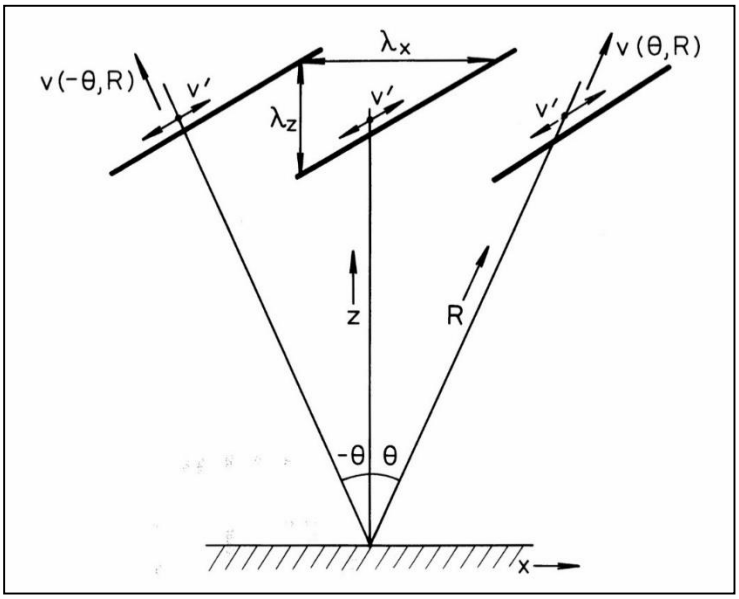

Figure (4.9) Idealized situation in which a single plane gravity wave propagates in the +x-direction. The direction of propagation may be obtained from a comparison of v' for each of the beams. The heavy lines represent the gravity wave phase fronts, and v' the perturbation wind velocities.

Figure (4-9) illustrates this beam arrangement for a single plane gravity wave propagating in the +x-direction with downward phase progression. If $F_R = F(R, \theta, \phi, \omega)$ is the Fourier transform of V_R such that

$$F_R = \int_{-\infty}^{\infty} V_R e^{i\omega t} dt$$

Then

$$F_E = (w'_0 cos\theta + u'_0 sin\theta)e^{-i(k_x l + k_z z)}\delta(\omega - \omega_0) \quad (4\text{-}78)$$

where δ = delta function.

Similarly, for the beam at ϕ= 270°,

$$F_W = (w'_0 cos\theta - u'_0 sin\theta)e^{-i(k_x l - k_z z)}\delta(\omega - \omega_0) \quad (4\text{-}79)$$

By substituting the polarization relations (4-14) into (4-78) and (4-79) and calculating the cross spectral power from

$$W_{EW} = W(z, \omega) = F_W F_E^* \quad (4\text{-}80)$$

where * indicates the complex conjugate, we obtain the phase of the cross spectrum as (Appendix 4)

$$\zeta = 2k_x l + \zeta' \quad (4\text{-}81)$$

where

$$\zeta' = \tan^{-1}\left[\frac{k_x(\omega_0^2 - k_x^2 c^2)Bc^2 sin2\theta}{(\omega_0^2 - k_x^2 c^2)cos^2\theta - k_x^2 c^2 k_z^2 sin2\theta}\right]$$

and the various terms have been defined previously. The most important thing to note about Equation (4-81) is that it is symmetrical in k_z and so only changes sign if the horizontal direction of motion is reversed. That is, ζ is the same for upward and downward propagating waves of the same horizontal direction of propagation. By writing k_z^2 in terms of k_x^2 using the dispersion relation, ζ can be evaluated for a given ω_0 and k_x, and Figure (4-10) illustrates the cross spectral phase in radians calculated from (4-81) plotted as a function of horizontal wavelength for different periods for the separation of beams at 85 km for this work. If the horizontal direction of propagation of the wave is known, the horizontal wavelength can be found for a wave of given frequency ω_0 by measuring the cross spectral phase at $\omega = \omega_0$, and comparing it with values calculated from Equation (4-81).

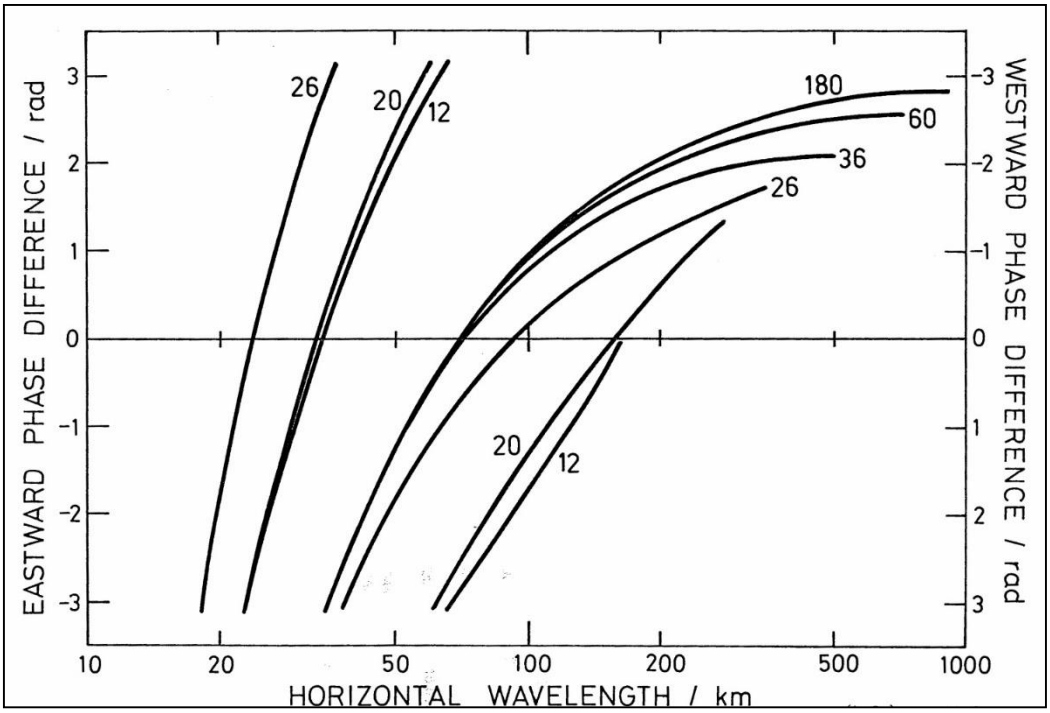

Figure (4.10) Plot of the cross spectral phase in radians calculated from (4.81), plotted as a function of horizontal wavelength for different periods. The numbers against each curve give the wave period in minutes.

To see how the horizontal direction of propagation can be determined (for downward phase progression at least), we need to reconsider Figure (4-9). By inspection of this diagram it is clear that larger radial velocities will be measured in the beam at $+\theta$ than in the beam at $-\theta$. Consequently, the difference of the mean squared velocities will be positive for waves propagating in the +x-direction and negative for oppositely directed waves. In general, the gravity wave motions will not be linearly polarized as shown in Figure (4-9), but elliptically polarized. However, the principle will still hold.

Returning now to Figure (4-10), it is obvious that there is an ambiguity in wavelength which arises because of the inherent $2\pi n$ phase ambiguity. For example, 20-minute period waves of 30 and l20 km horizontal wavelength will have the same phase. A direct way of resolving this ambiguity is to measure the vertical radial velocity in addition to those at $+\theta$ and $-\theta$, but before considering three Doppler beams we consider vertical and off-vertical beams. This leads naturally to the three beam case and illustrates the information that may be obtained from the conventional Doppler radar beam configuration.

4.3.2 Vertical and Off-vertical Beams

Consider two radar beams directed at 0 and $+\theta$ to the zenith in the xz-plane (Figure 4-2). With the radial velocities measured in these beams written as

$$V_V = V_R(z,t)$$

$$V_E = V_R(R,\theta,\phi = 90,t)$$

respectively, where $z = Rcos\theta$ the radial velocities are obtained from Equation (4-75) as

$$V'_E = (w'_0 cos\theta + u'_0 sin\theta)e^{i(\omega_0 t - k_x l - k_z z)} \quad (4\text{-}76)$$

$$V'_V = w'_0 e^{i(\omega_0 t - k_z z)} \quad (4\text{-}82)$$

The Fourier transform of (4-82) will be

$$F_V = w'_0 e^{-i(k_z z)}.\delta(\omega - \omega_0) \quad (4\text{-}83)$$

The Fourier transform of (4-76) has previously been given as (4-78). By applying the polarization relations for u6 and w6 as before and calculating the cross spectrum from

$$W_{VE} = F_V F_E^*$$

we obtain the phase of the cross spectrum as (Appendix 4)

$$\zeta = -k_x l + \zeta'$$

where

$$\zeta' = \tan^{-1}\left[\frac{-Bk_x c^2 sin^2\theta}{k_x c^2 k_z sin\theta + (\omega_0^2 - k_x^2 c^2)cos^2\theta}\right] \quad (4\text{-}84)$$

The most important feature of this expression is that it is not symmetrical in k_z and so depends upon whether the wave is up- or down- going. For upward propagating energy (i.e. downward phase) k_z will be negative. The corresponding term ζ' for a westward and vertical beam combination is identical, except that the +ve sign in the denominator becomes -ve.

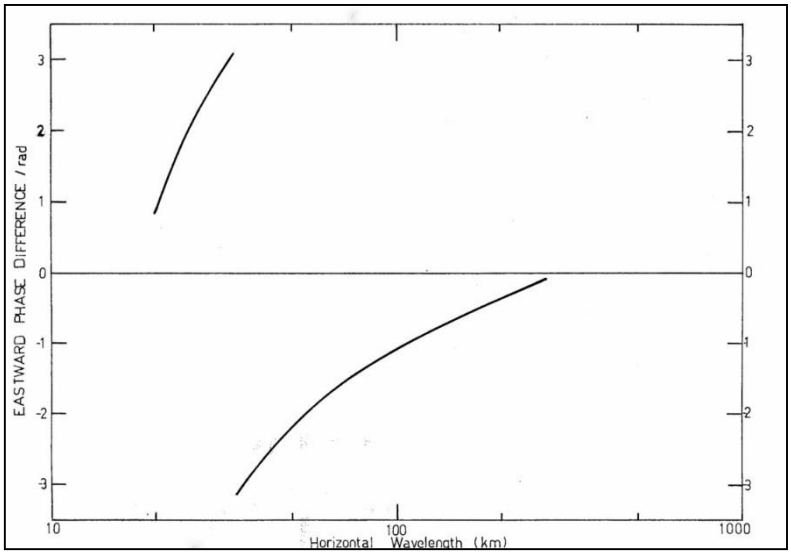

Figure (4.11) Plot of the cross spectral phase in radians calculated from (4-84), plotted as a function of horizontal wavelength for different periods. Case illustrated corresponds to propagation in the +x (eastward) direction with a downward phase progression.

Equation (4-84) is not symmetrical in k_x either and so two nomograms are required to illustrate the cross spectral phase. Figures (4 11) and (4-12) illustrate the cross spectral phase in radians calculated from (4-84) for Eastward and Westward propagating waves respectively plotted as a function of horizontal wavelength for different wave periods. This beam arrangement allows the vertical wavelength to be calculated directly, and can also be used to indicate whether the wave is up- or down- going.

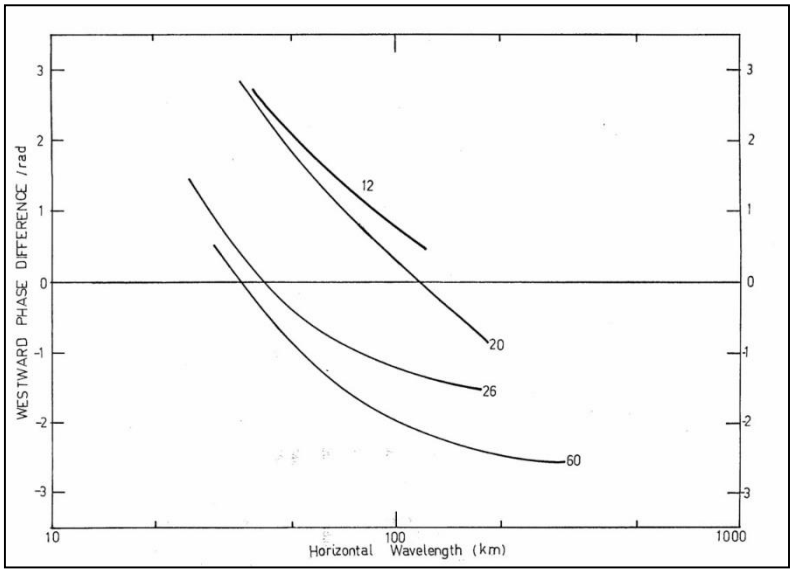

Figure (4.12) As for (4.11) but for propagation in the -x (westward) direction with downward phase progression.

Consider the radial velocity measured in the vertical beam at a height $z = z_1$.

Then from Equation (4-83) we obtain

$$F_{z_1} = F(z_1, \omega) = w'_0 e^{-i(k_z z_1)}.\delta(\omega - \omega_0) \tag{4-85}$$

Similarly, for a height $z = z_2$,

$$F_{z_2} = F(z_2, \omega) = w'_0 e^{-i(k_z z_2)}.\delta(\omega - \omega_0) \tag{4-86}$$

The cross spectrum is given by

$$W(R, \omega) = F(z_2, \omega)F^*(z_1, \omega) =, \omega) = w'_0 e^{ik_z(z_1 - z_2)} \tag{4-87}$$

and so the phase is

$$\zeta = -k_z(z_1 = z_2) \tag{4-88}$$

Thus, the vertical wavenumber can be obtained simply from

$$k_z = \frac{\zeta}{(z_1 - z_2)} \tag{4-88'}$$

Equation (4-88') is just the elementary expression used to calculate the wavelength if the phase of a wave at two spatially separated positions is known. By measuring the cross spectrum at a range of heights, the phase ambiguity inherent in this measurement can be resolved. More importantly, this procedure should indicate whether the wave is up- or down- going. If this last information is obtained, the assumption of downward phase progression is obviously not required.

4.3.3 Three Coplanar Beams

We now consider what is probably the optimum beam arrangement for measuring horizontal scales.

Consider three beams aligned at $+\theta, 0\ and\ -\theta$ to the zenith in the xz-plane, Figure (4-9). With this beam arrangement the phase ambiguity inherent in the measurement of horizontal scale can be reduced, because we are sampling three, rather than two, positions of the wave, and while an ambiguous result is still possible, it is less likely. In addition, if a measurement

of the vertical wavenumber (magnitude and sign) is obtained from the vertical beam the ambiguity can be removed entirely in principle.

To determine the horizontal wavelength with three coplanar beams, the procedure is:

(l) Determine the horizontal direction of propagation using the assumption of downward phase progression, or from the signs of $[S_E(\omega) - S_W(\omega)]$ and $[S_E(\omega) - S_V(\omega)]$ at $\omega = \omega_0$ or from the signs of these expressions plus the measured vertical phase velocity.

(2) Measure the phase of the cross spectrum $W_{EW}(\omega)$ at $\omega = \omega_0$. If the $(COH)^2$ is significant compare the measured value of ζ with that calculated from (4-81) and hence obtain the horizontal wavelength(s).

(3) If two wavelengths are obtained, measure the phase of the cross spectrum $W_{EV}(\omega)$ at $\omega = \omega_0$. If the $(COH)^2$ is significant, compare the measured phase with that calculated from (4-84) and obtain the correct wavelength.

The triple coplanar beam arrangement provides an additional check as to the reliability of the phase because the wavelength calculated from two off-vertical beams can be compared to that calculated from a vertical and both off-vertical beams for all significant events, not just those that produce an ambiguous horizontal wavelength result. This is rather important since even random data will produce a certain number of events with significant coherence. Because of this, it is essential that corresponding phases fit into a physically reasonable pattern that is consistent from height to height and from beam to beam. Isolated points with significant coherence are of little use.

4.4 Some Practical Considerations

In this Section we consider some practical considerations pertinent when applying the ideas of the last three Sections. The first concerns the method of obtaining the direction of propagation.

4.4.1 Horizontal Direction of Propagation

To determine the horizontal direction of propagation without the assumption of downward phase progression, additional information is required to the tilt of the phase surface ("aspect ratio") and this cannot be obtained directly from the mean square radial velocities measured in

DCC beams. However, the assumption of downward phase progression is reasonable for long period gravity waves at least. Vincent (1984) used a rotary spectral analysis to show that a lower limit of 65% of the vertical energy flux of these waves is up-going.

To determine the horizontal direction of propagation three coplanar beams are required, one of which is directed vertically (Section 4.2.2). This involves cross spectral analysis of vertical velocities obtained at successive height ranges. However, because the assumption of downward phase progression appears to be good, we can follow a. more time-efficient scheme similar to that applied to the DCC beam radial velocity variances.

If we consider the situation illustrated in Figure (4-9) and recall Equation (4-46) for a single gravity wave with linearly polarized perturbation velocities propagating at an angle θ to the horizontal, then the mean radial velocity measured in the beam at $+\theta$ is

$$\overline{V_E'^2} = \frac{\overline{v_0'^2}}{2} sin^2(\theta + \beta) \tag{4-58}$$

Similarly, for the beam at -θ

$$\overline{V_W'^2} = \frac{\overline{v_0'^2}}{2} sin^2(\theta - \beta) \tag{4-59}$$

so that

$$\overline{\delta V_{EW}'^2} = \overline{V_E'^2} - \overline{V_W'^2} = \frac{\overline{v_0'^2}}{2} sin2\theta sin^2\beta \tag{4-89}$$

In a similar fashion, we can calculate the difference between the mean square values of the radial velocities measured in a vertical and an off-vertical beam as

$$\overline{\delta V_{EV}'^2} = \overline{V_E'^2} - \overline{V_V'^2} = \frac{\overline{v_0'^2}}{2} \frac{[cos2\beta - cos2(\theta + \beta)]}{2} \tag{4-90}$$

β can be expressed 1n terms of the frequency of the wave by applying

$$\beta = \tan^{-1}(\frac{w'}{u'}) \tag{4-91}$$

which taken as a time average is

$$\beta = \tan^{-1}\left(\frac{k_x c^2 k_z}{\omega_0^2 - k_x^2 c^2}\right) \tag{4-91'}$$

Applying the dispersion relation this becomes

$$\beta = \tan^{-1}\left(\pm\frac{\omega_i}{N}\right) \tag{4-91''}$$

in the limit, where N = Väisälä-Brunt frequency, and the subscript refers to wave i. This approximation is valid for periods longer than about 30 min.

Equations (4-89) and (4-90) are plotted over a range of wave frequencies using (4-91") with the mean square perturbation velocity set as a constant, in Figure (4 13).

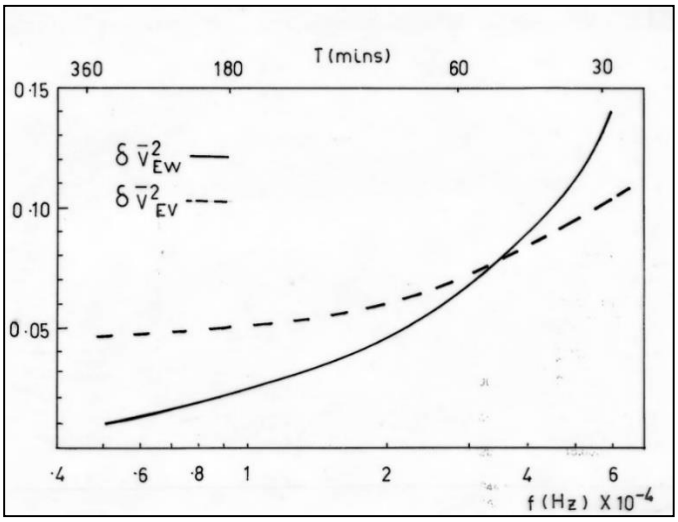

Figure (4.13) Plot of the difference in the mean square radial velocities for the DCC and DC beam configurations.

Thus this diagram only indicates the relative sensitivity of the two different beam geometries, and cannot be used to examine the sensitivity of the basic technique. This is because $\overline{v_0'^2}$ is itself a function of frequency and the exact dependence can only be determined by experiment. However, it is clear that the direction of propagation can be determined from both beam geometries as long as $\overline{v_0'^2}$ brings the difference of the variances of the radial velocities measured in each beam up to the sensitivity of the experimental equipment, and this is considered in Chapter 6.

The DCC beam arrangement is less sensitive, because the difference between the mean square radial velocities is larger, for most frequencies, but the sensitivity of both techniques increases with increasing frequency. $\overline{v_0'^2}$ decreased in general with increasing frequency (see Chapter 5) and for a given frequency interval $\Delta f = f_1 - f_2$ is given by

$$\overline{v_0'^2} = \left[\frac{S_0 f^{1-k}}{1-k}\right]_{f_1}^{f_2}$$

where S_0 and k are constants obtained by fitting a curve of the form $S_0 f^{-k}$ to $S(f)$, the power spectrum. A reasonable value for k is about 1.5 (Vincent, 1984) so that for a given frequency interval Δf,

$$\overline{v_0'^2} = [2S_0 f^{0.5}]_{f_1}^{f_2}$$

Taking two equal frequency intervals of 0.83-1h, and 1-1.25h, and evaluating this expression, we obtain $\overline{v_0'^2} \sim S_0(2.1)$ for 0.83-1h and $\overline{v_0'^2} \sim S_0(2.8)$ for 1-1.25h. Taking the center frequency of each of these intervals and substituting the appropriate values into Equation (4-89) we obtain,

$$\frac{\Delta\overline{V_{EW}'^2}(0.83,1)}{\Delta\overline{V_{EW}'^2}(1,1.25)} \sim 0.91$$

so that this method of obtaining the horizontal propagation direction is more sensitive for shorter period waves. This is reasonable, because longer period waves have perturbation velocities which are rather more horizontal than shorter period waves, and the difference between $\overline{V_E'^2}$ and $\overline{V_W'^2}$ will be smaller for longer period waves.

It is important to note that the greater sensitivity of the vertical/off-vertical beam combination applies only to the determination of the direction of gravity wave propagation, and not to measurements of momentum flux or horizontal scale. It may seem strange that the Reynolds stress terms $\overline{u'w'}$ and $\overline{v'w'}$ can be obtained from the mean square radial velocities measured in DCC beams but that the horizontal direction of propagation cannot. However, the reason for this can easily be seen from a simple example. From the polarization relations we may obtain

$$\overline{u'w'} = \frac{A^2}{2}\omega_0^2 k_x c^2 k_z (\omega_0^2 - k_x^2 c^2) \qquad (4\text{-}19)$$

where the various terms have previously been defined. For gravity waves $w_0^2 < k_x^2 c^2$ is a very good approximation so that the term in brackets will be negative.

For the case illustrated in Figure (4-8) the variance of the radial velocity measured in the beam at +θ will always be larger than that measured in -θ regardless of the horizontal direction of propagation. For propagation in the +x-direction, k_x is positive, k_z negative and $\overline{u'w'}$ is positive. For propagation in the –x-direction, k_x is negative, k_z is positive so that $\overline{u'w'}$ is still positive. A similar argument applies for the case in which the phase tilt is perpendicular to that shown in Figure (4-9). In this case $\overline{u'w'}$ will be negative regardless of the direction of propagation. Thus the difference of the mean square radial velocities measures the correct momentum flux regardless of the direction of propagation. This results from the symmetry in the $\overline{u'w'}$ term. It does not matter which component, u' or w', is negative or positive. For example, a negative value of this term can indicate upward transport of westward momentum, or downward transport of eastward momentum.

In the next Section we consider the significance of the cross spectral phases and hence of the measured horizontal scales.

4.4.2 Significance and Spectral Resolution

The measurement of horizontal scale is complicated in practice because any number of waves may be present in the region being observed. To ensure that the measured phase corresponds to a wave, and not just noise, a confidence level must be established for each frequency interval calculated with the cross spectral analysis. To do this, the "coherence squared" ($(COH)^2$) of the cross spectrum may be calculated for each frequency interval as

$$(COH)^2 = \frac{|F_E^* F_W|^2(\omega)}{|F_E(\omega)|^2 |F_W(\omega)|^2}$$

This term is analogous to the square of the correlation coefficient between the fluctuations in the two beams in given frequency band, except that it is independent of the phase relationship between the time series (see e.g. Jenkins and Watts, 1968). Essentially, it provides a measure of the similarity of observations made in the beams for a given range and frequency interval, which is really a way of measuring how well a wave model fits the observations. It is related directly to a significance level $(1 - p)$ by

$$\beta = 1 - p^{1/(df/2-1)} \tag{4-93}$$

Julian (1975), where df is the number of degrees of freedom, and β is the limiting $(COH)^2$ for significance at the $(1-p)$ level. $df/2$ is the effective number of Fourier components in a spectral range and thus β depends upon the amount of smoothing applied to the spectrum.

Any power spectral analysis produces a measure of the variance within a given frequency band (Δf) to the total variance of a time series. The contribution in each band consists of the vector sum of the spectral estimates contained within the band multiplied by the interval of angular frequency it represents, that is $2\pi\Delta f$. Averaging over spectral estimates reduces the resolution but improves the reliability of the measurement. This occurs because noise can be regarded as a random vector. Consequently, the noise components of adjacent spectral estimates are randomly phased and these tend to average out to zero as more spectral estimates are averaged over.

This means that to obtain both good frequency resolution and significance, long data lengths are required. However, if the time series contains periods in which the gravity wave activity various in amplitude or phase, then the $(COH)^2$ of a given frequency band will generally be lower than for that corresponding to the period of enhanced activity. In the extreme case, if the observation term is long, the wave activity may "wash out" so that no significant events are detected.

Good spectral resolution is also required to reduce the likelihood of more than one wave appearing in the same frequency band. If this does occur, and the $(COH)^2$ is significant, the measured wavelength will not necessarily correspond to either wave. If they are propagating in opposite horizontal directions, then the direction of propagation of both waves will be obscured. The $(COH)^2$ may decline rapidly with spatial separation in this case, (Wallace, 1971) and this is only likely to be evident in this work when vertical velocity cross spectra are calculated at a number of successive ranges. However, decreasing $(COH)^2$ with spatial separation is not necessarily indicative of superposed propagating waves, because evanescent modes could produce the same effect.

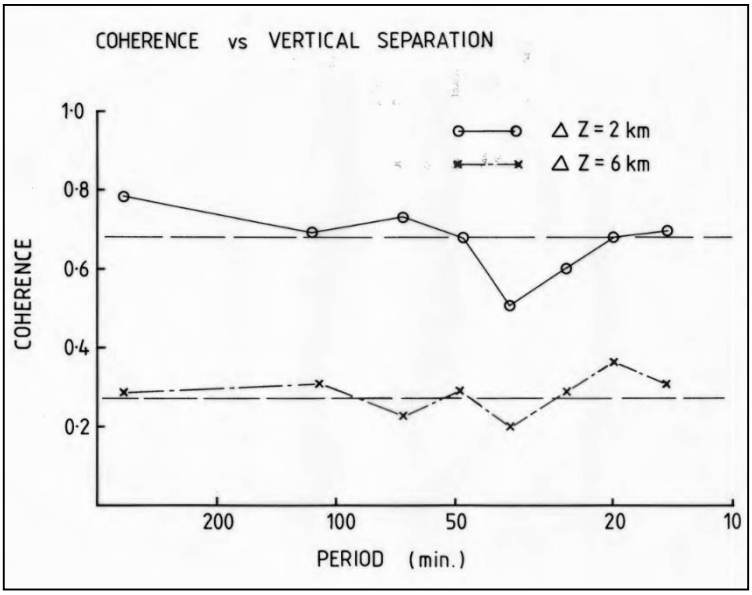

Figure (4.14) Vertical coherence for May 1982 data for two separations and a range of wave periods.

If two or more waves of the same frequency arrive at the spaced observation sites from different directions, the phase difference will be "smeared" and the $(COH)^2$ will be reduced. The variation of $(COH)^2$ with spatial separation is a very useful parameter in itself, and is exploited in oceanographic studies quite extensively.

In general, it will be a function of frequency and beam separation (see e.g. Figure 4-14), because the gravity wave field appears to be broadband and to consist of the superposition of many waves which may have similar frequencies, but different horizontal and vertical scales and this is considered in Gossard and Hooke (1975). The principles they outline are quite general, and are applied in many branches of geophysics. For example, various spaced array configurations are used to study internal waves in the ocean (see e.g. Garret and Munk, 1979).

Gossard and Hooke (1975) point out that the rate at which signal coherence decreases perpendicularly to the direction of propagation can give a measure of the extent of the source of the wave motion, which they term the "beamwidth" (although a better term would be angular spectrum). The rate at which coherence decreases parallel to the direction of propagation can be used as a measure of the velocity "bandwidth" of the propagation medium.

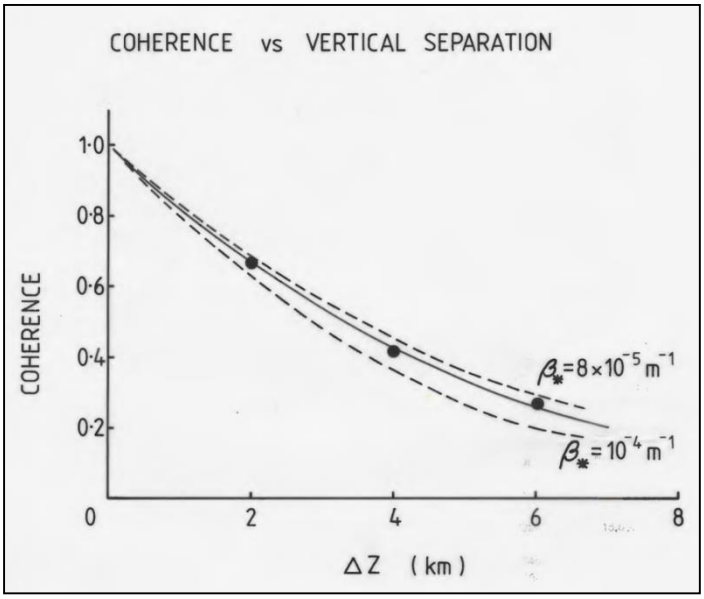

Figure (4.15) The coherence plotted as a function of vertical separation for May 1982 observations. For an interpretation of β_* see VanZandt (1982) (Vincent, 1983, private communication).

To measure these quantities obviously requires sampling at spaced positions in a horizontal plane and the vertical direction and exceeds the range of this work for the former case. However, radars with a beam swinging capability can obtain the necessary information.

It is also important from another point of view. Because the coherence decreases with increasing spatial separation in general, there must be an upper limit to the spatial separation between observing sites in relation to the measurement of the scale. Figure (4-15) illustrates coherence against vertical separation for DW data taken in May 1983 (Vincent, 1983, private communication). It clearly shows the decline in coherence with vertical separation, and this obviously has important consequences for the measurement of vertical wavelength. A similar variation in coherence would be observed with horizontal separation.

The $(COH)^2$ may also be reduced at a fixed separation by the presence of non-sinusoidal oscillations in the radial velocity time series. This is because cross spectral analysis will interpret such events as the superposition of a sinusoidal variation at a fundamental frequency and higher harmonics, and these will appear in other frequency bands. This may reduce the $(COH)^2$ sufficiently to produce an event or events that are not significant. This could be important for damped and breaking waves, which together with saturated waves will produce changes in the mean flow. However, it is only likely to be of any consequence if the perturbations vary significantly between the spaced observing positions, that is, the beam

separation. Since this is about 35 km in this work, it is most likely to affect only gravity waves with very short horizontal wavelengths, and observations made in the course of this work indicate that the assumption of the homogeneity of wave statistics in a horizontal plane is quite good. If this effect does occur, however, the horizontal scales measured by the DCC beam technique may not be representative of very small scales that may be influencing the mean flow.

Spurious contributions to spectral bands can occur for at least two other reasons. Because the radial velocity time series spectra have larger spectral densities at lower frequencies (so called "red" spectra), this can appear at higher frequencies through spectral leakage. This effect can be reduced by removing the low frequency components by high pass filtering and this requires a suitable filter function or this procedure will also introduce spurious frequencies.

According to Hines (1974), another possible contaminating effect can be produced if high amplitude, coherent waves are present, because their narrow bandwidth can cause contamination of other cross spectral phases, and some researchers omit records containing coherent waveforms from cross spectral analysis for this reason (e.g. Shibata and Okuzawa, 1983). However, if these waves can be identified, other methods of analysis, such as least squares fitting, may be applied. Generally, however, the wind field is rather complicated and to the eye at least, often appears quite random at higher frequencies.

Waves propagating at $+\theta$ and $-\theta$ from the zenith will not contribute to the radial velocities in one of the beams in the DCC beam arrangement. In this case, the $(COH)^2$ will not be significant and no horizontal scale will be obtained. However, the correct momentum flux will still be measured. Similarly, waves propagating at azimuth angles of 0 and 180° will not be detected if the beams are directed at 90 and 270° from North. However, these restrictions can be overcome by adding a vertical beam, and another pair of beams at $\phi = 0\ and\ 180°$, respectively. The limiting value of the $(COH)^2$ required for significance will also determine the uncertainty in phase and hence the uncertainty in the measurement of horizontal scale (Jenkins and Watts, 1968). For example, with a $(COH)^2$ = 0.68 (which has been used in this work) the uncertainty in phase will be 0.45 rad. It is evident from Figure (4-9) that phase errors of this magnitude make estimates of wavelengths greater than about 200 km very uncertain at 85 km with a beam separation of 35 km. The scheme applied to the analysis of radial velocity time series to measure horizontal scale in an effort to meet the conflicting demands discussed in this Section is given in Chapter 7.

In the next Section we briefly consider the ambiguity in the measurement of horizontal scale that occurs in the DCC beam experiment.

4.4.3 The Ambiguity in Horizontal Scale in the DCC Beam Arrangement

When only two beams are available to measure horizontal scale, an ambiguity in wavelength can occur. This can be resolved in principle by comparing the radial velocities measured at different ranges in the same beam to obtain the vertical wavelengths. Since the vertical and horizontal wavelengths are related to the wave frequency by the gravity wave dispersion relation, it is possible in principle to choose the correct horizontal wavelength. This procedure was used by Vincent and Reid (1983), but because the height resolution of their equipment was 4 km, short vertical wavelengths may not have been resolved. However, this technique may be useful for radars with superior height resolution.

4.4.4 Perturbation Velocities

When using the DCC beam arrangement, the horizontal component of the perturbation velocity cannot be separated from the vertical component as was shown in Section (4.1.1.2). However, as we noted in that Section, a good approximation can be obtained for the large period waves by adding the mean square radial velocities for the complementary coplanar beams for a given height and frequency interval because the vertical component is considerably smaller than the horizontal component. The radial velocities measured in off-vertical beams may be reduced in magnitude by effects related to the anisotropy of the scatterers and this will be discussed in Chapter 5, but the relative magnitudes should be consistent.

In addition, some care needs to be taken when removing the vertical perturbation velocity measured with a vertical beam from the sum of the variances of the radial velocities obtained from DCC beams because the vertical component will not be underestimates. If SA observations are available for adjacent periods of observation the horizontal component measured using the Doppler wind method may be rescaled, but these limitations must be borne in mind.

If the horizontal and vertical mean square perturbation velocities are available, then they may be used to give a further indication of horizontal scale, because they are related by the polarization relations. Figure (4-16) illustrates the ratio $\overline{w'^2}/\overline{u'^2}$ for a few short gravity wave

periods and from this diagram it is clear that some indication of horizontal wavelength may be obtained if the period and ratio are known.

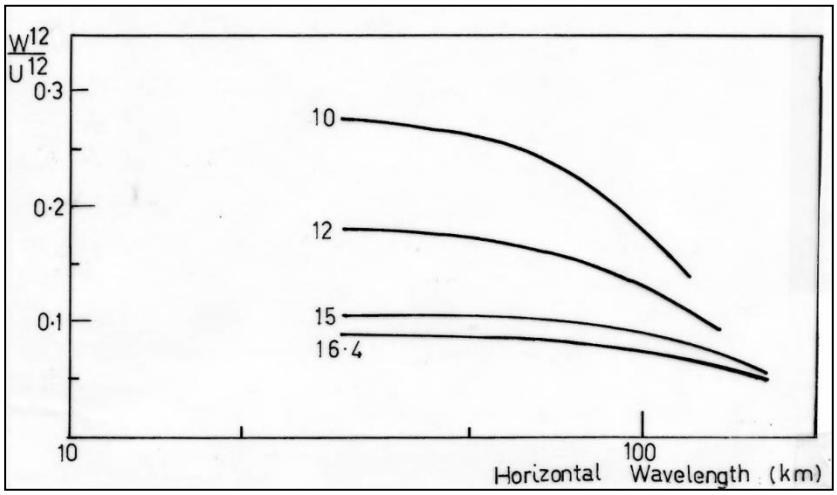

Figure (4.16) Ratio of vertical to horizontal kinetic energy calculated from the polarization relations for a number of wave periods. The number against each curve represents the wave period.

This type of diagram (see also Figures (4-4a) and (4-3d)) is useful in another way. If the period and horizontal scale of a particular wave have been obtained by applying the procedures described in Section (4-2), then the vertical and horizontal components of the kinetic energy can be separated, because the wave motions measured fit the model of Hines (1960), and the results shown in Figures (4-15) and (4-4a) will be quite accurate.

From Equation (4-35) we have the measured quantity

$$\overline{u'^2} + \overline{w'^2}cot^2\theta = \frac{\overline{V_E'^2} + \overline{V_W'^2}}{2sin^2\theta} = \overline{V_{EW}'^2} \tag{4-35}$$

If the normalized value of $\overline{V_{EW}'^2}$ calculated from the polarization relations is written as

$$\overline{V'^2} = \frac{\overline{V_{EW}'^2}}{\overline{u'^2}} \tag{4-94}$$

then

$$\overline{u'^2} = \frac{\overline{V_{EW}'^2}}{\overline{V'^2}} \tag{4-95}$$

and

$$\overline{w'^2} = \frac{\overline{V_{EW}'^2}(\overline{V'^2} - 1)}{\overline{V'^2} cot^2\theta} \tag{4-96}$$

for a given wave of frequency ω_0 and horizontal wavelength k_x. However, Figure (4-4a) indicates that the response of $\overline{V'^2}$ in terms of horizontal scale is relatively flat, so that for many periods approximate values for $\overline{u'^2}$ and $\overline{w'^2}$ may be obtained if the period is known.

In addition, if the horizontal scale of a wave of a given frequency has been measured using a vertical and off-vertical beam, a similar procedure can be applied to obtain the horizontal kinetic energy and Reynolds stress terms separately from Equation (4-27'). This Equation is

$$\overline{u'^2} + 2\overline{u'w'} cot\theta = \overline{V_{EV}'^2}$$

If the normalized value of VV calculated from the polarization relations is written as

$$\overline{V'^2} = \frac{\overline{V_{EV}'^2}}{\overline{u'^2}} \tag{4-97}$$

then

$$\overline{u'^2} = \frac{\overline{V_{EV}'^2}}{\overline{V'^2}} \tag{4-98}$$

and

$$\overline{u'w'} = \frac{\overline{V_{EV}'^2}(1 - \overline{V'^2})2}{\overline{V'^2} cot\theta} \tag{4-99}$$

This means that we can obtain all of the necessary information for coherent gravity waves through cross spectral analysis and the application of the polarization relations.

4.4.5 Finite Beam Widths and Height Resolution

4.4.5.1 Finite Beam Widths

The spatial equivalent of the half power full width of the radar beam at BP is about 14 km. at 85 km. This sets the smallest scale of turbulent and gravity wave motion that can be resolved by the analysis of radial velocity time series. In the DCC beam experiment with $\theta = 11.6°$, the separation between beam centers is about 35 km. With a vertical beam and a beam at 11.6°

to the zenith, the separation between the half power points of the beams is about 4km, so that scales less than about 30 km are unlikely to be resolved, and there will be considerable smearing of the phase difference for larger scales.

This means that better scale resolution will be obtained with the DCC beam arrangement, and if a vertical beam is added in an effort to resolve any scale ambiguity, the horizontal direction of propagation and wavelengths obtained from the pair of offset beams are likely to be the best estimates. If the results from a vertical/off-vertical combination support those from the pair of offset beams this gives extra significance to the measurement. If there is a contradiction, the results from the latter combination are probably better and should be preferred.

This last statement does not mean that all inconsistent results be accepted, because we have already stated that consistency from height to height and beam to beam should be sought. However, the limitations of the equipment must be considered, and in our case these are reasonably restricting for some beam arrangements. At any rate, consistency from height to height can still be checked.

4.4.5.2 Finite Height Resolution

Since heights are sampled every 2 km, and the height resolution of the system is about 4 km, cross spectral analysis of time series corresponding to adjacent heights measured in a vertical beam results in significant correlations for most spectral bands. At a separation of 4 km, some significant events will result from the limited resolution of the system. This requires calculation of cross spectra at successive 4 km intervals to establish significance. However, this also has the advantage of reducing the possibility of ambiguous vertical wavelengths being obtained. Since the average vertical wavelength is about 12-20 km (Vincent, 1984; Manson et al., 1979) and rocket observations indicate that vertical wavelengths less than about 4 km occur relatively rarely (Philbrick, 1981), the 4 km height resolution will not discriminate against many waves. However, the vertical wavelength depends on the background wind, and this is likely to vary rapidly with height. To obtain consistency in the measured wavelengths, better height resolution would be an advantage.

Note that the horizontal wavelength also depends upon the background wind, but because this is less subject to large spatial variation over typical beam separations, determination of horizontal wavelengths made at spatially separated locations in the same horizontal plane are

not affected in the same way. However, the background wind $\bar{u}$ will Doppler shift the wave frequency so that the intrinsic frequency n can be obtained from

$$\Omega = \omega_0 - \boldsymbol{k} \cdot \boldsymbol{u} \tag{4-100}$$

where ω_0 is the observed frequency and $\boldsymbol{k}$ is the horizontal wavenumber.

4.5 The Measurement of Momentum Flux for Scales Smaller than the Radar Pulse Volume

The discussion in this Chapter has been concerned with the analysis of radial velocity time series. Consequently, it is applicable for scales larger than the radar pulse volume. However, a similar analysis to that applied to the mean square radial velocities can be applied to scales smaller than the spatial resolution determined by the beam widths and radar pulse length. This can be done by substituting the spectral width of the backscatter Doppler spectrum for the mean square radial velocity into Equation (4-4). However, this requires a radar with a high time resolution capability so that the spectrum of radial velocities within the radar pulse volume can be measured accurately. In practice, this means that very narrow beamwidths and pulse lengths are necessary. In the ideal case, with no background wind, the various components contained in Equation (4-4) for scales smaller than the radar pulse volume may be obtained in much the same way as for the analysis of radial velocity time series. For instance, if the average spectral widths of the Doppler spectra measured in eastward and westward beams are $\overline{\sigma_E^2}$ and $\overline{\sigma_W^2}$ respectively, then the momentum flux $\overline{u'w'}$ is given by

$$\overline{u'w'} = \frac{\overline{\sigma_E^2} - \overline{\sigma_W^2}}{2sin2\theta} \tag{4-34'}$$

for scales smaller than the radar pulse volume. This type of analysis appears to have been applied to multi-beam Doppler sonar observations of tidal flow turbulence in the ocean (Lhermitte and Poor, 1983).

In practice, the spectral width is partially determined by finite beam widths, pulse lengths and background wind (see e.g. Hocking, 1983a). However, because these effects should be the same for both beams in the DCC beam arrangement, the momentum flux could be measured in principle, if both spectral widths are wider than the width of the spectrum due to the finite beamwidths and the assumption of horizontal homogeneity is valid, because Equation (4-34')

describes a difference rather than a sum. On the other hand, Equation (4-35) could not be used to obtain the sum of the horizontal and vertical mean square fluctuations in turbulent velocity without considering spectral broadening, because it involves the sum of the spectral widths.

This type of analysis is likely to be quite involved in practice because of the numerous effects that may contaminate the spectral width of the Doppler backscatter time series, but is worth noting because of the amount of useful information related to small scale motion that could be obtained. The momentum flux terms $\overline{u'w'}$ and $\overline{v'w'}$ are generally assumed to be negligible when compared with $\overline{u'^2}$ and $\overline{w'^2}$ in most studies which extract information about small scale motion from spectral widths (e.g. Hocking, l983a), and the accuracy of this assumption will depend upon the data length used to calculate the Doppler spectrum. Certainly, $\overline{u'w'}$ and $\overline{w'^2}$ may be of comparable magnitudes. However, this problem will not be pursued in this work but we note that the extension of the DCC beam arrangement to the measurement of these scales is likely to be very important.

4.6 Summary and Conclusion

This Chapter has concentrated on presenting the various quantities that can be obtained from a multi-beam Doppler radar. The conventional Doppler radar beam configuration, that is, a vertical and an off-vertical beam can be used to measure horizontal and vertical scales of gravity wave motion and to obtain a measure of the horizontal kinetic energy.

However, this last quantity requires a spectrum of gravity waves isotropic in azimuth for the results to be correct and even then it will only be correct for scales larger than about 100 km. and periods greater than about 60 minutes for a height of 84 km and an off-vertical angle of 11.6°. There may also be an ambiguity in the measurement of k_x.

The upward flux of horizontal momentum can be measured for scales longer than about 200 km at a tilt angle of 11.6° by using spatial covariances, but without additional information about the actual gravity wave spectrum scales cannot be separated. Consequently, the validity of this measurement must be established (or refuted) by comparison with a measurement of the Reynolds stress made with a technique that does not depend on scale. If the horizontal scale has been measured, then the Reynolds stress for that motion may be obtained.

Two Doppler beams offset at equal angles from the zenith in the same plane can be used to obtain an accurate measurement of the Reynolds stress with only the assumption that the

statistics of the atmospheric motions are horizontally homogeneous. However, spatial covariance estimates of the horizontal and vertical kinetic energy are poor. A term containing both the horizontal and vertical components of the kinetic energy may be obtained, but unless the period and scale of the wave are known, these components cannot be obtained separately.

Horizontal scales of the motion can be measured directly, but the vertical scale cannot, and there may be an ambiguity in k_x. The beams do not have to be complementary, and the Reynolds stress can be obtained, as long as neither beam points vertically. With a suitable choice of beam geometry, accurate measurements of the horizontal kinetic energy should be possible.

With three coplanar beams the horizontal and vertical kinetic energy can be obtained using only the assumption of the horizontal homogeneity of the wind field. In addition, both horizontal and vertical scales of the wave field can be measured unambiguously in principle and the Reynolds stress may be obtained. Thus, three coplanar beams is the optimum arrangement in one vertical plane.

Consequently, if fixed beam positions are used five beams is the minimum number required to measure all of the parameters presented in Section 4.1.4. However, if the radar is capable of scanning a range of zenith angles in a plane in a time during which the atmosphere can be regarded as statistically stationary, and radial velocity time series are obtained at the same height for complementary zenith angles, the analysis described in this Chapter can be applied.

Then with either two complementary coplanar beams fixed in the orthogonal plane, or another scanning beam, all of the parameters presented in Section (4.1.4) may be obtained. Obviously, the greater the number of horizontal positions sampled at a fixed height, the better the statistics and reliability of the derived parameters will be.

5. The Measurement of Mesospheric Wind Velocities with the Doppler Wind Techniques at Buckland Park

In the last Chapter we considered the ideal form of the DW experiment, in that the antenna beamwidths were assumed to be infinitely narrow, and the scattering regions were assumed to be isotropic. This is not the case in practice, and in this Chapter we discuss some practical considerations that are important when observations of mesospheric winds are made with finite beamwidths using the DW technique.

It will be recalled (Chapter 2) that in addition to the DW technique, the SA technique was available at BP in November 1980. Both of these methods may be applied at 2 MHz to measure the neutral wind in the ionospheric D-region (60-100 km) and simultaneous observations of D-region winds were made with these two techniques. The total data length obtained was six days, with a time resolution of one hour. The results of this comparison are discussed in this Chapter.

After considering the problems inherent in DW measurements of wind using relatively wide beamwidths, and the November 1980 results, we present the mean DW derived winds for the various observational periods in which the Reynolds stress and horizontal wavelength were measured. Direct measurements of the vertical component of the wind field were made in most observational periods during the course of this work. The results of these observations are also presented in this Chapter.

Uncertainties in the measurement of winds made with the DW technique arise from the nature of the scattering mechanism, and in the next Section we consider very briefly, scattering from the ionospheric D-region, and its importance for DW measurements made at BP.

5.1 Backscatter from 60-100 km and its importance for the Doppler Wind experiment at BP

5.1.1 Backscatter from 60-100 km

In this Section we consider partial reflection and backscattering of radio waves from the ionospheric D-region. The main area of interest is MF and HF partial reflection and backscatter, although some results at VHF are pertinent.

The received backscattered signal will always depend upon the type of scattering or reflection mechanism operating, and the polar diagram of the receiving array and pulse length used to observe it. The polar diagram of the array can be easily determined by calculation, and the pulse length is under experimental control. At BP the half width at half power of an entire array is $\pm 4.5°$ (Figure 2-5) and a typical pulse length is $30\ \mu s$.

The backscatter polar diagram is harder to determine, but a great deal of observational data has been collected which gives a good picture in a statistical sense, but has not produced a complete picture of what causes the scattering regions themselves. Since we are only interested in the nature of the received backscatter as far as it influences the properties of the Doppler spectrum, this is not a major issue in this work.

The observations related to the backscatter polar diagram can be divided roughly into indirect and direct methods. Indirect observations have been made by Vincent and Belrose (1978) who compared the gain of antennae of very different beamwidths to estimate the off-vertical angles from which significant energy is returned, and by Lindner (1975b) who used the relative phase of backscattered radiation received at spaced antennae to measure its mean angular spread. This last technique is described in Lindner (1975a). Direct methods involve measuring the power received at various zenith angles relative to that received from the zenith with narrow Doppler beams. By assuming a Gaussian fall-off in power with zenith angle, the mean angular spread of the backscattered radiation may be calculated. This last procedure has been followed by Hocking (1979) and Jones (1980) at HF, and by Fukao et al. (1981) at VHF. Agreement between the indirect and direct methods is good.

The general conclusion of these studies is that at D-region heights, the scattering regions often exist in the form of horizontally stratified layers, and scatter is returned only from angles close to the zenith. The scattering properties are observed to vary with height, and the D-region may be roughly divided into two regimes on the basis of the character of the backscatter. Below about 75-80 km, radar returns appear to be due to specular type reflection from thin horizontal steps in refractive index, and these are observed to be both spatially and temporarily intermittent. Hocking (1979) found that at 2 MHz, strong bursts of power lasting 2-5 minutes were quite common, and that scatter was returned only from angles up to $2 - 3°$ from the zenith. These results are in good agreement with those of Lindner (1975b) and Jones (1980). Above these heights, backscatter is found to be more isotopic in character, and is received from angles up to 10-15° from the zenith (Vincent and Belrose, 1978; Jones, 1980; Lindner, 1975b).

Temporal variations in signal strength appear to be smaller at these heights (Hocking, 1979). However, even though there is spatial variability in the occurrence of backscatter over the height range of 60-100 km, strong and persistent echoes often come from so-called "preferred heights". Observations at widely separated stations indicate that the ranges of 65-68 km, 70-74 km, 82-84 km, 85-88 km and 90-94 km are strongly scattering regions (Hocking and Vincent, 1982b).

The irregularities in this height range can also cause backscattering of VHF signals (see e.g. Röttger et al, 1979) and consequently, irregularities with vertical scales of only a few meters must exist. Specular reflections are also observed at these frequencies (Fukao et al., 1980) and this requires a vertical fluctuation of less than one eighth the radar wavelength over a horizontal scale larger than the first Fresnel zone (see e.g. Röttger, 1980). This is $(\lambda z)^{1/2}$ where z is the height of scatter, and λ is the radar wavelength, and as is pointed out by Hocking and Vincent (1982b), this means that the reflecting surface cannot vary in height by more than a few meters over horizontal distances of the order of a kilometer. The effective production mechanism for such structures is not well understood at present, but Röttger (1980) gives a review of mechanisms that could cause specular reflections in the atmosphere up to E-region heights.

Turbulence is considered to be the cause of the more isotropic scattering above about 80 km, although this has not been demonstrated conclusively, but a specular component is also present. Hocking and Vincent (1982a) found significant specular reflection associated with the ledge in electron density often observed at about 85 km, and Hocking (1981) found that at 80-85 km, HF backscatter appears to be composed of approximately equal proportions of specular and random components. Röttger (1980) has suggested that specular type reflectors with rough reflecting surfaces could produce this type of effect, and he has termed the process "diffuse reflection".

To summarize the current picture of backscatter from the D-region, we note that: scatter is returned from angles close to the zenith, with heights below about 75-80 km having scatter characteristic of quasi-specular reflection, and heights above 80 km having scatter characteristic of a more isotropic scattering mechanism, but with a significant specular component. Over the entire height range, the scatter is both spatially and temporally intermittent, but is less so above about 80 km. However, strong and persistent backscatter is often observed from certain preferred heights.

5.1.2 The Effective Beam Angle

When radar beams are used to observe backscatter, the effective beam pointing direction is determined by the convolution of the angular polar diagrams of the backscatter and the receiving array. Figure (5-1) is redrawn from Röttger (1980) and illustrates this situation schematically for a radar beam of finite width and a backscatter polar diagram which is narrow about the zenith. In this diagram, θ_A is the apparent pointing direction of the radar beam. The convolution of the two polar diagrams centered at these angles produces an effective beam at a mean pointing angle of θ_E. The effect of this is that radiation is received closer to the zenith and the measured radial velocity is an underestimate.

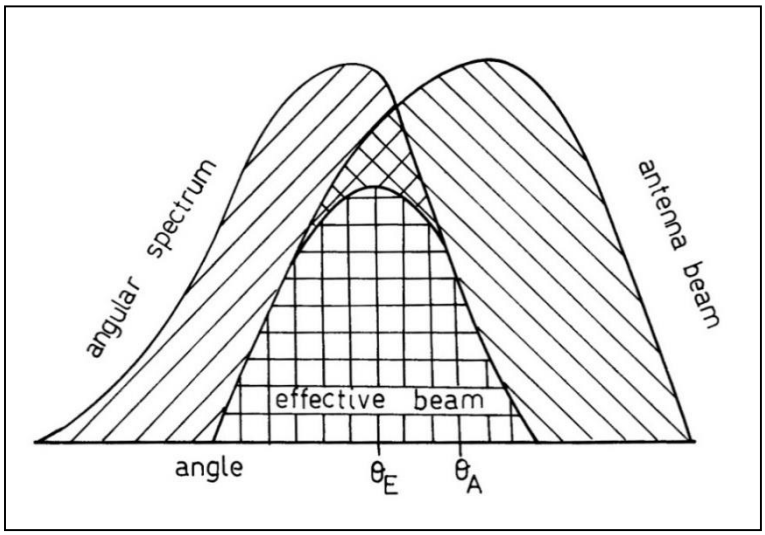

Figure (5-1) Schematic illustration of the formation of the effective antenna beam. For details see text.

If the beam width is narrow (~1°) the effective tilt angle cannot be changed much (although the returned power will be reduced) and the resulting error is small. If the beam width is relatively large, as at BP say, large errors can result. For instance, if the beam is nominally tilted at 11.6° to the zenith but is effectively pointing at the half power angle of 7.1°, the measured mean horizontal velocity $\overline{u^*}$ after the vertical component is removed will be

$$\overline{u^*} = (0.6)\bar{u} - (0.5)\bar{w}, \tag{5-1}$$

where $(\bar{u}, \bar{w})$ are the true horizontal and vertical components of the wind respectively. Since $\bar{u} >> \bar{w}$ generally, this means that the measured value of the mean horizontal velocity would underestimate the true value by about 40% in this case. The general expression for the measured horizontal velocity $\overline{u^*}$ is simply given by

$$u^* = u(\frac{sin\theta_E}{sin\theta_A}) - w(\frac{cos\theta_E - cos\theta_A}{sin\theta_A}), \quad (5\text{-}2)$$

Where u^* is defined by Equation (5-2) and the other terms have previously been defined.

That this effect would occur was first noted by Donaldson (1965) and is discussed in Browning and Wexler (1968) in relation to meteorological radars. It has recently been suggested independently by Röttger (1980) who gives a discussion more pertinent to this work. Experimental evidence of this effect has come from observations at VHF. Röttger and Czechowsky (1980) found that when the SOUSY VHF radar was used in a DW mode for tropospheric observations, deviations of up to 10 ms^{-1} occurred in the horizontal velocity obtained from off-zenith angles of 3.5° and 7° at the radar observed tropopause. In this region contribution of reflection to backscatter is quite large, so that the backscatter polar diagram will be relatively narrow about the zenith. Since the radar beamwidth used in this work was about 5°, Röttger and Czechowsky (1980) suggest that the variation in the calculated horizontal velocity with zenith angle was due to the effective beam direction being somewhat less than the nominal beam pointing direction.

If both the backscatter and radar receiving array angular polar diagram are known, then it may be possible to correct for this effect. This has been pointed out by Whitehead et al. (1983). However, as we noted in the previous Section, the properties of the scattering medium may be changing quite rapidly and unless the radar has a rapid beam swinging capability (e.g. Bribie Island, MU radar) it is probably only realistic to measure the mean angular width of the backscattered radiation over a suitable period of time.

This has been done at BP using both direct (Hocking, 1979) and indirect (Lindner, 1975b) methods. Because the former measurements were made with relatively large beamwidths ($\pm 4.5°$), measurements of power may be subject to the same uncertainty in zenith angle as the measurement of radial velocity. The latter results are not subject to the same uncertainty and were made by a completely different technique, and while the agreement between these two studies is good, it seems more appropriate to consider Lindner's (1975b) results. These observations have an additional advantage over those of Hocking (1979) in that they were obtained over almost a year, so that the mean result should represent a seasonal average.

Figure (5.2) is taken from Lindner (1975b) and illustrates the RMS angular spread θ_0 from the zenith of backscattered radiation at 2 MHz for a number of heights, where θ_0 is defined such that the power received at an angle θ from the zenith is proportional to

$$exp\left(-\left(\frac{sin\theta}{sin\theta_0}\right)^2\right) \tag{5-3}$$

This diagram is actually a composite of results obtained from February to November 1971. However, only two months, June and September, showed the decrease in θ_0 above 90 km, so in this height region, θ_0 is somewhat uncertain.

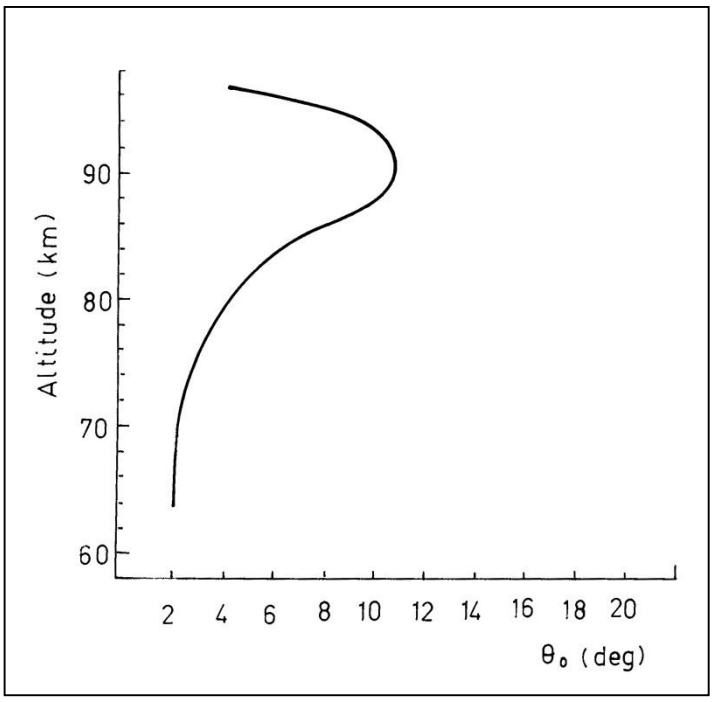

Figure (5-2) The RMS angular spread θ_0 from the zenith of backscattered radiation at 2 MHz (after Lindner, 1975b).

The variability of θ_0 above 90 km may be due to specular reflection from the 'tail' of the E-region, and may account for the variable quality of the data obtained from these heights (Chapter 3). Data obtained in February and October 1982 in this height range certainly showed evidence of returns from angles very close to the zenith in oblique beams, so that there is probably nothing special about June and September.

Lindner (1975b) found that values of θ_0 in June were much larger than in other months ($\theta_0 \sim$l4° at 88 km, the peak), and the winter months, June, July and August showed increased variability

of θ_0 in comparison with the other months. Inspection of Figure (5-2) indicates that the effective half width of the backscatter increases quite rapidly from 80-90 km, above which it decreases at a slightly faster rate. This means that the effective beam pointing angle will be less than the nominal beam angle over the entire height range, but the best agreement will be found at 90 km.

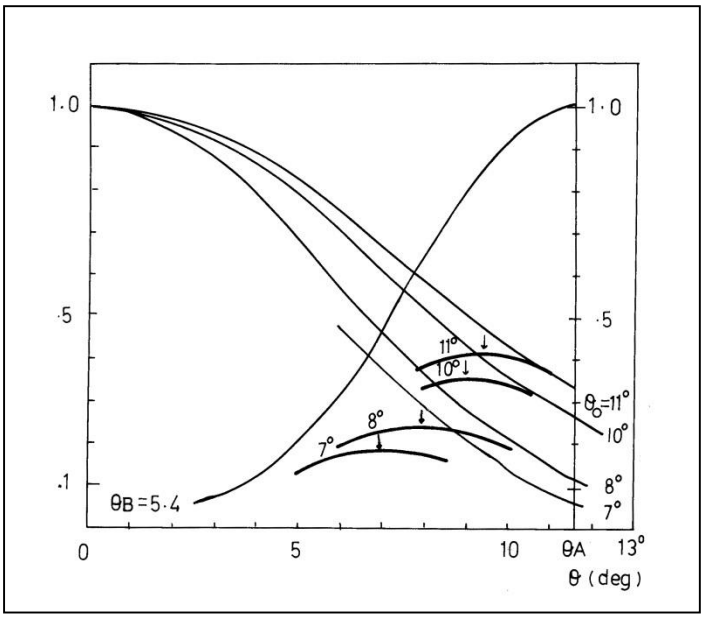

Figure (5-3) The effective antenna beam for an off-zenith angle of 11.6°, a half beamwidth at half power of 4.5°, and a range of values of θ_0.

It can be shown that the effective beam pointing We may estimate the effective antenna polar diagram we assume a similar functional form to that of Equation (5-3) for the antenna beam, which obviously neglects the sidelobes (see Figure 2-5). In this case the power P received at an angle θ, and hence the effective antenna polar diagram, will be given by

$$P \propto exp\left(-\left(\frac{sin\theta}{sin\theta_0}\right)^2\right)\exp(-\frac{\sin(\theta-\theta_A)}{sin\theta_B})^2 \quad (5\text{-}4)$$

where θ_B is the actual beam width, and the other terms have previously been defined.

angle is that at which the most power is returned (see e.g. Hocking, 1981; Whitehead et al., 1983) and so θ_E may be obtained from the maximum of Equation (5-4). This occurs when

$$\theta_E = \frac{1}{2}tan^{-1}\frac{(sin2\theta_A sin^2\theta_0)}{(sin\theta_B + cos2\theta_A sin^2\theta_0)} \quad (5\text{-}5)$$

which may be evaluated easily. However, it is also instructive to plot the effective antenna beam and this is shown in Figure (5-3) for a number of scattering half widths. The most interesting thing to note about the effective antenna beams for the various values of θ_0, is that they are rather flat, and do not show much directivity.

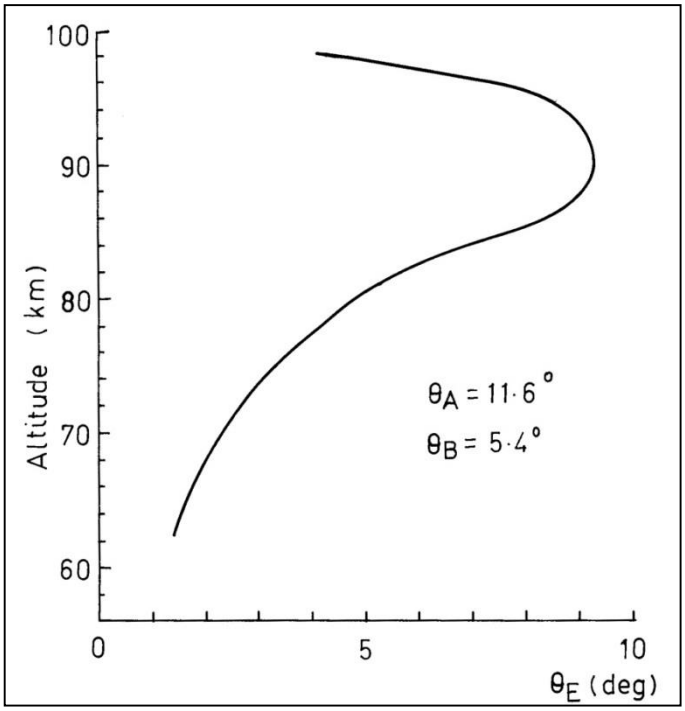

Figure (5-4) The effective beam pointing angle θ_E for an apparent beam angle of θ_A =11.6° and a beamwidth at half power of ±4.5°, calculated using Equation (5-5) and the values of θ_0 shown in Figure (5-2).

Although necessarily inexact, by substituting Lindner's results and the known beam width into Equation (5-5), we estimate θ_E~6° at 84 km, rising to about 9° at 90 km. Figure (5-4) shows the effective beam pointing angle θ_E, for an apparent tilt angle of θ_A~11.6° and beamwidth at half power of ±4.5° calculated from Equation (5-5) and Lindner's (1975b) results. From inspection of this diagram and Equation (5-2) it is clear that if Lindner's (1975b) results are typical, may be substantial errors in the measurement of velocity over the entire height range of 60-100 km. It is important to note that we have neglected the fact that the antenna beam is circular in cross Section, although the correction for this is likely to be small, and that we have neglected the fact that the radar has a finite pulse length. However, these results may be used to give an indication of the importance of the character of the backscatter for DW measurements. Two points should be noted. If the beam half-width is larger than the off-

zenith angle, it may not be possible to correct for the difference between the apparent and effective beam directions so that a measure of horizontal velocity may be obtained.

This is a consequence of the enhanced echo power from the zenith, and in this case, the effective beam direction may actually be vertical or very near vertical. For instance, with a beam tilted at an apparent angle of 3° from the zenith at BP, and with θ_0=3° which is appropriate for heights below about 80 km, the effective beam angle will be about 0.7°. If we note the lack of directivity in the effective beams illustrated in Figure (5-3), then it becomes apparent that it may not be possible to obtain a measure of the horizontal wind component.

Table (5-1) the heights calculated using the apparent beam direction of θ_A=11.6° and the effective beam direction shown in Figure (5-4).

Range (km)	**Alt (θ_A)**	**Alt (θ_E)**
78	76	78
80	78	80
82	80	82
84	82	83
86	84	85
88	86	87
90	88	89
92	90	91
94	92	93
96	94	95
98	96	98

The second point concerns the power returned. Even though it may be possible to obtain a measure of the effective beam direction at a fixed value θ_A there is a rapid decrease in the power returned as θ_0 decreases (see e.g. Figure (5-3)). Unless high powers are used in transmission, and the receiving equipment is sensitive, the returned signal may be lost in noise. Reference to Figure (3-5) indicates that below 80 km, most records are rejected because of low SNRs. Of course the backscattered power is smaller in this region than above 80 km in any case, but the combination of decreasing effective antenna gain and decreasing backscattered power as we move down in height from 90 km, means that may not be possible to recover the signal from the noise even if the effective beam pointing angle is known.

A further complication is that the height calculated from the range will also be incorrect. Table (5-1) gives the heights calculated using the apparent beam direction of θ_A=11.6° and the effective beam direction shown in Figure (5-4). Because the height resolution at BP is about 4 km, this is probably not a major correction, but in Section (5.5) we will show that it should be taken into account. We have mentioned the importance of these results for the measurement of the mean horizontal components of the wind using the DW technique, but in this work, measurements of the Reynolds stress and the components of the kinetic energy are of more direct concern.

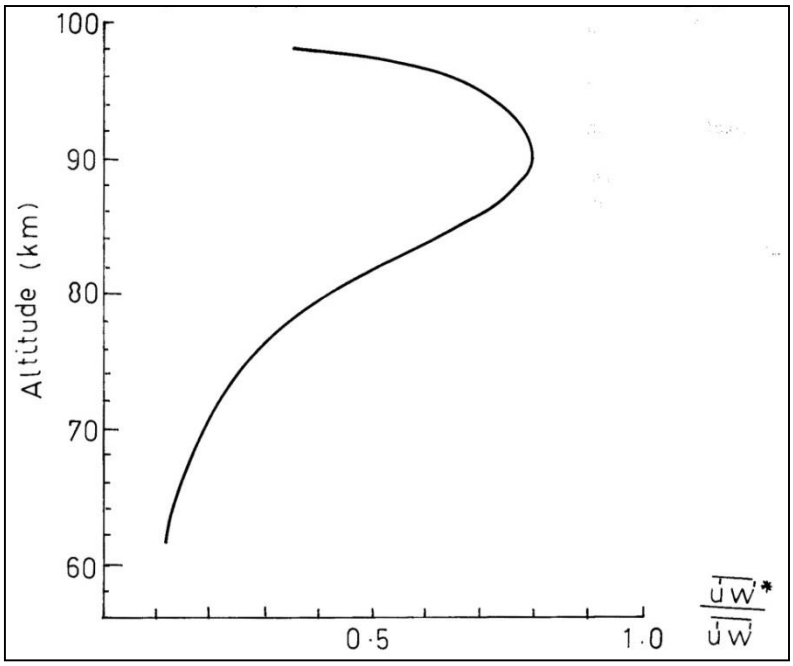

Figure (5-5) The ratio of the measured value of the momentum flux $\overline{u'w'^*}$ to the correct value $\overline{u'w'}$ for an apparent beam angle of 11.6°, but an effective beam angle as shown in Figure (5-4).

The Reynolds stress for the zonal component is given by Equation (4-34) as

$$\overline{u'w'} = \frac{\overline{V_E'^2} - \overline{V_W'^2}}{2sin2\theta} \tag{4-34}$$

This may be expanded in terms of θ_E and θ_A to obtain

$$\overline{u'w'} = \frac{1}{2sin2\theta_A}[(\overline{u_E'^2} - \overline{u_W'^2})sin^2\theta_E + (\overline{w_E'^2} - \overline{w_W'^2})cos^2\theta_E + 2\overline{u'w'}sin2\theta_E] \tag{5-6}$$

where the various quantities have been defined in Chapter 4. If the wind field is horizontally homogeneous then

$$\overline{(u'w')}^* = \overline{(u'w')}\left(\frac{sin2\theta_E}{sin2\theta_A}\right) \tag{5-7}$$

where $\overline{(u'w')}^*$ is the measured value of the momentum flux, and $\overline{u'w'}$ is the correct value. Consequently, the ratio of the measured to the true value of the Reynolds stress will be given by the ratio in Equation (5-7). This is plotted in Figure (5-5). Inspection of this diagram indicates that the difference between the apparent and effective beam angles must be taken into account in measurements of momentum flux made at BP.

The zonal body force F_u is given by

$$F_u = -\frac{1}{\rho}\frac{\partial(\rho\overline{u'w'})}{\partial z} \tag{5-8}$$

and if $\overline{u'w'}$ is monotonically increasing or decreasing with height, use of the measured value $\overline{(u'w')}^*$ will lead to an underestimate of F_u.

The measured values of the horizontal energy are affected rather more than the Reynolds stress terms. If we sum the mean square radial velocities obtained in eastward and westward directed beams, we obtain

$$(\overline{V_{EW}'^2})^* = \frac{\overline{V_E'^2} + \overline{V_W'^2}}{2sin^2\theta} = (\overline{u'^2})\left(\frac{sin^2\theta_E}{sin^2\theta_A}\right) + (\overline{w'^2})\left(\frac{cos^2\theta_E}{cos^2\theta_A}\right) \tag{5-9}$$

where $(\overline{V_{EW}'^2})^*$ is defined by (5-9) and the other terms have previously been defined.

If the vertical component measured in a vertical beam is removed without taking the difference between the effective and apparent beam directions into account, we obtain

$$(\overline{u'^2})^* = (\overline{u'^2})\left(\frac{sin^2\theta_E}{sin^2\theta_A}\right) + (\overline{w'^2})\left(\frac{cos^2\theta_E - cos^2\theta_A}{cos^2\theta_A}\right) \tag{5-10}$$

so that not only the measured horizontal mean square velocity underestimated, it contains a contribution from the vertical mean square component. For $\theta_E = 8°$, we obtain

$$(\overline{u'^2})^* = (0.5)\left(\overline{u'^2}\right) + (0.5)\left(\overline{w'^2}\right) \quad (5\text{-}11)$$

For periods less than about half an hour, the horizontal and vertical mean square perturbation velocities of gravity wave motion may be comparable (see e.g. Figure 4-16) and $(\overline{u'^2})^*$ will approximate $\overline{u'^2}$. At lower frequencies, there will be a general reduction in the values of $\overline{u'^2}$ and the vertical component will be much less consequential. This does not mean that measurements of $\overline{u'^2}$ are possible at higher frequencies, but does explain the form of the spectra when the vertical component is removed to obtain the horizontal component without taking the effective beam angle into account.

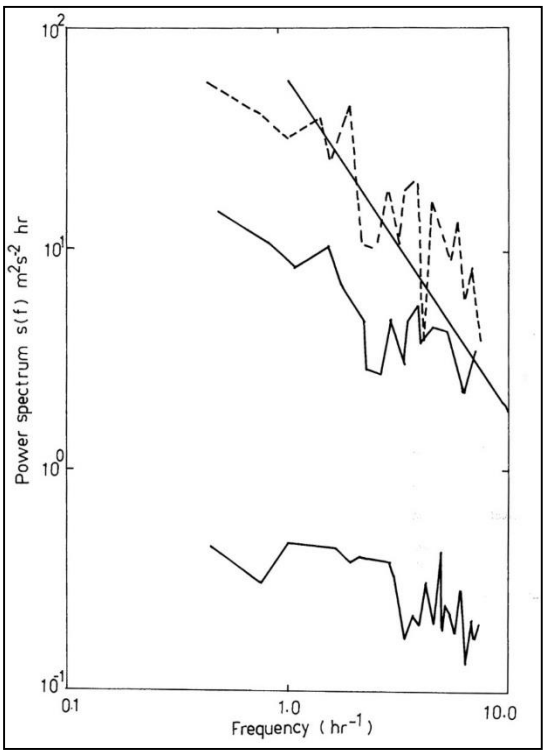

Figure (5-6) The power spectra for $\overline{u'^2}$ (upper solid line) and $\overline{w'^2}$ (lower solid line) for November 1981. The corrected value of $\overline{u'^2}$ calculated using the effective beam direction shown in Figure (5-4) is shown as the dashed line. The straight line indicates the line of best fit to Vincent's (1984) results.

Unlike the Reynolds stress, independent measurements of $\overline{u'^2}$ are available. Vincent (1984) has presented seasonally averaged spectra of $\overline{u'^2}$ for three widely spaced sites for 86 km including Adelaide. The Adelaide results were obtained from a series of SA measurements. The results of a DW run made November 1981 are presented as power spectra for the horizontal and vertical wind components for 86 km in Figure (5-6). We have taken the effective beam

angle for 86 km from Figure (5-4) and rescaled the mean square radial velocity obtained for this height accordingly, and removed the vertical mean square radial velocity measured in a vertically directed beam according to Equation (4-34). In the nomenclature described in Chapter 2, the beam arrangement was TC(CP). The results are presented 1n Figure (5-6) as a power spectrum along with the vertical velocity spectrum, and the horizontal spectrum that would have been obtained if the effective beam direction had not been taken into account. Also shown is the seasonally averaged result of Vincent (1984).

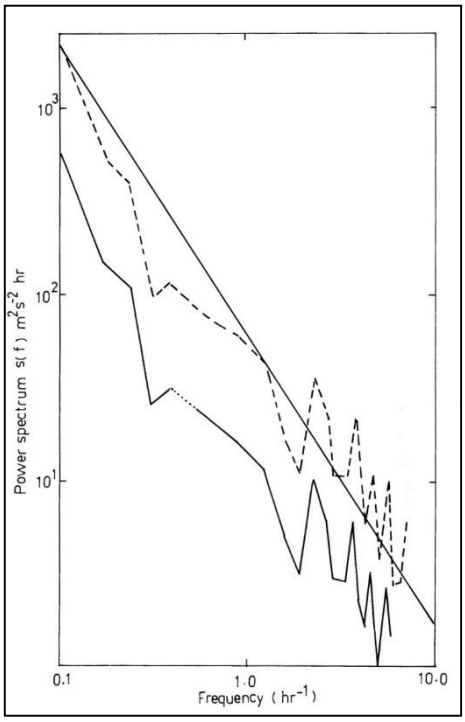

Figure (5-7) As for Figure (5-6), but for May 1982.

It is clear that the rescaled spectrum of $\overline{u'^2}$ is in good agreement with Vincent's results, whilst the unsealed results are somewhat lower. The few lowest frequency points of the spectra may be uncertain because the time series were filtered to remove periods longer than 8 hours, but the remaining points should give a good measure. It would appear from this result that the effective beam pointing direction for 86 km calculated from Lindner's (l975b) results is a good estimate. Note that the unsealed spectrum for $\overline{u'^2}$ shows better agreement with Vincent's results at high frequencies than at low frequencies.

Lindner's results would also appear to be typical of other months. Figure (5-7) illustrates similar power spectra for data obtained in May 1982. It is clear that if the value of θ_E from Figure (5-4) is applied to rescale $\overline{u'^2}$, agreement with Vincent's results is excellent. These

results are particularly encouraging, because if the values of θ_E illustrated in Figure {5-4) are typical, the task of correcting for the difference between the apparent and effective beam directions is considerably simplified.

This does appear to be the case, and the results for November 1981 and May 1982 presented above are quite typical of the other DW results obtained during the course of this work. The measurements of $\overline{u'^2}$ and $\overline{v'^2}$ derived from the various beam configurations are all smaller than the seasonally averaged results of Vincent (1984), and intercomparison of the same quantities measured in each month with SA results presented in Ball (1981) for the same months (but different years) indicates that DW measurements of the horizontal component of the kinetic energy are all too small.

They are also smaller in magnitude than similar mesospheric measurements obtained with the DW technique using narrow beamwidths at Poker Flat (Carter and Balsley, 1982; Smith and Fritts, 1983), with estimates of $\overline{u'^2}$ and $\overline{v'^2}$ based on rocket measurements (Vincent et al., 1977), and with SA measurements made at Saskatoon {Manson et al, 1981). Because we can relate the DW observations for the various months to the seasonally averaged results of Vincent (1984) through estimates of θ_E based on measurements of θ_0 made with a completely different technique, there is compelling evidence that the effective beam angle is less than the apparent beam angle, and that the measurements of θ_0 made by Lindner (1975b) give a good measure of this quantity.

However, it must be stressed that this correction is only valid for observations taken over a suitable period of time and is then only correct in a statistical sense. Since most observations presented in this work cover periods of about three days or more it is probably appropriate to apply the correction for the effective beam direction for the values of $\overline{u'w'}$ averaged over this period of time.

The variation between the apparent and effective beam directions has one other important consequence. The procedure for the measurement of horizontal scale outlined in Chapter 4 assumes a separation between DCC beams of about 35 km at 85 km altitude. Inspection of Figure (5-4) indicates that this is likely to be closer to about 22 km. This means that the measured horizontal wavelengths will be incorrect unless this variation is accounted for. We will consider this in Chapter 7.

In Sections (5.4 and 5.5) we present additional evidence for the discussed in this Section, but before considering this, we describe another effect that may reduce the magnitude of radial velocities measured in wide Doppler beams, and then briefly describe the SA technique.

5.2 Beam Width and DW Measurements at BP

Another effect that may lead to errors in DW measurements that is related to finite beam width, but not the character of the backscatter, has been modelled numerically by Hocking (1983a) and discussed in a qualitative way in Hocking (1983c). Figure (5-8) is from this last paper.

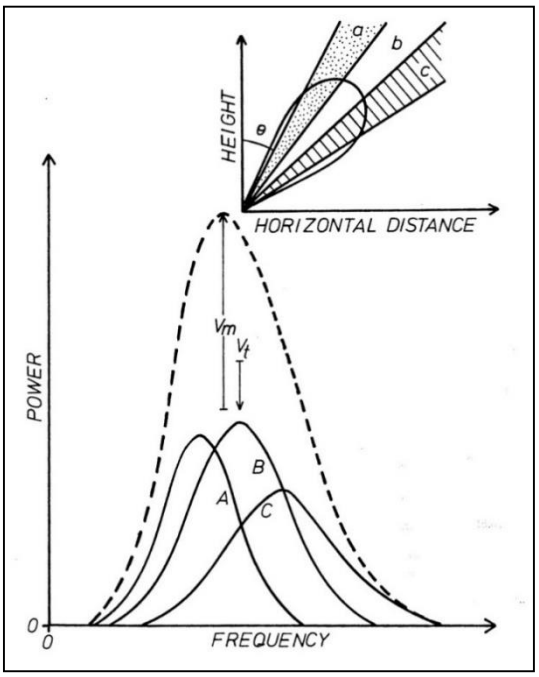

Figure (5-8) Schematic diagram of the formation of the Doppler spectrum for a radar beam of finite width (after Hocking, 1983c). For details see test.

This means that if significant horizontal fluctuations In this diagram, three scattering regions are considered from simplicity, but there is no real restriction on number. Doppler velocities from region 'a' produce spectrum A, likewise b, B and c, C. Spectra produced by backscatter from larger tilt angles have a broader range of frequencies, and because the tilt angle is larger, the mean frequency shift is larger. When spectra from each region are summed, there is a bias towards low frequency components and the peak of the spectrum is an underestimate of the value corresponding to the true horizontal component of the wind.

occur in the wind velocity during the interval of measurement, the measured horizontal velocity will be an underestimate of the true horizontal velocity. Hocking (1983a) suggests that

underestimates of about 20-25% could occur in horizontal velocities measured with the DW technique at BP in typical mesospheric conditions. Because this effect has only been suggested recently, no related experimental observations have been presented in the literature. The DW technique has been discussed in Chapters 3 and 4, but as yet we have not described the SA technique. This is done in the next Section.

5.3 The Spaced Antenna Technique

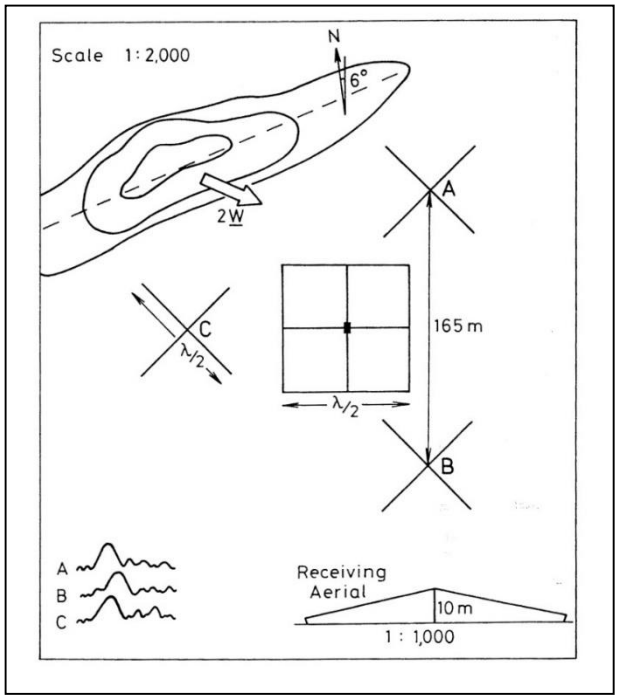

Figure (5-9) Schematic illustration of the portable SA system used in this work. For details see text.

The SA technique uses a minimum of three vertically directed radar beams which are spatially separated on the ground by about 200m for mesospheric observations at 2 MHz. For purposes of illustration, we will consider the portable SA equipment used in November 1980 as this has the advantage of introducing this particular equipment as it was signed to be used. The SA arrangement is illustrated in Figure (5-9).

The crosses at A, B and C represent crossed half wave dipoles, arranged at the vertices of an equilateral triangle with a side length 165 m between crossed dipole centers, and these are used for reception. The large square at the center of the triangle formed by the receiving aerials represents the transmitting array, each side of which represents a folded half wave dipole. Opposite sides are phased together and connected to a central site through transmission lines. Both transmitting and receiving equipment are situated at the central site.

The transmitted frequency of 1.94 MHz is partially reflected or backscattered from the D-region by irregularities refractive index, and a diffraction pattern represented by the contour pattern at the top LHS of Figure (5-9) is formed. The fluctuations in this returned signal are received at the three array sites, and in the presence of a horizontal wind at the backscatter height, these show relative time displacements. Using a cross correlation analysis, the mean time shifts are calculated for pairs of antenna, and from these the horizontal wind may be calculated. This method of "similar fades" results in a parameter called the "apparent velocity", and this basic procedure was applied by Mitra (1949).

If the ground diffraction pattern is on average circular, and does not change form as it moves, the velocity derived from the relative time displacements will correspond to the real wind velocity. In general, the pattern will change form as it moves and may be anisotropic. The velocity derived from the relative time displacements in this more realistic case may not correspond to the true wind velocity at the backscatter height, because part of the signal fading will be due to random changes in the pattern rather than to advection of the irregularities, and the diffraction pattern will not be aligned perpendicularly to the velocity vector.

To measure the true wind velocity, and not the apparent velocity of the diffraction pattern over the ground, the effects due to pattern anisotropy and random changes are removed using the so called "Full Correlation Analysis" (FCA). This was developed by Briggs et al. (1950) and Phillips and Spencer (1955) and details of the technique may be found in Briggs (1977). Because the ground diffraction pattern is sampled at only a few antenna positions and times, a number of acceptance criteria are applied to ensure that the estimate of the ground diffraction pattern is reasonable. Details may be found in Ball (1981), Vincent and Röttger (1980) and Hocking (1983c).

On the face of it, this technique appears to be quite different from the DW method. However, Briggs (1980) has shown that both methods use the same information. The DW technique exploits the change in the mean Doppler shift with zenith angle, and samples small spatially separated volumes. The SA method makes use of the fact that the variation in the Doppler shift with angle is such that the resultant field moves over the ground as a random pattern with a velocity twice that of the horizontal wind at the backscatter height. As discussed by Briggs (1980), the SA method is effectively a natural analogue computer that combines the Doppler shifts of the radiation received in the antenna beam for all angles of arrival to produce the moving ground diffraction pattern.

5.4 November 1980 Comparison of Spaced Antenna and Doppler Wind Derived Horizontal Wind Components

Intercomparison of different methods of remote sensing is essential, because this is the way in which their validity and suitability for particular applications may be assessed. Because the DW method had not previously been routinely applied to the measurement of wind at BP, six days of data were obtained in November 1980 at BP using both the SA and DW techniques.

Details of the experimental arrangement used have previously been in Chapter 2, and it will be recalled that the SA equipment used was not set up optimally, because only one dipole was erected at each receiving site, and these were not tuned to l.98 MHz but 1.94 MHz. This reduced the effective height range somewhat, as will be discussed later, but reasonable data acceptance rates were obtained on some days.

In addition, because the SA and DW equipment controlled the same transmitter using a time multiplexing system, the best data acquisition rate that could be obtained was three consecutive two-minute wind determinations every twenty minutes by each system. For SA observations this is a little low, because typical acceptance rates are about 50%, and for DW observations made with off-vertical beams without a vertical beam, there may be contamination of the true wind because of the unresolved vertical component and gravity wave effects (Section 4-1-1-1). Consequently, the best resolution considered to be practical was one hour.

5.4.1 Wind Results

A total of six days of SA and DW observations were obtained in November 1980 from the 21st—27th Figure (5-10) illustrates hourly mean values of the meridional and zonal wind components for five heights. The acceptance rates of individual two minute SA determinations of velocity are shown in Figure (5-11), and from this diagram it is clear that at 84 km data may be marginal. Nevertheless, the gross features appear to be in fair agreement between the techniques at this height. The DW data acceptance rates were similar to those shown for November 1981 in Chapter 3.

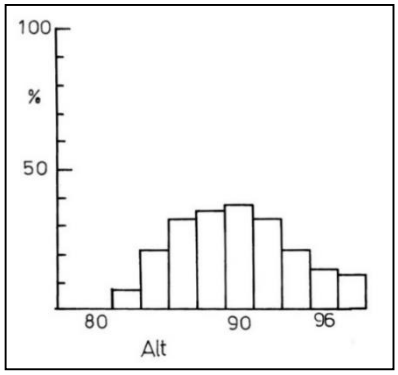

Figure (5-11) SA data acceptance rates for November 1980 for the range 80 to 98 km.

For the SA data plotted in Figure (5-10), 84 and 86 km have an average of three two minute determinations of velocity per hour, and the other heights an average of four per hour. This is somewhat lower than that obtained during a typical SA run, where run rates of 4 in 10 minutes compared with 3 in 20 in the present study would be considered adequate for hourly average values of wind. Since the acceptance rates shown in Figure (5-11) are lower than those obtained with the complete portable SA system or with BP operating in a SA configuration, these SA results are inferior in terms of quantity at all heights to those generally obtained.

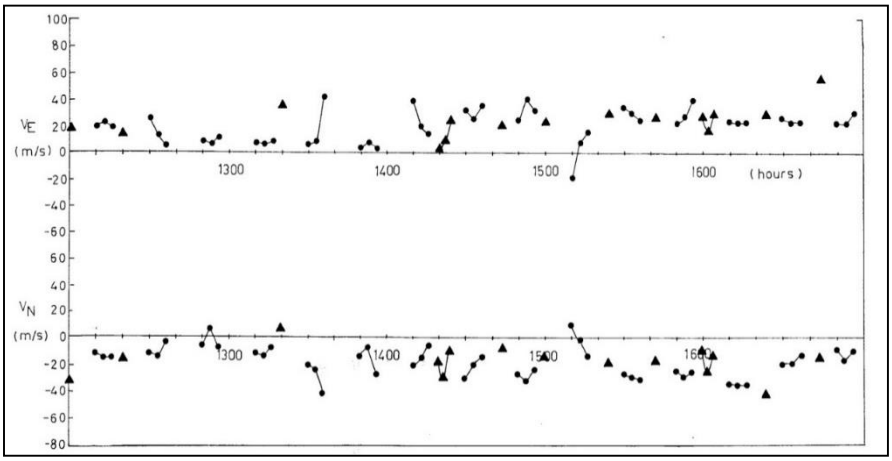

Figure (5-12a)102.4 s determinations of wind velocity for SA (triangles) and DW (circles) techniques for 88 km.

Individual data points from both techniques are illustrated in Figure (5-12a, b) for a height of 88 km for a few hours of observation, and these examples were selected at random from the available data. Agreement between the winds derived with each technique is good, and the variation between adjacent data points appears to be consistent for both techniques, although is somewhat larger in the eastward beam DW radial velocities on the 25th of November.

Although these times series are rather short, and the level of gravity wave activity unknown, we can suggest that there is not any evidence of atypical variations in velocity between techniques. Inspection of the time series plotted in Figure (5-10) indicates that generally, DW derived velocities tend to be smaller than those obtained with the SA technique. They are also

smoother, although low SA data acceptance rates are certainly contributing to the "noisier" time series in this case. However, overall agreement is good, with the main features evident in both time series, and cross correlation between the SA and DW observations for the entire observational period indicates values of 0.7 for the zonal component, and 0.8 for the meridional component for heights with sufficient data to make the calculation meaningful.

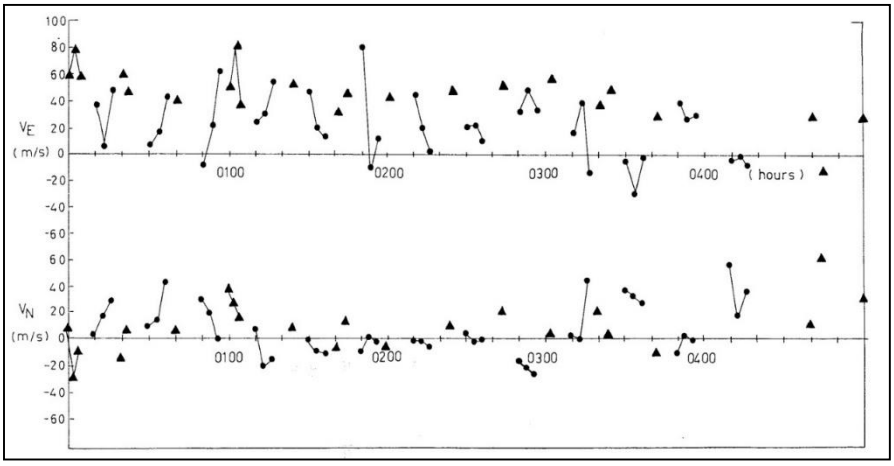

Figure (5-12b) As for Figure (5-12a)

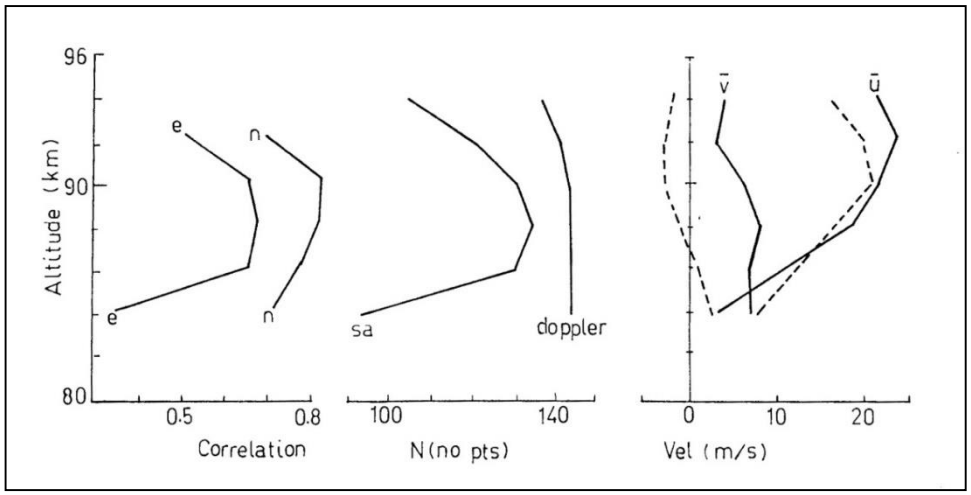

Figure (5-13) (a) The correlation coefficient between SA and DW derived winds for zonal (e) and meridional (n) wind components. (b) The number of hours with data points for the SA and DW methods. The maximum possible is 144. (c) The average wind velocity for the six-day period (SA, solid line; DW, dashed lines)

This is shown in Figure (5-13), along with the number of hours with data points. Also shown on this diagram are the average winds for the entire six days. From this diagram it is clear that

for heights above 84km, the average zonal Doppler winds for the 6-day period tend to be slightly smaller than the SA observations.

The average meridional velocities show good agreement in form but a difference of about 5 ms^{-1} is evident. On the whole, DW observations are much smoother than SA observations, but this could result from the much higher DW data acceptance rate. The DW derived winds show rather clearly the presence of the tidal components of the wind field, and exhibit excellent consistency in height and in time (Figure 5-14a, b). We note in passing that these height profiles indicate a tendency for a vertical wavelength of about 20 km which is consistent with that expected for the (1,1) tidal mode. In contrast, the SA winds have a larger variation in height and time, and generally have a larger irregular component superimposed on the hourly height profiles.

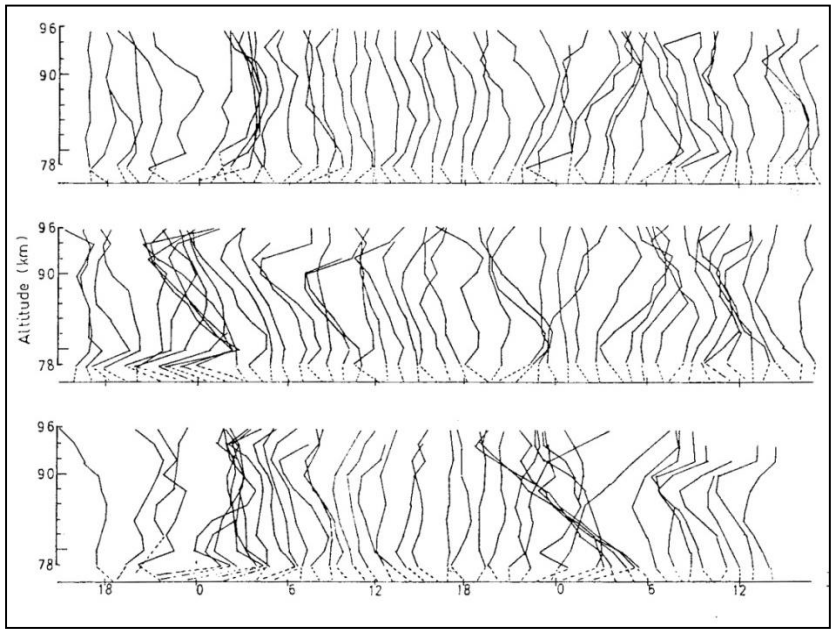

Figure (5-14a) Hourly average meridional winds for November 1980.

Some of this can be attributed to low data acceptance rates, but often consistency in height and time tends to indicate real variations. Hourly average meridional height profiles of SA and DW derived winds are shown in Figure (5-15) for two days of observations.

Harmonic analysis of the time series plotted in Figure (5-10) indicated good agreement in the phase of the tidal components calculated from the DW and SA derived winds, whilst there was some variation in the agreement between the tidal amplitudes. To obtain a more general

comparison of the winds derived from each technique, we have applied a power spectral analysis, the results of which are discussed in the next Section.

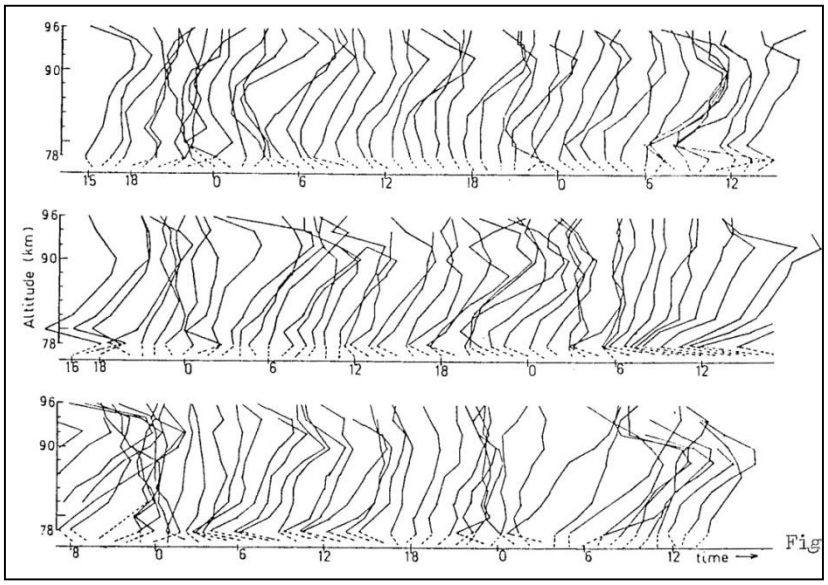

Figure (5-14b) Hourly average zonal winds for November 1980.

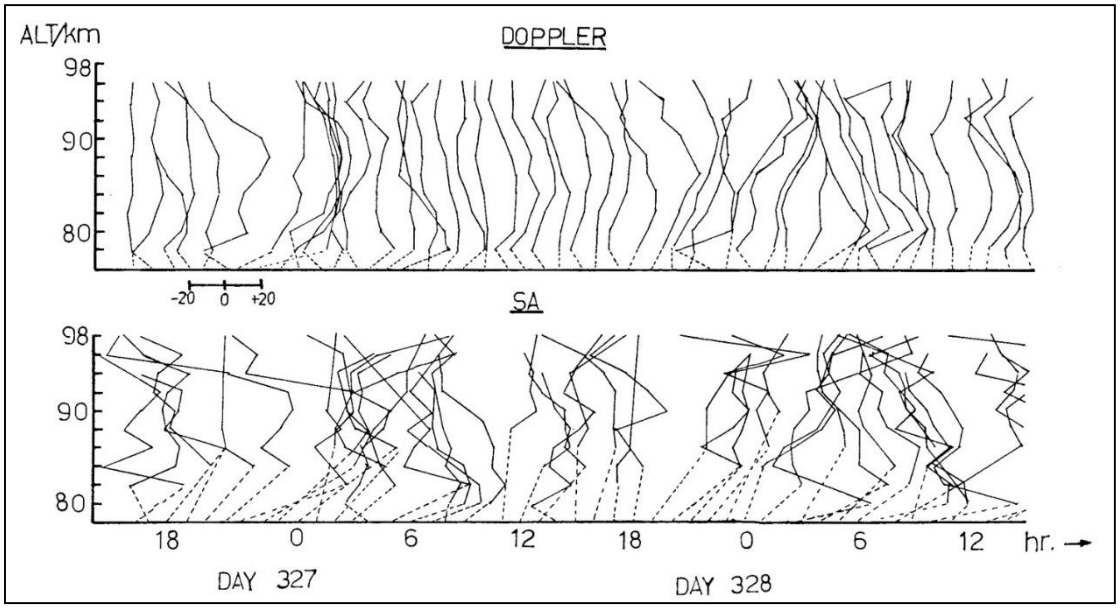

Figure (5-15) Height profiles of the hourly average meridional wind velocity derived from the SA and DW techniques.

5.4.2 Power Spectral Analysis of November 1980 Winds

To check for differences between the wave energy calculated from the two methods in terms of wave frequency, power spectra were calculated for each height. The significant gaps in the

SA data at heights below 86 km and above 92 km make these time series unsuitable for this analysis, and we have concentrated on 86-92 km height range.

A cubic splines interpolation procedure was applied to smooth over small gaps in the data, and to improve the reliability the spectral estimates, the raw estimates from four adjacent frequency bands were averaged to produce one estimate. NS and EW spectra were similar and so to improve the estimate further, these have been averaged together to form composite spectra. This procedure has previously been applied by Ball (1981) and Vincent and Ball (1981). This amount of averaging has obscured tidal peaks at 24 and 12 hours, but since we are rather more interested in the general form of the spectra, and all of the spectra have been processed in the same way, this is of little direct consequence.

We have noted that the zonal wind components measured with each technique are in better agreement than the meridional wind components. It could be possible that because of an error in the phasing cables used to tilt the beams from the zenith, the NS radar beam was tilted at an angle less than that of the EW beam from the zenith. This would mean that the composite spectra would underestimate the true spectra.

However, integrating under the individual spectra for a height of 88 km yields for the NS components, V_{rms} = 24 ms^{-1} and 17 ms^{-1} for the SA and DW winds respectively, and for the EW components, V_{rms} = 24 ms^{-1} and 15 ms^{-1} for the SA and DW results respectively. Consequently, the RMS values for NS and EW components measured with the same technique are in agreement. These values are typical for the 86-92 km height region. It is not clear why the meridional components as measured with each technique did not agree as well as the zonal components, but it is very unlikely that it was because of an error in the phasing cables used.

It important to note that the power spectra the DW results are actually given by

$$(\overline{u_E'^2})^* = \frac{\overline{V_W'^2}}{sin^2\theta} = \overline{u_W'^2} + \overline{w_W'^2}cot^2\theta + 2(\overline{u'w'})_W cot\theta \qquad (5\text{-}12)$$

and

$$(\overline{v_E'^2})^* = \frac{\overline{V_N'^2}}{sin^2\theta} = \overline{v_N'^2} + \overline{w_N'^2}cot^2\theta + 2(\overline{v'w'})_N cot\theta \qquad (5\text{-}13)$$

and the average spectra plotted represent

$$\frac{(\overline{u_E'^2})^* + (\overline{v_E'^2})^*}{2}$$

$$= \frac{\overline{u_W'^2} + \overline{v_N'^2}}{2} + \frac{(\overline{w_W'^2} + \overline{w_N'^2})cot^2\theta}{2} + ((\overline{v'w'})_N - 2(\overline{u'w'})_W)cot\theta \quad (5\text{-}14)$$

where $(\overline{u_E'^2})^*$ and $(\overline{v_E'^2})^*$ are defined by Equations (5-12) and (5-13) respectively, and the subscript refers to the beam in which the bracketed quantity is measured. Since the quantity required is that given by the first term on the RHS of Equation (5-14), there is some uncertainty in these spectra.

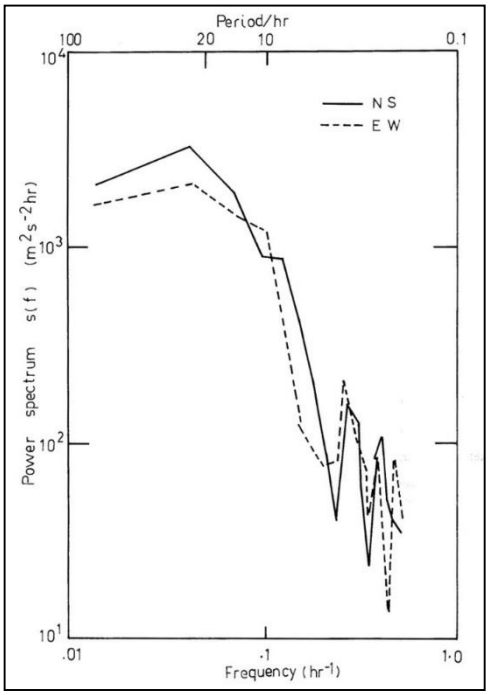

Figure (5-16) The power spectra for zonal (EW) and meridional (NS) wind velocities measured with the DW technique at 88 km during November 1980.

The effect of the second two terms in this Equation will become more important as we move up in frequency and will depend on the signs of the covariance terms as to whether the spectra are raised or lowered in a particular frequency interval. For periods down to about an hour, $(\overline{v'^2}) \approx (\overline{u'^2}) \gg \overline{w'^2}$ and $\overline{w'^2} \sim |\overline{u'w'}| \sim |\overline{v'w'}|$ are reasonable assumptions. Because of the $cot^2\theta$ dependence of the $\overline{w'^2}$ term and because the covariance terms are signed quantities, the second is more important than the last term in Equation (5-14). We have already noted that EW and NS DW derived spectra are quite similar, and an example is shown in Figure (5-16).

This similarity indicates that the covariance terms are not likely to be significant and the general conclusions of the following discussion are valid. The agreement between DW spectra for NS and EW components is comparable to that for the NS and EW components of the SA spectra.

To give some indication of the effect of the vertical mean square component and the covariance terms on the November 1980 spectra, November 1981 data were analyzed to obtain hourly averages of $\overline{V_E'^2}/sin^2\theta$ and $(\overline{u'^2})_{EV}$ and these were used to calculate power spectra in the same way as those for November 1980. This indicated a difference of 1 ms^{-1} in RMS velocity calculated over the entire frequency range for most heights. However, there was no significant difference in spectral slope or general form over the entire frequency range. The November 1981 spectra with the vertical component and covariance terms removed are in agreement with those for November 1980, although they are somewhat smaller at the higher frequency end of the spectrum. Given that only three days of data were obtained in November 1981, and only the EW component was obtained, agreement between November 1980 and 1981 data is good, and it appears that November 1980 DW spectra are quite typical of the horizontal fluctuation in velocity in each frequency range as measured with the DW technique.

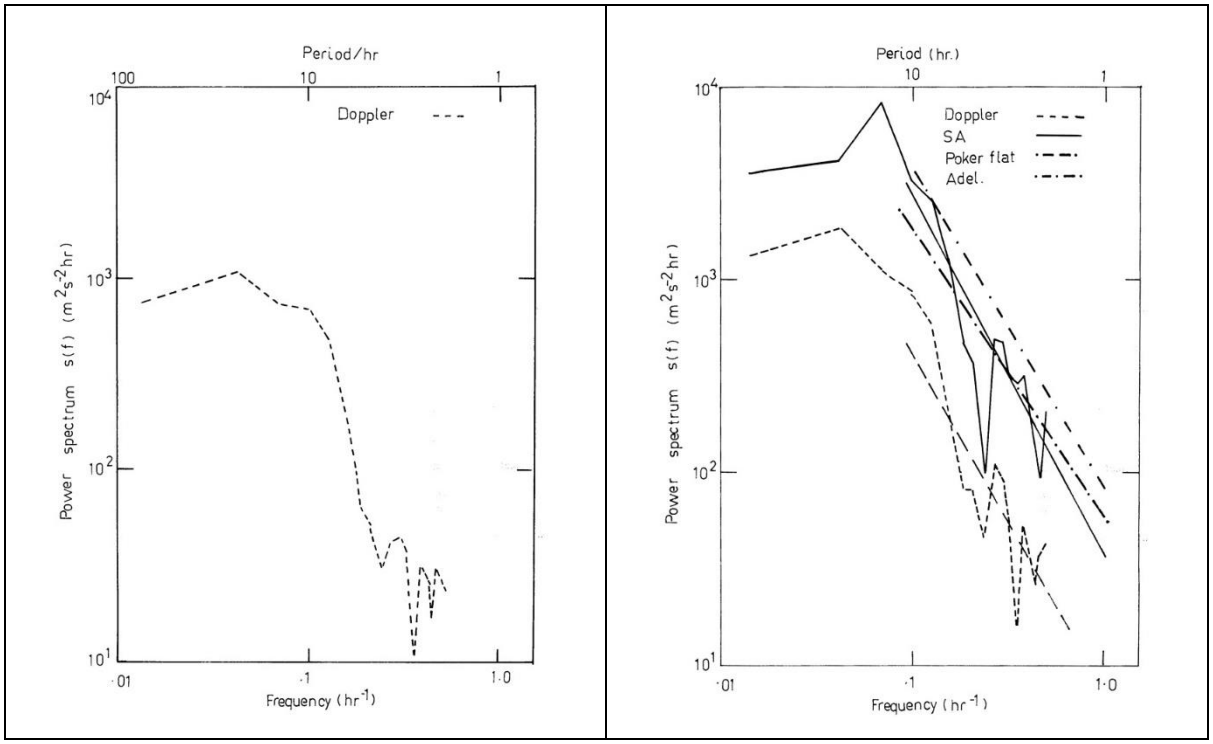

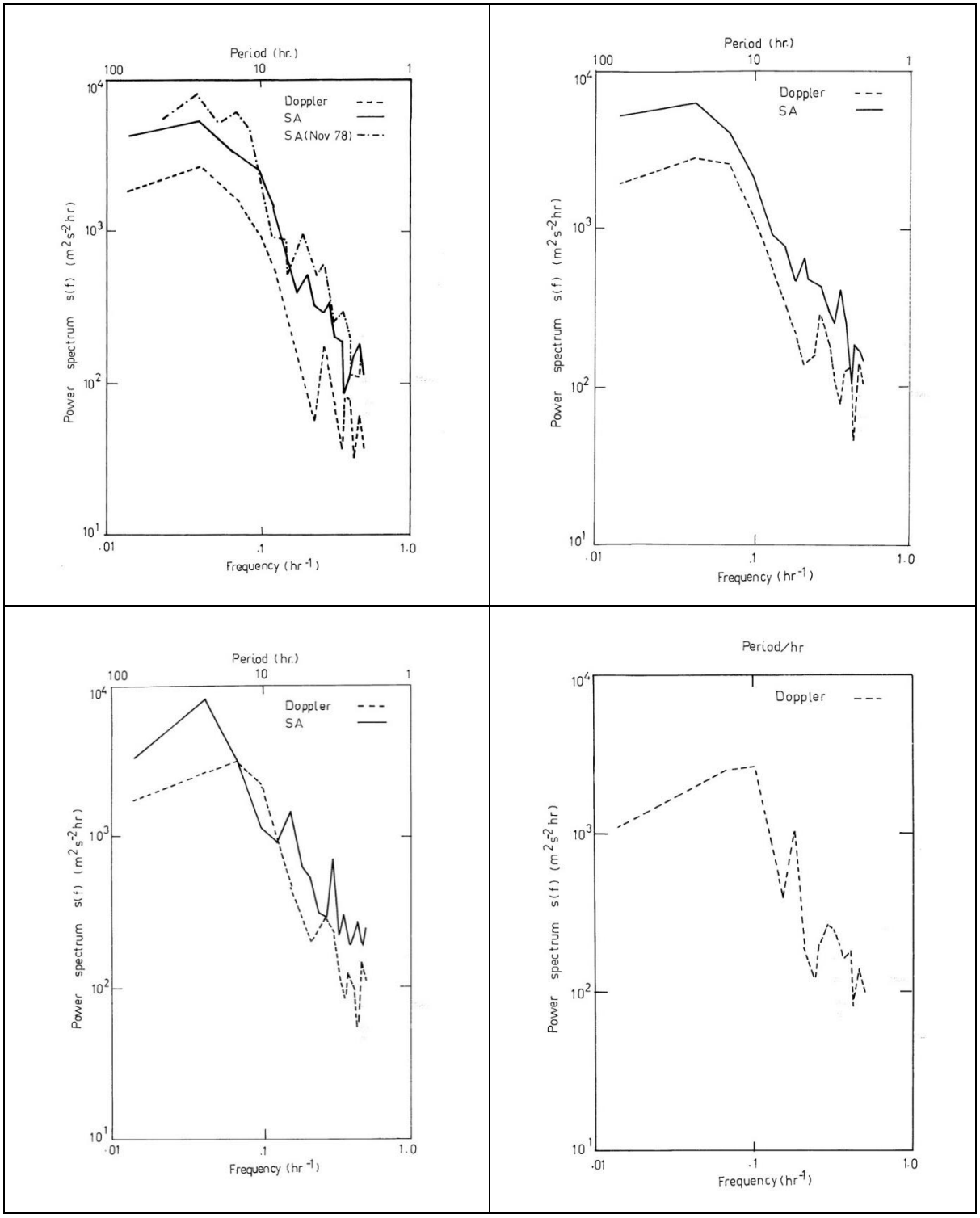

Figure (5-17a-f) The DW and SA wind velocity spectra for 84 to 94 km for November 1980. SA results are not shown for 84 and 94 km. Figure (5-17b) (top right previous page) also shows the lines of best fit to the 2-8h period range for these spectra, and the lines of best fit to the seasonally averaged results of Vincent (1984) (Adelaide) and summer results from Poker Flat. Figure (5-17c) (bottom left previous page) also shows the SA wind velocity power spectrum for November 1978.

Consequently, the DW spectra should be reasonable estimates of $\frac{(\overline{u_E'^2})+(\overline{v_E'^2})}{2}$ but the uncertainty due to the unresolved vertical component must be borne in mind, and we could reasonably expect errors of 1 ms^{-1} in RMS velocity when evaluated over the entire frequency range.

The spectra for 86-92km are shown in Figure (5-17a to 5-17f). The DW spectra for 84 and 94 km are also included. On the spectral plot for 86 km we have presented the lines of best fit to the seasonally averaged results for Adelaide for 85 km, obtained from Vincent (1984) and some summer results obtained at Poker Flat for the same height using a VHF radar presented by Carter and Balsley (1982) which were also obtained from Vincent (1984). The SA results for this height are clearly in good agreement with Vincent's seasonally averaged result, and with the DW results from Poker Flat. Since the Poker Flat radar has a narrow beam width (~1°), it should not be subject to uncertainties in the effective beam angle because of the effects we have discussed earlier in this Chapter.

We note that the BP DW results are somewhat smaller than the BP SA results. On the spectral plot for 88 km we have included the SA power spectrum for November 1978 taken from Vincent and Ball (1981). Agreement between the SA spectra at this height is quite good, although the November 1980 spectrum tends to be somewhat lower over most of the frequency range. Some of this difference can be attributed to differences in the total data lengths and the different number of spectral estimates averaged over, and to the separation in time of the observations, but it is clear that this SA data is quite typical of that obtained at BP at this time of year.

Agreement in form between SA and DW spectra is good, but in a given frequency interval the values of the DW spectra are typically half of the corresponding SA values. For example, for 88 km the mean square horizontal velocity fluctuations for either component is 256 m^2s^{-2} for DW observations and 576 m^2s^{-2} for SA observations. This corresponds to RMS fluctuations of 16 ms^{-1} and 24ms^{-1} respectively. It is interesting to note that if we take Hocking's (1983c) estimate of a 20% reduction in DW velocities because of the effects of a significant horizontal RMS fluctuation in velocity and a finite beam width (see Section 5.2), then this indicates an effective beam pointing direction of 9° at 88 km. As we shall see later, this is a reasonable estimate.

Both DW and SA spectra show typical behaviour for this type of power spectrum, in that power decreases on average with increasing frequency from the inertial period (20.9h), to the

frequency limit imposed by the sampling interval (about 2h). This would be true in fact down to the Väisälä-Brunt period (about 5 min). Over this frequency range, the spectra may be approximated by a power law relationship of the form $S(f) = Sof^{-k}$ we have evaluated this expression for the frequency range of 8h to 2h because this range is of interest in this work. The spectral slope k of each of the spectra for 86-92 km evaluated using a least squares fitting procedure are shown in Figure (5-18). Agreement is very good, indicating a general reduction in DW values rather than a reduction of particular frequency bands.

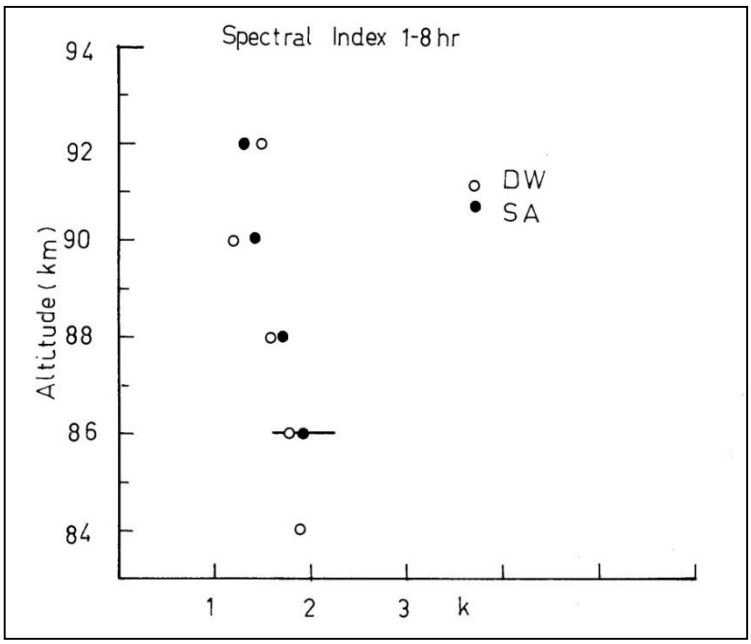

Figure (5-18) The spectral index k for the period range of 2-8 h for the DW and SA power spectra for November 1980 shown in Figures (5-15a- f)

This is in fact generally true of each DW spectrum for each height over the entire frequency range. Agreement between the SA and DW spectra improves somewhat with height as is indicated by inspection of Figures (5-17a to 5-17f). The RMS velocity each spectrum for either component evaluated over the entire frequency range is shown in Table (5-2). We have estimated the RMS value for SA observations at 84km for the days with sufficient data, and so the uncertainty in this value is likely to be higher than the other values.

It obvious from the data presented in this table that SA RMS values are relatively constant with height, which could be indicative of a broad spectrum of breaking waves. On the other hand, the DW RMS velocities increase with height, which could indicate wave energy was growing with height. The results in Table (5-1) are consistent with the RMS velocities calculated for the

periods $1 - 8h$, and these results are shown in Table (5-3). There is an even larger uncertainty in these results, because they were obtained by integrating under the line of best given by $S(f) = S_0 f^{-k}$ for the appropriate frequency limits.

Consequently, Table (5-2) is likely to provide the best estimate of the ratio of DW/SA RMS velocities. However, it is clear that in this period range, where the diurnal and semi-diurnal tidal amplitudes have no effect, the wave amplitudes indicated by the SA observations could suggest a broad spectrum of breaking waves, while the DW observations could indicate growth in wave amplitude with height.

Height	SA RMS	DW RMS	RATIO	θ_E^*	θ_E	DW*
84	~25	11	~0.4	5	7	18
86	25	14	0.6	6	8.2	20
88	24	16	0.7	8	9.0	21
90	25	18	0.7	8	9.4	23
92	25	19	0.8	9	9.2	24
94		18				

Table (5-2) The RMS SA and DW derived wind velocity, the ratio of DW to SA RMS velocity, the effective beam angle θ_E^* calculated by assuming that the DW derived wind velocity is reduced solely by the effective beam angle being less than the apparent beam angle, the effective beam angle θ_E obtained from Lindner's results, and the DW velocity rescaled to account for the effective beam angle DW.*

Height	SA RMS	DW RMS
84	~12	5
86	13	5
88	11	6
90	12	8
92	12	9
94		10

Table (5-3) The RMS SA and DW derived wind velocity for motions with periods in the 1-8 hour range.

If for the time being, we take the SA observations as being correct, we may calculate the effective beam pointing angle θ_E^* for the large array with the assumption that the DW results are being reduced solely by this effect. This is shown in Table (5-2). Also shown are the values of θ_E calculated using Lindner's (1975b) results as discussed in Section (5.1.2.). It will be noted that the values of θ_E^* calculated from the November 1980 results are lower than those

calculated earlier in the Chapter. Lindner's (1975b) results for November are 1-2° lower than the average value presented in Figure (5-2) and so would reduce these values somewhat, but since this was obtained from relatively few observations, it is uncertain as to whether this would be a typical result. Nevertheless, the values of θ_E and θ_E^* presented in Table (5-2) are in fair agreement. If we apply the correction indicated by the values of θ_E calculated from Lindner's result, DW RMS velocities would be increased by 15-25%, giving fair agreement with the SA RMS velocities. The values of DW RMS velocities corrected using $\theta_E(DW^*)$ are shown in the last column of Table (5-2).

There is considerable uncertainty in both the SA and DW RMS velocities. The DW RMS velocities may be in error because of the unresolved vertical wind component, and the "noise" in the SA time series would tend to increase the mean square velocities. We estimate the error in θ_E calculated from the November 1980 DW results to be about 1° and we would reasonably expect a similar error in the SA results. This means that θ_E and θ_E^* agree within the accuracy of the results. However, the fact that the values of θ_E^* are consistently smaller than those for θ_E suggests that another effect may be important. This could be the overestimation of SA RMS velocities because of "noise", or it could be the effect suggested by Hocking (1983a). It is not possible to determine which effect is dominant, but it is interesting to consider how Hocking's (1983a) estimate of a reduction in DW radial velocities affects the present results.

Table (5-4) the values of θ_E calculated from Lindner's (1975b) results, and the effective beam pointing direction $\theta_E(.8)$ calculated from the DW and SA RMS velocities

ALT	$\boldsymbol{\theta_E}$	$\boldsymbol{\theta_E(.8)}$
84	7.0	6
86	8.2	8
88	9.0	9
90	9.4	10
92	9.2	11

We have already noted that a 20% reduction in DW velocities due to RMS fluctuations in the horizontal gives an effective beam angle of about 9° at $88km$, in agreement with the value of GE we have obtained from Lindner's results. If we take 20% as the reduction at each height, which seems reasonable because the RMS velocities indicated by the SA results are approximately constant with height, then the agreement is good. Table (5-4) illustrates the values of θ_E calculated from Lindner's (1975b) results, and the effective beam pointing

direction $\theta_E(.8)$ calculated from the DW and SA RMS velocities, with the assumption that the DW RMS velocities are underestimated by an additional 20%. We note that agreement is better than that in Table (5-2).

If we note that the uncertainty in the value of $\theta_E(0.8)$ for 84 km is larger than other values because we have estimated the SA RMS value for only those days with sufficient data, and that there may be some uncertainty in Lindner's results for heights above 90 km, the agreement between θ_E and $\theta_E(0.8)$is quite good. However, all that we may really say about these results is that is about 20% difference between the DW and SA RMS values that we cannot account for even after applying the correction for θ_E. What is clear is that if we use the results calculated in Section (5.1.2) to correct the DW results, there is a significant improvement in the agreement between the RMS velocities obtained from each technique.

5.4.3 Discussion of the November 1980 Results

In the preceding discussion we have assumed that the SA RMS velocities were closer to the correct values than the DW RMS velocities. This seems reasonable because of the agreement between the November 1980 SA results and the seasonally averaged SA results of Vincent (1984) and hence with the DW results from Poker Flat. This validity of this argument depends on the geographical variation of the wind field and upon the notion of a universal spectrum of gravity waves which has not been demonstrated conclusively. There are obviously uncertainties in measurements obtained with either technique. In this study the uncertainties in the SA derived winds arise because of the relatively low data acceptance rates and the corresponding "noisy" and intermittent time series. Uncertainties in the DW derived winds arise because the vertical component of the wind has not been removed.

An unresolved general problem in the SA technique is the “Triangle Size Effect” (TSE). The theory of the method indicates that the true velocity should not vary with the spacing between the receiving antenna sites. However, it does. Golley and Rossiter (1970) found that the true velocity increased with the triangle size up to the correct value at a spacing of about 200m for D-region observations at 2 MHz. By intercomparison with other methods, the technique has been optimized, but the reason for the TSE has not been determined.

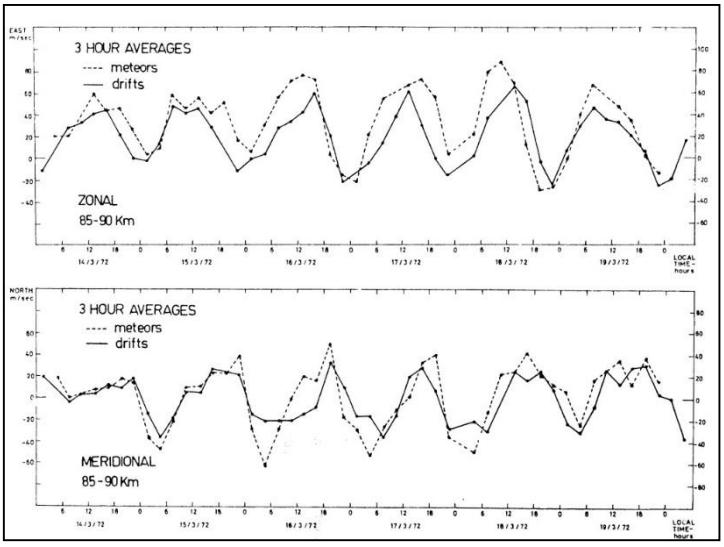

Figure (5-19) Comparison of SA ("drift") and meteor radar derived wind velocities (after Stubbs and Vincent, 1973).

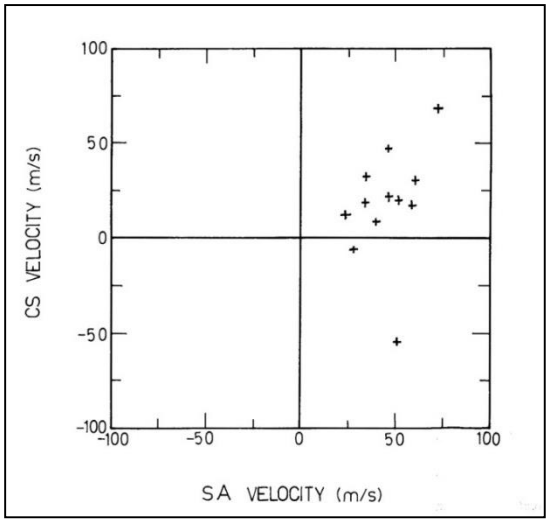

Figure (5-20) Comparison of VHF DW and HF SA derived wind velocities for 84 km (after Ruggerio and Bowhill, 1982)

Many comparisons between SA derived winds and winds derived from other methods have been reported for mesospheric observations at a variety of scales. These include a comparison of high time resolution (~4 minutes) SA results with winds obtained from dropsondes and falling spheres in the 60-90 km height range (Vincent et al., 1977), tidal components and mean winds using both meteor and SA techniques (Stubbs, 1973; Stubbs and Vincent, 1973), and mean winds and global circulation models (Smith, 1983). Agreement between the various methods is good. It is noteworthy that the comparison between SA derived winds and meteor derived winds at Adelaide (Stubbs, 1973; Stubbs and Vincent, 1973) indicated that SA derived

wind velocities tended to be slightly smaller than meteor wind velocities (Figure 5.19). However, because of the way in which the meteor data is analyzed, it is more likely to overestimate the wind velocity than underestimate it (Craig, 1984, private communication).

Like the SA technique, the DW technique had been compared with many other methods. DW results in these studies are mainly at VHF and UHF and restricted to the lower atmosphere. However, when narrow antenna beamwidths are used, agreement between the various methods is comparable to that found when the SA technique is compared with other methods. These studies include intercomparison of UHF DW and radar tracked balloon wind measurements (Balsley et al, 1977), VHF DW and aircraft wind measurements (Gage and Green, 1979) and of mesospheric incoherent scatter DW wind measurements and meteor radar wind observations (Walker, 1979).

When wider beamwidths, or beamwidths which are wide when compared to the off zenith angle are used, agreement is a little more variable. We have already noted that Röttger and Czechowsky (1980) found a variation in the DW derived horizontal wind velocity with off-zenith angle, and a comparison of (HF) SA and (VHF) DW derived D-region winds by Ruggerio and Bowhill (1982), made with a Doppler radar beamwidth of ±2.0° (Allman and Bowhill, 1976) and an apparent beam angle of l.5° indicates considerable variability in agreement with height. The data set is rather limited, but the authors suggest that the best agreement is found at heights where the scattered power is highest, and if we select such a height, we note that DW results generally underestimate SA values (Figure 5.20).

This diagram shows hourly averaged winds obtained April 1982 in the Northern Hemisphere, and so corresponds to late spring. It appears that DW derived wind magnitudes are typically half of those for SA derived winds. At 80 km agreement is better, but there is still a tendency for DW derived winds to be smaller in magnitude than SA derived winds. Data from other heights presented by Ruggerio and Bowhill (1982) shows a rather large spread, and so it is hard to assess the reliability of the data they present. Since the beamwidth of their equipment is about ±2° and the beam is pointed at 1.5° from the zenith, there may be considerable contamination of DW spectra by scatter from the zenith. However, there is some indication that DW derived winds are too small.

Ruggerio and Bowhill (1982) suggest that the SA results may be overestimating the true wind because the results of Pitteway et al. (1971), who simulated the SA experiment by using a

computer model, indicated that as random changes in the ionosphere increase, then so do the measured SA values. While this may be the case, it seems more likely that the dominant effect in Ruggerio and Bowhill's (1982) comparison and that for November 1980 is the reduction in calculated radial velocities because of the difference between apparent and effective beam angles.

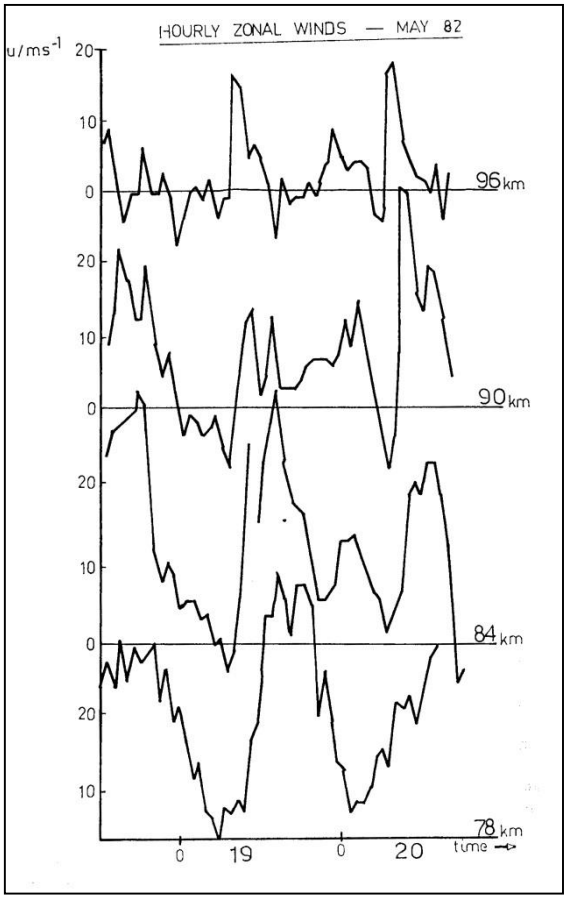

Figure (5-20a) Times series of hourly averaged velocity measured using the DW technique. Values have not been smoothed, and have not been rescaled to account for the effective beam angle.

As was the case in Section (5.1.2) we can relate the SA and DW wind velocities using information derived from Lindner's (1975b) results, so that there is strong evidence that both techniques are measuring the same thing, although there are variations in agreement between the techniques even when the effective beam angle is taken into account. There are many possible explanations for this, but given the inexact nature of the measurements, agreement seems reasonable and within the limitations of the experiment, we may conclude that acceptable results may be obtained from the DW method at BP, as long as some care is taken. An impressive aspect of this comparison is that the only essential difference between the SA

and DW equipment were the aerials used for reception. We recall that there were three single droopy half-wave dipole aerials for SA observations, and two arrays, each consisting of 89 half-wave dipoles for DW observations.

This highlights the efficiency of the SA method rather well, and the addition of the other dipoles generally used with this particular SA equipment would have extended the height range. The obvious advantage of the DW technique 1n this experiment is its excellent height and time coverage, which results from the higher gain of the receiving array used. Even if the DW derived velocities are underestimates, information about the phase of the various tidal components is useful, and in the 80-100 km height range, the continuity of the time series means that problems associated with harmonic analysis of intermittent time series (see e.g., Crary and Forbes, 1983) are reduced. An example of hourly mean winds obtained with high data acquisition rates is shown in Figure (5-20a). These data have not been smoothed in any way, and the diurnal variation of the wind field is clearly evident at 78 km.

The poor quality of the SA winds obtained in this study when compared to those generally obtained have limited its conclusions somewhat, and there is an obvious need for more simultaneous comparisons between SA and DW derived winds. This is now possible using the BP facility only, and with one wind determination at each height every two minutes possible (before rejection criteria are applied), a clearer picture should emerge.

In the next Section we present the mean winds for each DW run, and discuss some additional evidence of variation between the apparent and effective beam directions. Except where indicated, the DW results have not been corrected for the effective beam angle.

5.5 The Mean Doppler Wind Derived Winds for Other Periods of Observation

In this Section we present the mean winds measured for each observational period in which measurements of the Reynolds stress and horizontal scales were obtained. These results are important for the assessment of gravity wave mean flow interactions, and we will refer to them in Chapter 6. We also present the mean SA derived winds for adjacent or nearby adjacent observational periods. This provides some indication of the general agreement between the winds derived from both techniques, but because there is often considerable variability in the tidal wind components from day to day, and because the daily "mean" wind varies because of planetary scale waves a detailed comparison is generally not possible. However, 16 days of

DW observations were obtained in July 1982 and these data should provide a representative measure of the mean wind.

In the following results, there is generally more uncertainty in the DW meridional component than the zonal component because all of the zonal components were obtained using the DCC beam configuration, while the meridional components, with the exception of the last ten days of the July 1982 results, were obtained using the DC beam configuration. The latter beam arrangement requires the vertical mean wind component to be removed for the northward directed beam radial velocity to obtain the meridional component of the horizontal wind. The relative error in the mean vertical velocity is about ±30% (see Chapter 2) and the mean vertical velocity was often 1 ms^{-1} while the northward beam mean radial velocity seldom exceeded 5 ms^{-1} (±10% relative error). Consequently, there is an accumulation of errors when Equation (4-68) is applied to recover the mean meridional wind.

We consider the July 1982 results first.

5.5.1 July 1982

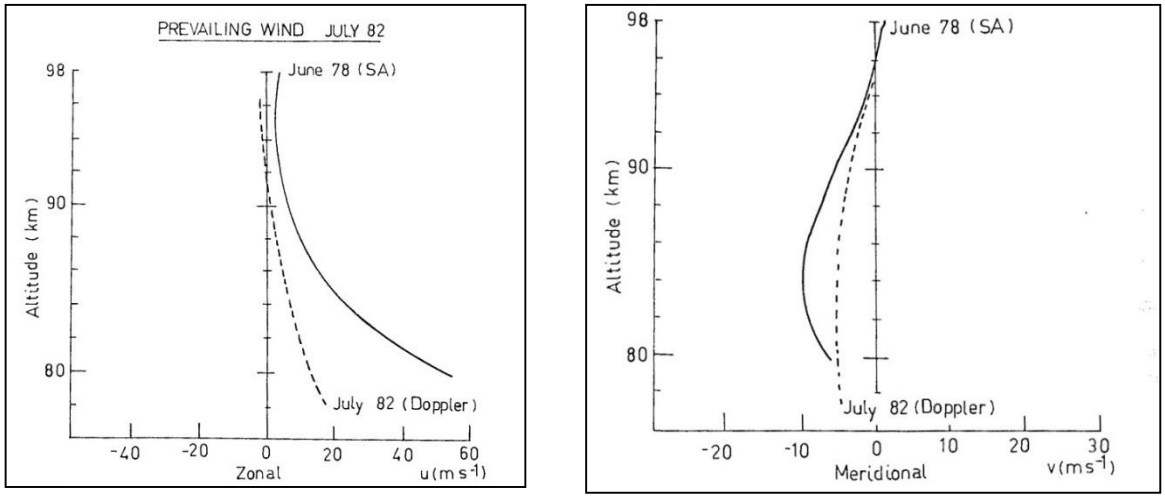

Figure (5-21) Mean DW winds derived for 30 June to 16 July 1982. Also shown are the SA derived winds for July 1978.

A total of sixteen days of DW observations were obtained in July 1982. For the first six days the OPDC beam arrangement was used. We recall that this is three beams directed at 11.6° to the zenith Eastwards, Westwards and Northwards respectively, and one beam directed vertically. The remaining ten days of observations were obtained using the OPDCC beam arrangement, in which beams are directed at 11.6° to the zenith Eastwards, Westwards,

Northwards and Southwards. The abrupt changes in radial velocity in this data set discussed 1n Chapter 2 do not change the mean winds significantly, and do not affect the general conclusions of this discussion.

The mean winds for the sixteen days of observation obtained from harmonic analysis are shown in Figure (5-21). Also shown are the SA derived winds for June 1978, which are quite typical of mean winds at this time of the year at Adelaide (these particular results have been presented in Vincent and Ball, 1981). The SA results are also in good agreement with the model of Groves (1969) and with the five-year average of SA winds at Adelaide.

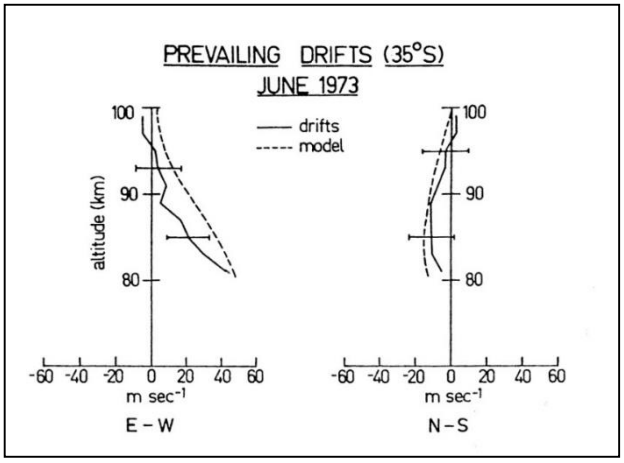

Figure (5-22) Mean SA derived winds for June 1973, and the mean winds from Groves (1969)

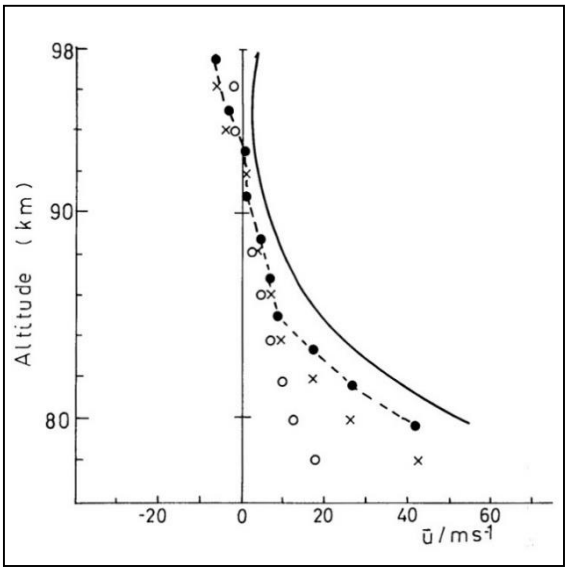

Figure (5-23) The DW derived winds for July 1982 corrected for the effective beam angle only (crosses), and with the additional correction for range (closed circles). The solid line indicates SA results for June 1978. Open circles indicate the measured wind velocity.

For reference we also present the mean winds for June (1973) for Adelaide together with the winds from the model of Groves (1969) in Figure (5-22). This diagram is from Briggs et al. (1973). It will be noted that the July 1982 observations are smaller in magnitude at all heights than the SA observations. The difference cannot be accounted for by inter-annual variability of the mean wind, and it appears that the DW derived wind velocities are underestimating the true wind velocity.

If we apply the corrections for the effective beam angle indicated in Figure (5-4) we obtain the results shown in Figure (5-23) as crosses. If we then correct for the range (see Table 5-1) we obtain the results shown as the dots in the diagram. The difference between these height profiles can now easily be accounted for by inter-annual variability, and agreement is good in any case. Inspection of Figure (5-22) indicates that the mean zonal wind does go westward in the 95 km height range at this time of year. These results support the evidence that the DW derived winds are underestimating the true wind, and that the effective beam direction θ_E calculated from Lindner's (1975b) results provides a good measure of this quantity. Furthermore, it appears that the range should be corrected to account for the effective antenna angle. This has important consequences for the magnitude of the body force calculated from values of $\overline{u'w'}$ and $\overline{v'w'}$ but does not change the general conclusions of such calculations. We will consider this in Chapter 6.

5.5.2 November 1981 TC(CP)

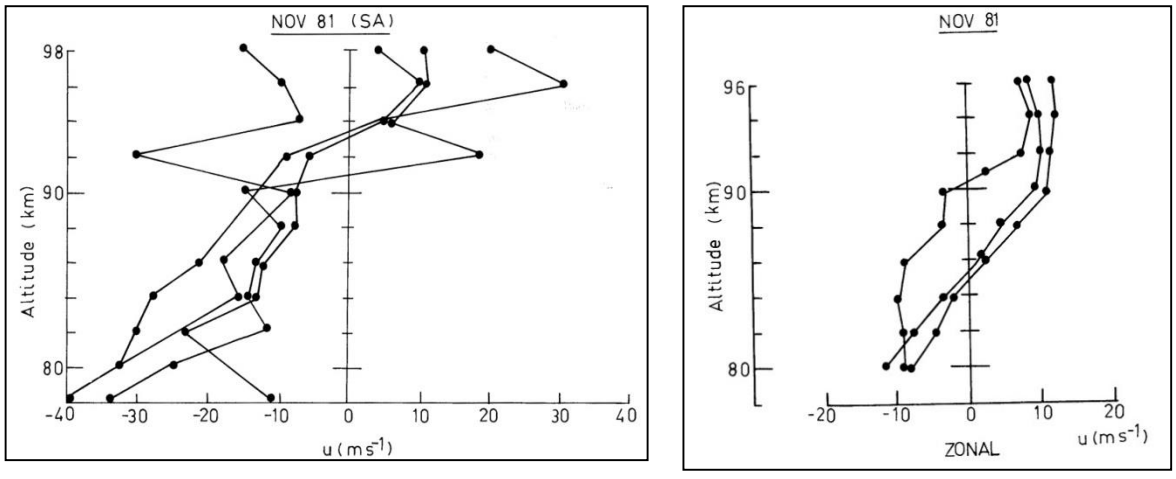

Figure (5-24) (a) Mean DW derived winds for 6-8 November 1981 (left), and (b) mean SA derived winds for 9-12 November 1981 (right).

Three days of observations made with the DW method were obtained for the zonal component and the mean values for each day obtained from harmonic analysis are shown in Figure (5-24a). These observations preceded the summer SA observational run and the mean wind values for SA observations for four days immediately following the DW observations are shown in Figure (5-24b). Agreement in form is good and values at heights of 94 and 96 km show excellent agreement. Other heights indicate a difference of 10-15 ms^{-1}, with DW derived winds being more eastward.

The DW profile for the 7th which shows the best agreement with SA observation was calculated from a time series with six hours of data missing because of a power failure, and so may be subject to some uncertainty because of this. The values from the 6th and 8th were calculated from complete data sets and show good agreement. The SA observations generally show a rather greater variability than the DW observations because of the lower data acceptance rates. This is particularly evident below about 84 km and above 90 km, and at 78 km for the four days only about 12-14 hours of data were available for analysis for each day, and so these values must be treated with some caution.

Figure (5-25) Time series of zonal velocities for periods longer than 36 hours for November 1981.

The time series of zonal velocities with periods greater than 36 hours is shown in Figure (5-25) and there is clear evidence for planetary wave activity. The tendency at most heights is to

Westward values of velocity for the first four days, although this is clearly variable. The main planetary wave periods appear to be about two days, although longer oscillations are also evident, and examination of Figure (5-25) indicates a tendency for a 2-day variation which is consistent with Figure (5-24a). Consequently, day 7 may reflect planetary wave action rather than a low data acceptance rate. Days 19-23 in Figure (5-25) do show a tendency for Eastward values of zonal velocity and it seems likely that the gross differences between the height profiles of zonal velocity derived from the SA and DW techniques are due to planetary wave activity. It is not possible to assess the relative magnitudes of the DW and SA derived wind velocities in this case, but we note that the results derived from each technique are consistent when the longer period motions are considered.

5.5.3 December 1981 (OPDC)

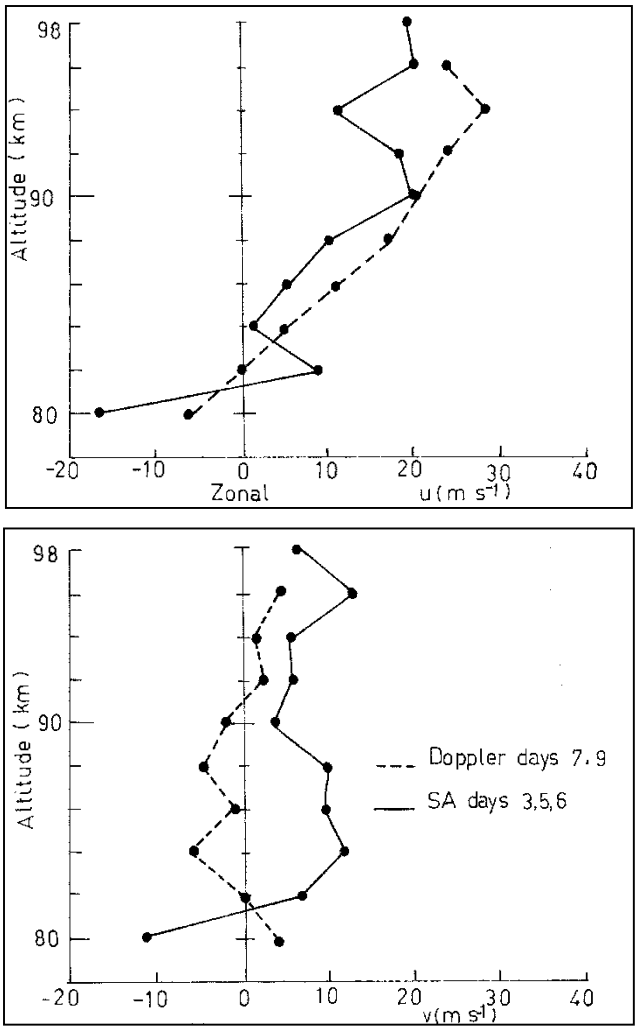

Figure (5-26) (a) Mean zonal winds for December 1981 for SA (solid line) and DW (dashed line) (left), and (b) the corresponding meridional winds (right)

Four days (3-6 December) of SA observations were made in December 1981 as part of a four channel experiment, in which three spaced antenna aerial arrays and one entire array were operated simultaneously. This allowed SA results and vertical winds obtained using a narrow Doppler beam to be obtained simultaneously. Immediately following these observations, three days of DW observations (7-10 December) were made using the OPDC beam arrangement. Power failures on 4 and 8 December made data from these days unsuitable for further analysis. The mean winds calculated by removing the 12 and 24 hour tidal components are shown in Figure (5-26). The zonal components show excellent agreement in form and we note that the DW results are larger than the SA results. However, there is a strong tendency to more positive values of zonal wind at heights between 80 and 92km, and so the agreement in magnitude seems reasonable.

The meridional components disagree in sign below 90 km, but as was the case in November 1981, this observational period was characterized by longer period motions, and there is considerable variability in the "mean" winds from day to day. The meridional DW component is in agreement with that for SA observations obtained over the period 28 November to 1 December.

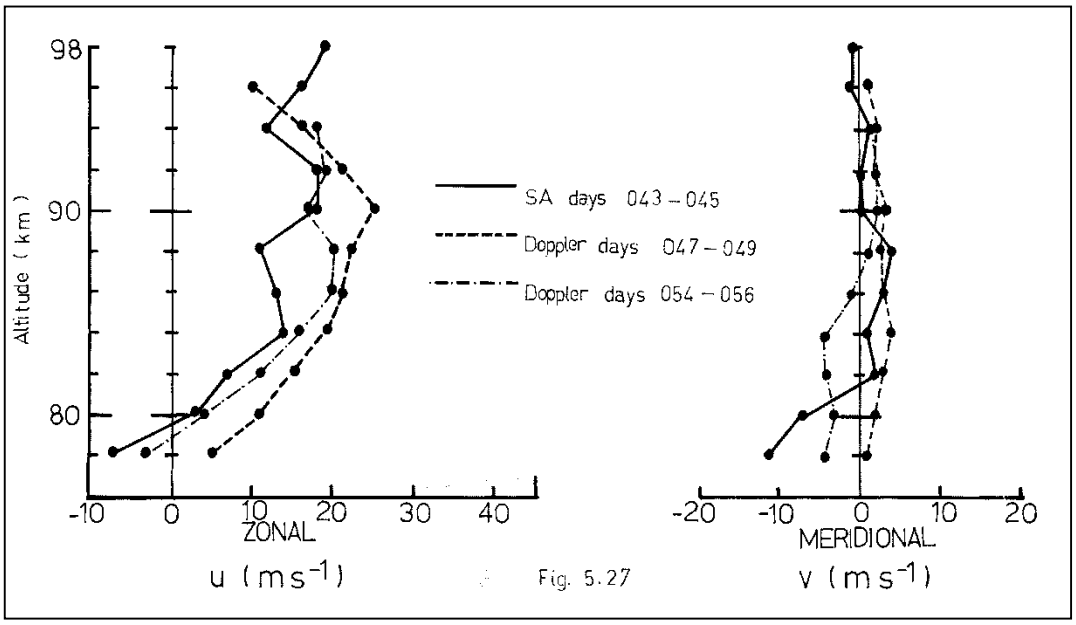

Figure (5-27) (a) (left) Mean zonal winds for February 1982 for SA (solid line) and DW (dashed and dot-dashed lines), and (b) (right) the corresponding meridional winds (right)

5.5.4 February 1982

A number of days of Doppler data were obtained in February 1982 with different beam positions (see Chapter 2). The "two-day wave" (see e.g. Craig et al., 1980) was particularly strong at this time and because of the dominance of this oscillation and because basic harmonic analysis of such data leads to questionable results, we have taken two day averages of the zonal and meridional components for SA observations for days (43-45) and DW observations for days (47-49) and (54-56). These are plotted in Figure (5-27). Agreement between the mean winds derived from technique is clearly very good given the separation in time of the observations and the presence of longer period motion.

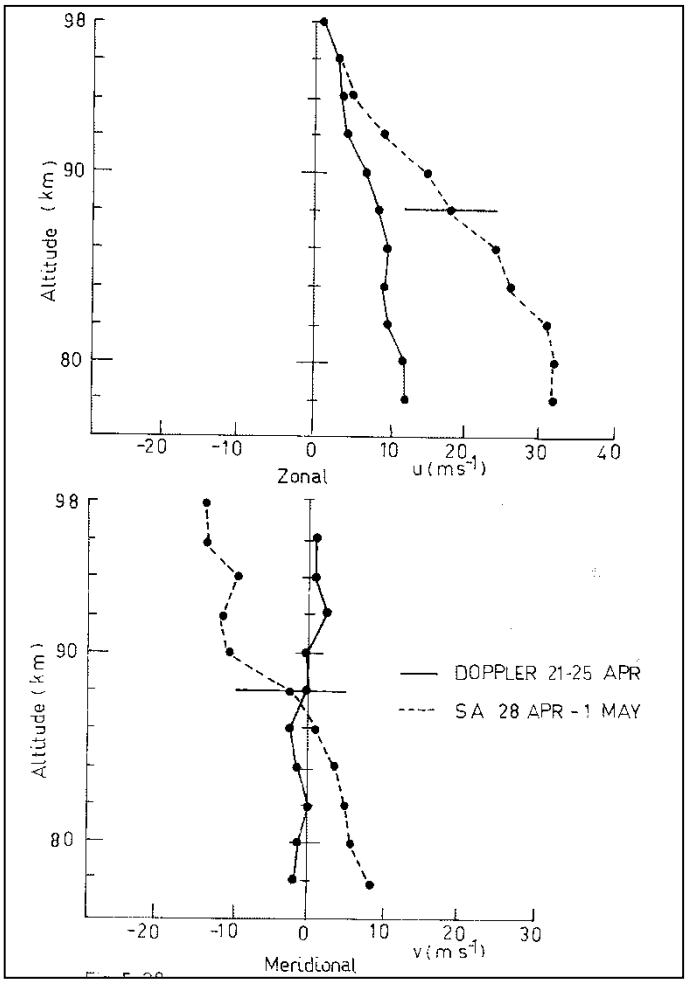

Figure (5-28) The mean DW results obtained by harmonic analysis for the five days of DW observations were obtained in April 1982 (21-26) are shown in Figure (5-28). Also shown in this diagram are the SA results for the 28 April to 1 May.

5.5.5 April 1982 (OPDC)

Five days of DW observations were obtained in April 1982 (21-26). For the last three days of the DW run observations were only taken over the height range of 78-90 km. The mean winds obtained by harmonic analysis are shown in Figure (5-28). Also shown in this diagram are the SA results for the 28 April to 1 May. The bars on the SA results indicate the mean absolute difference for the four days of observation. The zonal component of the DW derived winds shows a trend to more eastward values over the five days, while the meridional component exhibits evidence of planetary wave activity. The meridional component of the SA observations indicates similar behaviour.

Inspection of Figure (5-28) indicates that the zonal component of the DW observations is somewhat smaller than the SA component, although it agrees in sign and general form. The zonal SA component agrees well with the model of Groves (1969), showing the best agreement at 80 km, but underestimating it somewhat at higher heights. Agreement in form is good. The meridional components do not agree as well as the zonal components, as would be expected because of the longer period waves. The DW results are rather small, while the SA results are reversed relative to the model of Groves (1969).

Since these DW observations were obtained over a period of five days, and the zonal components of both SA and DW are well behaved, we may tentatively suggest that the DW derived mean zonal velocities are underestimating the correct wind velocity. Taking account of the trend in the DW zonal velocities, we estimate that the ratio DW/SA derived wind velocity is about 0.5 at 80 km, rising to about 0.7 at 88 km, a result in fair agreement with our estimate of θ_E.

5.5.6 May 1982 (OPDC)

Two days of DW observations were made in May 1982 and the mean winds obtained from harmonic analysis of the time series are shown in Figure (5-29). It will be noted that these observations are in agreement with the DW observations made in April 1982. The mean zonal SA winds for four days preceding the DW observations are also in agreement with the SA observations made in April 1982, although they are slightly larger at all heights, as is expected as the zonal circulation becomes more eastward as it moves into the winter region. As for April 1982, SA observations show better agreement with the Groves (1969) wind model, and we

cautiously suggest that the zonal DW derived winds are underestimating the true wind. General agreement in form is good however.

The mean zonal winds measured in May 1981 (DCC beam arrangement) are also smaller in magnitude than expected for this time of year, although of the correct sign, and agree well with the results for the May 1982 observations.

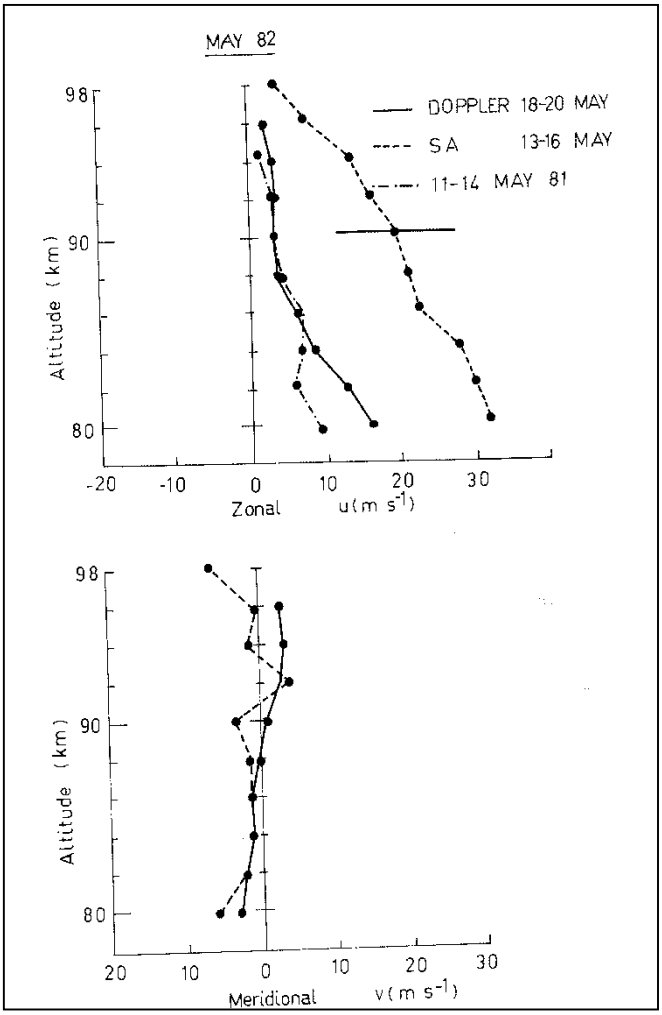

Figure (5-29) The mean winds obtained from harmonic analysis of the time series for two days of DW observations made in May 1982. The mean zonal SA winds for four days preceding the DW observations are also shown.

5.5.7 Discussion of the Mean Doppler Wind results.

With the exception of the July 1982 data set, these comparative observations do not allow a measure· of the relative magnitude of the DW and SA derived mean winds to be made but we can suggest that there is no evidence of atypical behaviour in the DW derived wind velocities

apart from the tendency to be somewhat small in magnitude. Observations taken in all seasons exhibit the correct signs for both mean wind components when longer period motions are taken into account.

The better agreement between the DW and SA observations in the summer months (December and February) may be due to more isotopic scattering, although it is not possible to say with any certainty in the present case. However, we note that the mean square horizontal velocities calculated from these data sets are consistently lower than similar observations made with other techniques. Consequently, we believe that the mean winds measured in the various observational periods provide a good measure of the true wind when the effective beam angle and range are taken into account.

5.6 Measurement of the Mean Vertical Wind Component

Measurements of the vertical wind component were made in most observational periods. Measurements of this type are subject to a number of uncertainties, the most obvious of which is whether the "vertical" beam is in fact directed vertically. We have considered this in Chapter 2, and it would appear that a vertical beam at BP is about 0.1° off vertical to the SW.

Another effect that could produce erroneous vertical velocities is scattering from tilted reflectivity structures. In this case, the echoes could return from small-off vertical angles and the mean shift of the backscatter Doppler spectra could include a contribution from the horizontal wind. The scatter plots of horizontal and vertical velocities presented in Chapter 2 indicate a very small contribution from the horizontal components, one that is consistent with the vertical beam at BP being off zenith by about 0.1°, so that on average, the scattering regions must have very small tilts from the horizontal. However, this argument must be treated somewhat cautiously, because we can measure the covariance term $\overline{u'w'}$ (Chapter 6), and we could expect a correlation between u' and w'.

The limited velocity resolution ln this work (±0.7 ms^{-1}) for individual (102.4s) wind determinations also restricts the measurement of vertical winds over short periods, but over periods of a few days it should possible to obtain an estimate of the mean wind with reasonable accuracy (±30%). Above 90 km, Sporadic-E may produce a downward velocity as the totally reflecting surface moves down, but the acceptance criteria outlined in Chapter 3 should reject such data. The possibility remains however, that some of the measured vertical motion in this

height range is due to down-coming Sporadic-E. In this part of the Chapter we present some representative observations of the vertical wind, but the uncertainty in these measurements must be borne in mind. The mean square vertical perturbation velocities periods less than eight hours are discussed in Chapter 6.

In the next Section we present the results of a comparison of vertical winds measured simultaneously in wide (±20°), and narrow (±4.5°), vertically directed beams.

5.6.1 Measurement of Vertical Wind with Wide and Narrow Beams.

Both of the SA and DW techniques allow the vertical component of the wind field to be obtained from the mean shift of the Doppler spectrum measured in a vertical beam. With the DW technique, one narrow beam may be directed vertically for this purpose. With the SA technique, this information may be obtained from any of the receiving antenna sites, but a better estimate can be obtained by calculating the average vertical velocity from each of the beams.

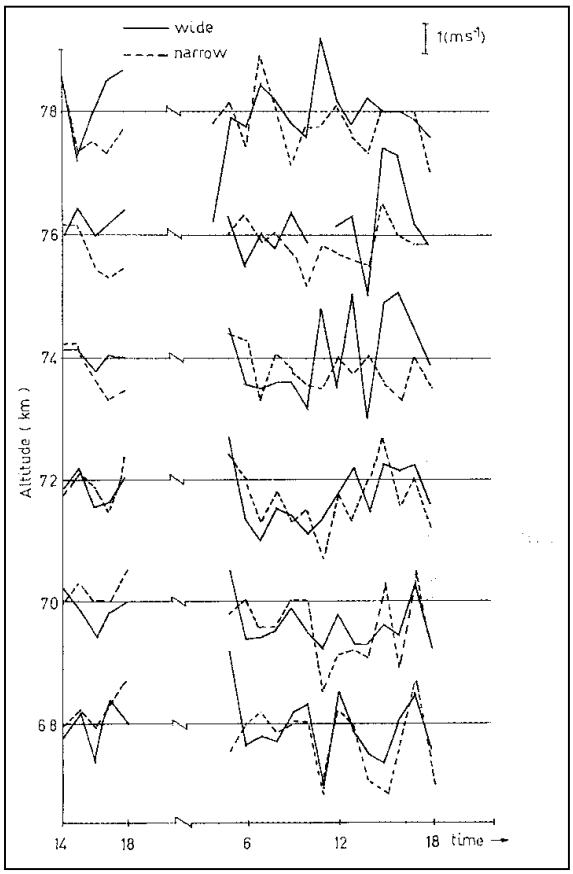

Figure (5-30) The vertical wind measured in both wide (solid line) and narrow (dashed line) vertically directed Doppler radar beams in the 68-78 km height range in December 1981

With the typical receiving aerial beamwidths of ±20° at half power that are commonly used in the SA technique (see Figure 2-6) vertical velocities measured using this method may be contaminated by scatter from off vertical angles. However, because of the restricted range of zenith angles from which scatter is returned, antenna beamwidths are relatively unimportant, particularly below about 75-80 km.

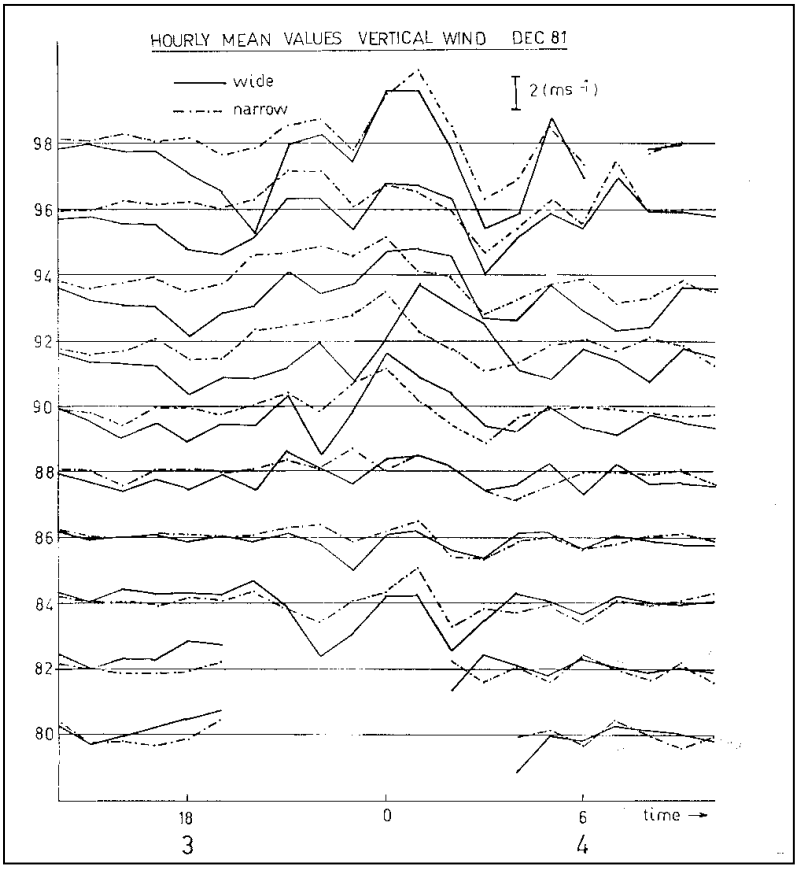

Figure (5-31a) The vertical wind measured in both wide (solid line) and narrow (dashed line) vertically directed Doppler radar beams for 3-4 December 1981

Above these heights, the mean Doppler shift should be unchanged for measurements made with wider beamwidths, as long as strong returns are not returned from off vertical angles. The Doppler spectrum will be wider and flatter, and consequently the uncertainty in the mean shift will be larger. If the reflecting surface is tilted or distorted in some way, then contamination from horizontal velocities will occur, and if strong specular reflections are returned from off vertical angles, the "spikes" produced in a Doppler spectrum may shift its mean value (Röttger, 1980). This will affect vertical velocities measured using either wide or narrow beams, and its exact nature will depend upon the spatial variation of the tilt or corrugation. Röttger (1980) has suggested that the incidence angle of the returned signal should be measured to correct for

off vertical velocity components. This can be done in SA experiment if phase information is obtained, and is routinely done for meteor radar observations (e.g. Elford and Craig, 1980). The effectiveness of this will obviously depend upon the number of specular reflections present in the beam, but it would make better use of the phase information which is not exploited fully at present. The enhanced echo power received from the zenith means that in principle, good measurements of vertical velocity can be made at BP at heights down to about 60 km during the day, and above 80 km at night.

In December 1981, observations of vertical velocity measured in both wide (±20°) and narrow (±4.5°) vertically directed beams were made. No attempt was made to correct for off vertical returns, and the observations are essentially a "quick look" at how well vertical velocities could be measured with the SA beam configuration. No previous comparisons of this type have previously been reported, although Röttger (1981) has measured vertical velocities at stratospheric and tropospheric heights with the SOUSY VHF SA radar.

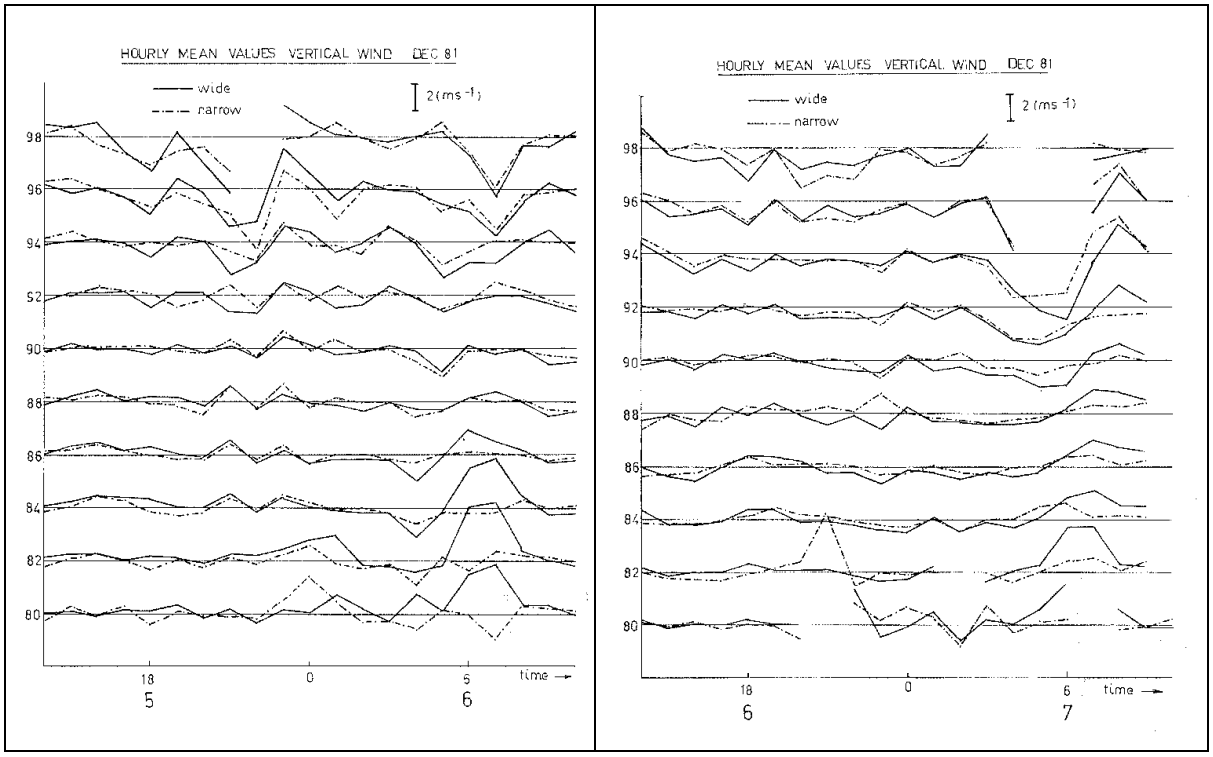

Figure (5-31b) (left) As for Figure 5.31a but for 5-6 December 1981, and Figure (5-31c) (right) As for Figure 5.31a but for 6-7 December 1981

Figure (5-30) illustrates hourly averaged vertical velocities measured in the 68-78 km height range in December 1981. Data were not obtained between 1800 and 0500 LT, and observations were taken at a rate of 1 in 4 minutes, which is consistent with typical run rates for SA

observations made at BP. Data from the three SA receiving beams were averaged, and apart from this, all data were processed in exactly the same way (see Chapter 3). Below 74 km, agreement is excellent. At the higher height ranges the wide beam velocities are rather more "noisy", but general agreement is fair. This is what we expect, as above about 75-80 km scatterers become more isotropic. It is noteworthy that a strong echo was evident at 72 km on the CRO at the field site on this day. Figure (5-31a, f) illustrates the results for 78-96 km and 90 km in a little more detail. Agreement is a little more variable, particularly on the 3rd, but general features are in good agreement. Days 5 and 6 show better agreement, although the run rate for these days was 1 in 8 minutes, and it is clear that both beamwidths are measuring the same thing.

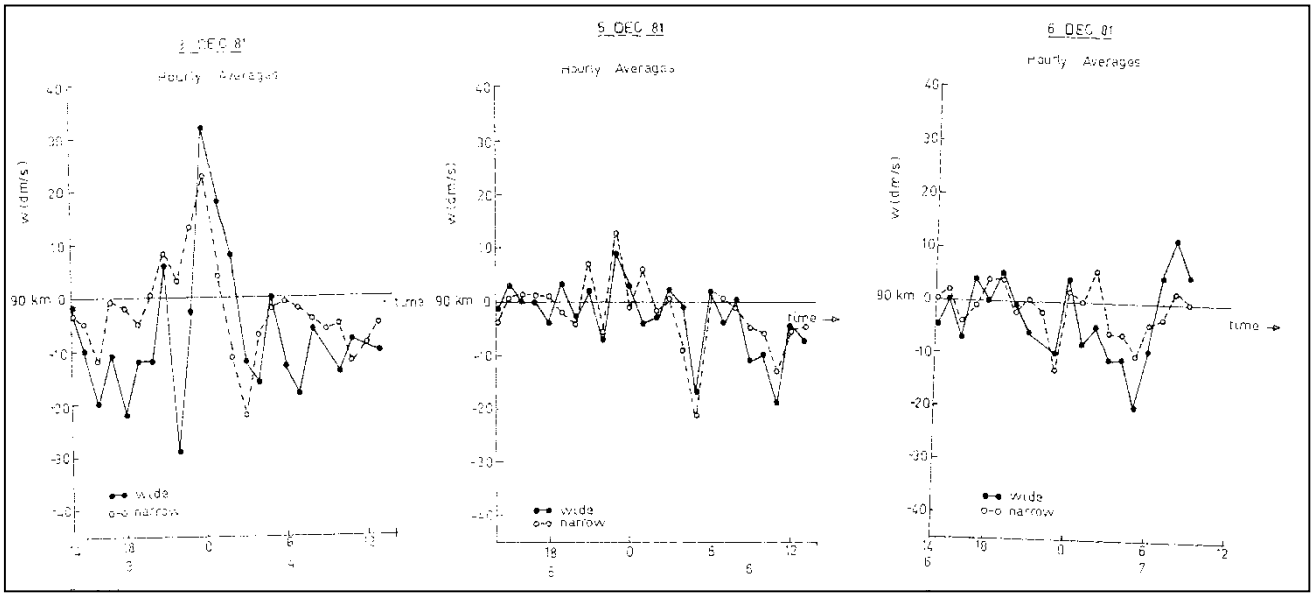

Figure (5-31d) (left), Figure (5-31e) (center) and Figure (5-31f)

The mean wind obtained from harmonic analysis for each day are shown in Figure (5-32a, b and c) for 78-96 km. However, the actual range is 80-90 km and so the profiles should be shifted up together. Worst agreement is found on the 3rd, but agreement on 5 and 6th December is good. The mean of the three days (Figure 5-32d) clearly shows good agreement in form, and agreement would be excellent if the 3rd was omitted from the average.

These results are particularly encouraging, and indicate that mean vertical winds over 2-3 days can be measured at BP with the basic SA configuration. This is not particularly important at BP, where a narrow Doppler beam is available simultaneously with the SA beam arrangement, but at other SA sites, indications are that the mean vertical winds may be measured. However,

the variable agreement between days indicates that correction for off-vertical returns should be applied.

5.6.2 Other Measurements of the Mean Vertical Wind.

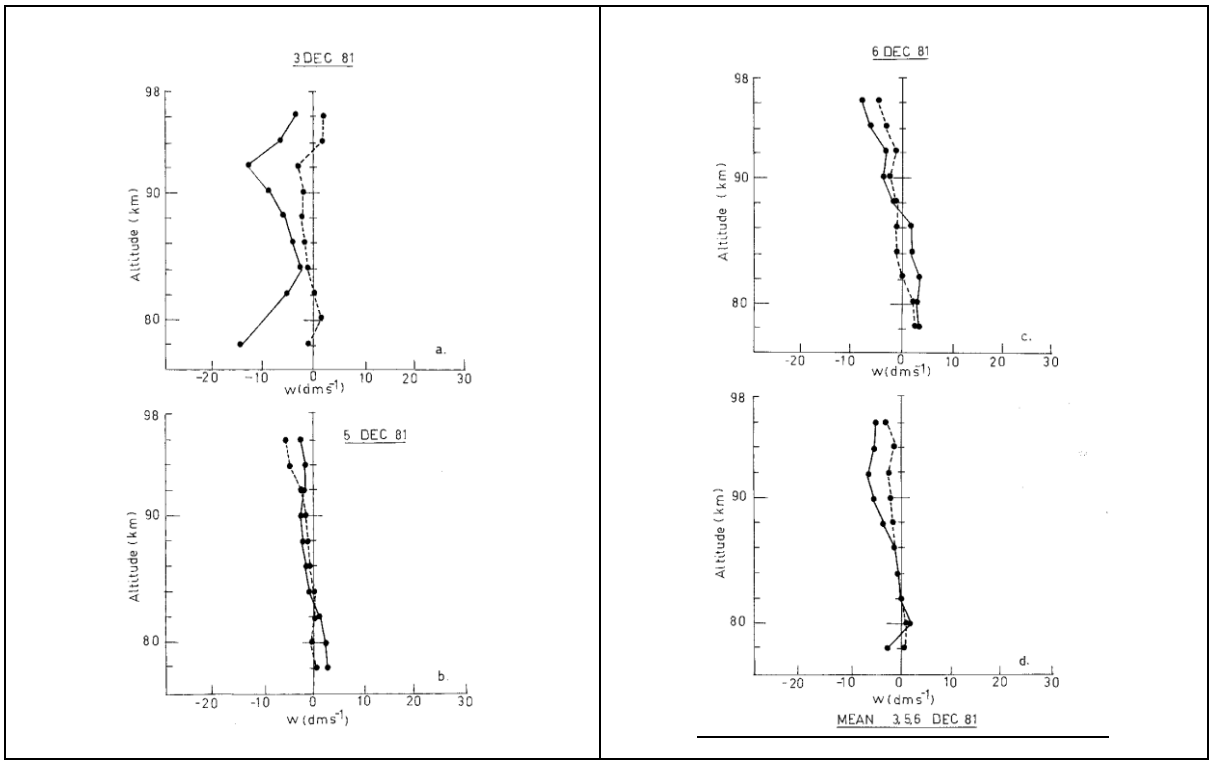

Figure (5-32a) (top left), Figure (5-32b) (bottom left), Figure (5-32c) (top right) and Figure (5-32d) (bottom right) The mean wind obtained from harmonic analysis for each day in December 1981

Inspection of Figure (5-32d) indicates that the mean vertical wind is downward over most of the height range. We recall that the monthly averaged vertical wind component for November 1983 (Chapter 2) was similar in form to that shown in (Figure 5-32d). The mean vertical wind measured over a three-day period immediately after that presented above is shown in (Figure 5-33). Also shown in this diagram is the value of $\overline{w_u^*}$ obtained from the radial velocities measured in eastward and westward directed beams. Agreement is excellent in this case, indicating that the spatial variation of $\bar{u}$ is small. This is also true of some other observational periods.

(Figure 5-34) illustrates $\overline{w_u^*}$ and $\bar{w}$ for one day of observations obtained in November 1981 (note that the signs of the vertical components are reversed in this diagram). Agreement is good, and the main features are evident in both time series. However, this agreement is not typical of the rest of the observational period.

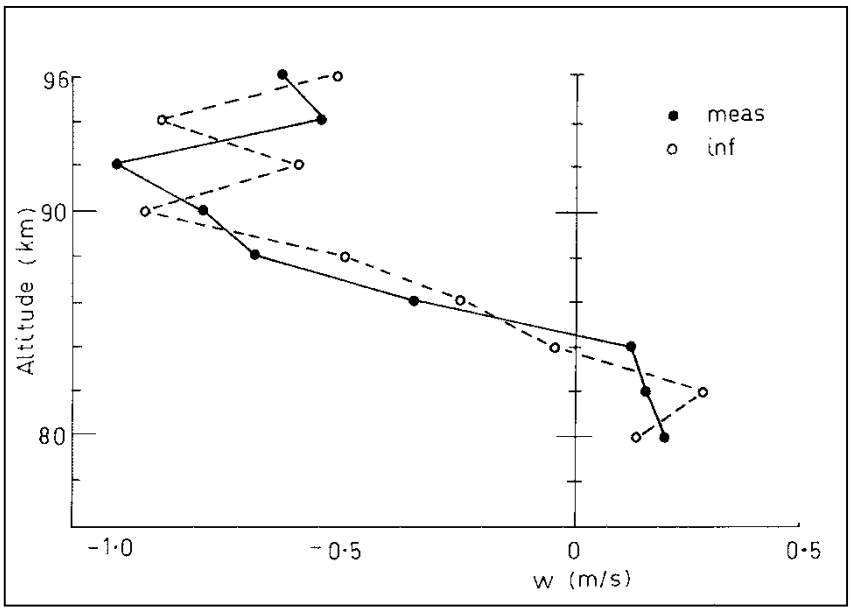

Figure (5-33) The mean vertical wind measured over a three-day period in December 1981

Neither is true in general. Figures (5-35a-g) summarize the mean vertical velocities measured in the various observational periods tabled in Chapter 2.

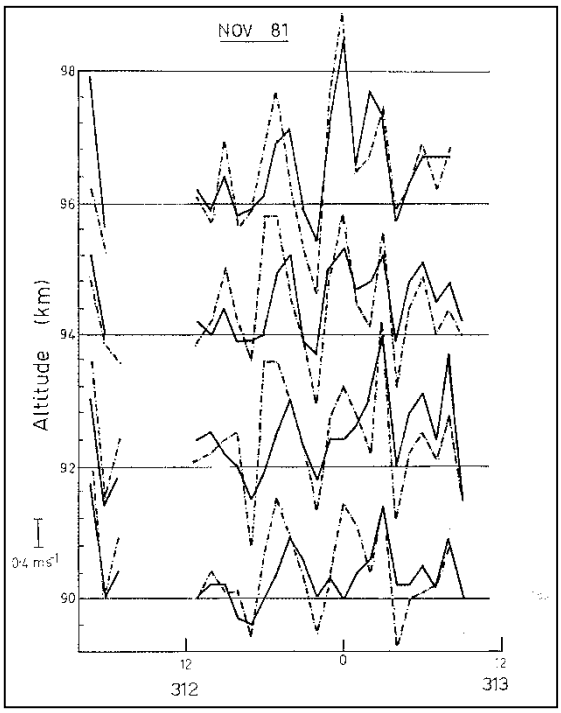

Figure (5-34) Time series of hourly averaged measured vertical velocity $\overline{w}$ (solid lines) and inferred vertical velocity $\overline{w^*}$ (dashed line) for four heights for data obtained in November 1981

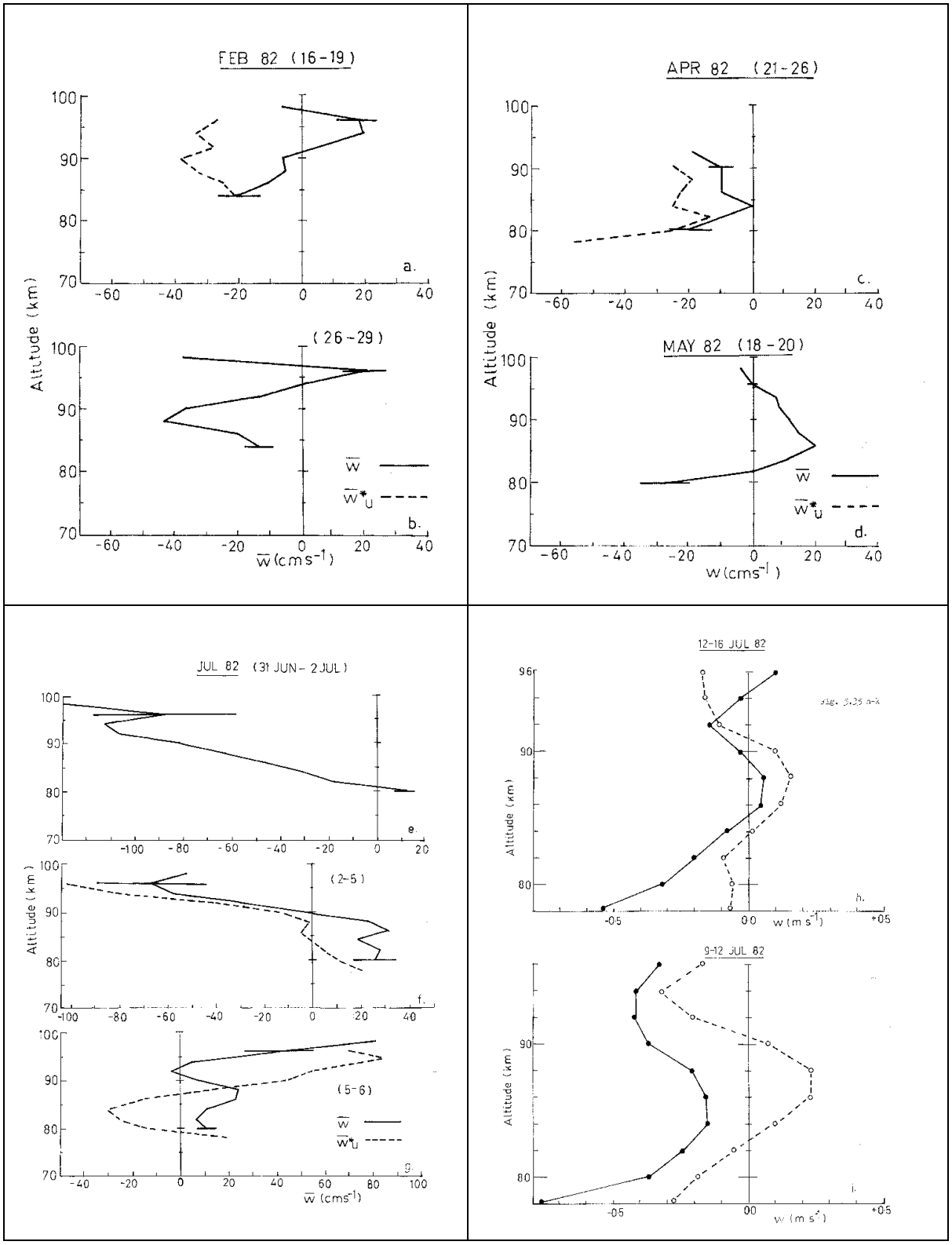

Figures (5-35a-i) the mean vertical velocities measured in the various observational periods tabled in Chapter 2

The agreement between $\overline{w}$ and $\overline{w_u^*}$ is quite variable, and this indicates that in general, the mean vertical wind cannot be obtained from the mean radial velocities measured in DCC beams.

There are also variations between $\overline{w_v^*}$, the vertical velocity inferred from Northward and Southward directed beams and $\overline{w_u^*}$ (Figure 5-35h-k) illustrates these two quantities for observations made in July 1982 and (Figure 5-351) illustrates similar results for October 1982. Inspection of these diagrams indicates that there are significant variations in $\frac{\partial \bar{u}}{\partial x}$ and $\frac{\partial \bar{v}}{\partial y}$ over the separation of the beams. We will not pursue the analysis of these data, but we note that if the spatial variation of the mean wind is measured, then it is possible in principle to obtain the time variation of the total mean wind $\frac{\partial \boldsymbol{u}}{\partial t}$, and hence the acceleration of the mean flow, by application of Taylor's transformation.

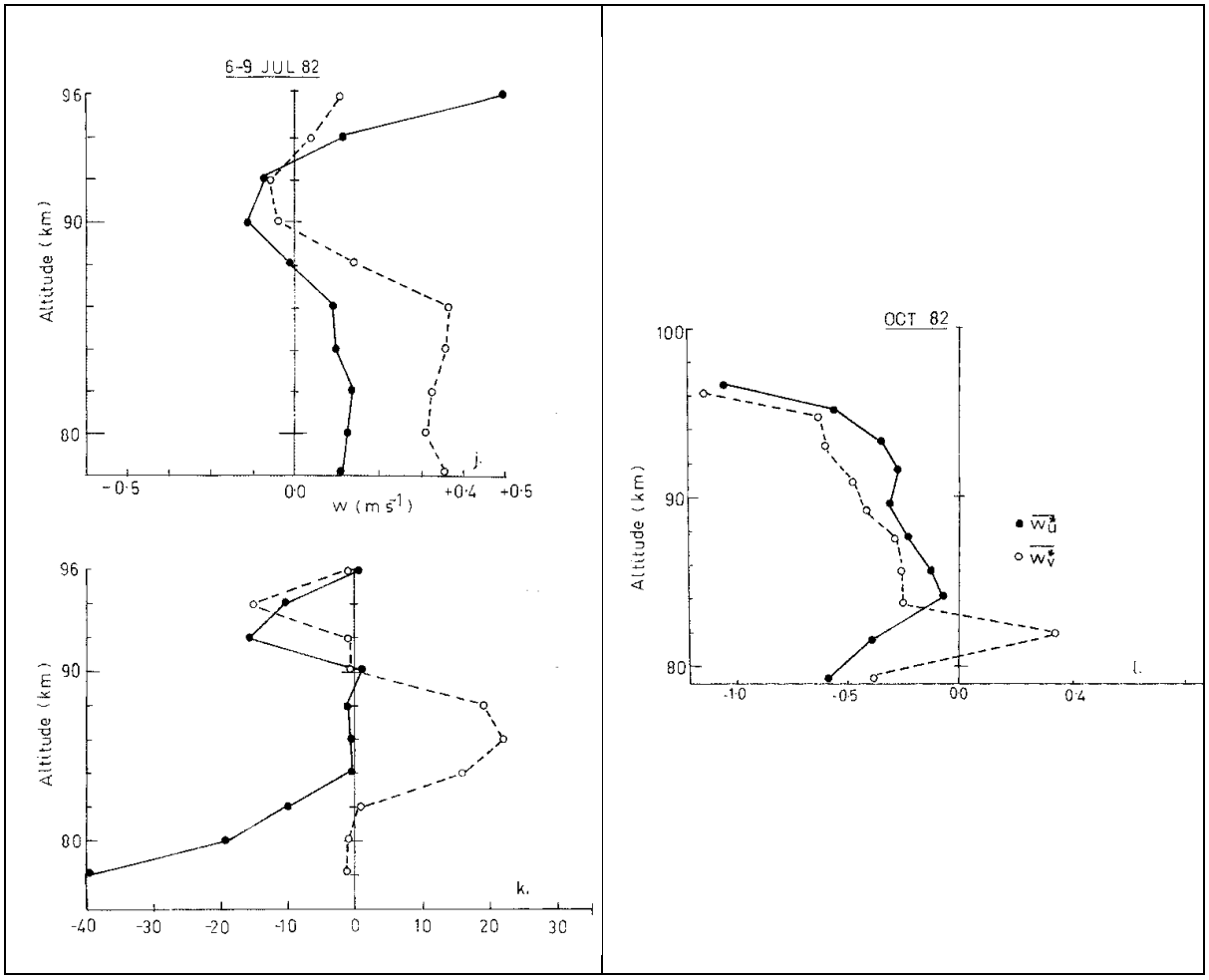

Figures (5-35j,k,l) the mean vertical velocities measured in the various observational periods tabled in Chapter 2

Returning now to Figure (5-35 a-g), we note that these diagrams illustrate mean winds over periods of 2-5 days, with the exception of (Figure 5-35g) which represents 21 hours of observations. The height profile of $\bar{w}$ for this last data set appears to have a wavelike variation, with a vertical wavelength of about 10 km. This may be due to the tidal components. Similar

structure is evident in the November 1981 and February 1982 (Figure 5-35b) height profiles, but because these observations were taken over three days, and horizontal tidal components show considerable day to day variability and we could reasonably expect similar behaviour in the vertical component, it is unclear what they represent. The most important thing to note about these vertical velocities is their magnitude. The winter results show vertical velocities of 0.8-1 ms^{-1} at heights above 90 km when averaged over three to four days.

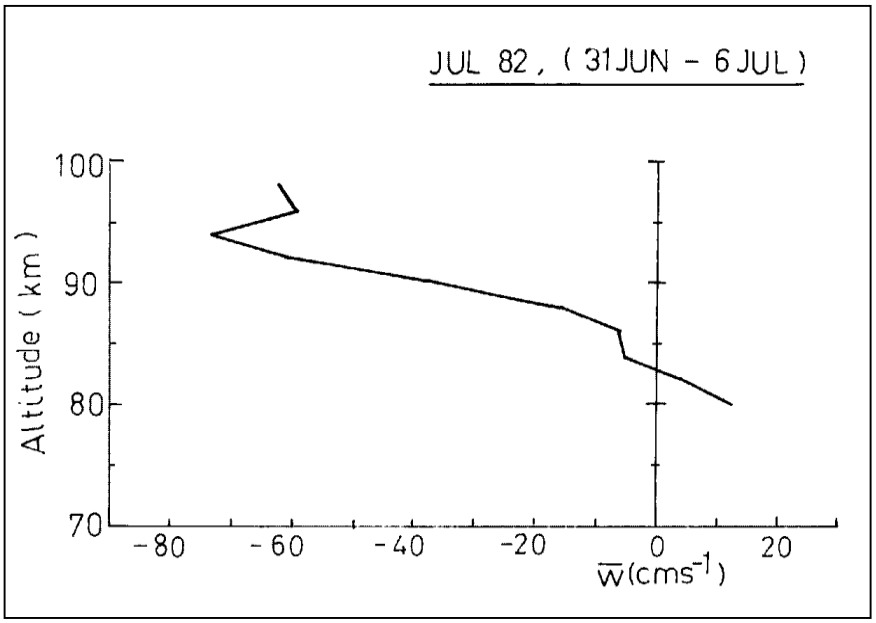

Figure (5-36) The mean vertical wind for the period 3ist June - 6th July 1982

The mean vertical winds for the six-day period represented by (Figures 5-35e-g) are shown in (Figure 5-36). Above 90 km, the mean vertical winds are comparable to the mean horizontal wind for this period (see Figure 5-21). We note that if these mean winds are real then ray-tracing of gravity wave motion to determine its source will be subject to considerable uncertainty unless the vertical wind is taken into account (Tilbrook and Jones, 1979). These results also indicate that the mean vertical wind cannot always be neglected when measurements of the horizontal mean wind are made with off vertical beams, but without a vertical beam.

Inspection of the diagrams of the mean vertical wind indicates considerable variability throughout the year, and because the observations were taken over short periods of time, it is not possible to draw any definite conclusions about their importance for the mean circulation. However, we note that the summer observations (December, February) tend to suggest a

downward flow in the 80-100 km region, as does the monthly mean for late spring (November), and the 5- and 16-day means for mid-autumn (April), and winter (July).

It would be unlikely that the observations were taken only when the mean vertical wind was downwards, and it is possible that the tendency during the entire year is towards downward vertical velocities. This result would be consistent with the model based on observed meridional flow patterns proposed by Portnyagin and Solovyova (1982) and illustrated in Figure (5-37), that the upper mesospheric-lower thermospheric has a multicellular circulation.

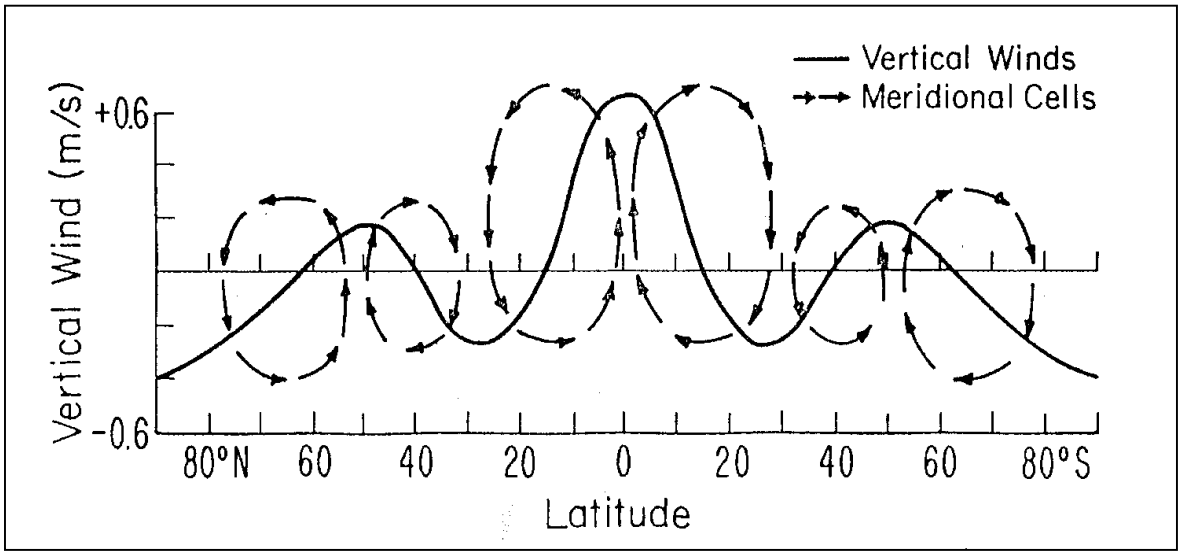

Figure (5-37) A conceptual picture of mesospheric-lower-thermospheric multicellular circulation proposed by Portnyagin and Solovyova (1982) (from Balsley and Riddle, 1984).

Inspection of this diagram indicates that at 35°S the annual mean wind is about 20 cms^{-1} downward between 80- 100 km, a result not inconsistent with our observations. We also note that a study by Ebel et al. (1983) of mesospheric heating and cooling rates due to small scale dynamical processes and eddy dissipation indicated a complex vertical circulation with downward vertical velocities at some latitudes in summer. Finally, we note that Balsley and Riddle (1984) found a downward flow in summer and an upward flow in winter at Poker Flat (65°N). Routine observation of mean vertical winds commenced at BP in November 1983 and it is hoped that this information will yield some additional insight into variations of the mean vertical wind.

5.7 Summary and Conclusions

In this Chapter we have considered some practical considerations important for DW observations made with relatively wide beamwidths. It has been shown that if the properties of the D-region and finite beamwidths are taken into account, agreement between the DW spectra and the seasonally averaged results of Vincent (1984) improves significantly. In addition, the comparison of DW and SA methods in November 1980 indicates that better agreement is found when the effective beam angle calculated from independent observations of the backscatter angular polar diagram is taken into account. Indirect comparisons of SA and DW measurements support the evidence that the DW derived radial velocities underestimate the true values of this quantity.

We have also presented some observations of vertical wind velocity made with the standard SA arrangement and a vertically directed Doppler beam which indicates mean vertical winds could be measured using the SA equipment over periods of 2-3 days. However, the variability in agreement from day to day indicates that the information about the angle of return of backscatter should be obtained. Preliminary investigations of the mean vertical wind indicate quite large magnitudes even when averaged over periods of 2-6 days, and there is some evidence that in the 80-100 km range, the motion is downward for much of the year. Longer data lengths are required before any definite conclusion can be made.

In general, it is not possible to obtain vertical mean wind from radial velocities measured in DCC beams because the horizontal variation of $\bar{u}$ and $\bar{v}$ is significant. However, with the TC(CP) beam arrangement and observations taken over a suitably long period, it may be possible to measure $\frac{\partial \bar{u}}{\partial x}$ and $\frac{\partial \bar{v}}{\partial y}$.

The importance of the character of the scattering medium for DW measurements has been emphasized, and for measurements of momentum flux using the DCC beam arrangement the variation between the apparent and effective beam angles should be taken into account. The use of Lindner's (1975b) result is considered adequate for the present work, but short term information about the backscatter angular polar diagram would increase the accuracy of the results. A need for further intercomparisons of the DW technique at BP with other methods is indicated.

6. Measurements of Momentum Flux

In this Chapter we present and discuss the measurements momentum flux obtained using the DCC beam arrangement. The majority of the results refer to the upward flux of zonal momentum, although some measurements of the upward flux of meridional momentum are presented.

The zonal and meridional body force calculated from the measured values of $\overline{u'w'}$ and $\overline{v'w'}$ and the neutral density obtained from the CIRA (1972) model are also presented. We have noted in the previous Chapter that there is very good evidence that the effective beam angle is less than apparent beam angle. However, in most cases, we have calculated the body force using both the measured values of momentum flux, and those rescaled to account for this effect. Short term variations in momentum flux, the alignment of the total body force F_T and the relative contributions of high and low frequency motions to the momentum flux are also considered.

Apart from the momentum flux measurements reported by Vincent and Reid (1983), and some measurements the momentum flux associated with coherent gravity waves presented in Smith and Fritts (1983), the mesospheric Reynolds stress results presented in this Chapter appear to be unique. However, using indirect methods, Manson et al. (1975) estimated the mean flow acceleration induced by the dissipation of a polarized gravity wave spectrum. By assuming all of the observed wave energy to be associated with a single coherent wave motion, Manson et al. (1975) estimated the mean flow acceleration in the 90-100 km. height region to be as high as $200\ m^{-2}s^{-1}day^{-1}$. Vincent and Stubbs (1977) considered the polarization of the observed mesospheric gravity wave field and obtained an estimate of $F_u \sim 10\ m^{-2}s^{-1}day^{-1}$. Smith and Fritts (1983) identified a ten-hour period oscillation and estimated a mean flow acceleration of about $25\ m^{-2}s^{-1}day^{-1}$.

These are the only estimates of the body force associated with mesospheric gravity waves of which we are aware, apart from those of Vincent and Reid (1983), although there are many theoretical studies. Vincent and Reid (1983) found a body force of $12 - 22\ m^{-2}s^{-1}day^{-1}$ between 80 and 94 km altitude in May, consistent in sign with that required to balance the Coriolis torque due to the meridional wind component. In the next Section we consider the data analysis and quality assessment procedures applied.

6.1 Data Analysis and Quality Assessment

6.1.1 Data Analysis

We have described the analysis of the radial velocity time series in Chapter 3 but we shall recapitulate briefly here.

Measurements of radial velocity were obtained at a rate of one every two minutes every two kilometres over the range of 80-100 km. Consecutive two minute determinations were averaged to give an overall sampling rate of 1 in 4 minutes at each height. A cubic splines interpolation routine was then applied to bridge small gaps in the radial velocity time for series. If there were significant gaps in the time series, they were low pass filtered to obtain the radial velocity for motions with periods longer than 8 hours, and this was substituted for the breaks in the original data, and the cubic splines interpolation routine applied again. These time series were then numerically filtered to obtain the radial velocities for those periods less than 8 hours. The mean square radial velocity was then calculated for each height and beam, and by applying Equation (4-34), the momentum flux $\overline{u'w'}$ was obtained.

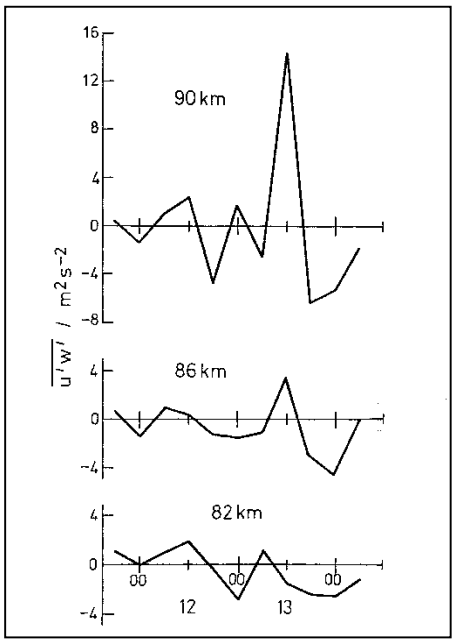

Figure (6-1a) Times series of the upward flux of zonal momentum for three representative heights for data obtained in May 1981 (After Vincent and Reid, 1983)

The mean square radial velocity could be obtained for the entire period of the observation, or for any suitably long period of time. To obtain the average momentum flux for a period sufficiently long to enable the mean local wind, and hence the Coriolis torque due to the mean

meridional wind to be obtained, we have attempted to calculate the momentum flux for all of the data in each period of observation. Because the data were not always continuous in time and height, the quality of the data were assessed. This is discussed in the next Section.

6.1.2 Data Quality

In Chapter 3 we presented representative data acceptance rates for DW observations obtained various months. It will be recalled that in some months, notably February and October, low data acceptance rates were obtained in the lowest and highest height ranges. For a valid measure of $\overline{u'w'}$ to be obtained at each height, for a given period of observation, the data acceptance rates must be similar. u'w' is also quite variable in time (Vincent and Reid, 1983) and this means that there are breaks in the time series, then they must occur over the same period at each height, if intercomparison of $\overline{u'w'}$ between deferent heights is to be valid. This is particularly important because the calculation of $\overline{u'w'}$ requires differencing two like quantities, and the calculation of the body force F_u in turn requires the differentiation of $\rho\overline{u'w'}$. Without careful data assessment, very large errors could result.

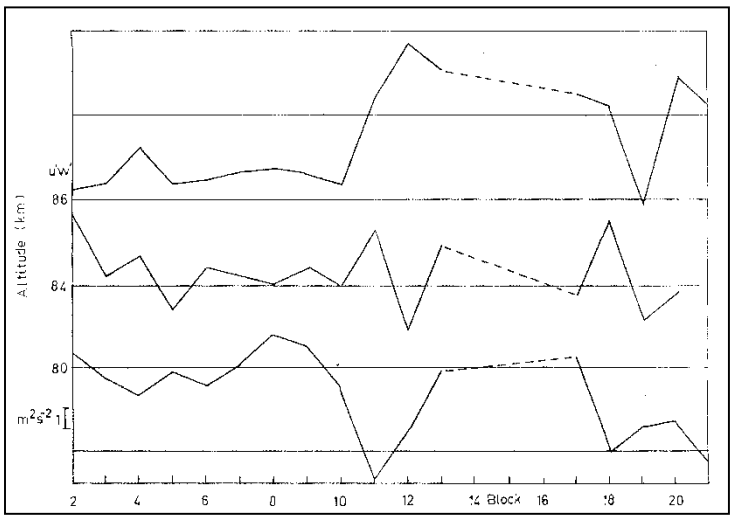

Figure (6-1b) As for Figure (6-1a) but for November 1981

To obtain a measure of the data quality, the radial velocity time series were plotted and examined by eye to check for differences between heights in terms of accepted records. An example taken from the February 1982 data set is shown in Figure (6.2). This diagram shows the high pass ($HP;\ T < 8\ hours$) filtered radial velocity time series for a beam directed at 11.6° Eastwards from the zenith. Calculation of -for 78-82 km is not likely to provide a representative measure of the average value of this quantity for the entire period of observation.

This is evident when we note the enhancement in radial velocity around midnight on the 17th at 84 and 86 km.

Another consideration in data quality assessment was that the interpolation routine did not cope very well with the combination of low data acceptance rates (~30%) and widely spaced data, and tended to introduce spurious, although small oscillations. The plots of the time series were examined very carefully for evidence of this, and data for these heights were rejected if this was the case, although these heights would have been rejected for low data acceptances in any case. Because there is some subjectivity in this quality assessment and this affects the calculation of the body force, we present in Section (6.3) the momentum flux calculated at each height for all heights, regardless of the data acceptance rates. However, we are confident that the removal of non-representative data at various heights is valid.

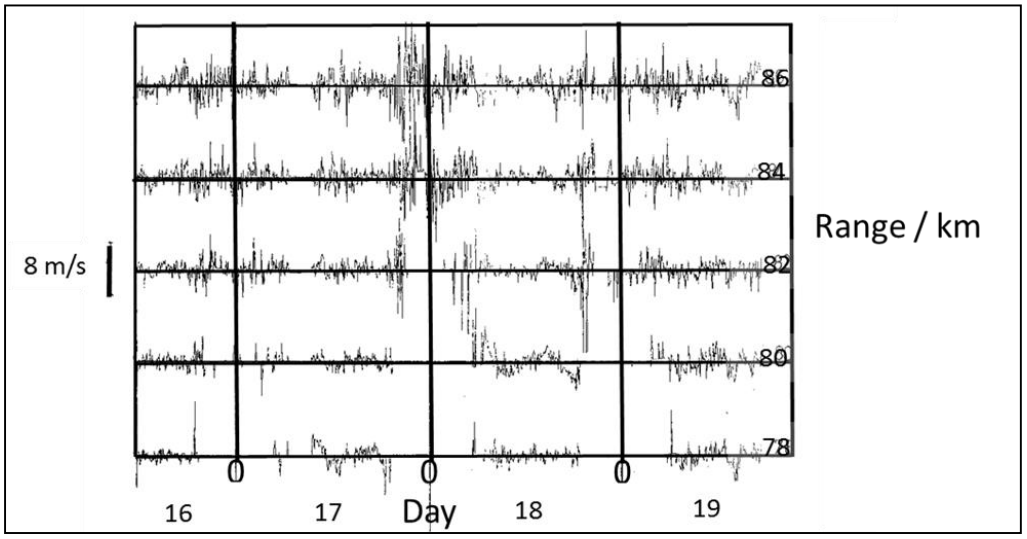

Figure (6-2) Time series of radial velocities for motions with periods less than 8 hours for 16-19 Feb 1982.

In this Chapter we also present the momentum flux obtained from observations in July 1982. Figure (6-3a, b) illustrates the high pass radial velocity for the four beams for the 9-12th of this month. Inspection of these diagrams indicates that around 1800 LT on each day (the time of the evening polarization change) the character of the time series often changed. However, removing these Sections of the data before calculating the momentum flux did not change the results significantly, and we have chosen to analyse these data as they are, but the possibility of errors must be borne in mind.

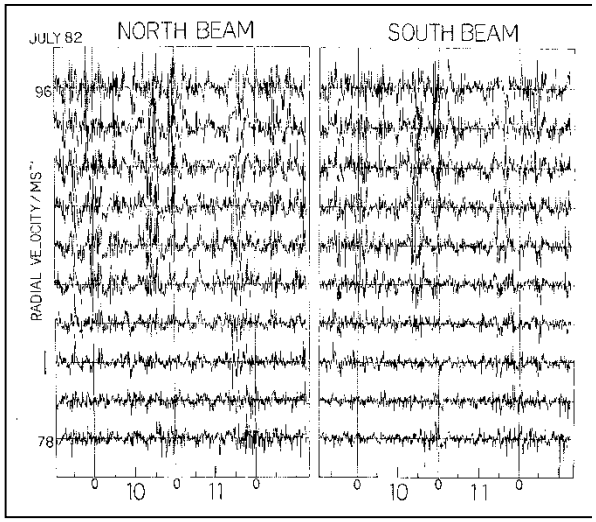

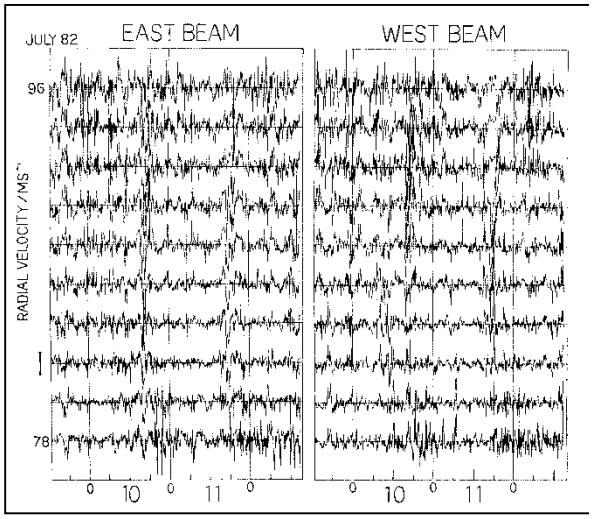

Figure (6-3a) (left) and Figure (6-3b) (right) Radial velocity time series for motions with periods less than 8 hours for 9-12 July 1982. The vertical bar represents 8 ms^{-1}

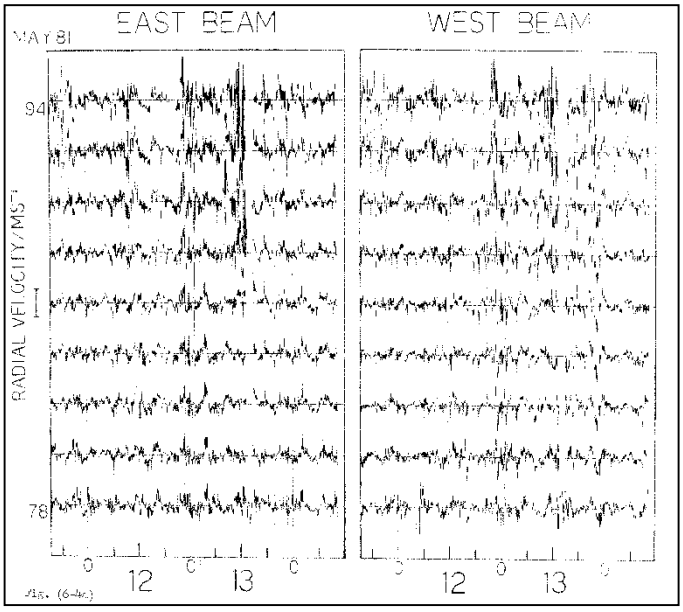

Figure (6-4a) As for Figure (6-3) but for 11-14 May 1981

Figure (6-4a) shows a similar time series for May 1981, and Figure (6-4b) shows an expanded Section of the same data set. This last diagram clearly shows the presence of an oscillation with a period of about one hour. Such clear examples of coherent motion occurred relatively rarely, and effort was directed at obtaining information of a statistical nature. Consequently, there may be other examples of this type of motion our observations which could be usefully exploited as case studies, but the volume of data precludes this in the present work. Inspection of Figure (6-4a) indicates similar behaviour in both beams and we note the enhancement in both beams on the 13th.

We recall that the major assumption made in the derivation of the Equation for the momentum flux for the DCC beam arrangement was the homogeneity of the statistics of motion in a horizontal plane, and this type of diagram is quite useful for a qualitative examination of the similarity of radial velocity time series. However, a quantitative measure of similarity is more appropriate, and to test the validity of this assumption, power spectra were calculated for each beam and height for the May 1981 and November 1981 data sets.

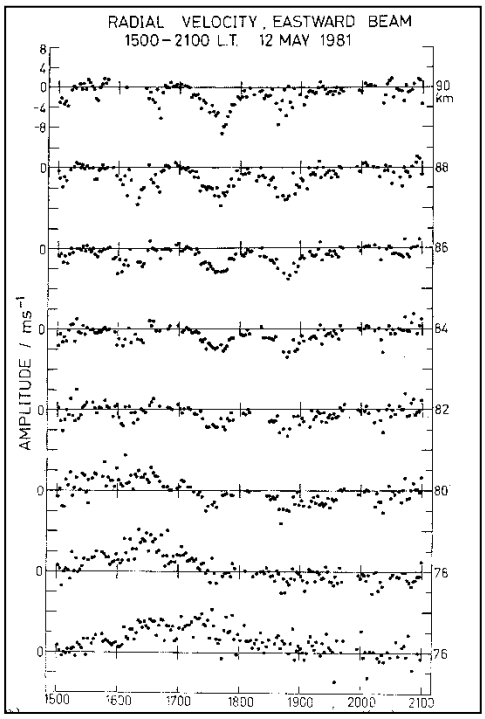

Figure (6-4b) Expanded section of the time series shown in Figure (6-4a) (After Vincent and Reid, 1983)

To measure the momentum flux there must obviously be differences between the power spectra for the DCC beams. However, the relative magnitudes of $\overline{u'^2}$, $\overline{w'^2}$ and $\overline{u'w'}$ indicate that the mean slope of the spectra should be the same for a fixed zenith angle and height, regardless of the azimuth angle at which the radar beam is directed. This appears to be an appropriate test of the homogeneity of the statistics of the motions measured. An example of power spectra for a range of heights, and Westward and Eastward beams, for the May 1981 data set (Figure 6-4a) is shown in Figure (6-5). Agreement between heights, and more importantly, between beams is good. The spectral slope, calculated by fitting a function of the form $S_0 f^{-k}$ to $S(f)$, the power spectrum, indicated no significant differences between beams for each height (Figure 6-6a). This was also true of the November 1981 data (Figure 6-6b). Power spectra were also calculated for each six-hour period of the time series for May 1981 for each beam, and again,

no significant differences between beams were found. Similar results were found for selected heights in other months, and the results for May 1981 and November 1981 appear to be typical. Consequently, the assumption of the homogeneity of the motions appears valid when statistics are averaged over periods at least as short as six hours.

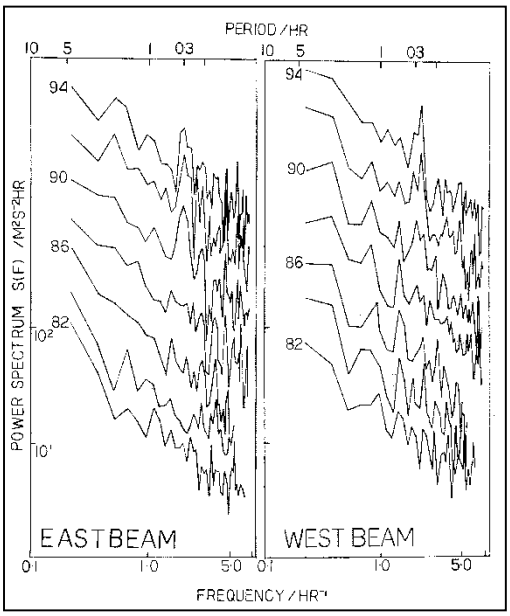

Figure (6-5) Power spectra for a range of heights for eastward and westward beams for time series shown in Figure (6-4a).

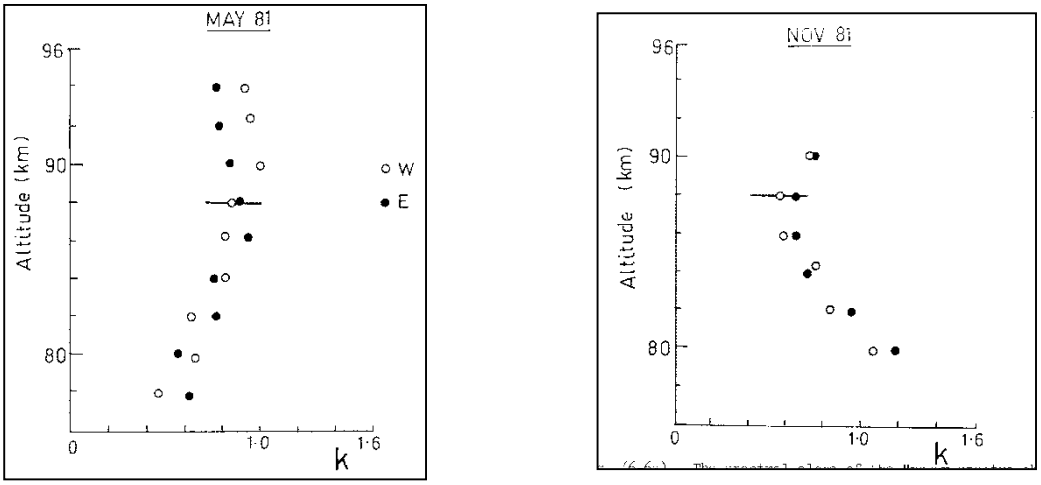

Figure (6-6a) (left) The spectral slope of the power spectra shown in Figure (6-5), and Figure (6-6b) (right) As for Figure (6-6a) but for November 1981.

6.2 Summary of Momentum Flux Measurements

Figure (6-7) summarizes the measurements of the Reynolds stress term $\overline{u'w'}$ for motions with periods less than 8 hours for the various observational periods for this work. The results are

divided into seasons, and the values considered unrepresentative because of the low data acceptance rates are indicated with a small arrow. The error bars represent the error calculated from the uncertainty in $\overline{V_R'^2}$ determined in Chapter 2.

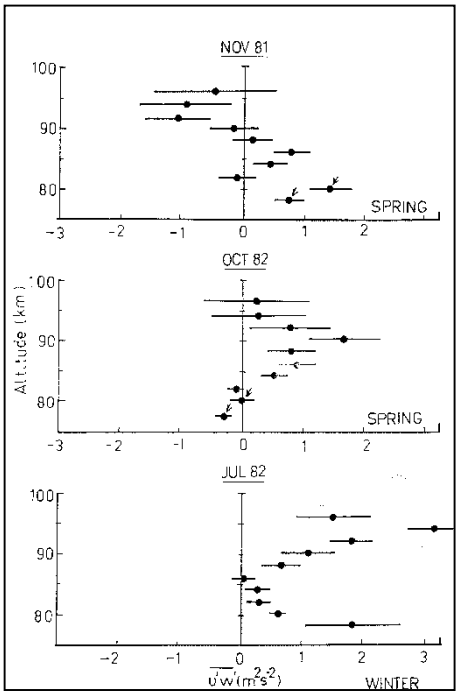

Figure (6-7a, b and c) Reynolds stress $\overline{u'w'}$ for motion with periods shorter than 8 hours for various periods of observation

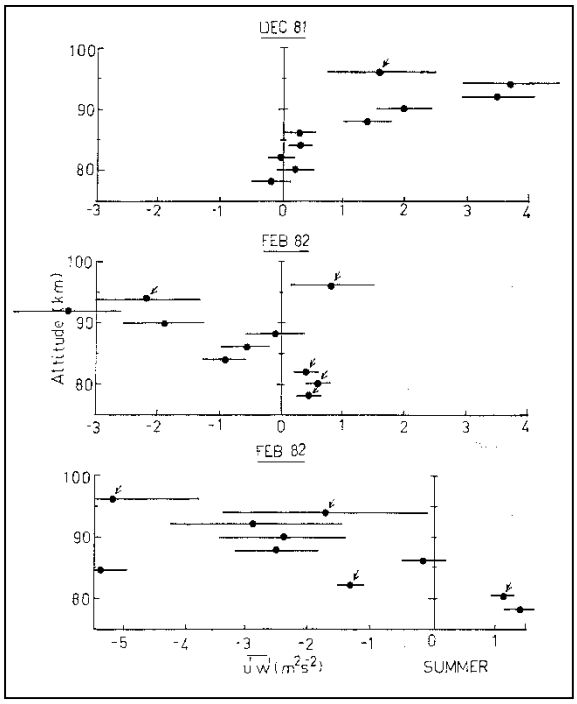

Figure (6-7d, e and f) as for Figures (6-7a, b and c)

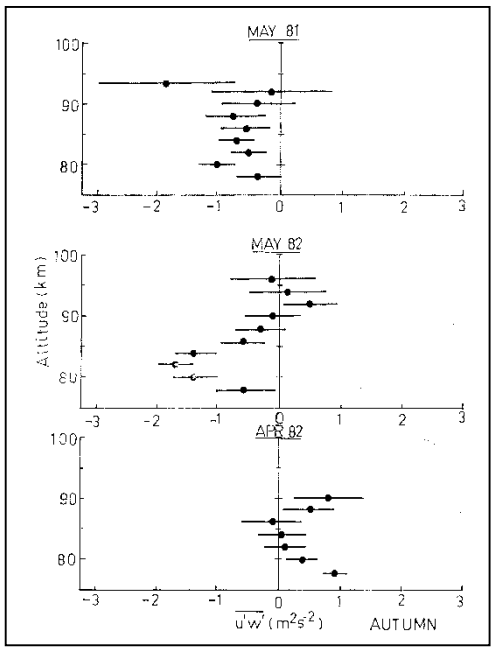

Figure (6-7g, h and i) as for Figures (6-7a, b and c)

These results have not been treated in any way, and represent the "raw" momentum flux values obtained from the difference of the mean square radial velocities measured in Eastward and Westward radar beams. Inspection of these diagrams indicates considerable variation in $\overline{u'w'}$ between periods of observation, and in height for any period of observation. When the unrepresentative values of $\overline{u'w'}$ are omitted from these height profiles, $\overline{u'w'}$ often appears to vary quite smoothly from height to height. The largest values of $\overline{u'w'}$ occur the summer and winter months, but in general the magnitude of the momentum flux is less than 3 $m^2\ s^{-2}$. Figure (6-8) summarizes the values of the Reynolds stress term $\overline{v'w'}$ for three periods of observation. We have also included the value of $\overline{u'w'}$ measured over the same period as that for $\overline{v'w'}$ for July 1982. The accepted values of $\overline{v'w'}$ for February show considerable variation with height, and we note that they are larger than the values of $\overline{u'w'}$ for the same period.

The results for July exhibit little variation in height, in contrast to the corresponding values of $\overline{u'w'}$, while the values of $\overline{v'w'}$ obtained in October are rather small, and generally little different from zero. Figure (6-9) illustrates the height profiles of $\rho\overline{u'w'}$ for the values of $\overline{u'w'}$ shown in Figure (6-7). The neutral air density ρ has been obtained from the CIRA (1972) model. The product of the neutral air density and momentum flux is observed to vary with height, indicating that there is a body force F_u associated with the motion of periods less than 8 hours.

Diagrams the $\rho\overline{v'w'}$ term (Figure 6-8) show a similar variation with height, indicating that there is also a meridional body force. However, before calculating the body force we need to consider other sources of error in these measurements. One possible error we have not yet considered is that due to the alignment of the array.

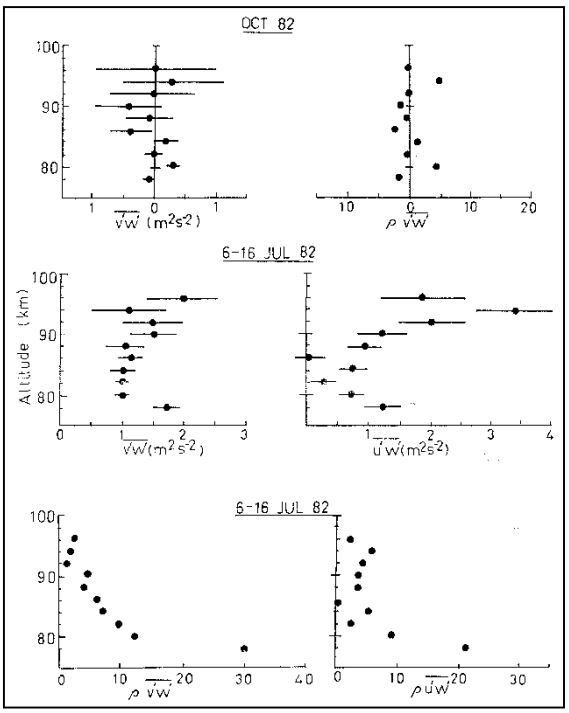

Figure (6-8) As for Figure (6-7) but for the $\overline{v'w'}$ term. Also shown are the values of the product of this term with the neutral air density. Units of $\rho\overline{u'w'}$ and $\rho\overline{v'w'}$ are $kgm^2\ s^{-2}\ \times\ 10^6$

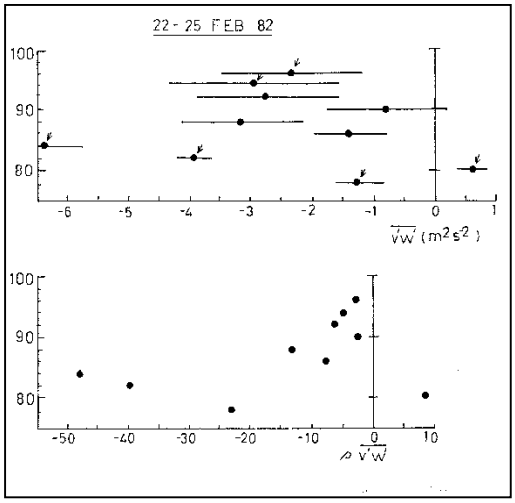

Figure (6-8) continued

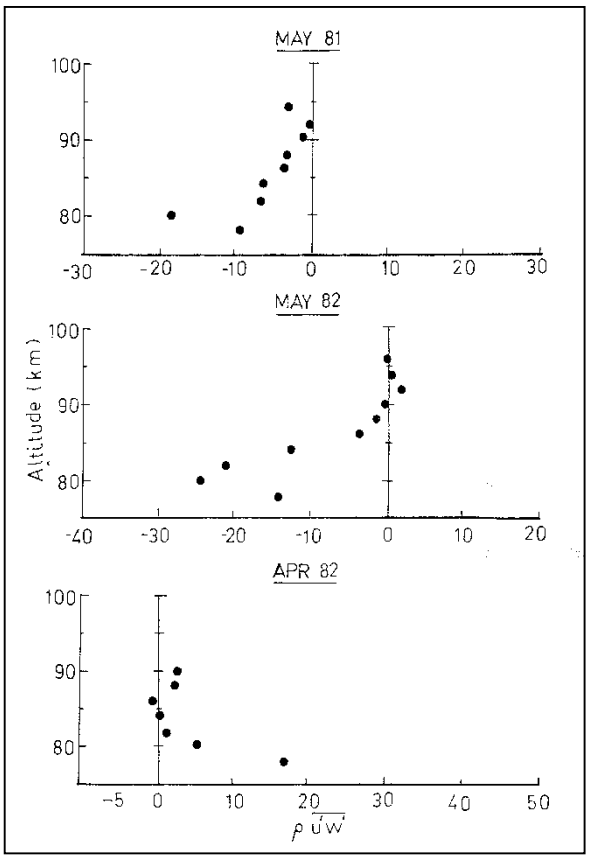

Figure (6-9) Height profiles of $\rho\overline{u'w'}$ for various periods of observation.

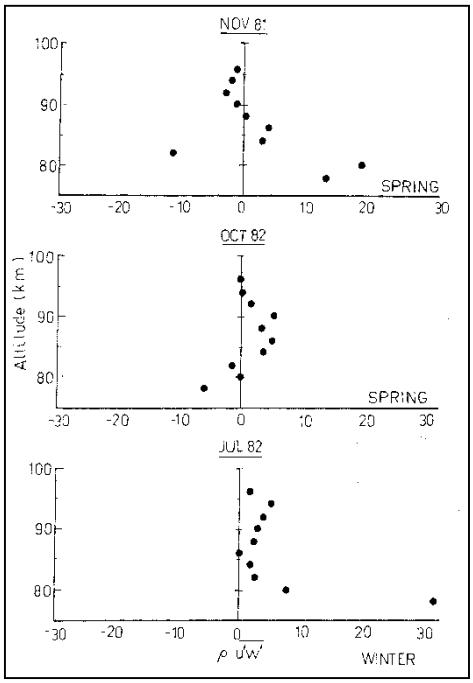

Figure (6-9) continued

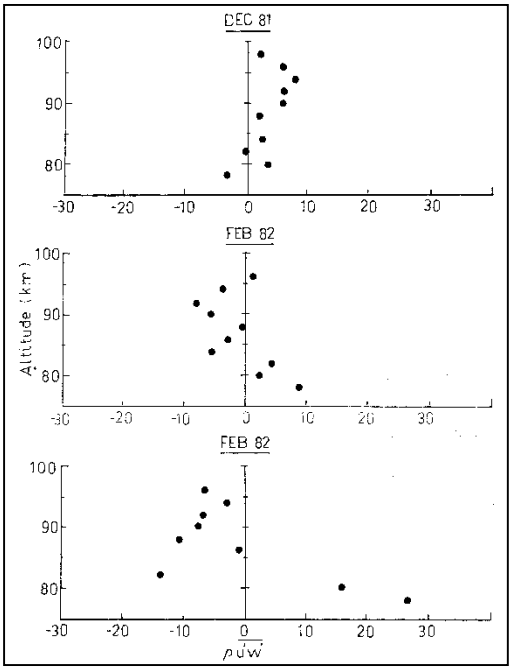

Figure (6-9) continued

6.3 Correction for the Alignment of the Array and the Effective Beam Angle

In Chapter 2 we noted that the MF array at BP is aligned so that the NS axis is 4° West of North. Consequently, measurements of the Reynolds stress term $\overline{u'w'}$ made with the EW pair of beams will include a contribution from $\overline{v'w'}$. Since most observations did not include both of these terms, this component is unresolved and it is of some interest to consider the importance of this.

If we consider the beams nominally aligned Eastward and Westward, then $\phi = 86° \; and \; 266°$ respectively. With $\theta = 11.6°$ and

$$\overline{V_E'^2} = \overline{V_R'^2}(86)$$

$$\overline{V_W'^2} = \overline{V_R'^2}(266) \tag{6-1}$$

and substituting these into Equation (4-4) we obtain after some rearranging

$$\delta\overline{V_{EW}'^2} = \frac{\overline{V_E'^2} - \overline{V_W'^2}}{2sin2\theta} = \overline{u'w'} + (0.07)\overline{v'w'} \tag{6-2}$$

and

$$\overline{V_{EW}'^2} = \frac{\overline{V_E'^2} + \overline{V_W'^2}}{2sin2\theta} = \overline{u'^2} + +(0.005)\overline{v'^2} + \overline{w'^2}cot^2\theta + (0.14)\overline{u'v'} \tag{6-3}$$

The corresponding relations for

$$\overline{V_N'^2} = \overline{V_R'^2}(356)$$

$$\overline{V_S'^2} = \overline{V_R'^2}(176) \tag{6-4}$$

Are

$$\delta\overline{V_{NS}'^2} = \frac{\overline{V_N'^2} - \overline{V_S'^2}}{2sin2\theta} = \overline{v'w'} + (0.07)\overline{u'w'} \tag{6-5}$$

and

$$\overline{V_{NS}'^2} = \frac{\overline{V_N'^2} + \overline{V_S'^2}}{2sin2\theta} = \overline{v'^2} + (0.005)\overline{u'^2} + \overline{w'^2}cot^2\theta - (0.14)\overline{u'v'} \tag{6-6}$$

We note in passing that the sum of Equations (6-3) and (6-6) is not significantly different from Equation (4-73) and that it may be possible to measure the covariance $\overline{u'v'}$ using the mean radial velocities if five beams are used.

The values of $\delta\overline{V_{EW}'^2}$ and $\delta\overline{V_{NS}'^2}$ are typically of the same magnitude, as we have noted in Section (6.3), and consequently the error involved in neglecting the meridional contribution will be rather small, since

$$\overline{v'w'} = \delta\overline{V_{NS}'^2} + (0.07)\delta\overline{V_{EW}'^2} \tag{6-7}$$

$$\overline{u'w'} = \delta\overline{V_{EW}'^2} - (0.07)\delta\overline{V_{NS}'^2} \tag{6-8}$$

Figure (6-11a, b) illustrates values of $\overline{u'w'}$ and $\overline{v'w'}$ corrected for alignment of the alignment of the array, and uncorrected values $\delta\overline{V_{EW}'^2}$ and $\delta\overline{V_{NS}'^2}$ for the 6-9th of July 1982. Also shown are the products of these quantities with the neutral air density ρ. Values plotted have not been smoothed in any way, and represent the values obtained before any correction for motions in the beam pointing direction have been taken into account. The error bars represent the

uncertainty calculated from the results obtained in Chapter 2. It is clear that the correction for the alignment of the array is less than the uncertainty due to that in the mean square radial velocity.

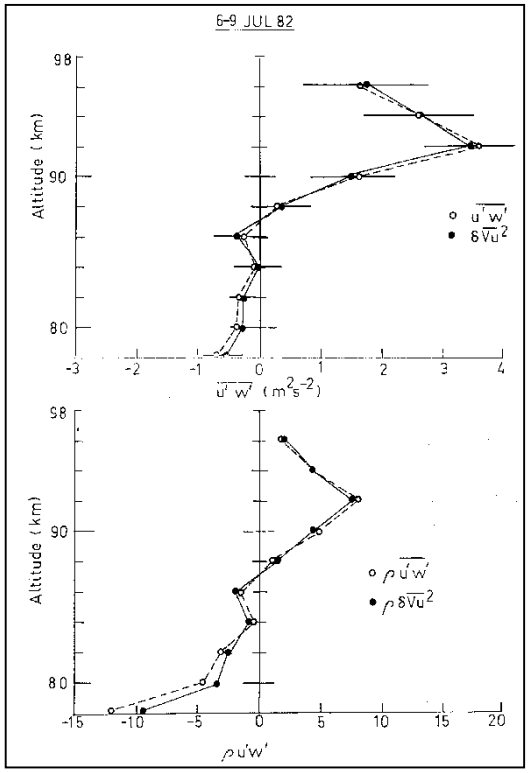

Figure (6-11a) Height profiles of upward flux of zonal momentum before correction for alignment of array is applied $\delta\overline{V_{EW}^2}$ *and after this correct1on has been applied* ($\overline{u'w'}$). *Also shown are height profiles of* $\rho\delta\overline{V_{EW}^2}$ *and* $\rho\overline{u'w'}$.

These results are typical for other observational periods, and consequently, the error in $\overline{u'w'}$ due to the alignment of the array is not significant, and the general features of the height profiles $\overline{u'w'}$ are consistent, so that the momentum flux measurements obtained in se months can be accepted. Figure (6-12a) illustrates the height profile for $\rho\overline{u'w'}$ shown in Figure (6-11a) after the corrections difference between the effective and apparent beam directions are taken into account. The heights have been corrected according to the values shown in Table (5-1) and the magnitudes of $\overline{u'w'}$' rescaled according to the value of ratio of $\overline{u'w'}/\overline{u'w'^*}$ shown in Figure (5-5).

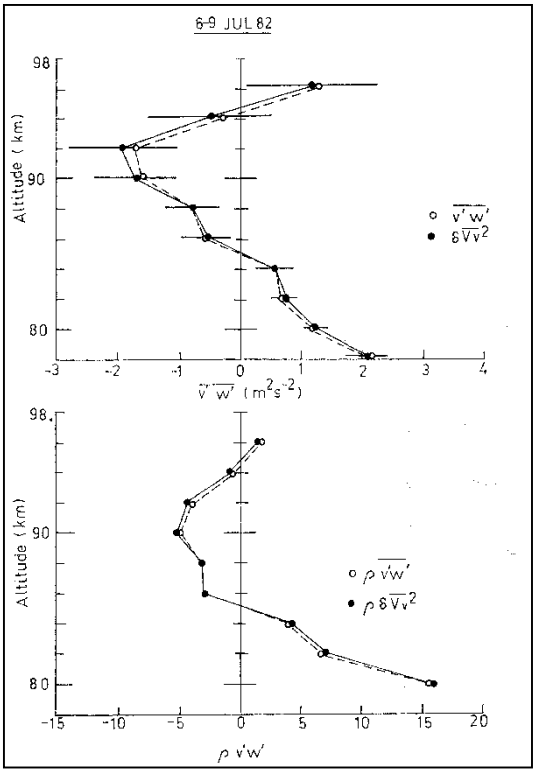

Figure (6-11b) As for Figure (6-11a) but for the upward flux of meridional momentum.

The horizontal bars on this diagram represent the error in $\rho\overline{u'w'}$ calculated from the systematic and random errors in $\overline{V'^2}$ obtained in Chapter 2. The vertical bars represent the uncertainty in height due to the effective beam angle. Inspection of this diagram indicates the essential features are unchanged from those of Figure (6-11a). The height profile of $\rho\overline{v'w'}$ treated in the same way as that for $\rho\overline{u'w'}$ is shown in Figure (6-12b). The error bars have the same meaning as those shown in Figure (6-12a). Some of the variation of the height profile of $\rho\overline{u'w'}$ and $\rho\overline{v'w'}$ can be accounted for by the uncertainty the height and mean square radial velocities. We note similarity in form in the height profiles of $\rho\overline{v'w'}$ and $\rho\overline{u'w'}$ when the errors are taken into account. The errors themselves are clearly substantial, but most values are significant.

Differentiation of these height profiles to obtain the body force will involve considerable uncertainty. The form of fitting applied to the height profiles of $\rho\overline{u'w'}$ and $\rho\overline{v'w'}$ to smooth the data and obtain an analytical expression for and F_v is considered in the next Section.

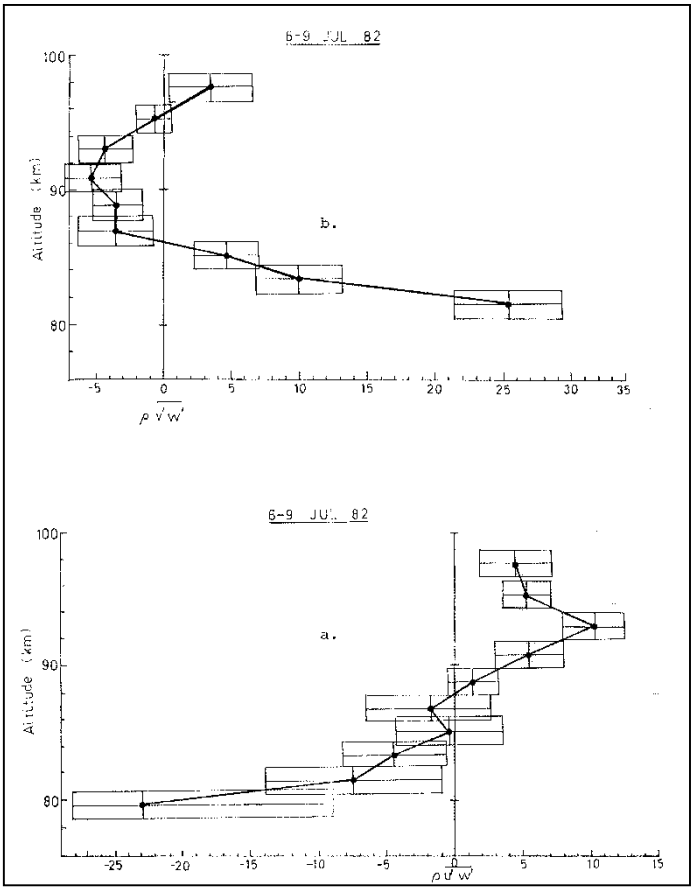

Figure (6-12a) Height profile of $\rho\overline{u'w'}$ shown in Figure (6-11a) after correction for effective beam angle has been applied. Figure (6-12b) As for Figure (6-12a) but for $\rho\overline{v'w'}$.

6.4 Calculation of the Body Force

Vincent and Reid (1983) fitted functions of the form $ae^{-z/h}$ where z is the height, h is the scale height of $\rho\overline{V'^2}$ and a is a constant, to the individual height profiles of $\rho\overline{V_E'^2}$ and $\rho\overline{V_W'^2}$. The values of $\rho\overline{V_E^2}$ and $\rho\overline{V_W^2}$ for data obtained in May 1982 are shown in Figure (6-13). These values of mean square radial velocity have not been smoothed in any way, and no corrections for the effective beam angle have been applied. A reasonable fit in this case would appear to be to the values of $\rho\overline{V'^2}$ in the range of 82-90 km.

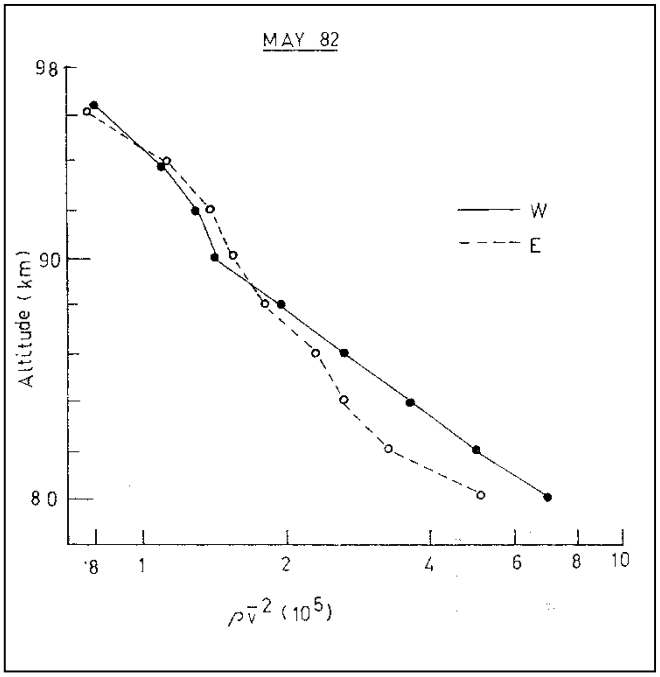

Figure (6-13) Height profiles of the product of mean square radial velocity for motions with periods less than 8 hours with neutral air density for westward (W) and eastward (E) beams.

Since

$$\rho\overline{u'w'} = \rho\frac{(\overline{V_E'^2} - \overline{V_W'^2})}{2sin2\theta} \tag{6-9}$$

the net acceleration per unit mass given by the flux convergence as

$$F_u = -\frac{1}{\rho}\frac{\partial}{\partial z}(\rho\overline{u'w'}) \tag{6-10}$$

becomes

$$F_u = -\frac{1}{\rho k}\frac{\partial}{\partial z}\rho(\overline{V_E'^2} - \overline{V_W'^2}) \tag{6-11}$$

where $k = 2sin2\theta$

Substituting the fitted function $ae^{-z/h}$ for $\rho\overline{V^2}$ this becomes

$$F_u = \frac{1}{k}(\frac{\overline{V_E'^2}}{h_E} - \frac{\overline{V_W'^2}}{h_W}) \tag{6-12}$$

The results of this calculation are shown in Figure (6-14), along with the error calculated from the standard error in value of h obtained in the fit and the errors in $\overline{V'^2}$ discussed in Chapter 2. The body force F_u is clearly substantial, but there is considerable uncertainty in the obtained values. The smoothed values of $\overline{u'w'}$ are shown as dots in Figure (6-14) along with the raw values of $\overline{u'w'}$ shown as crosses, and agreement is good.

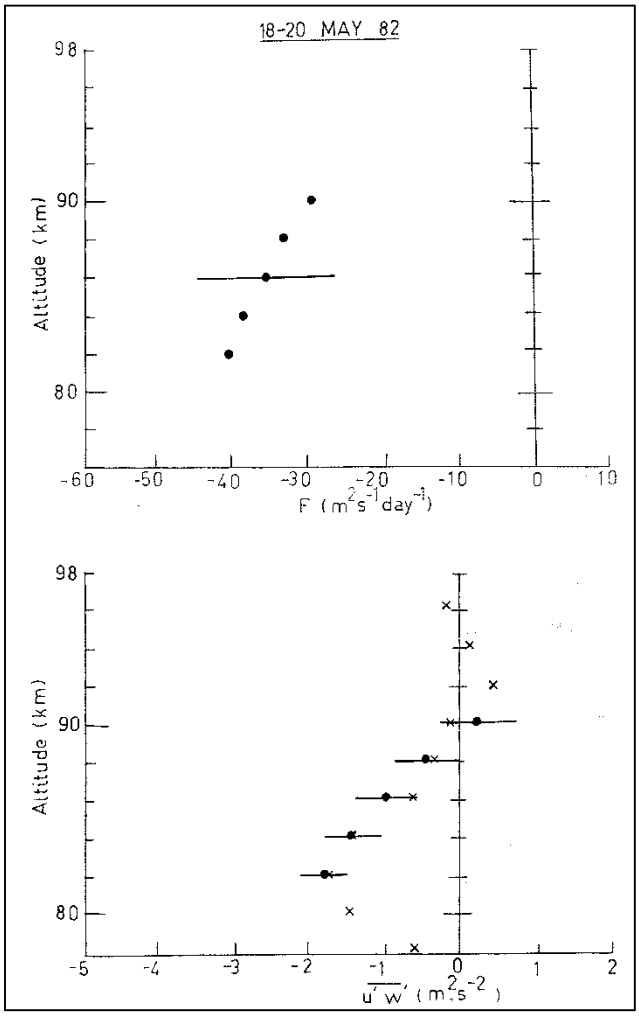

Figure (6-14) The zonal body force F_u calculated from values of $\rho\overline{V'^2}$ shown in Figure (6-13). Also shown are the "raw" values of $\overline{u'w'}$ and the corresponding smoothed values (dots)

The advantage of this type of fitting is that information about the scale height h is obtained, and erroneous values $\rho\overline{V'^2}$ may be detected quite easily if the height profile of $\rho\overline{V'^2}$ is well formed. The disadvantage is that the choice of heights to fit is subjective, and some cases, it may not be possible to select a suitable fit. There are also discontinuities at the end points of each fitting range, and in the case of the May 1982 data, choice of fits to the values of $\rho\overline{V'^2}$ for

the range of 80-82 km. and heights above 90 km. may produce errors if these values are considered separately from the rest of the data.

An alternate form of fitting is that of a polynomial fit to $\rho\overline{u'w'}(z)$. With an optimal fitting routine, no subjective judgement is involved, although this does not necessarily make the fit superior, and problems with discontinuities in the slope are avoided. It has the advantage that all of the data points are used in a single fit, but the disadvantage that anomalous values of $\rho\overline{V_E'^2}$ and $\rho\overline{V_W'^2}$ are not evident (but odd values of $\rho\overline{u'w'}$ may be), and no information about the height scale is obtained. There may also be uncertainty in the end points of the fit.

We have applied both types of fits to all of our results, and have generally found good agreement, although the advantages and disadvantages noted above were quite evident. In most data sets the type of fit does not affect the general conclusions, and in any case the sign of F_u is evident by inspection of the height profiles of $\rho\overline{u'w'}$. We have also calculated the zonal body force with both "raw" values of $\rho\overline{V'^2}$ and $\rho\overline{u'w'}$, and values corrected for the effective beam direction. The only variation evident is in the magnitudes of the body force, and not its sign.

6.5 Mean Meridional Winds and the Coriolis Torque

We have summarized the mean winds for each data run in which measurements of momentum flux were made in Chapter 5, but it is also instructive to consider the mean wind obtained over longer periods. There are difficulties in using the Groves (1969) and CIRA (1972) global circulation models because of their bias towards Northern hemisphere observations. Differences between Southern hemisphere observations and these models have been noted by Smith (1983) and Vincent (l984b).

Fortunately, a long sequence of observations is available at Adelaide. These include meteor radar observations dating from the 1960's and D-region SA observations covering the years since about 1973. Figure (6-15a, b) illustrate the monthly mean SA winds for a number of heights for the period 1978-1983. (Vincent, private communication). These results are particularly useful, because they provide a direct measure of the mean wind at Adelaide, and the associated standard deviations give some indication of inter-annual variations.

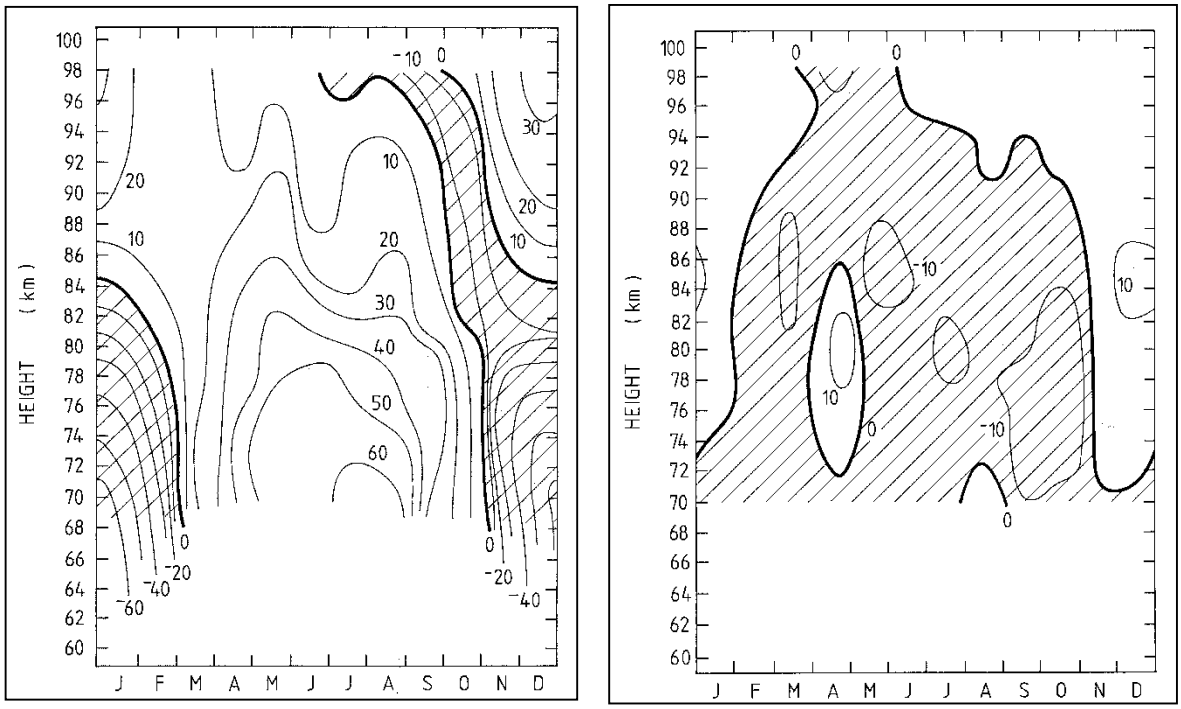

Figure (6-15a) (left) Five-year average of SA mean zonal winds. for Adelaide (35°S), and Figure (6-15b) (right) the corresponding meridional winds

As discussed in Chapter l, any zonal drag must be balanced by a torque due to the meridional component when these quantities are zonally averaged. We have found it convenient to work in units of $m^2 s^{-1} day^{-1}$ and at Adelaide (35°S), the Coriolis torque in these units may be obtained by multiplying the mean meridional wind by (7.2) and taking account of the sign.

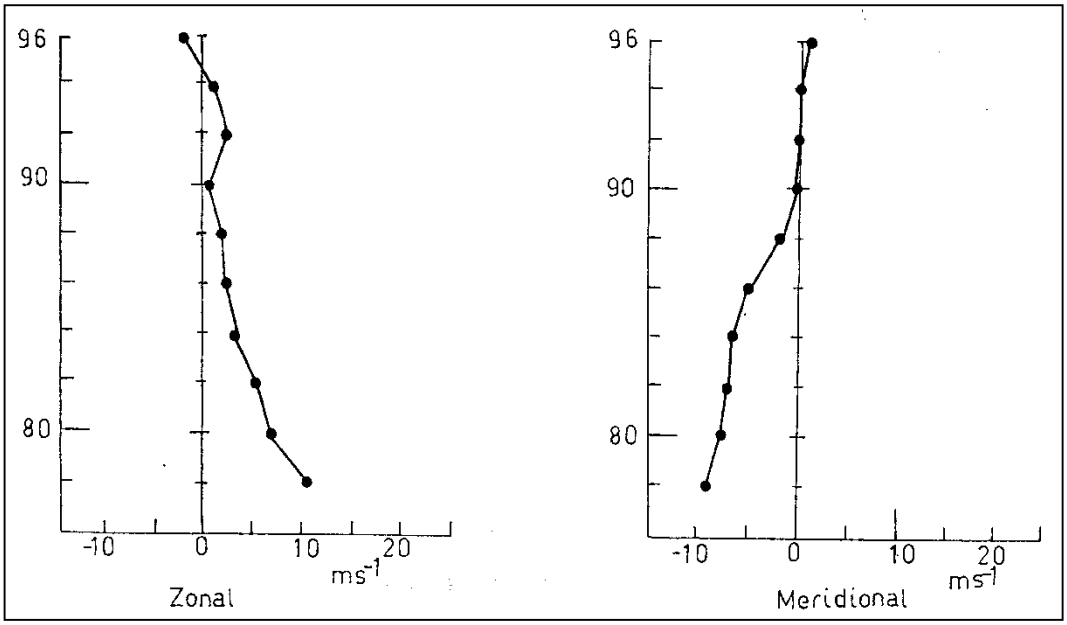

Figure (6-16) unscaled values of the mean wind for the 6-9th July 1982

6.6 The Zonal Body Force and the Meridional Coriolis Torque

In this Section we present the rescaled values of $\rho\overline{u'w'}$ for each period of observation, and the zonal body force calculated from both the measured values of $\overline{u'w'}$ and those corrected for the effective beam direction. The results have been divided into seasons, and first we consider the Winter results.

6.6.1 Winter: July 1982 (30th June-16th July)

The values of $\rho\overline{u'w'}$ for the 6-9th July 1982 are shown in Figure (6-12a). A 3rd order polynomial fit to this height profile produces the results for the zonal body force shown in Table (6-1). We may obtain the Coriolis torque due to the meridional mean wind from either the mean winds for the 6-9th July 1982, or from the results shown in Figure (6-15b). The mean winds for the 6-9th obtained from harmonic analysis are shown in Figure (6-16). These results have not been rescaled, and we note that the meridional component is in good agreement with the expected circulation for this month, while the zonal component is very much smaller.

Table (6-1) the zonal body force calculated from a 3rd order polynomial fit to the height profile shown in in Figure (6-12a).

Altitude (km)	$F_u\ (m^{-2}s^{-1}day^{-1})$
80	-32
82	-33
83	-32
85	-30
87	-26
89	-20
91	-12
93	-2
95	+5
98	-2

This observational period showed strong evidence of planetary wave activity, and this may account for the better agreement between the meridional component and the expected circulation. Figure (6-17a, b) illustrates the daily mean values for July 1982 obtained from harmonic analysis, and we note the 5-6-day period variation in velocity most evident at heights below 90 km. Inspection of days 6-9 indicates that the meridional wind velocities are in the

most Westward part of the cycle. We have rescaled the mean meridional wind illustrated in Figure (6-16) according to the results in Chapter 5 and plotted this and the mean SA profile from Figure (6-15b) ln Figure (6-18). Taking the planetary wave activity into account, agreement is excellent.

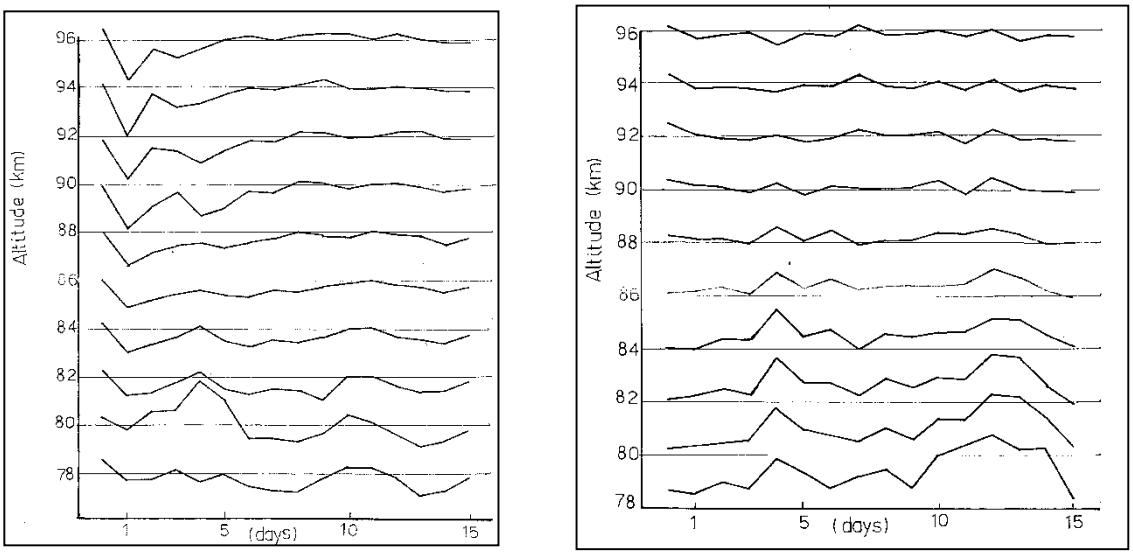

Figure (6-17a) (left) Daily values of the mean meridional wind obtained from harmonic analysis, and Figure (6-17b) (right) As for Figure (6-17a) but for the zonal wind component

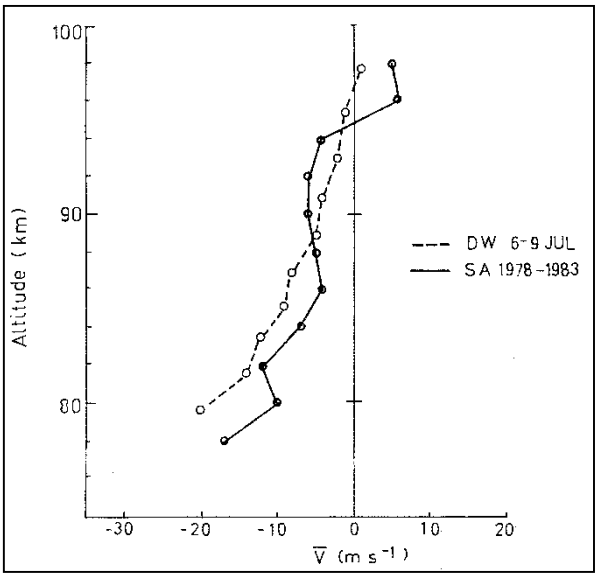

Figure (6-18) Meridional wind component shown in Figure (6-16) after the correction for effective beam angle has been applied. Also shown is the mean SA wind obtained from Figure (6-15b).

The meridional Coriolis torque a^* calculated from the rescaled DW values for the 6-9th July, the mean SA results for July and the results from Groves (1969) is shown in Figure (6-19)

along with the values F_u from Table (6-1). For the purposes of comparison, Coriolis torque has been reversed sign.

The error bars on values of $-a^*$ the 6-9th July have been calculated from the uncertainty in the mean radial velocity estimated in Chapter 2. Those for the values of F_u at 80 and 9l km. have been estimated by calculating upper and lower limits for the fit to the values of $\rho\overline{u'w'}$, which is a somewhat crude, but probably sufficient measure. The error bar on the value of $-a^*$ obtained from the mean SA results represents the standard deviation in $\bar{v}$, and provides a measure of the inter- annual variability in this quantity. Inspection of this diagram indicates agreement between F_u and the values of $-a^*$ for the mean SA results within the error of the calculation, while the values of $-a^*$for the 6-9th July and F_u are in general agreement. The values of $-a^*$ calculated from the results of Groves (1969) are noted to be somewhat larger than the other quantities in the diagram, except at 80 km., and for the remainder of the Chapter we will omit the results obtained from this model.

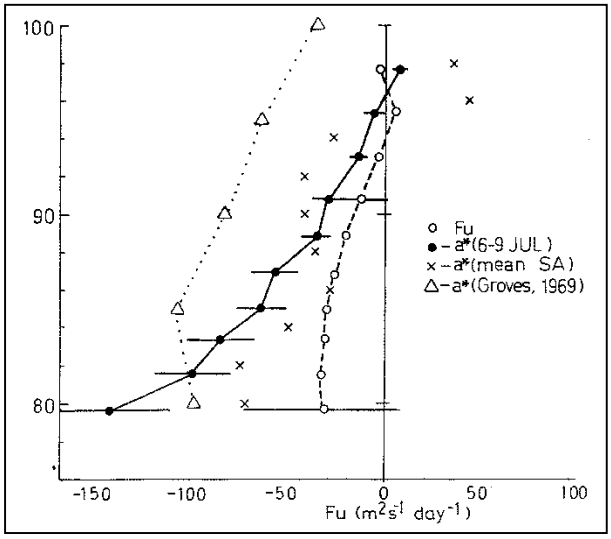

Figure (6-19) The zonal wave drag F_u calculated from the rescaled values of $\rho\overline{u'w'}$. For details see text.

The rescaled values of F_u are easily able to provide the necessary torque to balance the meridional flow in the SA average case, but below about 84 km., there is a significant difference between F_u and $-a^*$ due to the local mean meridional wind. The values of F_u calculated from the unscaled data by applying a fit of form $ae^{-z/h}$ to the individual height profiles of $\rho\overline{V_E'^2}$ and $\rho\overline{V_W'^2}$ are shown in Figure (6-20). The fit was made to the values in two separate height ranges, 80-88 and 88-92 km., and the error bars were calculated as for the May 1982 data.

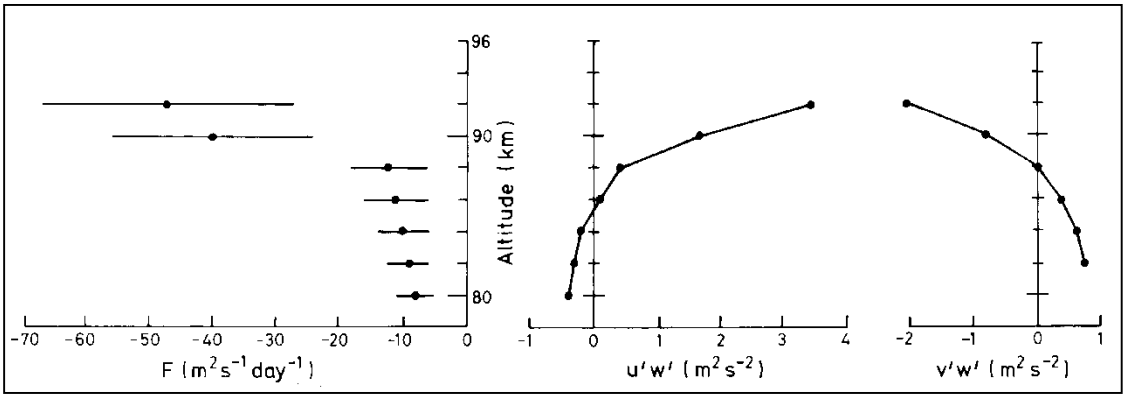

Figure (6-20) The values of F_u calculated from the unscaled data by applying a fit of form $ae^{-z/h}$ to the individual height profiles of $\rho\overline{V_E'^2}$ and $\rho\overline{V_W'^2}$

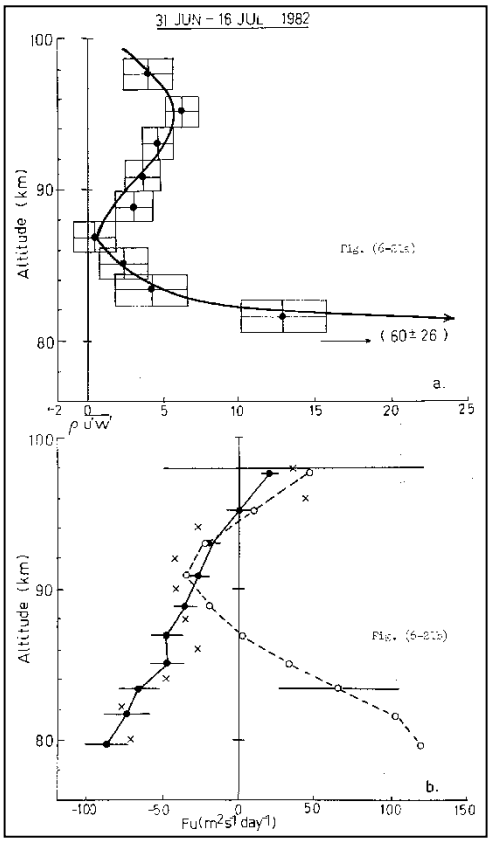

Figure (6-21a) (top) The rescaled values of $\rho\overline{u'w'}$ for the 16-day period of 3is[t] June- 16[th] July 1982, and Figure (6-21b) (bottom) The values of F_u calculated from this height profile by fitting a cubic. Also shown are the average SA value of $-a^*$, and the value of $-a^*$ calculated from the rescaled value of $\bar{v}$ for the 16 days.

These results agree with those obtained from the rescaled data to within the calculated error, but exhibit a rather more complex height profile. This is because of the limited height range of values to which the fit was made. An unweighted fit to the rescaled values of $\rho\overline{u'w'}$ using a

polynomial of order 5 agrees very well in form with the values shown in Figure (6-20). Our choice of a cubic fit to the rescaled values of $\rho\overline{u'w'}$ was made taking the uncertainty in the individual values of $\rho\overline{u'w'}$ at each height into account, and consequently, the height profile of F_u has been smoothed somewhat in this case.

The rescaled values of $\rho\overline{u'w'}$ for the 16-day period of 3is[t] June- 16 July 1982, are shown in Figure (6-21a). The values of F_u calculated from this height profile by fitting a cubic are shown in Figure (6-21b) along with the average SA value of $-a^*$, and the value of $-a^*$ calculated from the rescaled value of $\bar{v}$ for the 16 days. (We note that the agreement between these last two quantities is excellent.) Inspection of this diagram indicates that below about 88 km, the zonal drag does not balance the Coriolis torque, and is in the opposite sense. Above 86 km, agreement is excellent. Reference to Figure (6-17) indicates that at heights below about 88 km, the planetary wave oscillation is clearly evident and it is possible that this motion is providing the necessary drag.

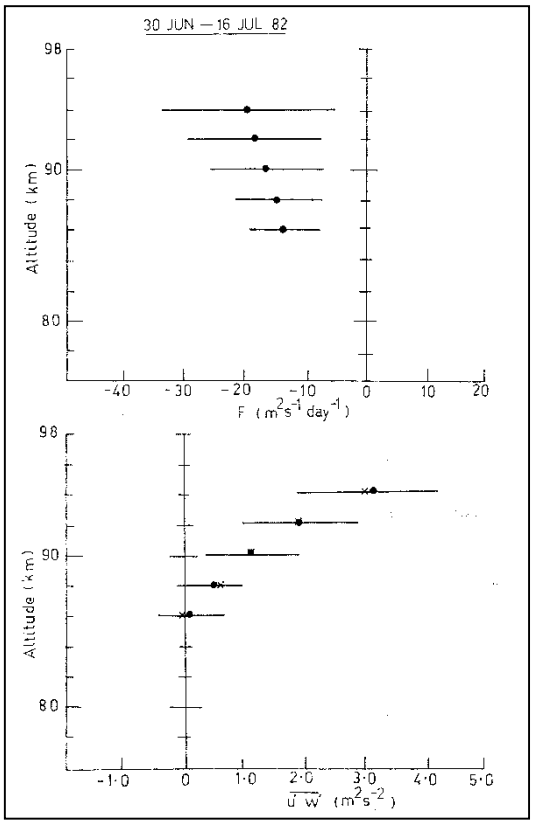

Figure (6-22). As for Figure (6-13) but for 30 June-16 July 1982

The results of a fit of form $ae^{-z/h}$ to the values of $\rho\overline{V'^2}$ in the 86-94 km. height range before the effective beam direction has been taken into account are shown in Figure (6-22), and we note that they are in general agreement with the rescaled results. The difference in the results

for the 6-9th and the 3ist June - 16th July indicates that there is some variation in momentum flux. Because of the way in which the data were obtained, is convenient to break entire data set into periods of 2-4 days to examine this. The rescaled values of $\rho\overline{u'w'}$ are shown in Figure (6-23). The number of days each represents is shown.

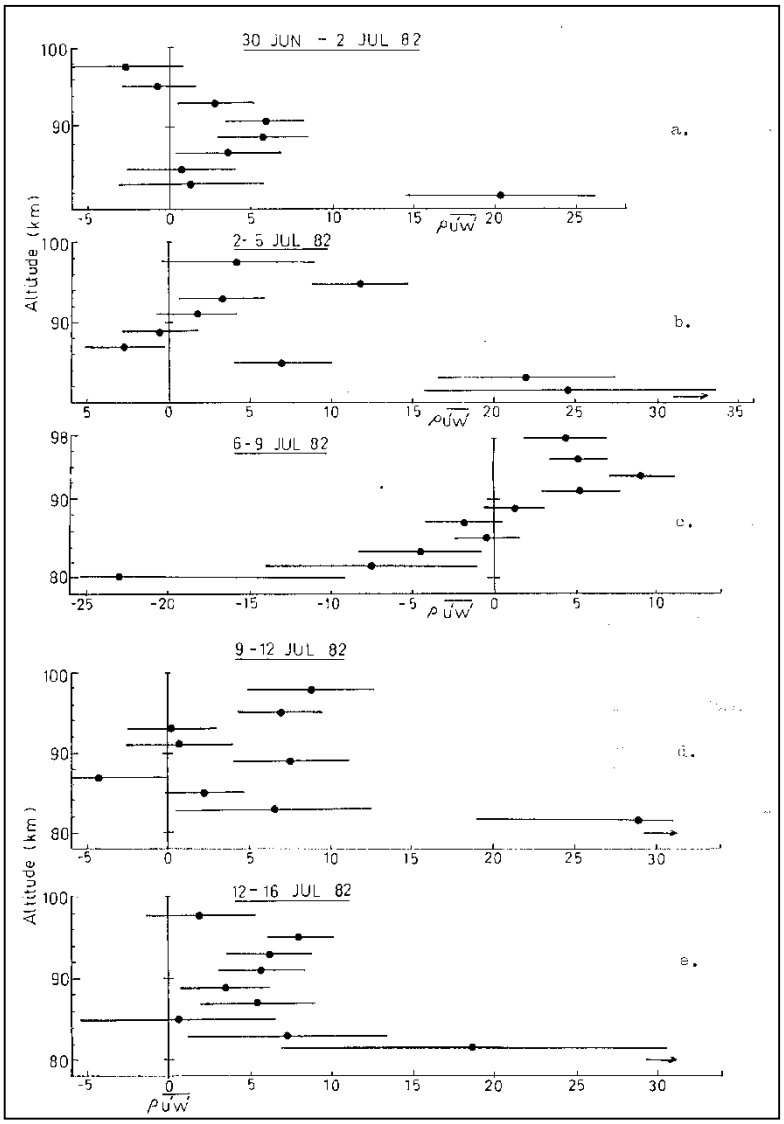

Figure (6-23) Height profiles of $\rho\overline{u'w'}$ for periods of 3-4 days for the July 1982 results

Careful inspection of these diagrams indicates that above about 85 km., the height profits are similar. Below this height, there is considerable variation, with the values shown in Figure (6-23c) exhibiting a slope the opposite sense to the other height profiles. With the exception of these data, the height profiles of $\rho\overline{u'w'}$ are consistent with the mean result for the entire period. The uncertainty in the values of $\rho\overline{u'w'}$ at the lower heights is considerable, and there often appears to be an abrupt change in slope at about 82 km. It is possible that we have overestimated

the correction for the effective beam angle at these heights, but this would not change the general conclusions of the previous discussion.

6.6.2 Spring

6.6.2.1 November, 1981.

The observations in November 1981 were made with the TC(CP) beam arrangement and consequently, no measurement of the local mean meridional wind was available.

However, the run was timed to coincide with a SA observational period so that a measure of this quantity was available. We recall that in this period (see Chapter 5) there was evidence of planetary wave activity with a dominant period of about two days. To remove the longer period motion we have taken an average over four days of the mean winds obtained from harmonic analysis. This is shown in Figure (6-24) along with the individual height profiles of the daily mean wind. We have smoothed through a variation in $\overline{v}$ at 94 and 96 km., which we believe was due to low data acceptance rates, but we will point out the effect of this when we present the Coriolis torque obtained from this profile.

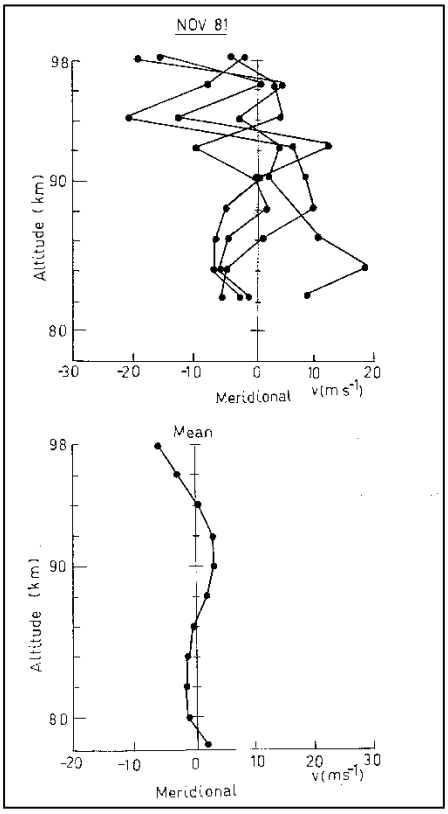

Figure (6-24). Daily Mean Meridional Wind Component for SA observations obtained on 9-13 November 1981. Also shown in the mean for the entire period.

We have calculated F_u by fitting functions of the form $ae^{-z/h}$ to the values of $\rho\overline{V'^2}$ measured in the Eastward and Westward beams, and no rescaling to account for the effective beam angle has been applied. The results are shown in Figure (6-25) along with the smoothed values of $\overline{u'w'}$ and the Coriolis torque ($\times -1$) calculated from the mean profile shown in Figure (6-24). Heights below 82 km were unsuitable for analysis because of low data acceptance rates and have been omitted from the fit. Agreement between F_u and $-a^*$ is excellent, although the profiles appear to be displaced vertically. The unsmoothed values of $\bar{v}$ are $-8\ ms^{-1}$ at 94 km. and $0\ ms^{-1}$ at 96 km, so that the corresponding values of the Coriolis torque are $58\ m\ s^{-1}\ day^{-1}$ and $0\ m\ s^{-1}\ day^{-1}$.

The rescaled values of $\overline{\rho u'w'}$ and the fitted polynomial are shown in Figure (6-26a). The value of F_u calculated from these values is shown in Figure (6-26b), We have also included the unsmoothed values of $-a^*$ as crosses, and note that the general agreement is unchanged if these points are included. The displacement between the height profiles of F_u and $-a^*$ evident in Figure (6-25) is reduced in Figure (6-26b) and although the magnitude of F_u is increased by rescaling the results, there is no change in the sign. We note that the profile of $-a^*$ for the local mean wind lies within the expected range of values for this month.

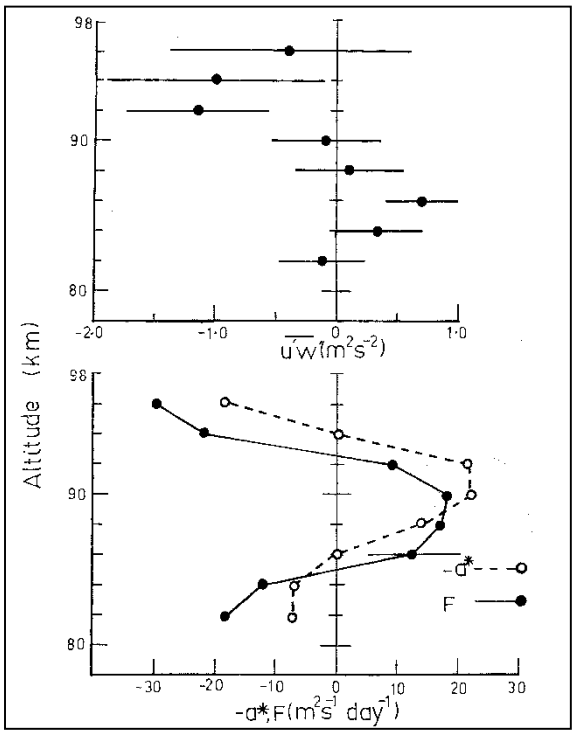

Figure (6-25). As for Figure (6-13), but for November 1981.

6.6.2.2 October 5-8, 1982

We recall data obtained in October, 1982, were characterized by low data acceptance rates. The beam arrangement was OPDCC so that measurements of both $\overline{u'w'}$ and $\overline{v'w'}$ were obtained. While we will present the results for this latter quantity here we will not discuss them until Section 6.9. The data distribution in time for these observations was such that a good measure of F_u can be made for all heights, with the exception of 78 and 80 km. which are marginal. The unscaled raw values of $\overline{u'w'}$ and $\overline{v'w'}$ are shown in Figure (6-27) as crosses. The smoothed values of $\overline{u'w'}$ calculated using a fit of the form $ae^{-z/h}$ are shown as dots. The fit was made to the values of $\rho\overline{V'^2}$ in the range 82-90 km but the results extrapolated smoothly to 78 km, so we have included them. However, they may not provide a good measure of $\overline{u'w'}$ or F_u for the entire period of observation. The body force F_u calculated from the unscaled values of $\overline{u'w'}$ is also shown.

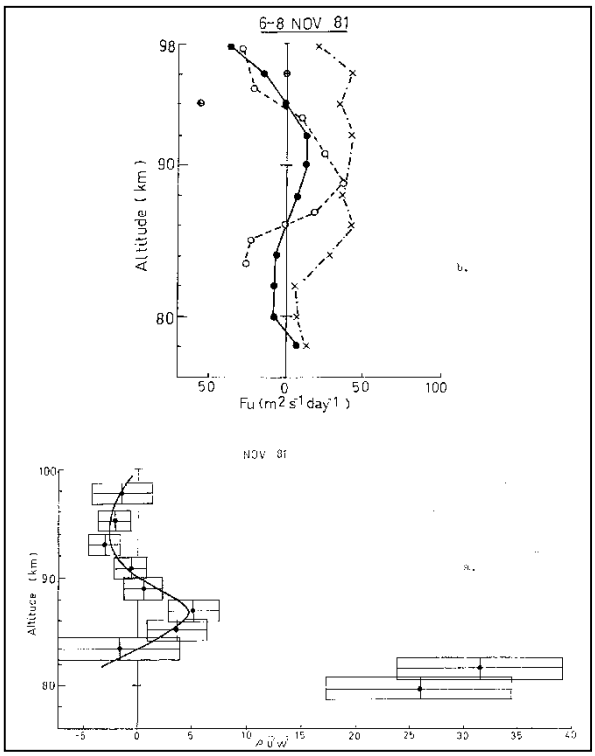

Figure (6-26a). Rescaled values of $\overline{\rho u'w'}$ and polynomial fit used to calculate the zonal body force shown in Figure (6-26b).

The rescaled values $\overline{\rho u'w'}$ and the fitted polynomial are shown in Figure (6-28a) and the values of the body force calculated from are shown in Figure (6-28b). so shown the latter diagrams are the values of $-a^*$ for the local mean meridional wind and for the mean SA results. Inspection of Figure (6-28b) indicates that the body force is in general agreement with the value

of $-a^*$ for the mean SA results, although it is smaller magnitude below about 90 km, it does lie within the expected range of values however. F_u and $-a^*$ due to the local mean wind agree to within the calculated error below 90 km. Above this height they are of opposite sign, but given the uncertainty in the values of $\overline{\rho u'w'}$ shown in Figure (6-28a) agreement is reasonable.

6.6.3 Summer

6.6.3.1 December, 1981 (7-10)

The beam arrangement for these observations was OPDC, so that the mean meridional wind was obtained from the DC beam arrangement, and as noted in Chapter 5, there is some uncertainty in this because of the relative errors and magnitudes of the vertical and meridional radial velocities. The values of $\overline{\rho u'w'}$ presented here represent the mean value of two periods of observation, being from 1346 LT on the 7th to 2209 LT on the 8th and 1044 LT on the 9th to 0912 LT on the l0th. The value of $\overline{\rho u'w'}$ for 98 km has been omitted from the fit because of low data acceptance rates and an intermittent time series.

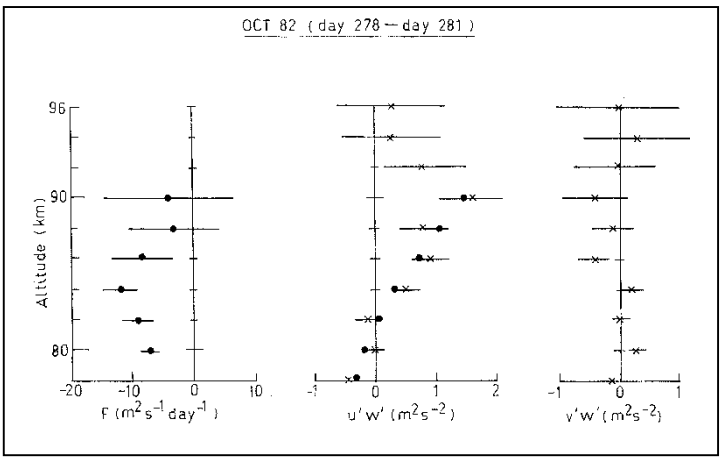

Figure (6-27). As for Figure (6-13) but for October 1982.

Inspection of the rescaled values of $\overline{\rho u'w'}$ shown in Figure (6-29a) indicates that the three lowest heights have values of $\overline{\rho u'w'}$ that do not differ significantly from zero. The body force F_u and the Coriolis torque $-a^*$ calculated from the rescaled values of $\overline{\rho u'w'}$ are shown in Figure (6-29b) along with the mean SA result. General agreement is good and the variation between the profiles of F_u and $-a^*$ calculated from the local mean meridional wind can be accounted for by the uncertainty in F_u and $-a^*$.

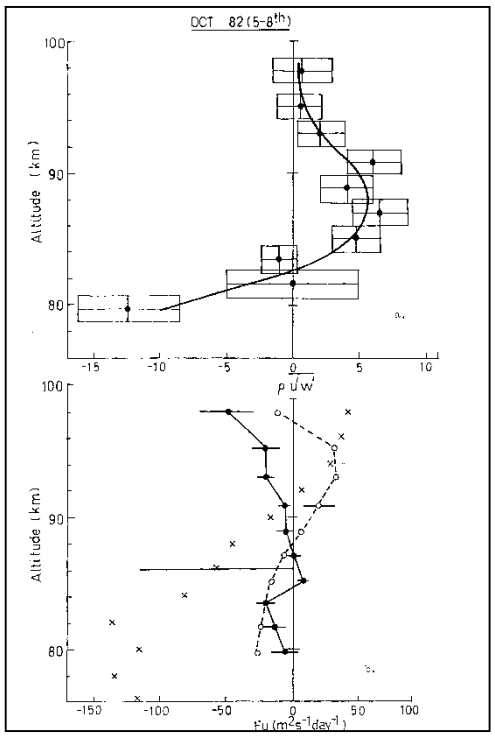

Figure (6-28a and b). As for Figure (6-26a and b) but for October 1982

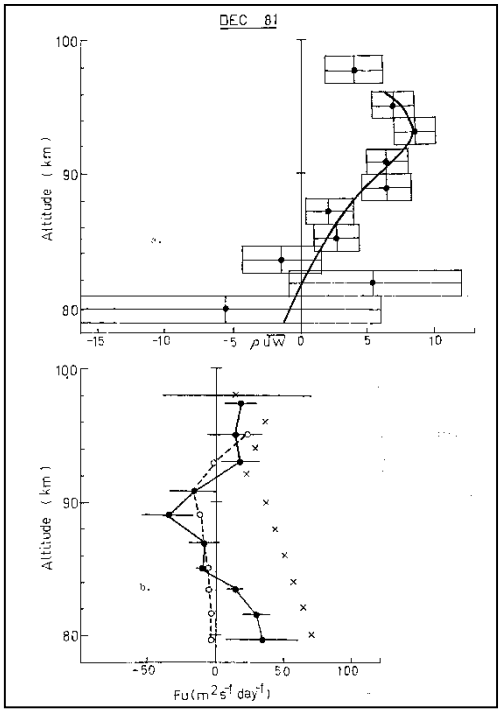

Figure (6-29a and b) As for Figure (6-26a and b) but for December 1981

6.6.3.2 February 1982 (16-19)

The beam arrangement was as for the December 1981 run. These data were characterized by low data acceptance rates, and the only heights suitable for analysis are those in the 85-9l km

height range. However, the values of $\overline{u'w'}$ for 83 and 95 km are marginal, and may give some indication of the correct value. The rescaled values of $\overline{\rho u'w'}$ for all heights are shown in Figure (6-30a). In the 85-91 km height range a parabolic fit is indicated, and such a fit to this height range, taking account of the values of $\overline{\rho u'w'}$ at 83 and 95 km allows the height profile of F_u shown in Figure (6-30b) to be obtained. The values of F_u are in general agreement with the Coriolis torque due to the local mean wind and the mean SA result. However, the uncertainty in this result is considerable, because the height range of the values of $\overline{\rho u'w'}$ is limited, and better fits may be possible. These data are more useful in examining shorter term variations in momentum flux and we will consider them in Section (6.8).

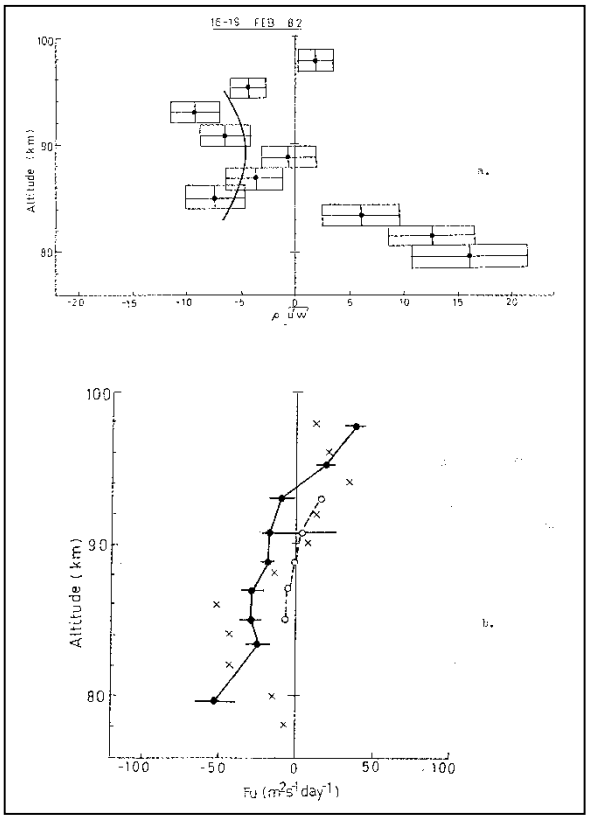

Figure (6-30a and b) As for Figure (6-26a and b) but for February 1982

The height range of suitable values of $\overline{u'w'}$ for data obtained later in the month was even more restricted, and we consider these particular data unsuitable for calculation of the body force.

6.6.4 Autumn

6.6.4.1 April 1982 (21-26)

The beam arrangement was as for December 1981. However, data were only obtained over the height range of 80-9l km for the entire five days. All heights proved suitable for analysis, and

the body force F_u calculated from a parabolic fit to the rescaled values of $\overline{\rho u'w'}$ is shown in Figure (6-31) along with the Coriolis torque $-a^*$. Agreement with the SA mean result below about 86 km is excellent, but since very few observations were available in this month, it is not a true average. In fact, the only April observations available are those presented in Chapter 5. We recall that three days of SA observations were obtained after the DW observations in this month.

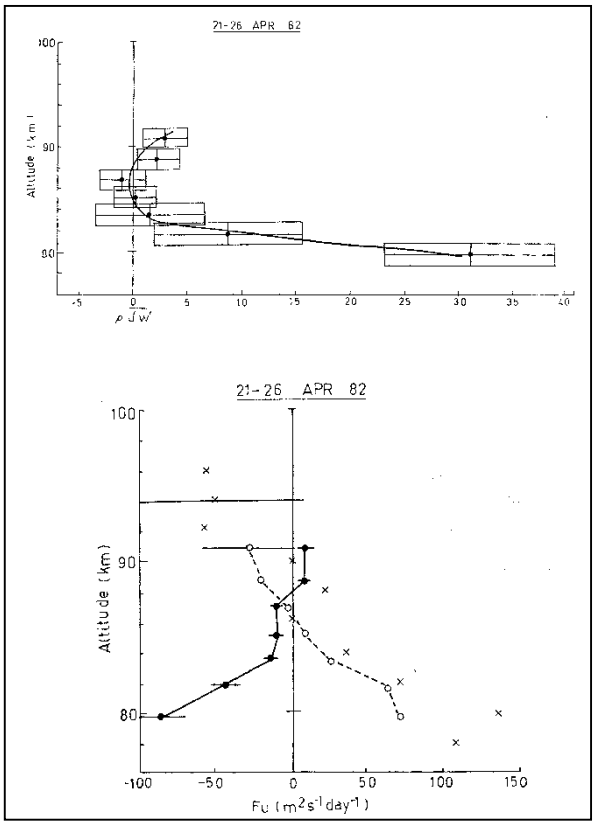

Figure (6-31a and b) As for Figure (6-26a and b) but for April 1982. My daughter Morgan was born on the 25th.

Below about 86 km the Coriolis torque calculated the rescaled DW results is of the same magnitude as F_u, but opposite in sign. It is possible that the "Northward" radar beam was actually directed Southward because of an error in phasing, but inspection of phase of the diurnal tidal component for the DW results indicates that the meridional phase leads the zonal phase by about six hours. This is very strong evidence that "Northward" beam was indeed directed Northward. The mean DW derived meridional component is also in agreement with the model of Groves (1969) and with SA and meteor radar results for the period (1973-1978). The variation in agreement between the meridional components is evidence that the meridional component was fluctuating in this period of observation. The values of $-a^*$ for the local

meridional wind agree with the values of F_u between 84 and 90 km to within the calculated error, and in this case, an extended height range would have been an advantage.

6.6.4.2 May 1981 (11-14)

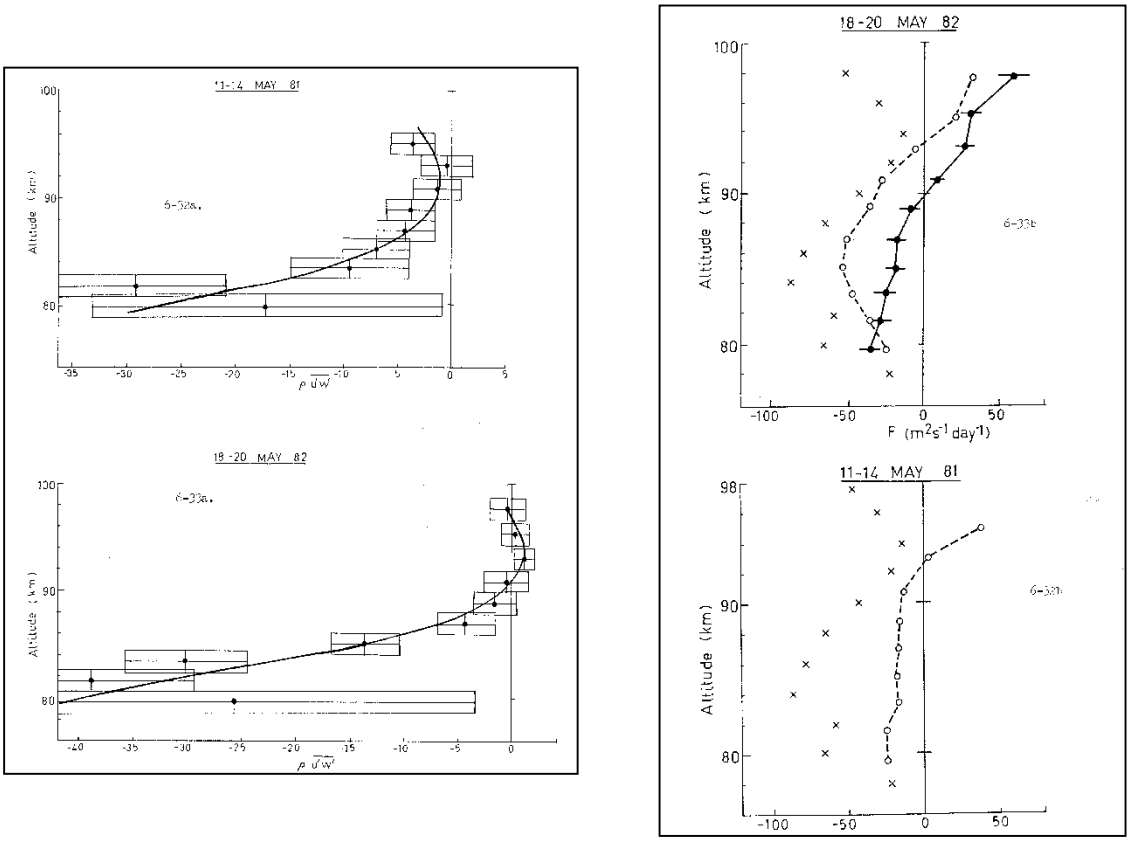

Figures (6-32a and 6-33a) (above left) As for Figure (6-26a) but for May 1981 and May 1982 respectively, and Figures (6-32b and 6-33b) (above right) As for Figure (6-26a) but for May 1981 and May 1982 respectively

The beam arrangement for these observations was DCC so that no measurements of the vertical or meridional mean wind were possible. The unscaled results for this period have been presented in Vincent and Reid (1983). The rescaled values are shown in Figure (6-32a). Inspection of the raw values of $\overline{u'w'}$ (Figure (6-7)) indicates that the results for 94 km appear to be different in character from the remaining data, and it was omitted from the fit made by Vincent and Reid (1983). However, we have included it in the fit to the rescaled values of $\overline{\rho u'w'}$ because there appears to be no reason to reject it after the effective beam direction has been taken into account. The height profiles of $\overline{\rho u'w'}$ for May 1982, also show a similar form.

The body force F_u for each height obtained from the fit indicated in Figure (6-32a) is shown in Figure (6-32b). Below about 93 km the body force is of the correct sign to balance the mean

SA result, but we note a change of sign above this height. Although F_u is smaller than $-a^*$ it does lie within the expected range of values for this quantity.

We recall from Chapter 5 that the mean zonal winds for DW observations made in May 1981 and 1982, were in good agreement, and it is possible, though by no means certain, that the agreement between the meridional components would be similar. Inspection of Figure (6-33b), which shows the Coriolis torque due to the rescaled meridional component measured in May (1982), indicates good agreement in form (and magnitude) with the values of F_u for May, 1981.

6.6.4.3 May, 1982 (18-20)

The beam arrangement was as for December, 1981, and all heights proved suitable for analysis. We have already presented some body force results calculated from the unscaled values of $\rho\overline{V^2}$ in Section 6.5. The rescaled values of $\overline{\rho u'w'}$ are shown in Figure (6-33a) The body force calculated from the fit indicated in Figure (6-33a) is shown in Figure (6-33b) along with the Coriolis torque due to the local mean meridional wind, and the mean SA results.

The body force agrees in sign with the Coriolis torque due to the local wind, and below about 90 km is larger in magnitude. General agreement with the mean SA result is excellent below about 93 km, but as for the May 1981 results, disagrees in sign above this height. Inspection of Figure (6-33a) indicates considerable uncertainty in the value of $\overline{\rho u'w'}$ above about 90 km, but the agreement in form between the May 1981 and May 1982 results indicates that this sign change may be real.

6.6.5 Discussion

The results we have just presented indicate that there is some variability in agreement between F_u and $-a^*$, but apart from the July and April results the body force is in the correct sense to balance the Coriolis torque due to the local mean meridional wind, and given the uncertainty in the momentum flux results, agreement in magnitude is very good. This need not have been the case.

The reasons for this may be briefly summarized as follows.

(a) The zonal body force and torque due to the mean meridional wind should balance when zonally averaged. Local variations in agreement are reasonable and would be expected.

(b) Stationary waves, that is waves with zero horizontal zonal phase velocities, are not measured with the DCC technique. In Winter, when these waves may be transmitted into the mesosphere, they may have an important contribution to the gravity wave drag.

(c) On theoretical grounds it is reasonable to assume that the transmission of gravity waves into the mesosphere would be intermittent, and that wave damping or dissipation would also be an intermittent or transient process. Schoeberl et al. (1983) found that in a numerical model of gravity wave breaking and stress in the mesosphere, steady gravity wave cooling rate would exceed the solar heating rate if it were not an intermittent process, operative less than $2 \times 10^{-2}\lambda_x(km)$ per cent of the time or less. They also found that in modelling gravity wave breaking in the lower troposphere, only in limited geographical locations where the zonal wind is substantially lower than its average value, could a significant flux of stationary gravity waves be transmitted through the lower stratosphere.

These three possibilities would possibly be sufficient to explain the variation in agreement between F_u and $-a^*$ for the different periods of observation, but we note that the two periods of observation in which substantial variations between F_u and $-a^*$ were noted (July and April) were characterized by planetary wave activity. These particular waves could have supplied the necessary zonal wave drag, but because we have omitted all motions with periods longer than 8 hours from the analysis, we cannot exclude the possibility of the importance of any motion with a period within this range. However, observational (Elford, 1979) and theoretical (Miyahara, 1980) evidence suggests that it is unlikely that atmospheric tides contribute significantly to the zonal wave drag at middle latitudes.

In contrast, dissipating planetary waves can provide at least some of the balancing torques in the Winter mesosphere (but do not appear to be important contributors to the Summer mesospheric momentum budget because of their absence from the Summer hemisphere; Houghton, 1978). It is noteworthy that the height profiles of F_u and $-a^*$ disagree most for heights less than about 86 km in the April and July results, where the planetary wave activity is most evident.

Unlike July, which is mid-Winter in the Southern hemisphere, and is characterized by a typical Winter mean circulation, April is a transitional month, in which the meridional circulation in the 80-100 km height region is changing from a Summer (equatorward) to a Winter (poleward) flow. The meridional wind when averaged over 4-5 days certainly fluctuated considerably in

this period of observation. Theoretical models which indicate the importance of the gravity wave drag for the mean circulation have been applied to the Summer and Winter hemispheres only, and its importance for the mean circulation in the transitional months is uncertain from a theoretical viewpoint.

What is clear from these results is that there is a substantial body force associated with the flux convergence with height for periods less than 8 hours, one which must have a profound influence upon the mean circulation. While these results admit the possibility that waves with periods greater than 8 hours are supplying some of the required wave drag in April and July, 1982, observations at a number of locations are required before this may be determined.

Table (6-2) The unscaled momentum flux $\overline{u'w'}$ (m^2s^{-2}) *calculated for the accepted 12-h blocks for February 1982*

Alt (km)	**Block 1**	**Block 2**	**Block 3**	**Block 4**	**Block 5**	**Block 6**
82	0.27	X	X	X	X	0.11
84	0.77	0.13	-2.05	-0.88	-3.47	-0.85
86	l. 77	0.25	-1.88	-0.86	-2.41	-0.89
88	1.19	2.86	-1.40	-1.83	-1.27	0.11
90	0.81	3.23	-10.2	-2.02	-1.85	l.22
92	-0.23	-1.99	-9.82	0.87	X	-2.76
94	-1.69	X	-10.3	0.22	X	X

Finally, we note that the preliminary measurements of the mean vertical wind velocity presented in Chapter 5, which could indicate a multi-cellular meridional circulation, may be important because numerical models incorporating wave drag and stress do not include (or reproduce) this effect. The heating or cooling due to compression or expansion may be substantial and could determine whether a given region becomes convectively unstable for gravity waves, and consequently whether momentum deposition occurs.

6.7 Shorter Term Variations in Momentum Flux and Evidence of Wave Saturation

We have noted in Section 6.2 that the momentum flux term $\overline{u'w'}$ is quite variable in time. In this Section we consider some examples drawn from various periods of observation. Because the February, 1982 momentum flux results show a somewhat complex variation in height, which makes the choice of the best fit difficult, we have selected these data to illustrate the variation of momentum flux in time. We also consider the April 1982, results to determine their consistency over the entire period of observation.

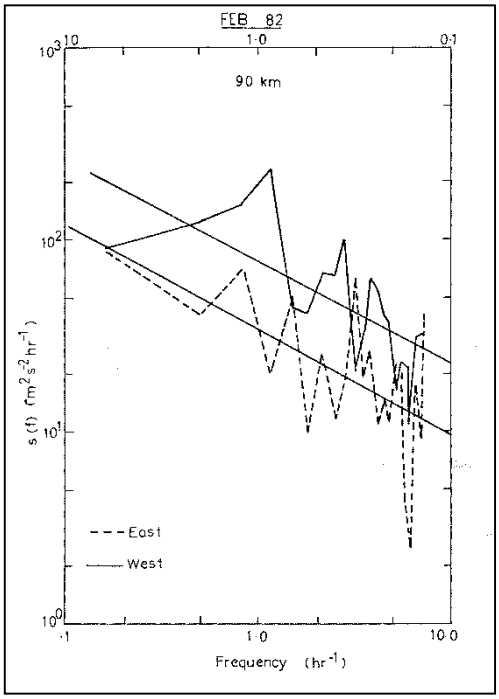

Figure (6-34) Power spectra for Westward and Eastward beams for Block 3 at 90 km for February 1982 results. Also shown are the lines for best fit.

6.7.1 Shorter Period Variation in Momentum Flux

6.7.1.1 February, 1982

The high passed time series for this period was split into 12 hour blocks, and examined for suitable date acceptance rates. The unscaled momentum flux $\overline{u'w'}$ calculated for the accepted blocks is shown in Table (6-2). Inspection of this table indicates considerable variation in time and height. In block three, above 90 km, there are very large values of momentum flux. The power spectra for the Eastward and Westward beam radial velocities for block three for 90 km are shown in Figure (6-34). The lines of best fit for functions of the form $S(f) = S_o f^{-k}$ are

also indicated. It is noted that there is little difference between the slopes of fitted curves. The values of k, the spectral index are (-0.54 ± 0.16) and (-0.54 ± 0.13) for the Eastward and Westward beam radial velocities respectively, so that the difference is not significant.

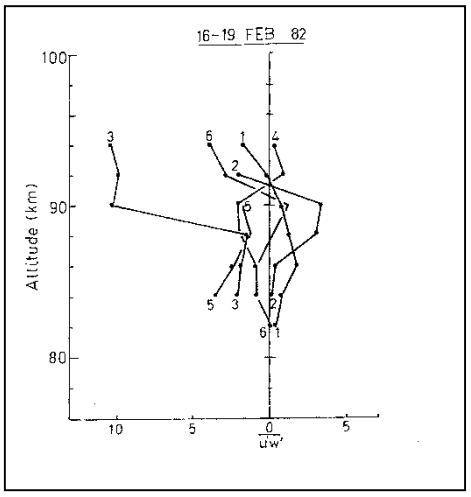

Figure (6-35) Height profiles of $\overline{u'w'}$ for the various blocks shown in Table (6-2).

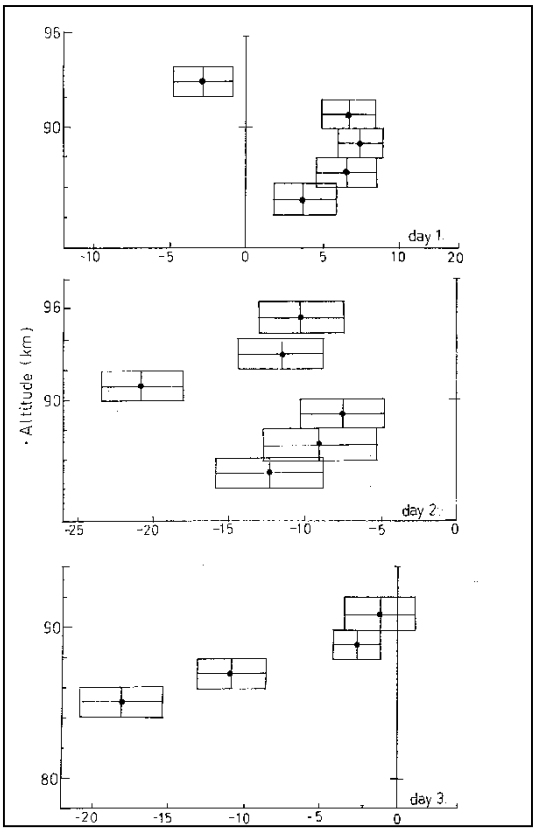

Figure (6-36). Rescaled height profiles of $\overline{\rho u'w'}$ for the three days of the February 1982 run. For details see text.

This result is typical for the other spectra in this period of time and indicates that the enhancement in momentum flux is real. The saturation process in this case appears to be broadband because the power spectra are separated by an approximately equal amount at each frequency, and transient in time because the adjacent data blocks do not show the enhancement.

Inspection of Figure (6-35), which illustrates the height profiles of the values of momentum flux shown in Table (6-2), emphasizes the need for data quality assessment and helps explain the complex height profile of $\overline{\rho u'w'}$ shown in Figure (6-30a), because the values above 90 km for block three appear to dominate the mean for the entire period. The horizontal scale in this diagram is considerably compressed when compared to those used to summarize the momentum flux observations (Figure (6-7)) and these particular data exhibit very large fluctuations in momentum flux.

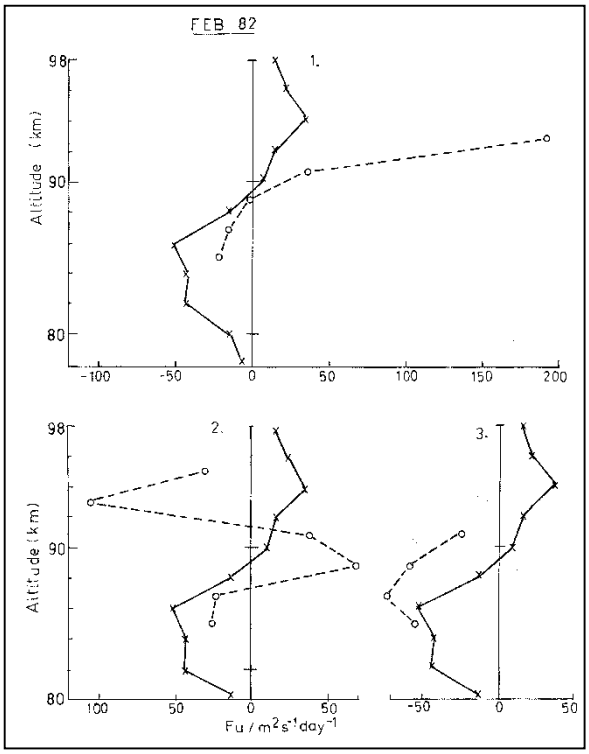

Figure (6-37) The body force F_u calculated from the height profiles of $\overline{\rho u'w'}$ shown in Figure (6-36). Also shown is the Coriolis torque due to the meridional component obtained from Figure (6-15b). The value of F_u for Day 1 at 91 km may be uncertain because of the type of fit used.

The rescaled value of $\overline{\rho u'w'}$ for each 24-hour period for those heights with suitable data acceptance rates are shown in Figure (6-36). By inspection we note that for day 1, the zonal body force is negative up to about 89 km, above which it changes sign. The available height range for day 3 is more restricted, but we note that the body force is negative up to 9l km. The

results for day 2 exhibit a more complex height profile, but in this case the body force is negative up to about 89 km, positive between 89 and 9l km, and negative above this height.

The zonal body force calculated from these results is shown in Figure (6-37). We have also included the Coriolis torque due to the mean SA result for February. We note that the body force for days 1 and 3 show a good agreement with the latter quantity, while that for the second day shows more variable agreement. It is noteworthy that the quasi 2-day wave was very strong at the time these data were obtained and it is possible that this oscillation has modulated the gravity wave flux.

Our choice of fit for the entire period (Section 6.7) appears to be justified and this may indicate that our selection procedures are appropriate. The obvious consequence of the variation of momentum flux with time is that the body force must also vary in time. This example indicates that the variation in this latter quantity can be significant. It also indicates that transient planetary waves may be important in the Summer hemisphere.

6.7.1.2 April 1982

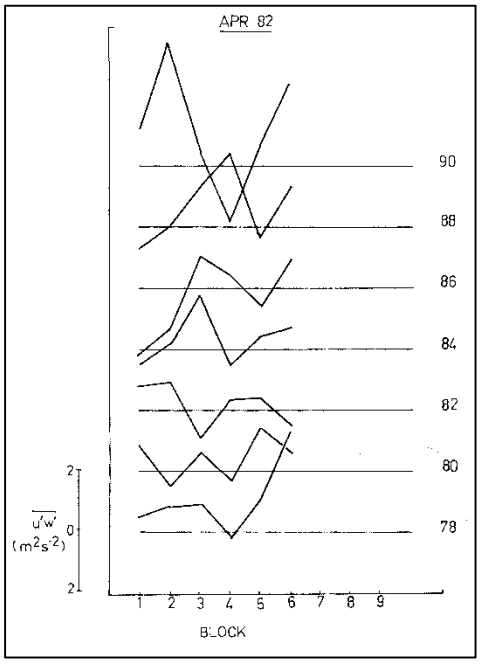

Figure (6-38a) As for Figure (6-1a) but for April 1982.

The high passed radial time series for this observational period were split into blocks of about 0.8 days. This allowed the entire data set to be used and gave six blocks of equal length. The time series of unscaled values of momentum flux $\overline{u'w'}$ for each block and height are shown in

Figure (6-38a). Inspection of this diagram indicates considerable variation in height and time, with an enhancement in magnitude at 90 km.

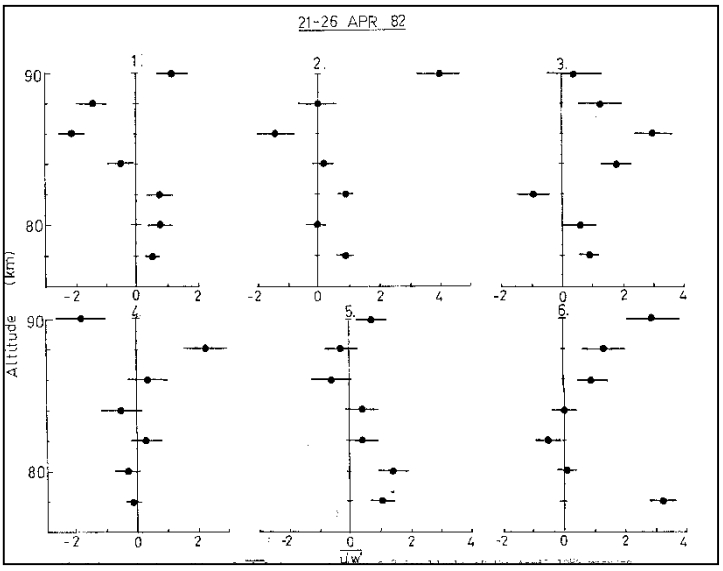

Figure (6-38b) Height profiles of $\overline{u'w'}$ for consecutive 0.8 day blocks of the April 1982 results

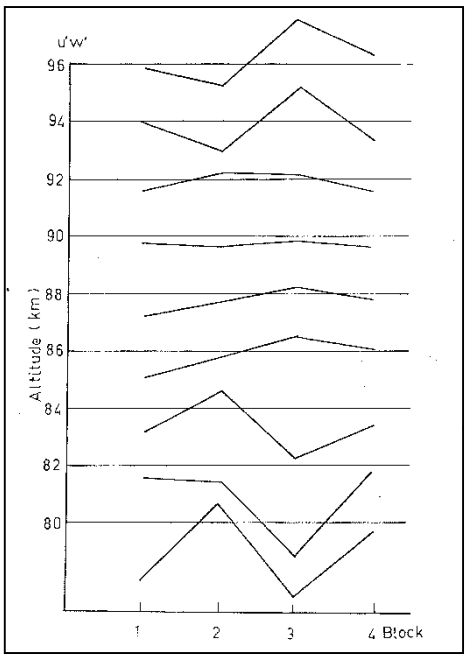

Figure (6-39). As for Figure (6-1a) but for May 1982. Adjacent heights have been displaced vertically by $3\ m^2s^{-2}$

The unscaled height profiles of momentum flux are shown in Figure (6-38b). With the exception of block three and four, these diagrams indicate that the zonal body force is positive below about 82-84 km and negative above this height. Block 3 indicates that the body force is positive below about 82 km, negative between 82 and 88 km and positive above this height.

Block four indicates that there is no significant body force below about 88 km. Unlike the February 1982 results, there are no dramatic enhancements in momentum flux and even though there is variability between these height profiles, the values for each 0.8-day period are generally consistent with the mean result for the entire period.

6.7.1.3 May 1982

The momentum flux for four 12-hour data blocks for May, 1982, are shown in Figure (6-39). We note that the largest variations in $\overline{u'w'}$ occur below 84 and above 94 km.

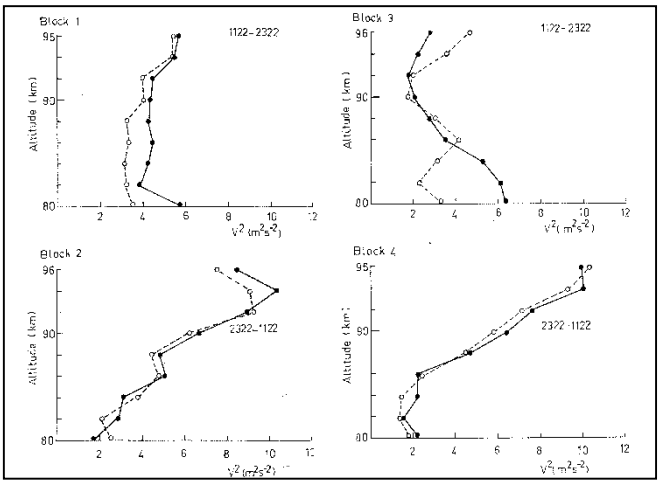

Figure (6-40a to d). Height profiles of mean square radial velocity for Eastward (dashed) and Westward (solid) beams for consecutive 12 hour blocks.

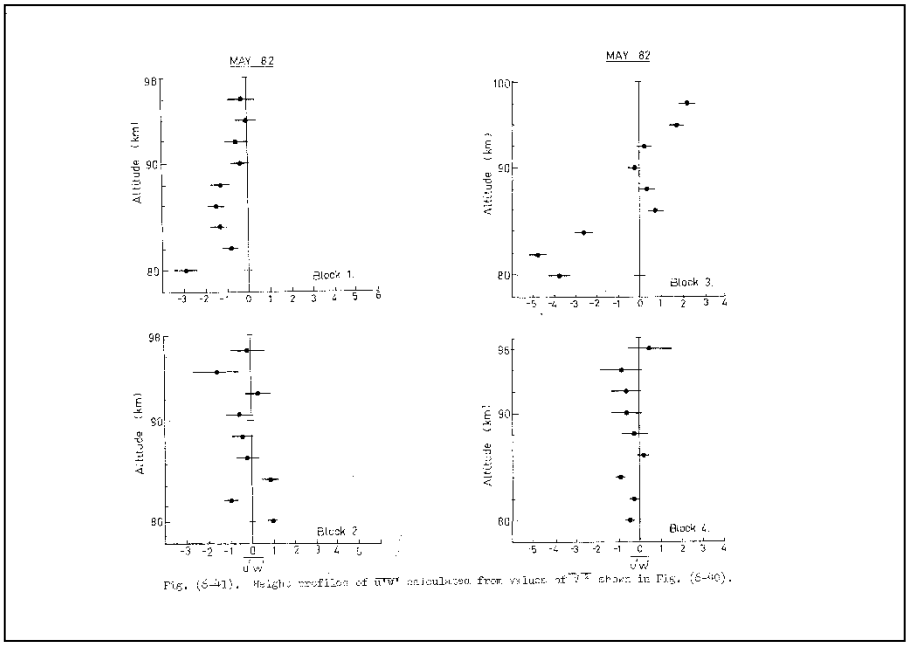

Figure (6-41a to d). Height profiles of $\overline{u'w'}$ calculated from values of $\overline{V^2}$ shown in Figure (6-40).

The mean square radial velocity for each height and beam for each 12-hour period are shown in Figures(6-40a-d). Even though these results have not been rescaled to account for the effective beam direction, the following conclusions are valid. Inspection of these diagrams indicates that block one and block three show a tendency for the mean square radial velocity to be constant or decrease with increasing height, indicating a broad spectrum of saturated waves. In contrast, blocks two and four indicate that wave energy is growing with height.

The corresponding height profiles of $\overline{u'w'}$ are shown in Figures (6-4la-d). We note that the largest contribution to $\overline{u'w'}$ occurs in blocks three and one, and that the measured values of $\overline{u'w'}$ in blocks two and four are generally not significantly different from zero. These results suggest that when the mean square radial velocities indicate wave saturation, there is a significant body force associated with the gravity wave momentum flux and that when they indicate that wave amplitude is growing with height, there is a very much smaller corresponding body force.

Table (6-3) The number of events successfully analysed to yield an unambiguous determination of this quantity for each 12-h block for May, 1982

Alt (km)	Block 1	Block 2	Block 3	Block 4
80	0	3	3	1
82	2	2	1	3
84	1	3	1	5
88	2	1	2	0
90	4	7	0	3
92	3	6	0	4
94	1	9	0	7
96	1	6	2	7

This indicates that the wave saturation process is transient in time, because the major contribution to the momentum flux for the entire period occurs in block three. It also suggests that the saturation process is broadband, because the mean square radial velocities for those periods less than 8 hours indicate similar behaviour within each block. It is instructive to consider how the variation in momentum flux evidenced in these four 12 hour blocks relates to the determination of horizontal scale. To do this, we anticipate the next Chapter in which measurements of horizontal scale are presented and show in Table (6-3) the number of events

successfully analysed to yield an unambiguous determination of this quantity for each block for May, 1982.

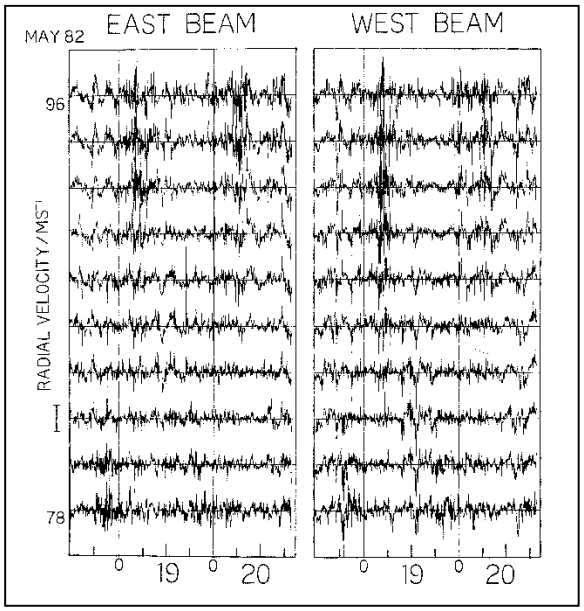

Figure (6-42). Time series of radial velocity for motions with periods less than 8 hours. Enhancements in radial velocity correspond to blocks 2 and 4 when more determination of horizontal scale were obtained.

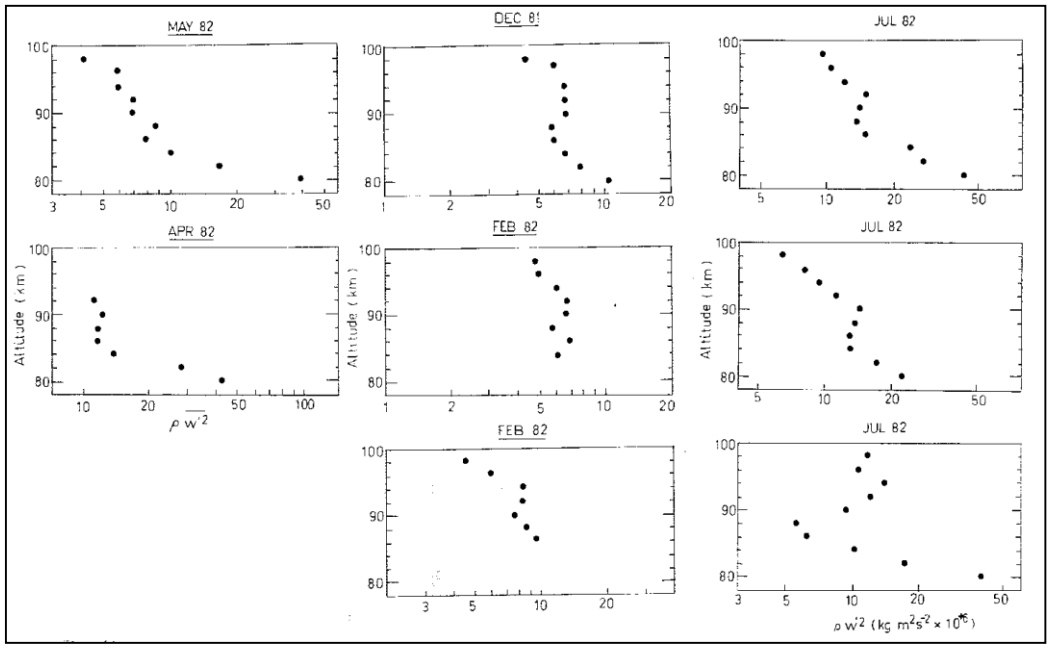

Figure (6-43). Height profiles of product of mean square vertical velocity with neutral air density for motions with periods less than 8 hours

Inspection of these results indicates a tendency for more unambiguous determinations of horizontal scale to be obtained in blocks two and four, that is, when the mean square radial

velocities indicated wave amplitude growth with height. The most dramatic variation is that between block three and the adjacent blocks. Figure (6-42) illustrates the high pass radial velocity time series for these observations. We note that the enhancements radial velocity corresponds to blocks two and four.

It is important to note that unlike the momentum flux observations, the measurements of horizontal scale are limited to a maximum horizontal wavelength of about 200 km, and scales larger than this may be contributing to the zonal drag. The measurements of scale are also biased to periods less than about an hour, though periods of 72 and 120 minutes were obtained because of the way in which they were analysed (see Chapter 7).

These results indicate that some gravity waves with periods less than about an hour are breaking down into turbulence, or are at least not coherent over the spatial separation of the beams when there is a significant contribution to the momentum flux. It is possible that the zonal wave drag was being supplied by motions with periods longer than 2 hours, but this does not explain the variation between the number of determinations of scale for each 12-hour block of data. We will consider the distribution of the measured scales in terms of frequency and height in Chapter 7.

6.7.2 Evidence of Wave Saturation

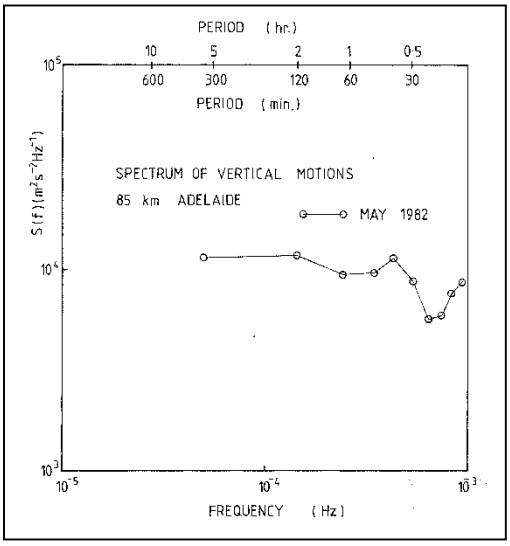

Figure (6-44). Representative spectrum of vertical motion

We have seen that the mean square radial velocities measured in off-vertical beams can be used to provide formation about the amplitude motions with height of motions in the range of periods from 8 minutes to 8 hours. There is some uncertainty in these results because of the effective

beam direction. However, there is no such uncertainty in the mean square vertical velocities. Table (6-4) summarizes this quantity for some representative periods of observation. Unrepresentative values have been omitted. Inspection of these results indicates that generally, values increase with increasing height. For conservation of wave energy, the product of the neutral air density and the mean square vertical velocity should be constant with height. Consequently, the variation of this quantity with height should give an indication of whether wave energy is varying with increasing height.

This quantity is shown in Figure (6-43) for the values shown in Table (6-4) where the values of ρ have been obtained from the CIRA (1972) model. A representative vertical velocity power spectrum is shown in Figure (6-44). Inspection of the former diagrams indicates considerable variability. In the height range of 84-90 km July, the results are indicative of wave amplitudes growing with height so that the value of $\rho\overline{w'^2}$ is constant. Outside of this range, wave amplitudes appear to be either constant or decreasing indicating wave saturation or dissipation. Reference to the rescaled values of $\overline{\rho u'w'}$ in Section 6.7 indicates that there is a tendency for $\overline{\rho u'w'}$ and $\rho\overline{w'^2}$ to be constant over the same height range.

Table (6-4) Mean square vertical velocities for periods between 8 minutes and 8 hours

Alt (km)	**7-10 Dec 8l**	**16-19 Feb 82**	**26-29 Feb 82**	**21-26 Apr 82**	**18-20 May 82**	**30Jun-2Jul 82**	**2-5 Jul 82**	**5-6 Jul 82**
80	0.80	X	X	2.65	2.58	1.46	2.74	2.53
82	0.81	X	X	2.44	l. 54	1.51	2.47	1.54
84	0.93	X	X	l.68	l. 24	1.61	2.89	1.21
86	1.11	l.56	1.11	l. 91	l.33	2.19	2.53	1.02
88	l. 48	l. 96	l. 29	2.68	2.04	3.10	3.15	1.23
90	2.31	2.41	2.09	3.87	2.18	4.45	4.49	2.85
92	3.09	3.62	2.90	4.96	3.01	4.67	6.47	5.09
94	4.22	5.08	3.67	X	3.48	5.29	7.10	8.15
96	5.07	X	X	X	4.76	6.25	8.26	8.43
98	4.96	X	X	X	4.69	6.86	10.3	12.8

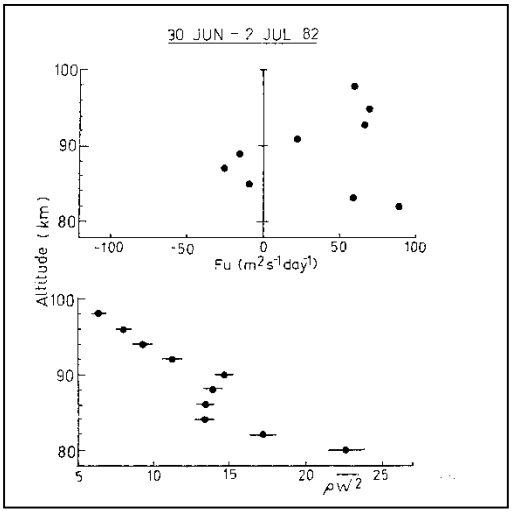

Figure (6-45) The zonal body force F_u (top) and the quantity $\rho\overline{w'^2}$ (bottom Constant values of up $\rho\overline{w'^2}$ corresponds with the smallest values of F_u. For details see text

In fact, we note that the July, May and April values of are similar in form to those $\overline{\rho u'w'}$ for the corresponding periods in that the largest slope in the height profile of $\overline{\rho u'w'}$ tends to occur in the same height range as that for $\rho\overline{w'^2}$. We give one example in Figure (6-45) for data obtained in July 1982. Inspection of this diagram indicates that the largest body force is associated with heights for which wave energy indicates saturation or dissipation. The turning point the height profile of F_u appears to correspond to a n where the wave amplitude growing with height so that energy is conserved. This is good evidence that momentum deposition is associated with wave motions that are saturated or dissipating, and is typical of observations made in July when a vertical beam was available, and for observations made in May 1982, and April 1982.

6.8 Alignment of the Total Body Force

There is no reason for the total gravity wave drag to be aligned in the zonal direction, because directional filtering of the gravity wave flux due to lower level winds could produce a spectrum of gravity waves not polarized in this direction. It is possible then that the zonal body force calculated in Section (6.7) represents some fraction of the total applied drag. While this fraction of the drag is much more consequential for the mean circulation than that in the meridional direction (see e.g. Schoeberl et al., 1983) a knowledge of both components is important for an understanding of the isotropy of the gravity wave field.

Observations made in only two months, July 1982, and October 1982, are suitable to obtain both the zonal and meridional body force. There are two points to note. Firstly, the uncertainty in the calculation of F_u and F_v means that only a general indication of F_T may be obtained, and secondly, it is unclear if it is reasonable to assume that the same form of fit should be made to the height profiles of $\overline{\rho u'w'}$ and $\overline{\rho v'w'}$. However, we can select a height range in which the choice of fit is unambiguous and, consequently, does not affect the results.

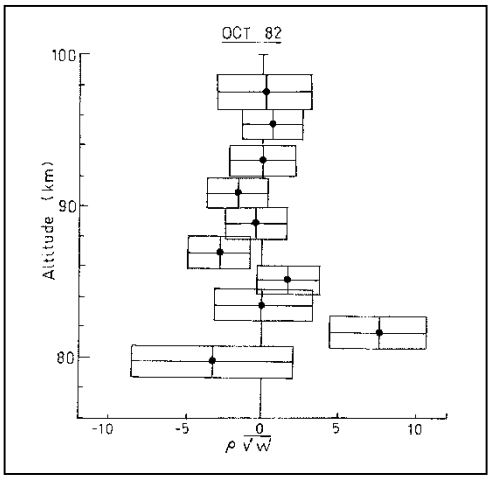

Figure (6-46) Height profile of rescaled values of $\overline{\rho v'w'}$ for October 1982

6.8.1 Results

6.8.1.1 October, 1982

The rescaled values of $\overline{\rho v'w'}$ are shown in Figure (6-46). Inspection of this diagram indicates only two heights, 82 and 87 km with values of $\overline{\rho u'w'}$ significantly different from zero. The error involved in calculating F_u in this case would make the result meaningless. It is clear, however, that since there is a significant body force in the zonal direction, the total applied drag is given to a very good approximation by the magnitude and direction of F_u calculated in Section (6.7) for this month, and the total drag is aligned in the East-West direction.

6.8.1.2 6-9 July, 1982

The rescaled values of $\overline{\rho v'w'}$ for this period have been presented in Section 6.7 and those for $\overline{\rho u'w'}$ have been analysed to yield to zonal body force F_u in Section (6.7). The meridional body force F_v calculated from a parabolic fit to the height profile shown in Figure (6-12b) is shown in Figure (6-47). In this case, F_v is greater than F_u over most of the height range, indicating that the total body force is aligned closer to the North-South direction. The total

body force F_T is shown in Figure (6-48). At the lowest four heights where there is little uncertainty due to the choice of fit, the total drag is aligned between 140° and 220° clockwise from North. Above these heights, the choice of fit does affect the results, but it appears that the total drag is aligned closer to the North-South than the East-West axis. The total body force also appears to rotate with height.

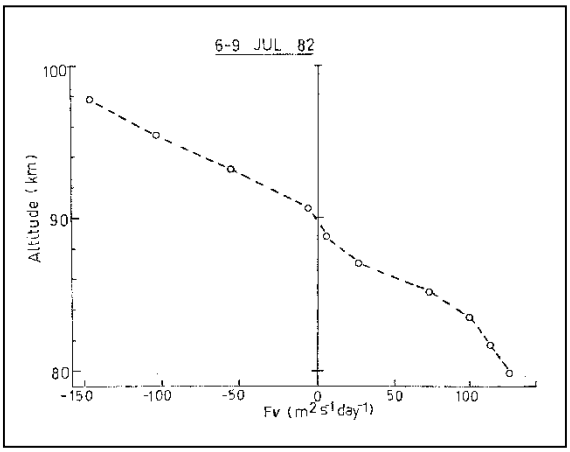

Figure (6.47) The meridional body force F_v calculated from height profile of $\overline{\rho v'w'}$ shown in Figure (6-12b).

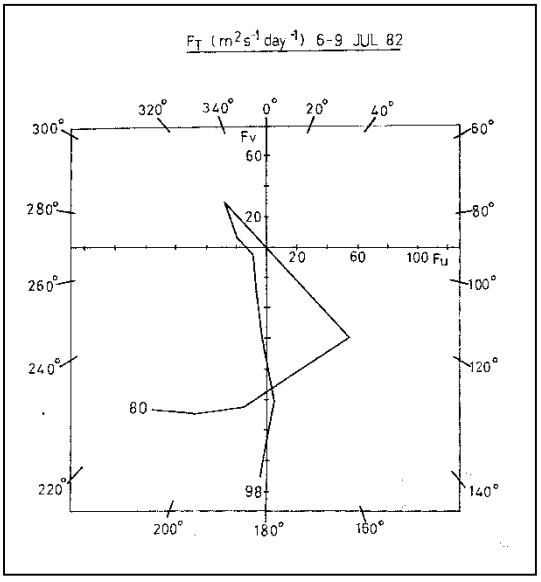

Figure (6-48) The total body force F_T for 6-9 July 1982. For details see text

6.8.1.3 6-16 July, 1982

The total drag calculated for a ten-day period (which includes the results for the 6-9th by fitting the forms indicated to the rescaled values of $\overline{\rho u'w'}$ and $\overline{\rho v'w'}$ (Figure (6-49), is shown in Figure (6-50). The fits in this case allow the best measure of F_T to be obtained in the height

range 80-85 km. Inspection of this diagram indicates that the gravity wave drag at these heights is aligned along an axis about 40° East of North. Above this height range the total body force appears to rotate in an anti-clockwise sense (when viewed from above). However, because of the dependence of F_T on the fit used, no definite conclusion may be obtained.

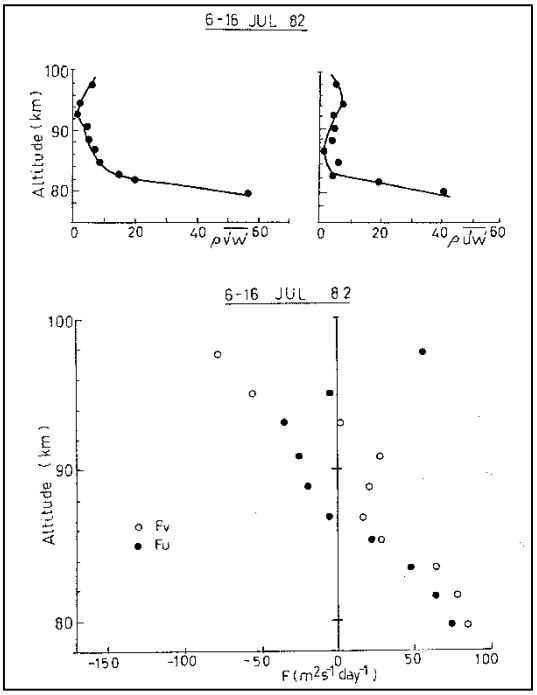

Figure (6-49) Rescaled values of $\overline{\rho u'w'}$ and $\overline{\rho v'w'}$ and fitted functions (top) and the zonal and meridional body force calculated from them (bottom).

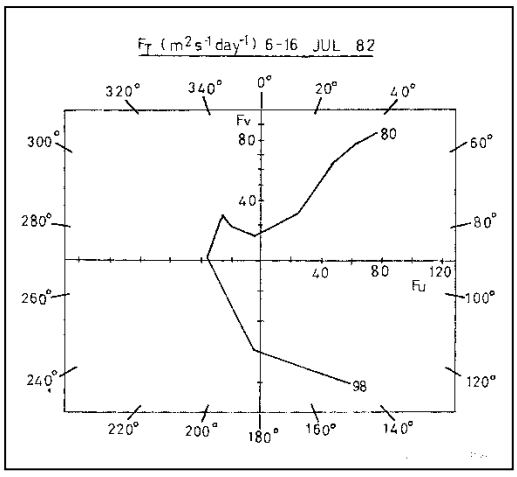

Figure (6-50) The total body force for 6-16th July 1982. For details see text.

What is clear is that in the 80-85 km height range, the total drag is not aligned along with the North-South or East-West axes and so the zonal body force represents a fraction of this total. There must also be considerable variation in the alignment of the total body force in time

because of the difference between the results for the 6-9th and those for the 6-16th July. The strongest statement we may make about the total body force is that it is variable in time, and in July 1982, was generally not aligned in the East- West direction.

6.9 The Frequency Dependence of the Reynolds Stress

We have considered the variation in momentum flux with height and time, but we have not yet considered the variation with frequency. Using an elementary argument based on the polarization relations we can consider which combination of frequency and scale is likely to carry the major proportion of momentum flux. In Chapter 4 we noted that

$$\overline{u'w'} = \frac{A^2}{2}\omega_0^2 k_x c^2 k_z(\omega_0^2 - k_x^2 c^2) \tag{6-13}$$

For a given frequency ω_0, k_x and k_z are free to take a range of values governed by the dispersion relation for gravity waves. This is

$$k_z{}^2 = \left(\frac{\omega_g^2 - \omega_0{}^2}{\omega^2}\right) k_x{}^2 + \left(\frac{\omega_0{}^2 - \omega_a^2}{c^2}\right) \tag{6-14}$$

where

ω_g=Väisälä-Brunt frequency, and

ω_a =Acoustic cut off frequency

and the other terms have previously been defined. Inspection of these Equations indicates a complicated expression for $\overline{u'w'}$ which is difficult to solve without additional information or simplifying assumptions.

With the assumptions that $\omega_0^2 \ll k_x{}^2 c^2, \omega_0^2 \ll \omega_g^2$, and $k_z{}^2 \gg \omega_a^2/c^2$ we may obtain

$$|\overline{u'w'}| = \left|\frac{A^2}{2}\omega_0^2 c^2 k_x{}^2 \frac{\omega_g}{\omega_0}(-k_x^2 c^2)\right|$$

$$= \left|\frac{A^2}{2}\omega_0 k_x{}^4 \omega_g c^4\right| \tag{6-15}$$

For a fixed A we note that:

(1) For a given ω_0, the largest value $|\overline{u'w'}|$ will be obtained for the largest k_x, that is the smallest λ_x;

(2) For a given k_x, the largest value of $|\overline{u'w'}|$ will be obtained for the largest value of ω_0, that is, frequency.

These results indicate that the high frequency short wavelength gravity waves will produce the largest contribution to $|\overline{u'w'}|$. We recall that for a given wave A is an arbitrary constant. For a spectrum of waves A will take a range of values. Consequently, it is important to obtain a more general expression for the Reynolds stress. To do this we may make use of an empirical relation for the mean square horizontal velocity.

We have noted elsewhere in this thesis that the power spectrum $S(f)$ of the fluctuation in horizontal wind velocity have a characteristic form which may be approximated by a power law relationship. This information is quite useful because the mean square fluctuation in horizontal velocity $\overline{u'^2}$ is given by

$$\overline{u'^2} = \int S(f)df = \int_{f_1}^{f_2} S_0 f^{1-k} df \tag{6-16}$$

so that for an elemental frequency interval

$$\overline{u'^2} \approx f^{-k} \propto {\omega_0}^{-k} \tag{6-17}$$

To simplify the problem, it is convenient to write $\overline{u'w'}$ in terms of a single variable, the most appropriate of which is the frequency. With the assumption that ${k_z}^2 \gg \omega_a^2/c^2$ and $\omega_0^2 \ll \omega_g^2$ the dispersion relation simplifies to

$$\frac{k_z}{k_x} \approx \pm\frac{\omega_g}{\omega_0} \approx \frac{u'}{w'} \tag{6-18}$$

so that we may write

$$w' \approx \pm\frac{\omega_0}{\omega_g} u' \tag{6-19}$$

and

$$\overline{u'w'} \approx \overline{u'^2}\frac{\omega_0}{\omega_g} \tag{6-20}$$

Substituting (6-17) into (6-20) we have

$$\overline{u'w'} \propto \frac{{\omega_0}^{1-k}}{\omega_g} \tag{6-21}$$

for a given elemental frequency interval.

The momentum flux for a frequency interval $\Delta\omega_0 = \omega_{02} - \omega_{01}$ is then

$$\overline{u'w'} \propto \frac{{\omega_0}^{2-k}}{\omega_g}|_{\omega_{01}}^{\omega_{02}} \tag{6-22}$$

Using Vincent's (1984) value of $k = 1.5$ we may estimate the relative contributions of high and low frequency motions to the momentum flux. Selecting two intervals, 1-8 hours and 1 hour-8 minutes we obtain

$$R \equiv \frac{(\overline{u'w'})_L}{(\overline{u'w'})_H} \sim 0.4 \tag{6-23}$$

so that the high frequency waves could be expected to contribute about 60% of momentum flux the range of periods between 8 hours and 8 minutes.

It should be emphasized that this argument is subject to a number of uncertainties, one of which is the value of k. Values presented in the literature generally lie in the range of 1-2 (Vincent and Ball, 1981; Carter and Balsley, 1982; Vincent, 1984; Frezal et al., 1981). The largest values of *k* are discussed by Frezel et al. (1981) who found that in the 1-8-hour period range for meteor observations that k values ranged from 1.5 at a low latitude site (Punta Borinquen, l8°N) to 2.1 at a high latitude site (Kiruna, 68° N). At mid-latitude sites *k* is generally close to 1.5. However, we note that the ratio R will range from about 0.14 for $k = 1$ to about 0.84 for $k = 1.9$, and is rather dependent upon the value k.

The value obtained by Vincent (1984) for Adelaide SA observations seems to be the most appropriate choice for our purposes. Another point to note is that the momentum flux is dependent upon the waves actually present and, consequently, upon various effects such as the filtering of the gravity wave spectrum by the background wind. However, it appears that for $k = 1.5$, higher frequency motions should contribute a major portion of the momentum flux.

6.9.1 Results

To obtain a measure of the relative contributions of high ($T < l\ hour$) and low ($T > l\ hour$) frequency motions to the momentum flux, data obtained in October 1982, were split into these two frequency intervals by application of a numerical filter. The results for $\overline{u'w'}$ and $\overline{v'w'}$ are shown in Figure (6-51a, b). Inspection of Figure (6-51a) indicates that above 84 km, the high frequency motions are contributing a significant component of the momentum flux. In contrast,

Figure (6-51b) indicates a significant difference between high and low frequency contributions at only three heights 86, 88 and 96 km, where there would appear to be a slightly larger contribution from the high frequency motions.

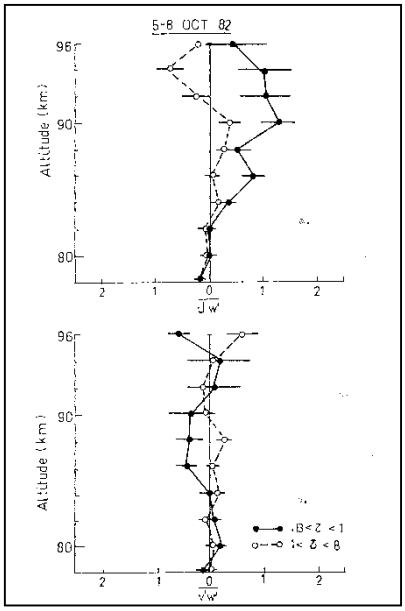

Figure (6-51) Height profiles of momentum flux for periods between 8 min and 1 hour (solid) and periods between 1 and 8 hours (dashed). See text for details

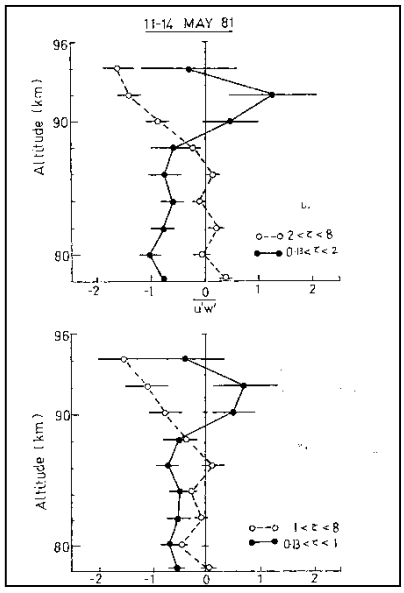

Figure (6-52a and b) Height profiles of momentum flux for (a), periods between 8 min and 1 hour and 1 hour and 8 hours and (b), for periods between 8 min and 2 hours, and 2 hours and 8 hours.

A similar diagram for data obtained in May 1981, is shown in Figure (6-52a) for the $\overline{u'w'}$ term. Below about 88 km the high frequency motions appear to be contributing a substantial portion

of the momentum flux. Above this height, the low frequency motions appear to contribute slightly more of the total.

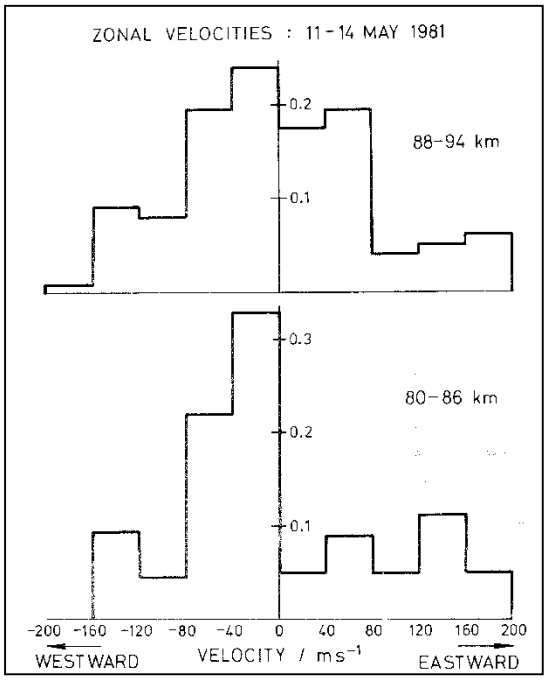

Figure (6-53) Zonal phase velocities for May 1981 (After Vincent and Reid, 1983)

Figure (6-52b) illustrates the momentum flux for periods less than 2 hours and for periods between 2 and 8 hours. Inspection of this diagram indicates that below about 88 km, the major contribution to the total momentum flux is due to the higher frequency motions. Above this height, the low and high frequency motions contribute approximately equally, but vary in sign. We have noted that the measurements of horizontal scale are biased towards periods less than about l hour. It is instructive then to consider the phase velocities for this period of observation and compare them with the momentum flux for this frequency interval. These are shown in Figure (6-53). In the 80-86 km height range, there are more waves propagating westwards. In the 88-94 km range we note a greater symmetry about zero phase velocity. Westward propagating waves with downward phase velocity will transport momentum so that the sign of $|\overline{u'w'}|$ is negative. This agrees generally with the momentum flux for periods less than about an hour in the 80-86 km height range, and it appears that these waves are responsible for the transport of momentum in this height range.

These results support the argument that high frequency motions contribute a significant portion of the total Reynolds stress for periods between 8 hours an 8 minutes. This indicates that even though shorter period motions have smaller amplitudes than larger period motions, the larger vertical group velocities associated with the shorter period waves more than compensate for

this, and they have a correspondingly larger momentum flux. We have also shown in Chapter 4 that the DCC beam arrangement is more sensitive to the measurement of higher frequency motions, but that this sensitivity is matched exactly by the contribution to the momentum flux from the same waves. That is, the longer period waves are associated with a smaller momentum flux than shorter period waves.

6.10 Summary and Conclusions

We have presented results in this Chapter which indicate that the body force associated with the momentum flux convergence the 80-98 km height range is substantial and appears to balance the Coriolis torque due to the mean meridional wind velocity in many months.

However, the Winter results indicate that longer period motions may supply the necessary wave drag. This is by no means certain, because the observations were made at a single site and the wave drag and Coriolis torque should balance when generally averaged. The need for observations at a range of locations is indicated.

The momentum flux has been shown to be variable at a variety of time scales, from 3 hours in the November, 1981, result, to 2 days in the case of the July, 1982, results. The natural consequence of this is that body force is variable in time. The results for February, 1982, indicate that planetary waves, notably the “2-day wave", may be important in the Summer hemisphere, because the body force varies considerably from day to day.

The zonal body force was found to be a component of a body force that was aligned closer to the North-South direction in July, 1982, and the meridional body force was correspondingly larger.

The results for February and May 1982, indicate that wave saturation is transient in time and broadband. The May results also indicate that momentum deposition is associated with saturated or breaking waves. The enhancement in momentum flux for the May 1982, results appeared to be associated with fewer determinations of horizontal scale.

The vertical mean square velocities support the evidence that momentum deposition was associated with saturated or dissipating waves.

The high frequency wave motions ($T < 2\ hours$) appear to contribute the substantial portion of the momentum flux for periods between 8 minutes and 8 hours.

On the whole, the results support theories stressing the importance of gravity wave drag, and the notion that gravity wave transmission and momentum deposition are transient in time.

We have presented a wide range of results and have not exploited the data fully, mainly because of its sheer volume. We have attempted, however, to address some problems of current theoretical interest.

The DCC beam technique is extremely powerful, but measurements at a number of sites will allow geographical variations in momentum deposition to be investigated and allow a measure of the zonally averaged wave drag to be obtained.

7. Observations of the Horizontal Scale of Mesospheric Gravity Waves

7.1 Introduction

In this Chapter we present some representative horizontal wavelengths measured using the DCC and TC(CP) beam configurations and the theory discussed in Chapter 4. Unlike the measurements of the Reynolds stress presented in the previous Chapter, some direct observations of horizontal scale of mesospheric gravity waves have been made with a variety of techniques.

Witt (1962), Grishin (1967) and Hauwitz and Fogle (1969) used photographic techniques to study wave forms in noctilucent clouds (NLC), and found horizontal wavelengths ranging from about 10 to 75 km, and horizontal phase speeds of about 10 to 60 ms^{-1}. However, observations of NLC are restricted in both time and space, because they occur only at the high latitude mesopause in the local summer. They do exhibit evidence of a wide range of wave motions when they are visible.

Similar observations of structure in air glow emissions have provided evidence of wave motions in limited height ranges. Moreels and Herse (1977) and Herse et al. (1980) have reported observations of horizontal wavelengths between about 30 and 100 km evident in the OH emissive layer occurring between 80 and 90 km, and a similar study by Armstrong (1982) reported evidence of a nearly monochromatic wave motion with a wavelength of about 244 km and a phase velocity of about 72 ms^{-1}. Like observations of NLC clouds, airglow observations are restricted in time and space, because they require clear nights and the airglow itself occurs in a restricted height range.

Rastogi and Bowhill (1976) have reported some estimates of the horizontal wavelengths of mesospheric gravity waves, but as we noted in Chapter 4, they were somewhat restricted in interpretation. Vincent and Reid (1983) reported observations of the horizontal scale of mesospheric gravity waves for periods less than about an hour, and scales less than 200 km, made using the DCC beam technique. The mean zonal wavelengths for this selective sample was 70 km. The zonal phase speeds (which have been presented in Chapter 6) ranged up to about 200 ms^{-1} with a mean of about 70 ms^{-1}. Assuming a wavefield isotropic in azimuth, these values would correspond to mean values of $\lambda_H \sim 50\ km$ and $c \sim 50\ ms^{-1}$

Smith and Fritts (1983) used the Poker Flat DW radar (63°N) in a DC beam configuration to estimate gravity wave parameters. With a combination of numerical bandpass filtering and some reasonable assumptions, these authors were able to obtain horizontal wavelengths and phase velocities. The technique that they describe is essentially the same as, but less general than that described in Chapter 4 for the DC beam configuration. Apart from the results presented by Vincent and Reid (1983), these are the best direct measurements of gravity wave parameters in the mesosphere using Doppler radar techniques of which we are aware, but note that these results must also be limited to wavelengths less than about 200 km. Like Vincent and Reid (1983), they found horizontal wavelengths of about 20 to 80 km and phase velocities of about 10 to 50 ms^{-1}

Indirect estimates of horizontal scale based on SA radar measurements have been made by Vincent (1984) and Manson et al. (1979). Vincent's results for the mean spectrum for SA observations at Adelaide have been mentioned earlier in this thesis. By integrating under this spectrum for octave period bands to obtain the mean square horizontal velocity, and applying the dispersion relation, Vincent was able to estimate the mean horizontal wavelength for each frequency band. The values thus obtained are only approximate as Vincent points out, especially when the scales became large enough for the curvature of the earth to be taken into account, but they are in agreement with other estimates. For periods in the range of 0.1 -0.5 and 0.5 - 1.25 hours Vincent found that A 60 and 108 km respectively, a result in good agreement with the values obtained by Smith and Fritts (1983) and Vincent and Reid (1983). In the period range of 5-10 hours Vincent found that $\lambda \sim 1160\ km$.

Manson et al. (1979) used SA wind measurements to estimate scales in the range of 150-1100 km for waves in the 2-8-hour period range, which are in agreement with Vincent's (1984) results. Recent direct measurements of gravity wave horizontal wavelengths using three SA radars separated on the ground by about 40-50 km (and known as GRAVNET), indicate a mean wavelength of about 100 km for periods less than 200 minutes (Manson and Meek, private communication), a result which is in good agreement with the direct measurements of Vincent and Reid (1983) and Smith and Fritts (1983) and the indirect estimates of Vincent (1984) and Manson et al. (1979).

7.2 Data Analysis and the Importance of the Effective Beam Direction

7.2.1 Data Analysis

The basic data analysis and quality assessment of the data presented in this Chapter is essentially the same as that outlined for the measurement of Reynolds stress in Chapter 6. The high pass ($T < 8\ h$) time series of radial velocity were broken into consecutive blocks of 6 or 12 hours in length and plotted. If continuous breaks of more than 10% of the length of the block was present, the entire block was omitted. The remaining blocks were then used to calculate the cross spectrum for a given height and a particular pair of coplanar beams.

The theory and some practical considerations relating to the measurement of scale have been discussed in Chapter 4. We recall that in order to obtain good resolution of the wave velocities as a function of time, it is desirable to use short length records. Otherwise, changes in the direction of waves of a given period will lead to "smearing" of the phase differences and a reduced coherence. However, to obtain good spectral resolution and significance, it is desirable to use long records and average over a number of frequency bands. As a compromise between these conflicting demands, data lengths of six or twelve hours' duration were used with averaging over four adjacent frequency points to give eight degrees of freedom for each estimate.

The values of the $(COH)^2$ of the cross spectrum were used to estimate the degree of similarity of the spatially separated data at a given frequency (Julian, 1975). Values as low as 0.54 were on occasion accepted (nominally significant at the 90% level), but most of the accepted values had a $(COH)^2$ greater than or equal to 0.68 (nominally significant at the 95% level). For $(COH)^2 = 0.68$, the uncertainty in the phase is 0.45 rad (Jenkins and Watts, 1968) and as we noted in Chapter 4, phase errors of this magnitude make estimates of wavelengths greater than 200 km very uncertain.

In addition, the analysis of data in six hour blocks with averaging over adjacent spectral estimates biased these particular results to periods less than one hour. The lowest frequency of each cross spectrum was omitted, and the periods available for analysis were then 60, 36, 26, 20 and 12 minutes. To extend this range of periods, some data sets were analysed in twelve hour blocks. This gave additional periods longer than those listed above of 120 and 72 minutes. However, these results are still biased principally to periods less than one hour.

Consequently, the measured horizontal wavelengths presented here may not be representative, and constitute only a selected portion of the total gravity wave spectrum.

As a further limitation, the measured wavelengths have not been corrected for the Doppler shift of the gravity wave frequency by the background wind. However, the October 1982 results obtained during a period of very weak zonal and meridional winds should provide a good measure of the scales of motions present with periods less than about an hour, even without correcting for the Doppler shift in wave frequency. These particular data are the only results which have been analysed to obtain both of the zonal and meridional scales, because the July 1982 results evidenced some abrupt changes in radial velocity which could contaminate the cross spectral phases, and the February 1982 results obtained using the OPDCC beam arrangement were intermittent in time and restricted in height.

7.2.2 The Importance of the Effective Beam Angle

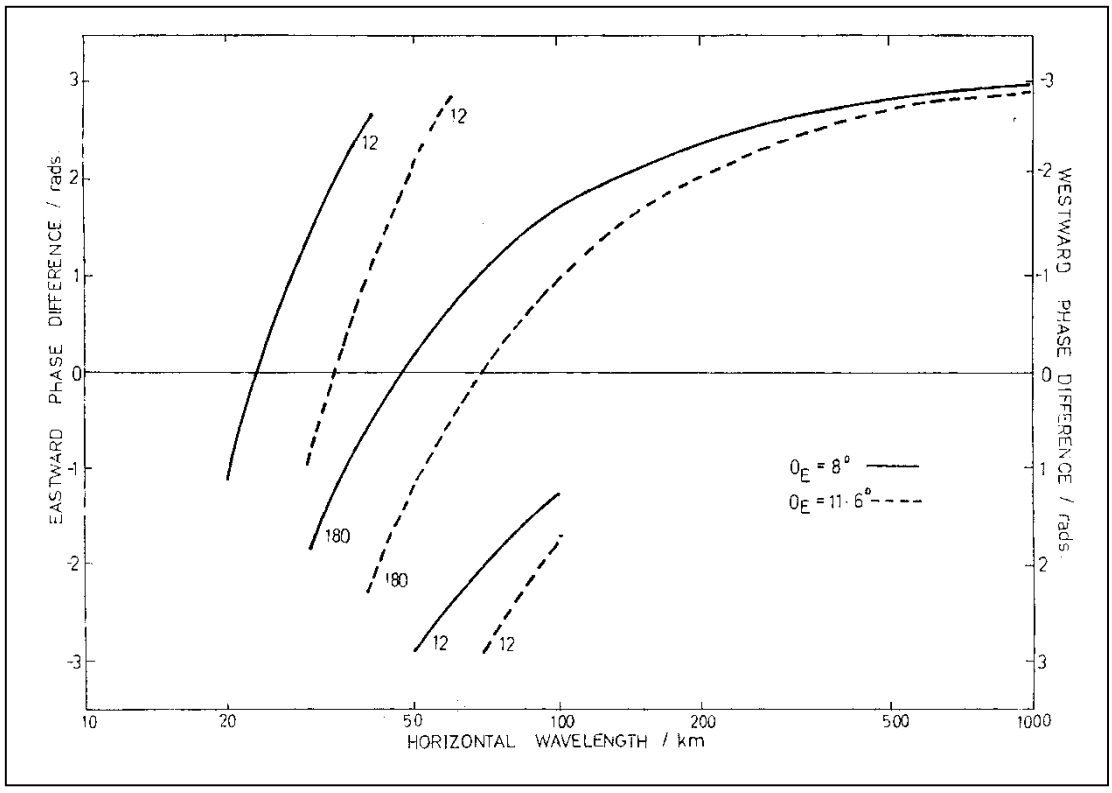

Figure (7-1) Cross spectral phase for two tilt angles. The 12-minute period has only been plotted to 100 km. For details see text.

We recall that in Chapter 4, a beam off zenith angle of 11.6° was assumed when the phase was calculated from Equation (4- 81). We noted in Chapter 5 that at 86 km, this would be closer to about 8°. To examine the effect of this variation in θ the expected cross spectral phase has

been calculated for two periods for the latter angle and is shown in Figure (7-1). The results for $\theta_E =$ 11.6° are also shown for reference.

Inspection of this diagram indicates that the horizontal scale calculated by assuming $\theta_E =$ 11.6° overestimates the correct value. A reasonable estimate would be about 50% for $\theta_E =$ 8°. For smaller values of θ_E, corresponding to lower heights, the overestimate will be somewhat larger. It turns out that the correct wavelength can be obtained by taking the ratio $sin\theta_A/sin\theta_E$ and multiplying this by the measured wavelength. This is a consequence of the dominance of the first term on the RHS of Equation (4-8l), that is

$$\varsigma = -2k_x + \varsigma'$$

This means that there is a simple method of correcting the measured wavelength for the variation between the apparent and effective beam angles. The heights and perturbation velocities can also be corrected by using the inverse of the same ratio as was indicated in Chapter 5. Because the values of ς obtained from Equation (4-81) for a height of 86 km have been used to calculate the horizontal wavelength for all heights, the measured scales above this height will be overestimates, and below it will be underestimates. However, the error due to this is generally less than that due to the uncertainty in the cross spectral phase.

7.3 Results

In this Section we present the horizontal wavelengths measured using the DCC and TC(CP) beam techniques. All of the results presented here have been rescaled to account for the effective beam angle. Of those data sets obtained using beam configurations incorporating a vertical, as well as DCC beams, only the May 1982 and November 1981 results have been analysed using the theory developed in Chapter 4 to measure scale with the TC(CP) beam arrangement.

All of the other results have been obtained using the DCC beam technique. No attempt was made to measure scale by applying the DC beam technique alone, but this could have been done to obtain measurements of meridional horizontal wavelengths for the February, April and May 1982 observations discussed in this Chapter. The two data lengths used, six and twelve hours, complicate the comparison of results obtained in different months, because some waves that are coherent over periods of six hours may not be coherent over periods of twelve hours.

The results are valuable nevertheless, and they also illustrate the usefulness of the DCC beam technique. We consider the best results to be those for October 1982 and May 1982. The former results because the mean winds were very weak when the observations were obtained, and because both zonal and meridional scales were measured and the latter results because they have been analysed completely to determine the horizontal scale, and were characterized by very high data acceptance rates.

We present the October 1982 results first.

7.3.1 October 1982 (CPDCC)

(a) These data were analysed in 6 hour blocks. A total of 87 and 111 gravity wave events were identified in the zonal and meridional planes respectively. Since no vertical beam was available, these events represent unambiguous determinations of scale, and are consequently quite selective, because some combinations of frequency and wavelength are more likely to produce an ambiguous determination of scale.

1000 events were possible for each pair of EW and NS aligned beams so that only 9 and 11% respectively of calculated phases lead to unambiguous determinations of scale. However, about 25% of the calculated phases had significant values of $(COH)^2$. With this point noted, we present the measurements of wavelength and phase velocity as histograms in Figure (7-2). The mean and standard deviation of the zonal and meridional wavelengths are 36±11 and 37±13 km respectively.

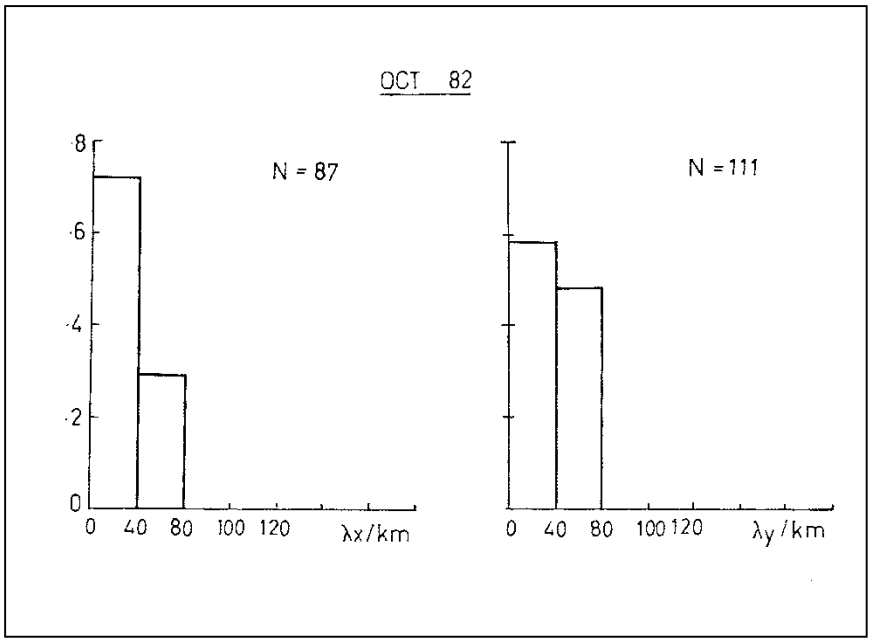

Figure (7-2) a. Histograms of occurrence of zonal and meridional wavelength for heights between 80 and 98 km for. October 1982

More waves are propagating Eastwards than Westwards (68 and 32% respectively). If these waves are propagating with downward phase progression, the momentum flux will have a sign such that $|\overline{u'w'}|$ is positive. Reference to Figure (6-28a) indicates that it is indeed positive. Like the results for May 1981 discussed in Section (6.10.1), these waves would appear to be associated with the mean momentum flux $\overline{u'w'}$ for this period of observation.

The phase velocities for the meridional scales indicate more waves propagating Northwards than Southwards (71 and 29% respectively.) These waves would transport momentum so that the sign of $\overline{v'w'}$ is positive if the phase progression is downward. However, as we noted in Chapter 6, the meridional momentum flux is not significantly different from zero. This is one of the limitations in presenting the data in this form; the amplitude and period of the waves are not evident.

Before considering the data in more detail, we note that more determinations of scale were made in the NS direction, and this could reflect the source region of the gravity waves on the filtering of zonally propagating waves by the lower level wind. Of the 198 determinations of scale only 15 were obtained in both planes for the same period and time. Most of these events occurred at heights above 90 km, and were in the 60 and 36-minute period range which are easy to resolve unambiguously. They were also often isolated events. Those that were not are shown in Table (7-1)

Table (7-1) summary of wave characteristics for coherent events identified between 80 and 98 km for October 1982. In this, and all of the other tables presented in this Chapter, the perturbation velocities have units of ms^{-1}, the wavelengths km, the Reynolds stress terms m^2s^{-2}, the horizontal phase velocity ms^{-1} and the angle of wave propagation α is measured in degrees clockwise from North.

ALT	u'	v'	λ_x	λ_y	λ	c	α	$\overline{u'w'}$	$\overline{v'w'}$
60 minutes, Block 5									
82	5	4	-67	39	34	9	-31	-0.08	+0.03
92	17	13	62	46	37	10	37	+0.85	+0.70

94	19	16	56	22	21	6	17	+1.41	+1.28
36 Minutes, Block 1									
90	9	6	65	-57	43	20	139	0.40	-0.02
92	9	8	48	41	31	14	41	0.42	+0.15
94	7	7	36	39	26	12	48	0.50	+0.41
36 Minutes, Block 6									
92	7	8	65	-62	21	137	0.10	-0.47	
94	10	10	43	-44	14	135	0.30	-0.29	

The Reynolds stress terms $\overline{u'w'}$ and $\overline{v'w'}$ have been calculated by applying Equation (4-34) to each frequency interval. The apparent decline in wavelength with height may be due to the fact that we have not taken the variation in beam separation with height into account, but since other measurements of wavelengths do not show similar behaviour, this seems unlikely. The mean wavelength of the 60-minute period wave is about 30 km, with a mean phase velocity of about 8 ms^{-1}. The variation in the sign of the zonal phase velocity with height may indicate that the wave at 82 km is not that detected at 92 and 94 km but it may also be due to an incorrect determination of the direction of propagation. As we noted in Chapter 4, this could occur if a number of waves propagating at different azimuth angles, but with similar frequencies are present.

The momentum flux term $\overline{u'w'}$, which is a measure of the difference between the mean square radial velocities measured in the Eastward and Westward beams is not significantly different from zero at 82 km. This means that it is not possible to determine the direction of propagation unambiguously, and it is likely that this is the reason for the variation in the zonal phase velocity with height in this case. We note that the $\overline{v'w'}$ term is also small at 82 km, but that the meridional phase velocity for this height is the same as that for the other heights. This is probably fortuitous. A similar situation applies in block one of the results for the 36-minute period wave for the meridional phase velocity.

The mean wavelength of the 36-minute period wave is about 36 km, with a mean phase velocity of about 17 ms^{-1}We note that apart from the direction of propagation, the character of the motions with this period are similar for observations separated by 24 hours.

At 92 and 94 km, the 60-minute motion is supplying a substantial momentum flux, which is consistent in sign with that for the entire period. The 36 period motions are also associated with a substantial momentum flux, but it is smaller in magnitude than that for the 60-minute motion. The upward flux of meridional momentum is opposite in sign for the 36 period motion for block 1 and 6, while the upward flux of zonal momentum is consistent in sign.

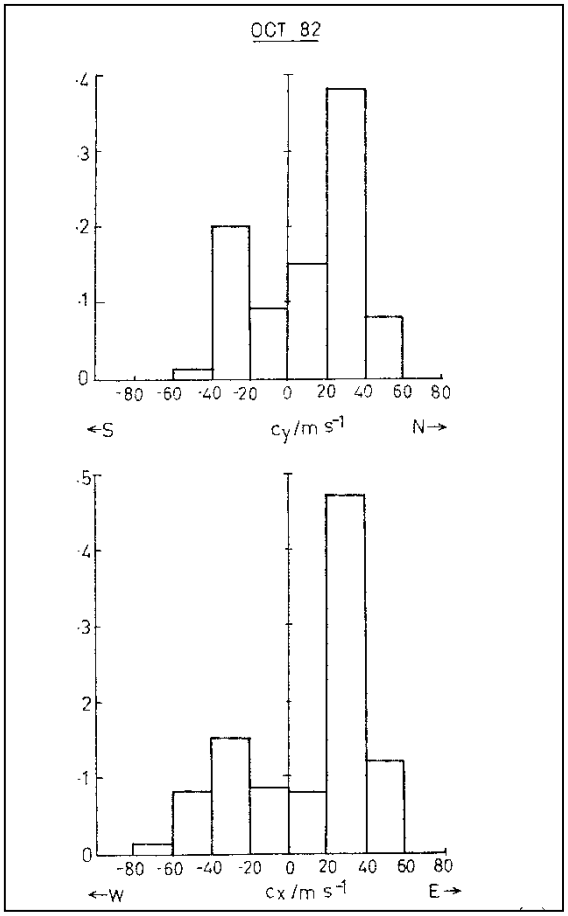

Figure (7-2b). Histograms of occurrence of zonal (c_x) and meridional (c_y) phase velocity for heights of 80-98 km for October 1982. Phase velocities are positive Northward and Eastward

If we omit the values in these results for which the direction of propagation is uncertain, we note that the 60-minute period wave is propagating towards the North-East, as is the 36-minute period wave in block 1. The 36-minute period wave in block 6 is propagating towards the South-East. Whether this reflects the filtering of the gravity wave spectrum by lower level winds, or the source region of the waves is uncertain.

Even though these are the only occasions when both zonal and meridional scales were determined simultaneously, we may obtain additional insight into the gravity wave field by grouping the results in each block of data according to the wave period. Because of the volume of these data, we present some representative examples in Table (7-2). Inspection of these results indicate that generally, consistency in scale from height to height is good. The perturbation velocities often increase with height, indicating wave growth. As for the results in Table (7-1), there is a tendency for the waves measured in each beam to be aligned so that they contribute approximately equally to the NS and EW beams. There are also occasions when adjacent heights indicate oppositely directed waves.

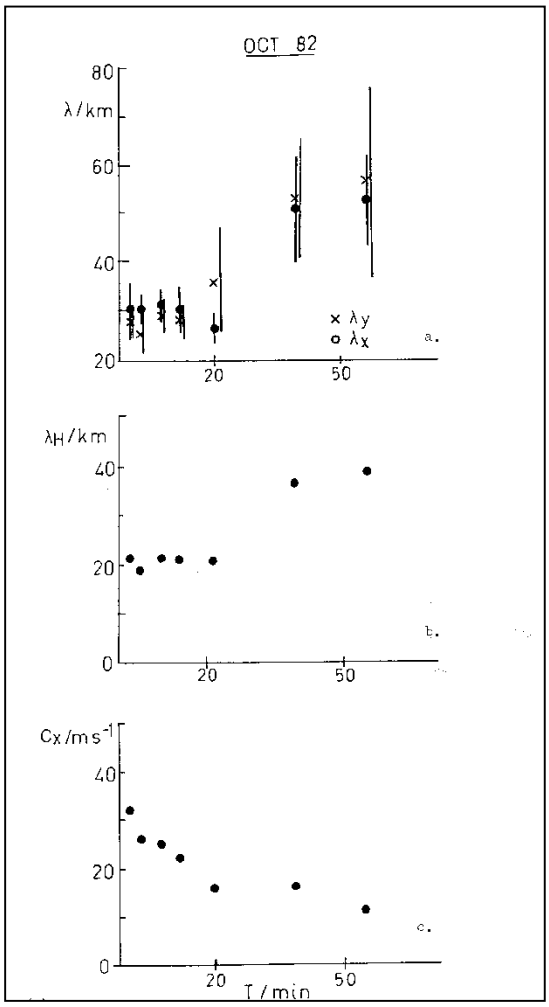

Figure (7-3a) The mean zonal and meridional wavelengths plotted as a function of wave period, Figure (7-3b), as for (a) but for total horizontal wavelength λ_H, and Figure (7-3c), the mean absolute phase velocity.

Table (7 -2a) 60 minutes

ALT	u'	v'	λ_x	λ_y	c_x	c_y	λ	c	α	$\overline{u'w'}$	$\overline{v'w'}$	Block
83	-	3	-	39	-	11	-	-	-	-	0.03	
89	8	-	-72	-	-20	-	-	-	-	-0.14	-	6
93	17	12	61	46	17	13	37	1	0 37	0.85	0.70	
95	19	15	56	56	16	16	40	11	46	1.41	1.61	
89	-	7	-	52	-	14	-	-	-	-	0.49	
91	-	6	-	-63	-	-18	-	-	-	-	-0.06	7
93	-	9	-	-55	-	-15	-	-	-	-	-0.60	
95	-	12	-	-49	-	-14	-	-	-	-	-0.25	
85	-	7	-	·55	-	-15	-	-	-	-	-0.41	
87	-	8	-	-58	-	-16	-	-	-	-	-0.27	9
95	-	11	-	52	-	14	-	-	-	-	0.66	
83	6	-	-48	-	-13	-	-	-	-	-0.13	-	
85	-	8	-	54	-	15	-	-	-	-	0.18	
87	4	-	-40	-	-11	-	-	-	-	-0.06	-	10
91	-	7	-	45	-	13	-	-	-	-	0.46	
93	-	11	-	42	-	12	-	-	-	-	1.31	
95	11	13	-42	37	-12	10	28	8	- 42	-0.25	1.90	

When all of the results are analysed to yield the mean horizontal wavelength, we note an increase in scale with period. This is shown in Figure (7-3a). mean wavelength increases from about 30 km at 11 minutes to about 54 km at 60 minutes. This result is in general agreement with that of Vincent and Reid (1983), who found an increase in scale from 45 km at 12 minutes to l20 km at 60 minutes. As we have noted, the results for October are somewhat more selective than those of Vincent and Reid (1983), because unlike these authors we have made no attempt to resolve the ambiguity in horizontal scale, or to obtain results for periods longer than 60 minutes. The mean horizontal wavelength λ_H *is* shown in Figure (7-3b). Inspection of this

diagram indicates that for periods less than 20 minute, $\lambda_H \sim 20\ km.$ For the 36 and 60 minute periods $\lambda_H \sim 40\ km.$ The corresponding mean absolute phase velocities are shown in Figure (7-3c). These are observed to decrease with increasing period from 32 ms^{-1}at 11 minutes to 11 ms^{-1}at 60 minutes.

Table (7 -2b) 36 minutes

ALT	u'	v'	λ_x	λ_y	c_x	c_y	λ	c	α	$\overline{u'w'}$	$\overline{v'w'}$	Block
91	8	6	+65	-57	+30	-26	43	20	139	0.40	-0.02	
93	9	8	48	41	22	19	31	14	40	0.54	0.20	2
95	7	7	36	39	17	18	26	12	46	0.50	0.41	
85	-	2	-	73	-	34	-	-	-	-	0.60	
87	-	2	-	50	-	23	-	-	-	-	0.01	3
93	-	8	-	55	-	26	-	-	-	-	0.18	
95	7	12	52	48	24	22	35	16	52	0.11	0.10	
85	-	3	-	43	-	20	-	-	-	-	0.01	6
95	10	7	-49	50	-23	23	35	16	-46	-1.33	0.07	
85	-	4	46	-	21	-	-	-	-	0.24	7	
91	6	-	63	-	29	-	-	-	-	0.20	-	7
93	6	8	65	-50	30	-23	40	18	142	0.10	-0.36	
95	10	9	49	-51	23	-24	35	16	134	0.30	-0.29	
83	-	3	28	-	13	-	-	-	-	0.08	-	
87	-	5	-	+67	-	31	-	-	-	-	0.09	
89	-	6	-	-50	-	-23	-	-	-	-	-0.02	8
91	-	9	-	-55	-	-26	-	-	-	-0.25	-	
93	-	8	-	-41	-	19	-	-	-	-	0.83	

89	-	4	-	66	-	31	-	-	-	-	0.23	
93	10	-	32	-	-15	-	-	-	-	-1.14	-	9
95	12	-	32	-	-15	-	-	-	-	-0.77	-	
85	-	6	-	46	-	+21	-	-	-	-	0.21	
87	-	8	-	43	-	-20	-	-	-	-	-0.05	10
95	-	6	-	50	-	-23	-	-	-	-	-0.28	
83	-	6	-	-37	-	-17	-	-	-	-	8.22	
85	3	-	43	-	20	-	-	-	-	0.00	-	
89	-	5	40	-	19	-	-	-	-	0.26	-	11
93	-	6	-	85	-	39	-	-	-	-	0.21	
95	10	7	49	63	23	29	39	18	53	0.73	0.38	
82	-	5	-	-27	-	-13	-	-	-	-	-0.07	
87	3	- 67	-	31	-	-	-	-	0.05	-	-	
89	4	-	58	-	27	-	-	-	-	0.00	-	
91	6	5	81	106	38	49	64	30	52	0.14	0.11	12
93	-	7	-	57	-	26	-	-	-	-	0.25	
95	10	-	52	-	24	-	-	-	-	1.03	-	

Table (7 -2c) Various other periods

ALT	u'	v'	λ_x	λ_y	c_x	c_y	λ	c	α	T
85	-	2	-	30	45	-	-	-		
89	-	11	-	32	-	51	-	-	-	11
91	10	8	-33	30	-52	48	22	33	132	
87	2	-	29	-	40	-	-	-	-	12

89	4	-	30	-	42	-	-	-	-	
91	8	4	31	26	43	36	20	28	40	
93	7	8	27	25	38	35	18	29	44	
95	-	12	-	26	-	36	-	-	-	
89	-	2	-	28	-	33	-	-	-	
91	1	3	33	33	39	39	23	27	46	14
93	7	27	-	32	-	-	-	-	-	
87	4	-	30	-	31	-	-	-	-	
89	10	-	28	-	29	-	-	-	-	16
91	6	10	31	29	32	30	21	22	43	
82	3	-	21	-	18	-	-	-	-	
83	2	-	28	-	23	-	-	-	-	
89	-	3	-	45	-	38	-	-	-	20
91	8	-	29	-	24	-	-	-	-	
95	-	24	-	27	-	23	-	-	-	

7.3.2 May 1982 (OPDC)

These data were analysed using the procedure outlined in Chapter 4 for the TC(CP) beam arrangement. The distribution of wavelengths and phase velocities for this entire period of observations is shown in Figure (7-4). Inspection of this diagram indicates a strong peak in the 40-80 km wavelength range. The mean zonal wavelength is 41 ±20 km.

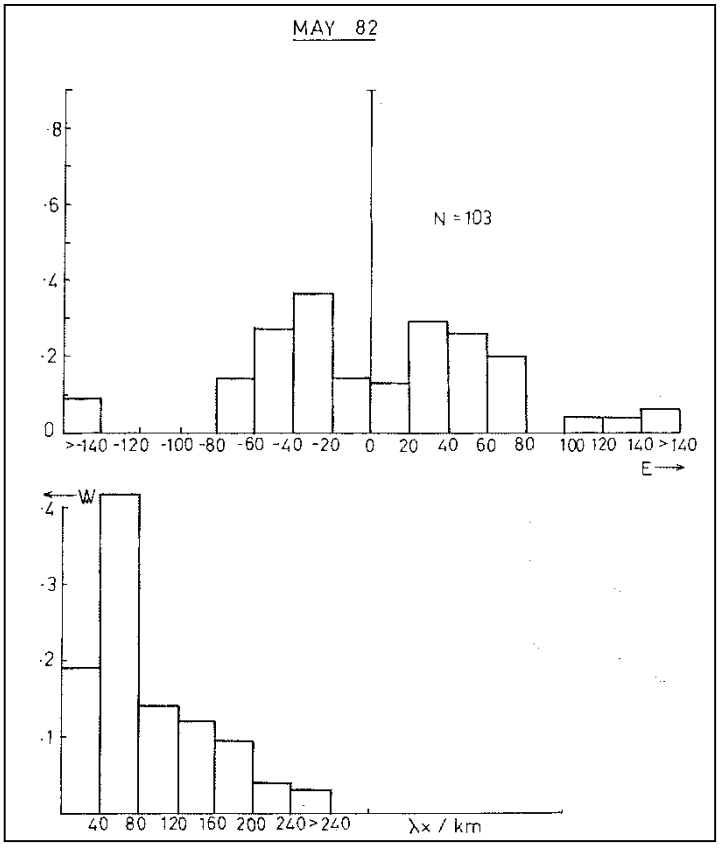

Figure (7-4a) (Top) As for Figure (7-2a) for May 1982 but for zonal component only. Figure (7-4b) as for Figure (7-2b) but for zonal component only.

Table (7-3a) characteristics of a 120-minute period wave in May 1982 data

Alt	u'	λ_x	c_x	$\overline{u'w'}$	**Block**
94	16	63	9	0.64	1
90	10	63	9	0.10	2
80	7	20	3	0.21	4

The majority of phase velocities lie in the range of +80 to -80 ms^{-1}, although there are a few events with phase velocities greater than 140 ms^{-1}. The distribution of phase velocities appears to be reasonably symmetrical about zero phase velocity, unlike those for May 1981 and October 1982. However, as we noted in Chapter 6, most determinations of scale were made in two twelve hour blocks which corresponded to. minimums in momentum flux, and there was a tendency for more determinations to be made with increasing height. The lower occurrence of waves with phase velocities near zero may reflect the stronger lower level winds during this period of observation. The longer data lengths used in this analysis extended the

range of periods suitable for cross spectral analysis so that periods of 72 and 120 minutes were available. Few determinations were made at the longer period; three out of a possible 40. These are shown in Table (7-3a).

Better results were obtained for motions with a period of 72 minutes and these are shown in Table (7-3b). In block 2 there is good evidence of a wave with a zonal horizontal of about 35 km. In block 4 there is evidence of a gravity wave with a large horizontal wavelength. The question mark indicates that there is considerable uncertainty in this estimate.

Table (7-3b) Characteristics of a 72-minute period wave in May 1982 data

Alt	u'	λ_x	c_x	$\overline{u'w'}$	**Block**
86	8	92	21	0.27	1
80	7	-30	-7	-0.06	2
86	6	-38	-9	-0.18	2
88	6	-33	-8	-0.19	2
90	7	-38	-9	-0.11	2
94	9	+43	+10	+0.13	2
96	10	-44	-10	-0.45	2
80	10	400?	93?	0.21	4

If the gravity wave spectrum is broadband, analysis in discrete frequency intervals may be misleading. A more general picture can be obtained by presenting the results as in Table (7-4). The blocks in this table represent 12 hour periods of data. We note the sparsity of events in block three, which corresponds to the major enhancement in momentum flux discussed in Chapter 6. There are also fewer determinations of horizontal scale in block 1.

Table (7-4) The zonal wavelength (λ_x) for various periods and heights measured in block one of the May 1982 data

Alt	**120**	**72**	**51**	**40**	**33**	**28**	**24**	**21**	**19**	**17**	**16**	**14**	**13**	**12**	**11**	**10**	**9**	**8.78**	**8.23**
80																			
82																			
83										-21									34

85															26			
87		90		109								29						
89												31			-28			
91							-29			-34		37						-33
93			-127	100								38						
95	63										27							
98															-23			

Table (7-4) The zonal wavelength (λ_x) for various periods and heights measured in block two of the May 1982 data

Alt	**120**	**72**	**51**	**40**	**33**	**28**	**24**	**21**	**19**	**17**	**16**	**14**	**13**	**12**	**11**	**10**	**9**	**8.78**	**8.23**
80																			
82		-30												19		19			
83			45			-17													
85		-37	46	-42										28					
87		-33	54	-59						-26									
89		40																	
91	63		85		69				-26	28							49		
93		-43		-55					-26	25		29						29	29

95		-44		-49		-35			27		26			-26		29	-25		26
98								-26	-21					25					28

Table (7-4) The zonal wavelength (λ_x) for various periods and heights measured in block three of the May 1982 data

Alt	**120**	**72**	**51**	**40**	**33**	**28**	**24**	**21**	**19**	**17**	**16**	**14**	**13**	**12**	**11**	**10**	**9**	**8.78**	**8.23**
80																			
82				-25					-26										-19
83						-19													
85						-23													
87																			
89															50	168			
91																			
93																			
95																			
98					64							25							

Table (7-4) The zonal wavelength (λ_x) for various periods and heights measured in block four of the May 1982 data

Alt	**120**	**72**	**51**	**40**	**33**	**28**	**24**	**21**	**19**	**17**	**16**	**14**	**13**	**12**	**11**	**10**	**9**	**8.78**	**8.23**
80																			
82		392																	
83	23		70	64															
85		50												-29		31	27	54	

87		-62	105	17								32		
89														
91	203					30				-32				
93					26		29	-32	-32					
95	58	43	47		25					-23	26			25
98			66		24	25	91			-27	25		25	

In block 2 we note a tendency for events to occur in the 72-40-minute period range. In the period range of 17-19 and 8-11 minutes, a number of events are noted, generally above 90 km. At these shorter periods, the scales determined appear to have been resolved correctly, because they are consistent in height. The same general distribution of scales is noted in Block 2 and 4, when the momentum flux was not significantly different from zero, and the pattern is not evident 1n block 3. The importance of this observation is uncertain. There does not appear to be any obvious reason for fewer determinations of horizontal scale to be made when there is an enhancement in momentum flux.

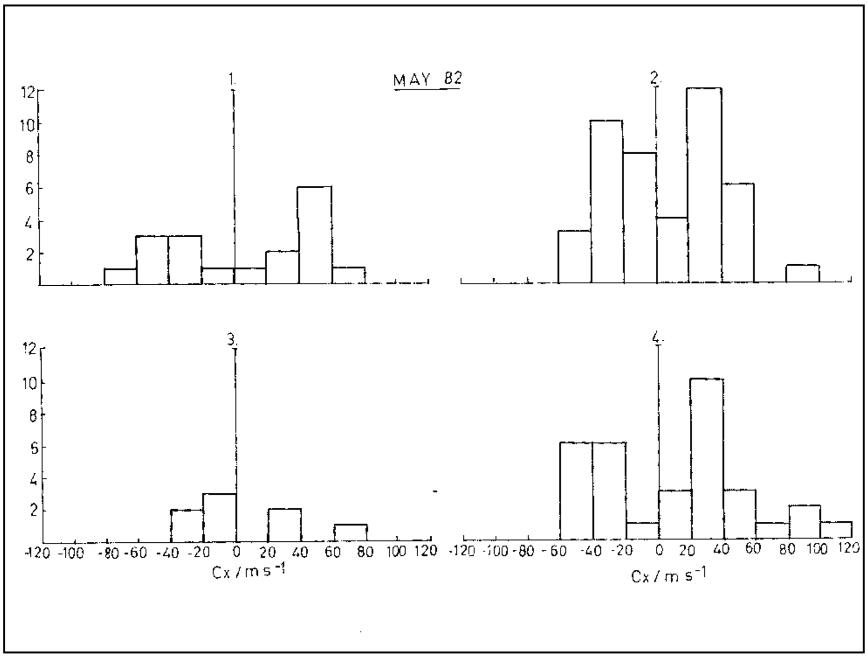

Figure (7-5) Zonal phase velocities for consecutive 12 hour periods of the May 1982 data. For details see text

The phase velocities for each 12-hour block are shown in Figure (7-5). The number of events in each velocity range are shown as a percentage of the total number of wavelengths

determined. These results indicate general agreement in the distribution of phase velocities for each 12-hour period of data for blocks 1, 2 and 4, but because so few determinations of scale were made in block 3, there is little more that we may say. The mean wavelength for each period is shown in Figure (7-6) and although there is considerable scatter, there is a tendency for the horizontal scale to increase with increasing period. Table (7-5) provides a little more detail on motions with periods of 51, 40 and 19 minutes.

Table (7-5) Characteristics of waves of various periods identified in the May 1982 data

Alt	u'	λ_x	c_x	$\overline{u'w'}$	**Block**
51 minutes					
93	6	-127	-7	-0.34	1
83	8	45	15	0.12	2
85	6	46	15	0.14	2
87	9	54	18	0.01	2
91	6	85	28	0.23	2
83	7	70	23	0.16	4
91	6	203	66	0.11	4
95	9	-58	-19	-0.08	4
40 minutes					
87	4	109	36	+0.07	1
93	5	-100	-33	-0.16	1
85	6	-42	-14	-0.09	2
87	6	9	-19	-0.31	2
93	8	-55	-18	-0.05	2
95	12	-49	-16	-0.07	2
82	10	-25	-8	-0.28	3
83	4	64	21	+0.01	4
87	5	-62	-20	-0.06	4
95	7	43	14	0.19	4
19 minutes					
91	**7**	-26	-23	-0.16	2
93	**9**	-26	-23	-0.14	2
98	**9**	-26	-23	-0.12	2

82	**4**	-26	-23	-0.05	3
93	**7**	26	-23	0.02	4
95	**13**	25	-22	0.29	4
98	**13**	24	-21	0.07	4

To partially overcome the lack of resolution for those motions with periods greater than about an hour, the entire data lengths for May was cross spectrally analysed. The mean zonal wavelength for periods greater than about 30 minutes is shown in Figure (7-7). The error bars indicate the standard deviation in the measured scales for each period. Between 30 and 100 minutes, the results are in good agreement with those shown in Figure (7-6). Above 100 minutes' period, there is a rapid increase in measured scale, and it is evident that a motion with a very large horizontal scale was present during this period of observation.

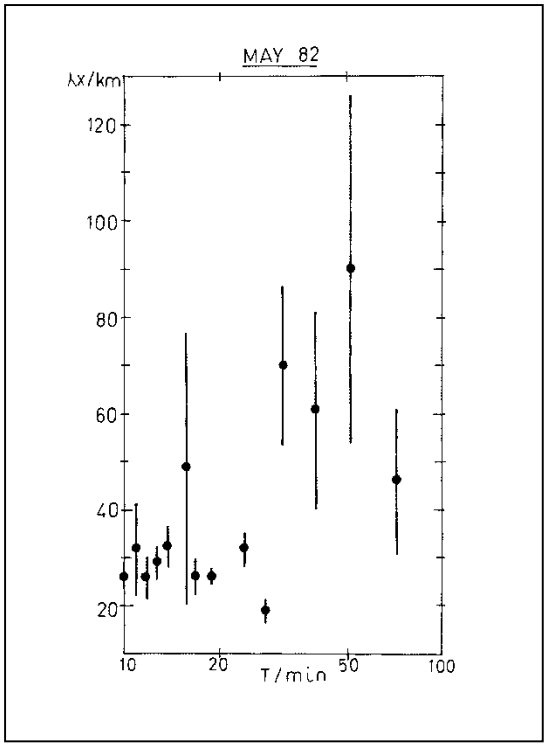

Figure (7-6) The mean zonal wavelength for May 1982 plotted as a function of wave period.

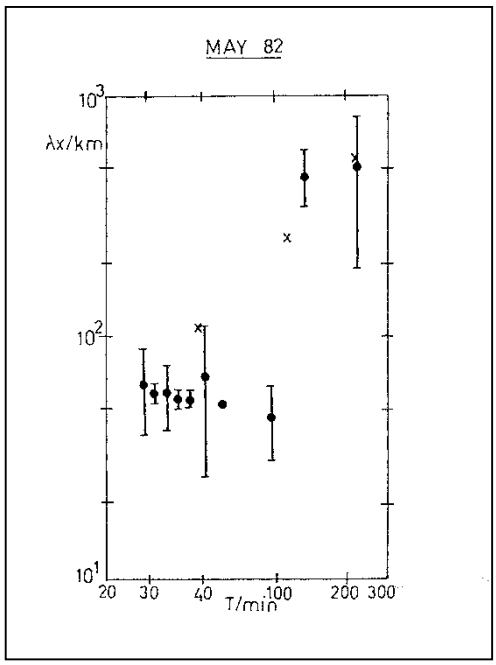

Figure (7-7) As for Figure (7-6) but results were obtained by cross spectral analysis of the entire May 1982 data set. Vincent's (1984) results are shown as crosses.

Also shown in Figure (7-7) are Vincent's (1984) estimates of the horizontal wavelengths. These results have been plotted at the centre frequency of each octave band. These results were obtained by assuming a mean vertical wavelength of about 12 km, and since we would expect the vertical wavelengths to increase with increasing frequency, Vincent's estimate for the short periods may be uncertain. At the longer periods, agreement between Vincent's (1984) results and those for May 1982 is reasonable. It should be noted that Vincent's results refer to the horizontal wavelength, while the May 1982 results refer to its zonal component.

For an isotropic wavefield, the mean horizontal wavelength for the May results would be about 40 km for motions with periods between 30 and 100 minutes, and about 350 km for the longer period motions. If this correction is applied, the agreement at the longer periods is still reasonable.

7.3.3 February 1982 (OPDC)

Like the May 1982 results, these data have been analysed in twelve hour blocks, and whilst a vertical beam was available, the data presented here have been analysed using the DCC beam theory only. Rather few determinations of scale were made for these observations. Out of a possible 580, only 46 were obtained.

The phase velocity and horizontal wavelength are shown in Figure (7-8). Two peaks are evident in the wavelength histogram, but this may be due to the small sample. The mean wavelength is 84±95km, and this corresponds to periods less than and including 2 hours. The mean wavelength for periods less than an hour is 44±ll km. The phase velocities indicate a tendency for Westward wave propagation, although there is a peak at +60 - 80 ms^{-1}

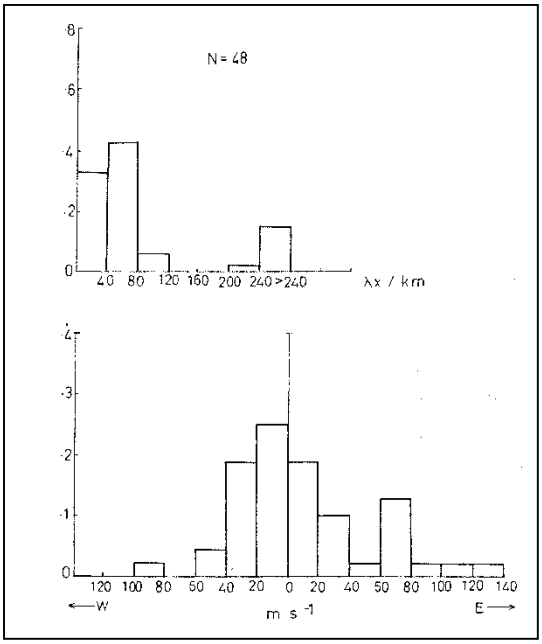

Figure (7-8) As for Figure (7-4a and b) but for February 1982

Sixteen events with periods between one and two hours were detected. The mean wavelength of these was 221±219 km. Those corresponding to the 120-minute period are shown in Table (7-6). Inspection of these results indicates that in block 1 and 5, a motion with a large horizontal scale was present. Because of the uncertainty in the phase, all we may say is that the horizontal wave- length is in the range of 300 – 1000 km. The corresponding phase velocities are large and Eastward, and correspond to the peak in the phase velocity histogram noted above. Block 3 and 6 indicate waves with shorter wavelengths propagating Westwards. We note that the perturbation velocities are relatively large for the waves of this period for all blocks.

The results for motions with a period of 72 minutes show evidence of a long wavelength gravity wave in block 5, but apart from this, most measured wavelengths are in the 50-70 km range. The 14-minute period wave has smaller perturbation velocities and wavelengths which are consistent between blocks 1 and 4. Propagation is westward in both cases. The mean wavelength for each period is shown Figure (7-9), and the results are generally consistent with those for May (1982).

Table (7-6) Characteristics of waves of various periods identified in February 1982 data

Alt	u'	λ_x	c_x	$\overline{u'w'}$	Block
120 Minutes					
85	8	460	64	0.18	1
87	9	450	63	0.36	1
89	8	560	78	0.06	1
85	11	-32	-4	-0.28	3
93	19	·-215	-30	-2.02	3
89	9	600	83	0.04	5
91	13	570	79	0.20	5
91	8	-110	-15	-0.11	6
95	9	-87	-12	-0.03	6
72 Minutes					
85	8	52	12	-0.21	3
87	9	71	16	-0.29	3
93	8	47	9	-0.26	4
98	18	41	10	-2.34	4
89	9	-560	130	-0.05	5
93	10	-90	-21	-0.01	6
95	9	-70	-46	-0.12	6
14 Minutes					
33	4	-28	-33	-0.03	1
85	3	-25	-30	-0.02	1
87	4	-33	-39	-0.01	4
95	7	-29	-35	-0.02	4

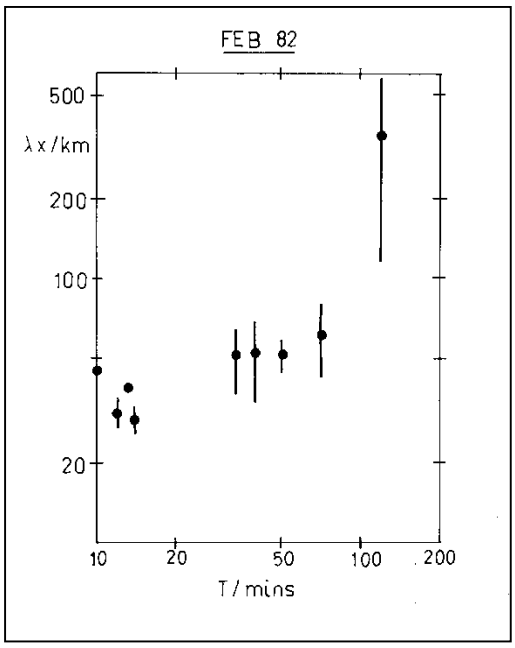

Figure (7-9) As for Figure (7-6) but for February 1982.

7.3.4 April 1982 (OPDC)

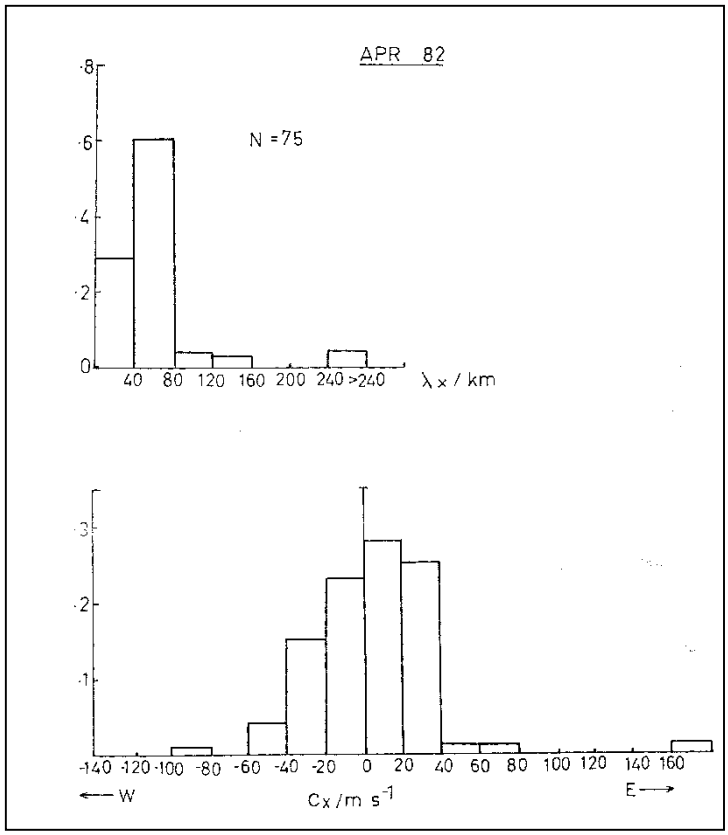

Figure (7-10) As for Figure (7-4) but for April 1982

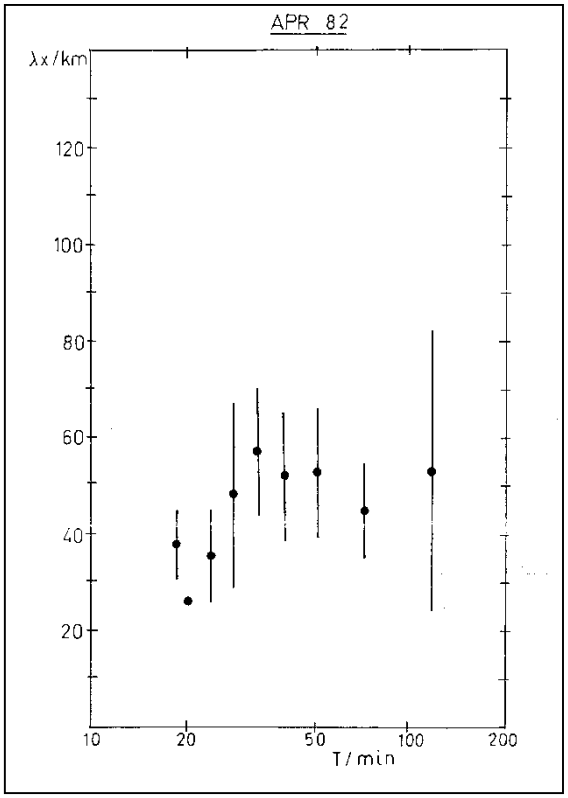

Figure (7-11) As for Fig, (7-6) but for April 1982.

These data were analysed in 12 hour blocks and like the February 1982 results, only the DCC beam analysis has been applied. The zonal wavelengths and phase velocities are shown in Figure (7-10). 75 wavelengths were determined, and like the other results obtained using DCC beams, this constitutes a small proportion of the total. number of coherent events. This may be reflected in the distribution of wavelengths. The mean zonal wavelength is 45±12 km. There are more waves propagating Eastward than Westward (57 and 43% respectively), and most phase velocities lie in the ±40 ms^{-1} range.

We have given numerous examples of gravity wave events for the other observational periods, and little additional information will result from doing the same for this period. However, we note that the results are consistent with the other observations. The mean wavelength for each period is shown in Figure (7-11).

7.3.5 November 1981 TC(CP)

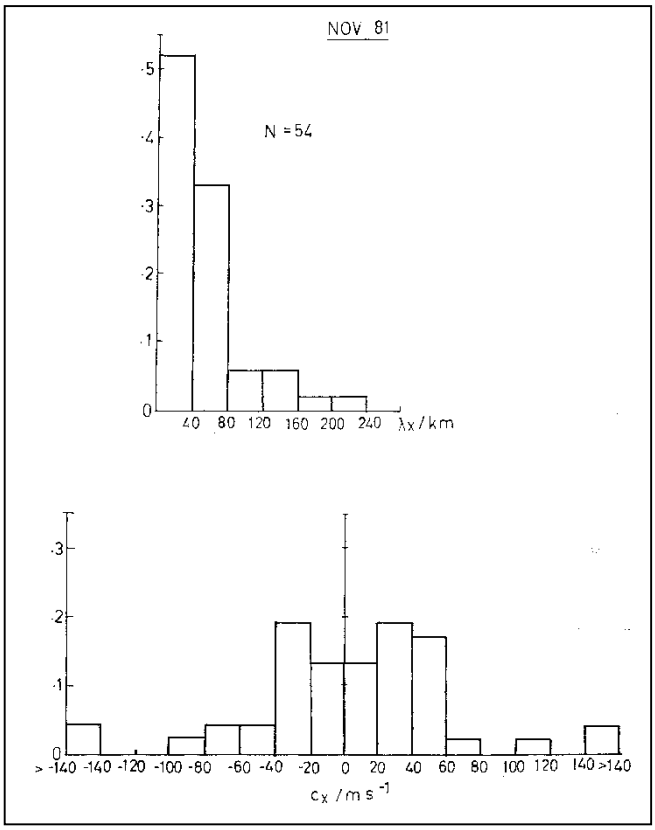

Figure (7-12) As for Figure (7-4) but for November 1981

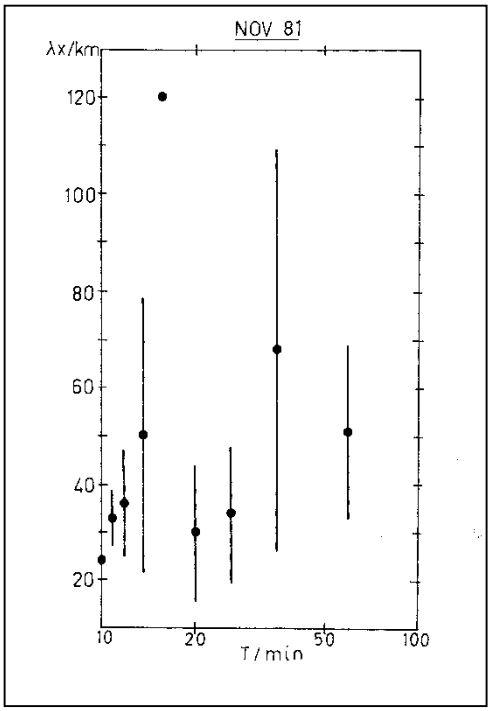

Figure (7-13) As for Figure (7-6) but for November 1981.

These data were analysed in six hour blocks. Only the 82 – 90 km height range has been analysed but all three beams were used to measure scale. A total of 54 events were detected, and the distributions of zonal wavelength and phase velocity are shown in Figure (7-12). The mean zonal wavelength is 48±28km. Most phase velocities are in the ±40 ms^{-1} range, although there are some events with phase velocities in excess of ±140 ms^{-1}. There are slightly more events propagating Eastwards than Westwards (56 and 44% respectively). The mean wavelength for motions at each period is shown in Figure (7-13). These results exhibit considerable scatter and a large mean wavelength is evident at 16 minutes. Only three events were detected at this period, two of which had wavelengths of about 170 km.

7.4 Discussion

The results we have presented are representative of a much larger data set. Because of the weak mean horizontal winds during the October 1982 run, and because both zonal and meridional wavelengths were obtained, we have tabled numerous examples of phase velocities and wavelengths for this period. These should provide a good measure of the scales present with periods less than about an hour.

It is clear that the DCC beam technique as described in Chapter 4 results in the determination of numerous events which are consistent with a gravity wave interpretation. However, there are occasions when the phase velocities measured at different heights for the same time and period are of opposite sign. Sometimes this can be ascribed to similar powers being received in the DCC beams for that frequency interval and time. This complicates the determination of the direction of propagation, and is a limitation of the technique. At other times, oppositely directed phase velocities are measured for a given frequency interval and time at heights separated by about 10 km. These events allow the interpretation that different waves are being measured. We believe that these two explanations of inconsistency in the phase velocities with height are sufficient to explain our results.

We have also measured a longer period wave motion with a period of about 120 minutes in the February 1982 results. The uncertainty in the cross spectral phase means that determinations of scale greater than about 200 km are very uncertain. However, this is a fundamental restriction on the measurement of horizontal scale for closely spaced antenna beams and is related to the separation of the beams. The results of Smith and Fritts (1983), who found a

long period wave with a large horizontal wavelength using the DC beam configuration at the Poker Flat DW radar, must be subject to a similar uncertainty.

We stress that while there is a restriction on the measurement of scale, there is no such restriction on the measurement of momentum flux. For instance, the momentum flux calculated for the 120-minute period motion detected in the February 1982 results should be correct to within the accuracy of the mean square radial velocities for the frequency interval determined by the cross spectral analysis, and this is not related to the beam separation. About 25% of all calculated cross spectral phases had significant $(COH)^2$ these, about half allowed the horizontal scale to be determined unambiguously.

By calculating the cross spectral phase between vertical and eastward beams for the data obtained in May 1982 and November 1981, and applying Equation (4-84) about 80-90% of the total number of events with significant $(COH)^2$ led to determinations of horizontal scale. This consistency indicates that the events we are measuring correspond to wave motion and are generally not random events. This is evident in any case by inspection of most of the tabled results.

Table (7-7) summarizes the mean zonal wavelengths for each period of observation for those motions with periods less than one hour, and the mean zonal wavelengths for motions with periods within the octave bands analysed by Vincent (1984). Also shown are the standard deviations in the measured wavelengths. Inspection of the values shown in this table indicate good agreement in the mean wavelength for motions with periods less than one hour. The standard deviations in the results for May and November are larger than those for the other periods, and this may reflect the more complete analysis of these particular results. The mean wavelengths for all of the observational periods in this range of wave frequencies is 42 km.

Vincent's (1984) values for motions with periods in the range 0.1-0.5 and 0.5-1.25 hours are $\lambda_H = 60$ and $\lambda_H = 108\ km$ respectively. Reference to Table (7-7) indicates that the values of and hence λ_H (for a wave field isotropic in azimuth) obtained in this work are somewhat lower. This may be due to the fact that some of the results have been incompletely analysed, but it is noteworthy that only 25% of all cross spectral phases calculated have significant values of $(COH)^2$. There may be many other gravity waves present which are not resolved by the DCC technique, the reasons for which have been discussed in Chapter 4.

Table (7-7) The mean zonal wavelengths for each period of observation for those motions with periods less than one hour, and the mean zonal wavelengths for motions with periods within the octave bands analysed by Vincent (1984).

$\lambda_x(km)$	$T < 1h$	$0.1 < T < 0.5\ h$	$0.5 < T < 1.25\ h$
February	44±11	41±9	72±41
April	44±11	37±9	52±5
May	38±21	30±9	76±13
October	36±11	29±2	-
November	48±28	45±31	-
Mean	42	36	67

Figure (7-14b) illustrates all of the measured zonal wavelengths plotted as a function of wave period. Vincent's (1984) results are included for reference and are shown as crosses and the mean zonal wavelength plotted as a function for each wave period is shown in Figure (7-14a). We note the tendency for the zonal wavelength to increase with increasing period, and the consistency between the values of horizontal scale for each wave period for the various observational runs.

These results would appear to be the most complete set of observations of the horizontal scale of gravity waves with periods less than about an hour available.

7.5 Summary and Conclusions

The theory described in Chapter 4 to measure the horizontal scale of gravity waves using DCC beams has been applied to observations taken over a period of about two years. The mean zonal wavelength for motions with periods less than about an hour was found to be about 42 km. A number of tables summarizing various gravity wave parameters have been presented.

consistency of these results indicates that the events being measured are gravity waves and not just noise.

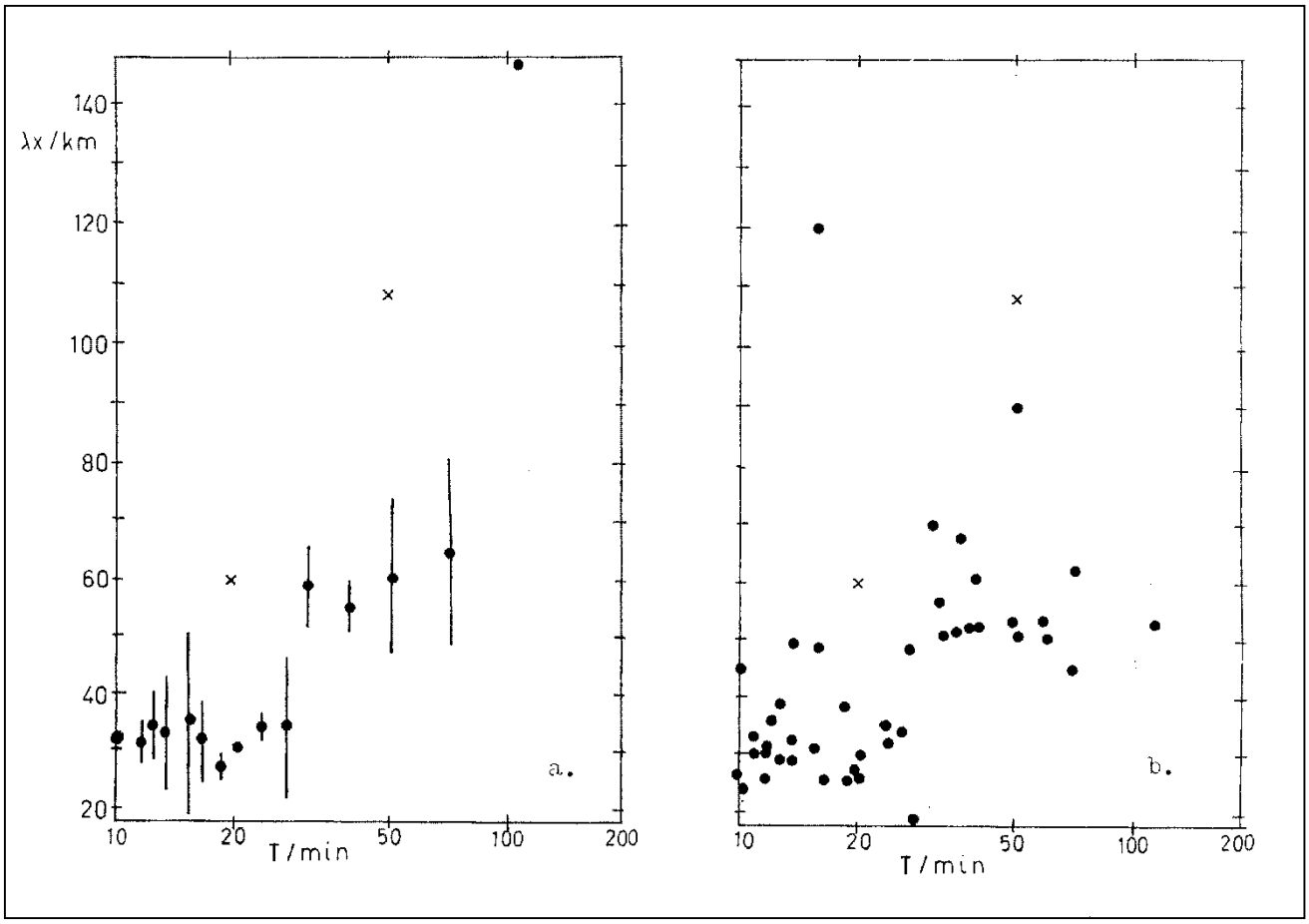

Figure (7-14a) The mean zonal wavelength plotted as a function of wave period for all observations presented in this Chapter, and Figure (7-14b) all of the zonal wavelengths for each period of observation plotted on same diagram. Vincent's (1984) results are shown for reference as crosses.

The results presented are preliminary, and like the momentum flux measurements described in the last Chapter, have not been exploited fully. An obvious extension of this work is the calculation of the ratio of the momentum flux associated with coherent motions to that obtained from the mean square radial velocities measured in DCC beams. A limitation of these observations is that with the exception of the October 1982 results, only the zonal scale of wave motions has been obtained. Obtaining both components of the wavelength would allow a measure of the isotropy of the gravity wave field to be obtained.

8. Summary and Conclusions

Doppler radar techniques have been used to study internal atmospheric gravity waves in the ionospheric D-region. Using a radar beam configuration that differs from that usually applied in that the beams are offset at equal angles from the zenith in the same vertical plane, the upward flux of zonal and meridional momentum have been measured. This allowed the gravity wave drag on the mean flow to be measured. The same beam configuration also enabled the horizontal scale of gravity waves with wavelengths less than about 200 km to be measured. In this Chapter the main results of the work are summarized.

8.1 Measurement Techniques

8.1.1 Ideal Case

Examination of the parameters that can be measured using multi beam radars, or radars with a beam swinging capability, has shown that the conventional Doppler radar beam configuration, that is, a vertical and an off-vertical beam, can be used to measure horizontal and vertical scales of gravity motion and obtain a measure of the horizontal kinetic energy.

The upward flux of horizontal momentum can be measured for scales longer than about 200 km with a tilt angle of 11.6° at a height of 85 km, but without additional information about the actual gravity wave spectrum, scales cannot be separated.

The DCC beam technique, in which two Doppler radar beams are offset at equal and opposite angles from the zenith in the same vertical plane, can be used to obtain an accurate measurement of the Reynolds stress with only the assumption that statistics of the atmospheric motions are horizontally homogeneous.

Spatial covariance estimates of the horizontal and vertical kinetic energy are poor, but a term containing both the horizontal and vertical components may be obtained. However, unless the period and scale of the wave are known, these components cannot be obtained separately. Horizontal scales of the motion can be measured directly, but the vertical scale cannot, and there may be an ambiguity in k_x. The beams do not have to be complementary, and the Reynolds stress can be obtained, as long as neither beam points vertically.

With three coplanar beams the horizontal and vertical kinetic energy can be obtained using only the assumption of the horizontal homogeneity of the wind field. In addition, both

horizontal and vertical scales of the wave field can be measured unambiguously in principle, and the Reynolds stress may be obtained.

8.1.2 DW Measurements with Relatively wide Beamwidths

The effective antenna beam angle, that is, that formed by the convolution of the receiving array polar diagram and the backscatter angular polar diagram, was found to significantly underestimate the apparent beam angle when the BP aerial array was used to measure the horizontal wind velocity in the D-region. Using independent measurements of the polar diagram of the backscatter, and the known antenna beam, it was shown that agreement between DW spectra measured in this work and seasonally averaged independent measurements of the spectra of horizontal wind velocity obtained at the same site improved significantly. A direct comparison of SA and DW methods indicated that better agreement is found when the effective beam angle is taken into account, and indirect comparisons of SA and DW measurements supported the evidence that DW radial velocities underestimate the true values of this quantity.

8.1.3 Vertical Velocities

A comparison of vertical velocities measured in both wide and narrow vertically directed Doppler radar beams indicated that vertical velocities could be obtained using phase coherent SA equipment when averaged over periods of 2-3 days, but the variability in agreement from day to day suggested that better results would be obtained if information about the angle of return of backscatter was obtained. It was found that in general, it was not possible to obtain the vertical wind from radial velocities measured in DCC beams because the horizontal variation of $\bar{u}$ and $\bar{v}$ is significant.

8.2 Observations

8.2.1 Vertical Velocities

Preliminary measurements of the mean vertical wind ln the 80-100 km height range indicated magnitudes as large as $0.5 - 1\ ms^{-1}$ were typical. There was some evidence that in this height range, the vertical motion was downward for much of the year. Typical mean square radial velocities for motions with periods between 8 min and 8 hours were found to be about $7\ m^2s^{-2}$ rising to about $7\ m^2s^{-2}$ at 98 km.

8.2.2 Momentum Flux and Gravity Wave Drag

The largest values of $\overline{u'w'}$ and $\overline{v'w'}$ were found in the summer, and in general, the magnitude of either term was less than 3 $m^2 s^{-2}$. The momentum flux was found to be variable at a variety of time scales, from 3 hours in November 1981 results to 2 days in the case of the July 1982 results.

The body force associated with the flux convergence in the 80-98 km height range was found to be substantial, and appeared to balance the Coriolis torque due to the mean meridional wind velocity in many months.

The Winter results indicated that longer period motions, in particular transient planetary waves, could supply the necessary wave drag, but this is by no means certain, because the observations were made at a single site and the wave drag and Coriolis torque should balance when zonally averaged. The results obtained in February 1982 indicated that transient planetary waves, notably the "2-day wave" may be important in the summer hemisphere because the body force varied considerably from day to day.

The zonal body force was found to be a component of a total body force that was aligned closer to the North-South direction in July 1982, and the meridional body force was correspondingly larger. In October 1982, the total body force was aligned closer to the East-West direction.

Results obtained in February and May 1982 indicated that wave saturation is transient in time and broadband. The May results also suggested that momentum deposition is associated with saturated or breaking waves. An enhancement in the momentum flux in the May results appeared to be associated with fewer determinations of horizontal scale.

The vertical mean square velocities supported the evidence that momentum deposition was associated with saturated or dissipating waves.

High frequency wave motions ($T < 2\ hours$) appeared to contribute the substantial portion of the momentum flux for periods between 8 minutes and 8 hours in results obtained in October 1982 and May 1981.

The results as a whole supported theories stressing the importance of gravity wave drag for middle atmosphere dynamics, and suggest that gravity wave transmission and momentum deposition are transient in time.

8.2.3 Horizontal Scale

About 25% of all calculated cross spectral phases had significant $(COH)^2$. Of these, about half allowed the horizontal scale to be determined unambiguously. By also calculating the phase between a vertical beam and one off vertical beam to reduce the ambiguity, about 80-90% of those events with significant $(COH)^2$ led to determinations of horizontal scale.

The mean zonal wavelength of gravity wave motions measured with the DCC beam configuration for periods less than one hour was found to be about 42 km. The zonal wavelength tended to increase with increasing period rising from about 30 km at 20 minutes to 500 km at about 200 km in the May 1982 results.

The zonal phase velocities measured in the May 1981 and October 1982 observational periods had preferred directions of propagation that appeared to be associated with the upward transport of zonal momentum.

8.3 Future Work

Doppler radar technique in general, and the DCC beam arrangement in particular, have been shown to be particularly powerful devices for investigating the dynamics of the middle atmosphere. The extension of the procedures outlined in this work to MST VHF radars should greatly increase our understanding of the dynamics of this region.

9. References

Armstrong, E.B., 1982. The association of visible airglow features with a gravity wave. *Journal of Atmospheric and Terrestrial Physics*, *44*(4), pp.325-336.

Arnold, F. and Krankowsky, D., 1977. Ion composition and electron-and ion-loss processes in the Earth's atmosphere. In *Dynamical and chemical coupling between the neutral and ionized atmosphere* (pp. 93-127). Springer Netherlands.

Awe, O., 1964. Effects of errors in correlation on the analysis of the fading of radio waves. *Journal of Atmospheric and Terrestrial Physics*, *26*(12), pp.1257-1271.

Balsley, B.B., Cianos, N., Farley, D.T. and Baron, M.J., 1977. Winds derived from radar measurements in the Arctic troposphere and stratosphere. *Journal of Applied Meteorology*, *16*(11), pp.1235-1239.

Balsley, B.B. and Riddle, A.C., 1984. Monthly mean values of the mesospheric wind field over Poker Flat, Alaska. *Journal of the atmospheric sciences*, *41*(15), pp.2368-2380.

Blackman, R.B. and Tukey, J.W., 1958. The measurement of power spectra, Dover, New York

Booker, J.R. and Bretherton, F.P., 1967. The critical layer for internal gravity waves in a shear flow. *Journal of Fluid Mechanics*, *27*(03), pp.513-539.

Bretherton, F.P., 1969a. Waves and turbulence in stably stratified fluids. *Radio Science*, *4*(12), pp.1279-1287.

Bretherton, F.P., 1969b. Momentum transport by gravity waves. *Quarterly Journal of the Royal Meteorological Society*, *95*(404), pp.213-243.

Bretherton, F.P., 1969c. On the mean motion induced by internal gravity waves. *Journal of Fluid Mechanics*, *36*(04), pp.785-803.

Briggs, B.H., 1977a. Ionospheric drifts. *Journal of Atmospheric and Terrestrial Physics*, *39*(9), pp.1023-1033.

Briggs, B.H., 1980. Radar observations of atmospheric winds and turbulence: A comparison of techniques. *Journal of Atmospheric and Terrestrial Physics*, *42*(9), pp.823-833.

Briggs, B.H., Phillips, G.J. and Shinn, D.H., 1950. The analysis of observations on spaced receivers of the fading of radio signals. *Proceedings of the Physical Society. Section B*, *63*(2), p.106.

Briggs, B.H., Elford, W.G., Felgate, D.G., Golley, M.G., Rossiter, D.E. and Smith, J.W., 1969. Buckland Park aerial array. *Nature*, *223*, pp.1321-1325.

Browning, K.A. and Wexler, R., 1968. The determination of kinematic properties of a wind field using Doppler radar. *Journal of Applied Meteorology*, *7*(1), pp.105-113.

Brownlie, G.D., Dryburgh, L.G. and Whitehead, J.D., 1973. Measurement of the velocity of waves in the ionosphere: A comparison of the ray theory approach and diffraction theory. *Journal of Atmospheric and Terrestrial Physics*, *35*(12), pp.2147-2162.

Carter, D.A. and Balsley, B.B., 1982. The summer wind field between 80 and 93 km observed by the MST radar at Poker Flat, Alaska (65 N). *Journal of the Atmospheric Sciences*, *39*(12), pp.2905-2915.

Caton, P.A.F., 1963. Wind measurement by Doppler radar. *Meteor. Mag*, *92*(21), pp.3-222.

Chapman, S. and Lindzen, R.S., 1970, *Atmospheric Tides*, D. Reidel, Dordrecht, Holland

Charney, J.G. and Drazin, P.G., 1961. Propagation of planetary-scale disturbances from the lower into the upper atmosphere. *Journal of Geophysical Research*, *66*(1), pp.83-109.

Craig, R.L., Vincent, R.A., Fraser, G.J. and Smith, M.J., 1980. The quasi 2-day wave in the Southern Hemisphere mesosphere, *Nature*, 283, pp. 319-320.

Crary, D.J. and Forbes, J.M., 1983. On the extraction of tidal information from measurements covering a fraction of a day. *Geophysical research letters*, *10*(7), pp.580-582.

Curtis, P.D., Houghton, J.T., Peskett, G.D. and Rodgers, C.D., 1974, March. Remote sounding of atmospheric temperature from satellites. V. The pressure modulator radiometer for Nimbus F. In *Proceedings of the Royal Society of London A: Mathematical, Physical and Engineering Sciences* (Vol. 337, No. 1608, pp. 135-150). The Royal Society.

Donaldson Jr, R.J., 1965. Resolution of a radar antenna for distributed targets. *Journal of Applied Meteorology*, *4*(6), pp.727-740.

Doviak, R.J., Zrnić, D.S. and Sirmans, D.S., 1979. Doppler weather radar. *Proceedings of the IEEE*, *67*(11), pp.1522-1553.

Dunkerton, T.J., 1982. Stochastic parameterization of gravity wave stresses. *Journal of the Atmospheric Sciences*, *39*(8), pp.1711-1725.

Ebel, A., 1984. Contributions of gravity waves to the momentum, heat and turbulent energy budget of the upper mesosphere and lower thermosphere. *Journal of atmospheric and terrestrial physics*, *46*(9), pp.727-737.

Elford, W.G., 1979. Momentum transport due to atmospheric tides. *Journal of Geophysical Research: Space Physics*, *84*(A8), pp.4432-4436.

Elford, W.G. and Craig, R.L., 1980. Upper atmosphere wind observations at Adelaide 35° S, August 1974. *Journal of Atmospheric and Terrestrial Physics*, *42*(1), pp.61-67.

Fritts, D.C., 1979. The excitation of radiating waves and Kelvin-Helmholtz instabilities by the gravity wave-critical level interaction. *Journal of the Atmospheric Sciences*, *36*(1), pp.12-23.

Fritts, D.C., 1984. Gravity wave saturation in the middle atmosphere: A review of theory and observations. *Reviews of Geophysics*, *22*(3), pp.275-308.

Frezal, M.E., Glass, M., Fellous, J.L. and Massebeuf, M., 1981. Simultaneous meteor radar observations at Monpazier (France, 44° N) and Punta Borinqnen (Puerto Rico, 18° N). III—The latitudinal variations of the energy of gravity waves (2–8 h) in the high mesosphere. *Journal of Atmospheric and Terrestrial Physics*, *43*(5), pp.543-547.

Fukao, S., Sato, T., Harper, R.M. and Kato, S., 1980. Radio wave scattering from the tropical mesosphere observed with the Jicamarca radar. *Radio Science*, *15*(2), pp.447-457.

Gage, K.S. and Balsley, B.B., 1978. Doppler radar probing of the clear atmosphere. *Bulletin of the American Meteorological Society*, *59*(9), pp.1074-1093.

Gage, K.S., Carter, D.A. and Ecklund, W.L., 1981. The effect of gravity waves on specular echoes observed by the Poker Flat MST radar. *Geophysical Research Letters*, *8*(6), pp.599-602.

Garrett, C. and Munk, W., 1979. Internal waves in the ocean. *Annual Review of Fluid Mechanics*, *11*(1), pp.339-369.

Geller, M.A., 1983. Dynamics of the middle atmosphere. In *Progress in Solar-Terrestrial Physics* (pp. 359-375). Springer Netherlands.

Golley, M.G. and Rossiter, D.E., 1970. Some tests of methods of analysis of ionospheric drift records using an array of 89 aerials. *Journal of Atmospheric and Terrestrial Physics*, *32*(7), pp.1215-1233.

Gossard, E.E. and Hooke, W.H., 1975. Waves in the atmosphere: atmospheric infrasound and gravity waves-their generation and propagation. *Atmospheric Science*, Elsevier, New York

Groves, G.V., 1969, Wind models from 60 to 130 km altitude for different months and latitudes, *Journal of the British Interplanetary Society*, 32, pp. 285-307.

Haurwitz, B. Fogle, B.; (1969) Wave forms in noctilucent clouds. *Deep-Sea Research*, 16, pp. 85-95.

Hersé, M., Moreels, G. and Clairemidi, J., 1980. Waves in the OH emissive layer: photogrammetry and topography. *Applied optics*, *19*(3), pp.355-362.

Hines, C.O., 1960. Internal atmospheric gravity waves at ionospheric heights. *Canadian Journal of Physics*, *38*(11), pp.1441-1481.

Hines, C.O., 1968. A possible source of waves in noctilucent clouds. *Journal of the Atmospheric Sciences*, *25*(5), pp.937-937.

Hines, C.O., 1970. Eddy diffusion coefficients due to instabilities in internal gravity waves. *Journal of Geophysical Research*, *75*(19), pp.3937-3939.

Hines, C.O., 1974. Observed ionospheric waves considered as gravity or hydromagnetic waves. *Journal of Atmospheric and Terrestrial Physics*, *36*(7), pp.1205-1216.

Hirota, I., 1975, Spectral analysis of planetary waves in the summer stratosphere and mesosphere, *J. Met. Soc. Japan*, 53, pp. 33–44.

Hirota, I., 1976. Seasonal variation of planetary waves in the stratosphere observed by the Nimbus 5 SCR. *Quarterly Journal of the Royal Meteorological Society*, *102*(434), pp.757-770.

Hocking, W.K., 1979. Angular and temporal characteristics of partial reflections from the D-region of the ionosphere. *Journal of Geophysical Research: Space Physics*, *84*(A3), pp.845-851.

Hocking, W.K., 1983a. On the extraction of atmospheric turbulence parameters from radar backscatter Doppler spectra—I. Theory. *Journal of Atmospheric and Terrestrial Physics*, *45*(2-3), pp.89-102.

Hocking, W.K., 1983. Mesospheric turbulence intensities measured with a HF radar at 35° S—II. *Journal of Atmospheric and Terrestrial Physics*, *45*(2), pp.103-114.

Hocking, W.K. and Vincent, R.A., 1982. A comparison between HF partial reflection profiles from the D-region and simultaneous Langmuir probe electron density measurements. *Journal of Atmospheric and Terrestrial Physics*, *44*(10), pp.843-854.

Hocking, W.K. and Vincent, R.A., 1982. Comparative observations of D region HF partial reflections at 2 and 6 MHz. *Journal of Geophysical Research: Space Physics*, *87*(A9), pp.7615-7624.

Hodges, R.R., 1967. Generation of turbulence in the upper atmosphere by internal gravity waves. *Journal of Geophysical Research*, *72*(13), pp.3455-3458.

Hodges, R.R., 1969. Eddy diffusion coefficients due to instabilities in internal gravity waves. *Journal of Geophysical Research*, *74*(16), pp.4087-4090.

Holton, J.R., 1982. The role of gravity wave induced drag and diffusion in the momentum budget of the mesosphere. *Journal of the Atmospheric Sciences*, *39*(4), pp.791-799.

Holton, J.R. and Wehrbein, W.M., 1980. A numerical model of the zonal mean circulation of the middle atmosphere. *pure and applied geophysics*, *118*(1), pp.284-306.

Houghton, J.T., 1978. The stratosphere and mesosphere. *Quarterly Journal of the Royal Meteorological Society*, *104*(439), pp.1-29.

Jenkins, G.M. and D.G. Watts, 1968, *Spectral Analysis and its Applications*, Holden Day, New York

Jones, K.L., 1980. Angular variation of partial reflections from the D-region using a steerable beam radar. *Journal of Atmospheric and Terrestrial Physics*, *42*(6), pp.569-575.

Julian, P.R., 1975. Comments on the determination of significance levels of the coherence statistic. *Journal of the Atmospheric Sciences*, *32*(4), pp.836-837.

Larsen, M.F., Kelley, M.C. and Gage, K.S., 1982. Turbulence spectra in the upper troposphere and lower stratosphere at periods between 2 hours and 40 days. *Journal of the Atmospheric Sciences*, *39*(5), pp.1035-1041.

Leovy, C.B., Simple models of thermally driven mesospheric circulations, *J. Atmos. Sci.*, 21, 327–341, 1964

Lhermitte, R.M., 1966. Probing air motion by Doppler analysis of radar clear air returns. *Journal of the Atmospheric Sciences*, *23*(5), pp.575-591.

Lhermitte, R. and Poor, H., 1983, Multi-beam Doppler sonar observation of tidal flow turbulence. *Geophysical Research Letters*, 10, pp. 717–720.

Lindner, B.C., 1975. The Nature of D-region Scattering of Vertical Incidence Radio Waves. I. Generalized Statistical Theory of Diversity Effects Between Spaced Receiving Antennas. *Australian Journal of Physics*, *28*(2), pp.163-170.

Lindzen, R.S., 1967. Thermally driven diurnal tide in the atmosphere. *Quarterly Journal of the Royal Meteorological Society*, *93*(395), pp.18-42.

Lindzen, R.S., 1973. Wave-mean flow interactions in the upper atmosphere. *Boundary-Layer Meteorology*, *4*(1-4), pp.327-343.

Lindzen, R.S., 1981. Turbulence and stress owing to gravity wave and tidal breakdown. *Journal of Geophysical Research: Oceans*, *86*(C10), pp.9707-9714.

Lindzen, R.S. and Rosenthal, A.J., 1976. On the instability of Helmholtz velocity profiles in stably stratified fluids when a lower boundary is present. *Journal of Geophysical Research*, *81*(9), pp.1561-1571.

Maeda, S. and Handa, S., 1980. Transmission of large-scale TIDs in the ionospheric F2-region. *Journal of Atmospheric and Terrestrial Physics*, *42*(9), pp.853-859.

Manson, A.H., Gregory, J.B. and Stephenson, D.G., 1975. Winds and Wave Motions to 110 km at Mid-Latitudes. IV. Coupling Between Internal Gravity Waves and the Mean Flow. *Journal of the Atmospheric Sciences*, *32*(9), pp.1682-1688.

Manson, A.H., Meek, C.E. and Stening, R.J., 1979. The role of atmospheric waves (1.5 h-10 days) in the dynamics of the mesosphere and lower thermosphere at Saskatoon (52 N, 107 W) during four seasons of 1976. *Journal of Atmospheric and Terrestrial Physics*, *41*(3), pp.325-335.

Manson, A.H., Meek, C.E. and Gregory, J.B., 1981. Gravity waves of short period (5–90 min), in the lower thermosphere at 52 N (Saskatoon, Canada); 1978/1979. *Journal of Atmospheric and Terrestrial Physics*, *43*(1), pp.35-44.

Matsuno, T., 1982, A quasi-one-dimensional model of the middle atmospheric circulation interacting with internal gravity waves. *J. met. Soc. Japan*, 60, pp. 215–226.

Metcalf, J.I., 1975. Gravity waves in a low-level inversion. *Journal of the Atmospheric Sciences*, *32*(2), pp.351-361.

Miller, K.S. and Rochwarger, M.M., 1972. A covariance approach to spectral moment estimation. *Information Theory, IEEE Transactions on*, *18*(5), pp.588-596.

Mitra, S.N., 1949. A radio method of measuring winds in the ionosphere. *Proceedings of the IEE-Part III: Radio and Communication Engineering*, *96*(43), pp.441-446.

Miyahara, S., 1980. Solar diurnal tides and the induced zonal mean flows. *Meteorological Society of Japan Journal*, *58*, pp.302-306.

Mood and Graybill, 1963, *Introduction to the Theory of Statistics*, McGraw-Hill, New York.

Murgatroyd, R.J., The structure and dynamics of the stratosphere. GA Corby (Ed.), *The Global Circulation of the Atmosphere*, Royal Meteorological Society, London (1969), pp. 159–195.

Peterson, V.L. and Balsley, B.B., 1979. Clear air Doppler radar measurements of the vertical component of wind velocity in the troposphere and stratosphere. *Geophysical Research Letters*, *6*(12), pp.933-936.

Phillips, G.J. and Spencer, M., 1955. The effects of anisometric amplitude patterns in the measurement of ionospheric drifts. *Proceedings of the Physical Society. Section B*, *68*(8), p.481.

Pitteway, M.L.V. and Hines, C.O., 1965. The reflection and ducting of atmospheric acoustic-gravity waves. *Canadian Journal of Physics*, *43*(12), pp.2222-2243.

Pitteway, M.L.V., Wright, J.W. and Fedor, L.S., 1971. The interpretation of ionospheric radio drift measurements—III Validation of correlation analysis by computer simulation. *Journal of Atmospheric and Terrestrial Physics*, *33*(4), pp.635-660.

Rastogi, P.K. and Woodman, R.F., 1974. Mesospheric studies using the Jicamarca incoherent-scatter radar. *Journal of Atmospheric and Terrestrial Physics*, *36*(7), pp.1217-1231.

Rastogi, P.K. and Bowhill, S.A., 1976. Gravity waves in the equatorial mesosphere. *Journal of Atmospheric and Terrestrial Physics*, *38*(1), pp.51-60.

Reed, R.J. and Hardy, K.R., 1972. A Case Study of Persistent, Intense, Cleat Air Turbulence in an Upper Level Frontal Zone. *Journal of Applied Meteorology*, *11*(3), pp.541-549.

Rossiter, D.E., 1970. Coupling between aerials used for measuring ionospheric drifts. *Nature*, *228*, pp.1299-1300.

Ratcliffe, J.A., 1956. Some aspects of diffraction theory and their application to the ionosphere. *Reports on Progress in Physics*, *19*(1), p.188.

Röttger, J., 1980. Reflection and scattering of VHF radar signals from atmospheric refractivity structures. *Radio Science*, *15*(2), pp.259-276.

Röttger, J., 1981. Investigations of lower and middle atmosphere dynamics with spaced antenna drifts radars. *Journal of Atmospheric and Terrestrial Physics*, *43*(4), pp.277-292.

Röttger, J., Rastogi, P.K. and Woodman, R.F., 1979. High-resolution VHF radar observations of turbulence structures in the mesosphere. *Geophysical Research Letters*, *6*(7), pp.617-620.

Salah, J.E. and Holt, J.M., 1974. Midlatitude thermospheric winds from incoherent scatter radar and theory. *Radio Science*, *9*(2), pp.301-313.

Schoeberl, M.R. and Strobel, D.F., 1978. The response of the zonally averaged circulation to stratospheric ozone reductions. *Journal of the Atmospheric Sciences*, *35*(9), pp.1751-1757.

Shibata, T. and Okuzawa, T., 1983. Horizontal velocity dispersion of medium-scale travelling ionospheric disturbances in the F-region. *Journal of Atmospheric and Terrestrial Physics*, *45*(2-3), pp.149-159.

Skolnik, M.I., 1962, *Introduction to Radar Systems*, McGraw-Hill, New York.

Smith, M.J., 1983. Comparisons of winds at (44° S, 173° E), 65–110 km, with CIRA 72. *Advances in Space Research*, *3*(1), pp.25-28.

Stubbs, T.J., 1973. The measurement of winds in the D-region of the ionosphere by the use of partially reflected radio waves. *Journal of Atmospheric and Terrestrial Physics*, *35*(5), pp.909-919.

Stubbs, T.J. and Vincent, R.A., 1973. Studies of D-Region Drifts During the Winters of 1970? 72. *Australian Journal of Physics*, *26*(5), pp.645-660.

Thomas, L., 1980. The composition of the mesosphere and lower thermosphere. *Philosophical Transactions of the Royal Society of London A: Mathematical, Physical and Engineering Sciences*, *296*(1418), pp.243-260.

Tilbrook, A.P. and Jones, T.B., 1979. The effects of vertical winds on the propagation of medium scale atmospheric gravity waves. *Journal of Atmospheric and Terrestrial Physics*, *41*(6), pp.661-669.

VanZandt, T.E., 1982. A universal spectrum of buoyancy waves in the atmosphere. *Geophysical Research Letters*, *9*(5), pp.575-578.

Vincent, R.A. and Ball, S.M., 1977. Tides and gravity waves in the mesosphere at mid-and low-altitudes. *Journal of Atmospheric and Terrestrial Physics*, *39*(9-10), pp.965-970.

Vincent, R.A. and Ball, S.M., 1981. Mesospheric winds at low-and mid-latitudes in the southern hemisphere. *Journal of Geophysical Research: Space Physics*, *86*(A11), pp.9159-9169.

Vincent, R.A. and Stubbs, T.J., 1977. A study of motions in the winter mesosphere using the partial reflection drift technique. *Planetary and Space Science*, *25*(5), pp.441-455.

Vincent, R.A., Stubbs, T.J., Pearson, P.H.O., Lloyd, K.H. and Low, C.H., 1977. A comparison of partial reflection drifts with winds determined by rocket techniques—1. *Journal of Atmospheric and Terrestrial Physics*, *39*(7), pp.813-821.

Vincent, R.A. and Belrose, J.S., 1978. The angular distribution of radio waves partially reflected from the lower ionosphere. *Journal of Atmospheric and Terrestrial Physics*, *40*(1), pp.35-47.

Vincent, R.A. and Röttger, J., 1980. Spaced antenna VHF radar observations of tropospheric velocities and irregularities. *Radio Science*, *15*(2), pp.319-335.

Vincent, R.A. and Reid, I.M., 1983. HF Doppler measurements of mesospheric gravity wave momentum fluxes. *Journal of the Atmospheric Sciences*, *40*(5), pp.1321-1333.

Vincent, R.A., 1984. Gravity-wave motions in the mesosphere. *Journal of atmospheric and terrestrial physics*, *46*(2), pp.119-128.

Walker, J.C., 1979. Radar measurement of the upper atmosphere. *Science*, *206*(4415), pp.180-189.

Wallace, J. M., 197*1,* Spectral studies of tropospheric wave disturbances in the tropical western Pacific*, Reviews of Geophys*ics*,* 9*(*3*),* 557–612.

Wallace, J.M. and Chang, C.P., 1969. Spectrum analysis of large-scale wave disturbances in the tropical lower troposphere. *Journal of the atmospheric sciences*, *26*(5), pp.1010-1025.

Whitehead, J.D., From, W.R., Jones, K.L. and Monro, P.E., 1983. Measurement of movements in the ionosphere using radio reflections. *Journal of Atmospheric and Terrestrial Physics, 45*(5), pp.345-351.

Witt, G., 1962. Height, structure and displacements of noctilucent clouds. *Tellus, 14*(1), pp.1-18.

Woodman, R.F. and Hagfors, T., 1969. Methods for the measurement of vertical ionospheric motions near the magnetic equator by incoherent scattering. *Journal of Geophysical Research, 74*(5), pp.1205-1212.

Woodman, R.F. and Guillen, A., 1974. Radar observations of winds and turbulence in the stratosphere and mesosphere. *Journal of the atmospheric Sciences, 31*(2), pp.493-505.

Reference is also made to the following unpublished material

Allman, M.E. and S.A. Bowhill, 1976, Feed system design for the Urbana incoherent-scatter radar antenna. *Aeronomy Report No. 71*, Univ. Illinois, Urbana, USA.

Ball, S.M. ,1981, *Upper Atmospheric Tides and Gravity Waves at Mid- and Low- Latitudes*, Ph.D. Thesis, Adelaide University, Australia.

Briggs, B.H, 1977b, The analysis of moving patterns by correlation methods. *Dept. Report ADP 148*, Physics Dept., Adelaide University, Australia.

Briggs, B.H., T.J. Stubbs and R.A. Vincent, 1974, *Proc. Int. Conf. Structure, Composition and General Circulation of the Upper and Lower Atmospheres and Possible Anthropogenic Perturbations*, Vol. 2, Toronto, 474.

Green, J.L., K.S. Gage, W.L. Clark, T.E. Van Zandt and P.H. Hildebrand, 1980, Joint instrumented aircraft and VHF Doppler radar measurements of wind near Boulder, Colorado, *Proc. 19th Conf. Radar Meteorology*, Am. Meteor. Soc., Boston, Mass., 624.

Hocking, W.K., 1981, *Investigations of the movement and Structure of D-region ionospheric irregularities*, Ph.D. Thesis, Adelaide University, Australia.

Hocking, W.K., 1983c, The Spaced Antenna Drift Method. *Handbook for MAP*, 9, SCOSTEP Secretariat, Univ. Illinois, Urbana, pp. 171-186.

Lhermitte, R.M., 1968. Turbulent air motion as observed by Doppler radar, *Proceedings 13th Radar Meteorological Conference*, Am. Meteor. Soc., Boston, Mass., 489.

Philbrick, C.R., 1981 Measurements of structural features in profiles of mesospheric density, *Handbook for MAP*, 2, SCOSTEP Secretariat, Univ. Illinois, Urbana, 333-340.

Röttger, J., 1981b, Wind variability in the stratosphere deduced from spaced antenna VHF radar observations. *Proc. 20th Conf. Radar Meteorology*., Am. Met. Soc., Boston, Mass., pp. 22-29.

Röttger, J., 1983, Techniques for measurements of horizontal and vertical velocities. *Handbook for MAP*, 9, SCOSTEP Secretariat, Univ., Illinois, Urbana, pp. 150-163.

Röttger, J. and P. Czechowsky, 1980, Tropospheric and stratospheric wind measurements with the spaced antenna drifts technique and the Doppler beam swinging technique using a VHF radar. *Proc. 19th Conf. Radar Meteor., Am. Met. Soc*., Boston, Mass., pp. 577-584.

Ruggerio, R.L. and S.A. Bowhill, 1982, New advances in the partial reflection-drifts experiment using microprocessors. *Aeronomy: Report No. 106*, Univ. Illinois, Urbana, USA.

Smith, S.A. and D.C. Fritts, 1983, Estimation of gravity wave motions, momentum fluxes and induced mean flow accelerations in the winter mesosphere over Poker Flat, Alaska. *Proc. 21st Conf. Radar Meteor.* Boston, Mass., 104., Am. Met. Soc.

Strauch, R.G., 1983, Data analysis techniques: spectral processing. *Handbook for MAP*, 9, SCOSTEP Secretariat, Univ. Illinois, Urbana, pp. 528-531.

Vincent, R.A., 1980, *Proc. Discussion Meeting on Solar Terrestrial Physics*, Physics Dept., Latrobe University, Melbourne, Australia, 141.

Wilson, D. A., 1970: Doppler radar studies of boundary layer wind profiles and turbulence in snow conditions. *Proc. 14th Conf. on Radar Meteorology*, Tucson, Amer. Meteor. Soc., Boston MA, pp. 191-196.

Wilson, D.A. and A.J. Miller, 1971, *Remote Sensing of the Troposphere* (V.E. Derr, Ed.), Univ. of Colorado, Boulder, Co., p 13-1.

Appendix A

HF Doppler measurements of mesospheric gravity wave momentum fluxes

This is a reprint of an article published by R.A. Vincent and I.M. Reid in the Journal of Atmospheric Sciences, *40*(5), pp.1321-1333.

HF Doppler Measurements of Mesospheric Gravity Wave Momentum Fluxes

R. A. VINCENT AND I. M. REID

Department of Physics, The University of Adelaide, Adelaide, South Australia 5001

(Manuscript received 27 August 1982, in final form 5 January 1983)

ABSTRACT

Recent theoretical studies have emphasized the probable importance of internal gravity waves in balancing the momentum budget of the mesosphere. In this paper, we propose a method by which the vertical flux of horizontal momentum can be measured by ground based radars. The method uses two or more radar beams each offset from the vertical to measure the atmospheric motions by the Doppler technique. Provided there is horizontal homogeneity, the momentum flux is proportional to the difference of the variances of the Doppler velocities measured in each beam. The flux convergence and, hence, the associated body force acting on the atmosphere can be inferred by measuring the flux as a function of height. It is shown that mean wind components can also be measured by this method and, under certain circumstances, so can the horizontal wavelengths and phase velocities of the internal waves. Observations of the vertical flux of zonal momentum made with this technique using an HF radar located near Adelaide, Australia (35°S, 138°E) in May 1981 are discussed. At heights in the range of 80–90 km, a mean upward flux of westward momentum was measured, and from the flux convergence a body force equivalent to an acceleration of the order of -20 m s^{-1} day^{-1} is inferred. There were, however, significant variations in the flux both in direction and magnitude on the scales of the order of hours. Measurements using cross-spectral techniques of the gravity wave horizontal wavelengths and phase velocities suggest that values of $\sim$50 km and 50 m s^{-1}, respectively, are dominant at periods of less than one hour.

1. Introduction

Recent theoretical studies have stressed the role that internal gravity waves may play in transferring momentum from one region of the atmosphere to another. For example, it is well known that the observed thermal structure of the middle atmosphere at the solstice is not in radiative equilibrium and the differences are ascribed to a mean meridional circulation from the summer hemisphere to the winter hemisphere with rising and sinking motions over the summer and winter poles respectively. A transport of wave momentum into the region is required to maintain a quasi-steady zonal flow against the Coriolis torques generated by the meridional flow. In fact, if the wave contribution were not present, the residual circulation would collapse and so the mean circulation may be regarded as being wave driven (Plumb, 1982). Dissipating planetary waves can provide at least some of the balancing torques in the winter stratosphere and mesosphere, but they do not appear to be important contributors to the summer mesospheric momentum budget because of their absence from the summer hemisphere (Houghton, 1978). Atmospheric tides may play a role at low latitudes, but on observational and theoretical grounds it seems unlikely that they are important at mid- and high-latitudes (Elford, 1979; Miyahara, 1980). Internal gravity waves, however, are present in both winter and summer hemispheres, and their action in providing a wave drag has been examined by Lindzen (1981), Holton (1982) and Matsuno (1982).

In another context, Walterscheid (1981) has suggested that the tidal winds themselves may be modified by interactions with time varying gravity wave fluxes. This could cause the day-to-day tidal variability which is often observed in the mesosphere and lower thermosphere.

The theoretical studies mentioned above are limited because of the lack of sufficient data on mesospheric gravity waves in general and wave momentum fluxes in particular. It has been possible to make observations of the vertical structure of gravity waves on a quasi-synoptic basis using rockets (*e.g.,* Heath *et al.,* 1974) and ground based radar techniques (*e.g.,* Vincent and Ball, 1981). Some estimates of the horizontal scales of mesospheric gravity waves made with a VHF radar have also been reported (Rastogi and Bowhill, 1976). However, the bulk of what little information is available about the horizontal wavelengths and phase velocities comes from observations of wave forms in noctilucent clouds (Haurwitz and Fogle, 1969) and from studies of the structure in airglow emissions (Moreels and Herse, 1977). While such observations may give a useful visual picture of wave motions near the mesopause they are restricted in both space and time. Noctilucent clouds are only visible at the high latitude mesopause in the local

summer, and the airglow studies are restricted to clear nights and the emissions occur over a limited height range.

In this paper we describe a new technique by which ground based radars can be used to measure wave momentum fluxes directly. The method requires the comparison of the Doppler shifts in backscattered radar echoes from the upper atmosphere using two or more narrow beams offset from the vertical. It is assumed that fluctuations of the Doppler shifts are caused by gravity wave wind oscillations. With an appropriate choice of radio frequency such measurements can, in principle, be made with good time and height resolution over heights in the range 60–100 km. Consequently, the momentum flux can be measured as a function of height and the wave induced acceleration calculated from the observed convergence. The horizontal wavelengths of the waves can also be obtained from the observations. In the next section, the experimental arrangement and relevant theory are outlined and then we discuss observations made with a HF radar operating near Adelaide, South Australia (35°S, 138°E).

2. Theory

In the experiment we consider here, two radar beams are pointed at equal and opposite angles θ to the zenith, and the beams lie in the xz plane (Fig. 1). The observed radar echoes are due to backscattering from refractive index irregularities which are moving with the background wind. Because of the motion of the irregularities, the echoes will be Doppler shifted in frequency by an amount proportional to the wind component along a given beam direction. The frequency shifts Δf are conveniently measured in terms of a so-called Doppler velocity given by $(\lambda\Delta f)/2$ where λ is the radar wavelength. The Doppler velocities measured will be due to a combination of steady winds whose scales are much greater than the separation of the beams and to gravity wave and turbulent motions whose scales are comparable to the beam spacing at the height of observation. Information about both the steady and small scale motions can be obtained with the experimental arrangement. First, the statistics of the small scale motions are considered.

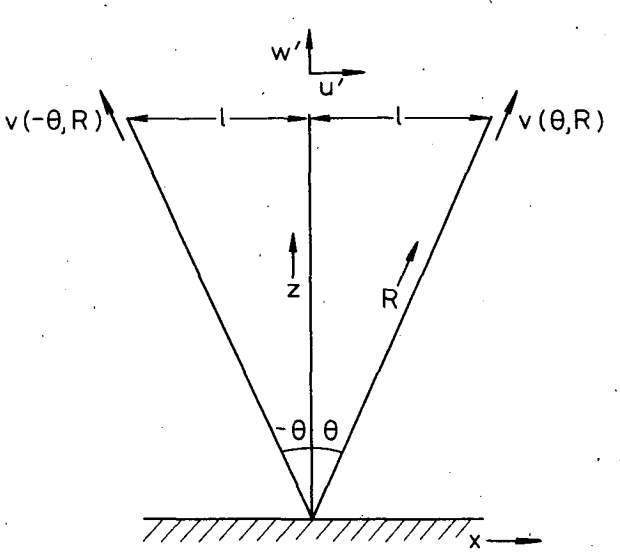

FIG. 1. Schematic representation of the two dimensional radar siituation, in which two narrow radar beams are directed at angles θ and $-\theta$ to the zenith.

a. *Small-scale motions*

If the instantaneous Doppler velocity measured at a range R along the positive x pointing beam is $v(\theta, R, t)$, then

$$v(\theta, R, t) = w'(\theta, R, t)\cos\theta + u'(\theta, R, t)\sin\theta, \quad (1)$$

where w' and u' are the vertically and horizontally directed wind components respectively. Similarly, the Doppler velocity measured along the complementary beam at $-\theta$ is

$$v(-\theta, R, t) = w'(-\theta, R, t)\cos\theta - u'(-\theta, R, t)\sin\theta. \quad (2)$$

If overbars denote a time average, then

$$\overline{v^2(\theta, R)} = \overline{w'^2(\theta, R)}\cos^2\theta + \overline{u'^2(\theta, R)}\sin^2\theta + 2\overline{u'w'(\theta, R)}\sin\theta\cos\theta, \quad (3)$$

$$\overline{v^2(-\theta, R)} = \overline{w'^2(-\theta, R)}\cos^2\theta + \overline{u'^2(-\theta, R)}\sin^2\theta - 2\overline{u'w'(-\theta, R)}\sin\theta\cos\theta. \quad (4)$$

If the statistics of the motions are assumed to be independent of horizontal position, then

$$\left.\begin{aligned}\overline{u'^2(\theta, R)} &= \overline{u'^2(-\theta, R)} = \overline{u'^2(z)}\\ \overline{w'^2(\theta, R)} &= \overline{w'^2(-\theta, R)} = \overline{w'^2(z)}\\ \overline{u'w'(\theta, R)} &= \overline{u'w'(-\theta, R)} = \overline{u'w'(z)}\end{aligned}\right\},$$

where $z = R\cos\theta$. These seem to be reasonable assumptions for propagating waves for the horizontal separation we are considering here. Subtracting (4) from (3) gives

$$\overline{v^2(\theta, R)} - \overline{v^2(-\theta, R)} = 4\overline{u'w'}\sin\theta\cos\theta,$$

that is,

$$\overline{u'w'}(z) = \frac{\overline{v^2(\theta, R)} - \overline{v^2(-\theta, R)}}{2\sin 2\theta}. \quad (5)$$

By measuring the mean-square Doppler velocites at a number of successive ranges it is possible to measure the vertical profile of the vertical flux of x-directed momentum and hence calculate directly the flux convergence with height.

It is noted that $\overline{u'w'}$ can be measured even if the beams do not make equal angles to the zenith (provided that neither points vertically), although (5) has to be modified to account for the different radar geometry. Experimentally, however, it is usually more convenient to use equal and opposite offsets which is the configuration used in the experiments reported here.

It is especially noteworthy that these dual-beam Doppler measurements of momentum flux do not require any knowledge of the horizontal scales of the wave or eddy motions involved. Information about the gravity wave scales is important if current theories of wave transport are to be tested and improved. In the present case, the scales can be obtained by measuring the time displacements between the fluctuating Doppler motions measured in the offset beams. The displacements are best obtained by using cross spectral techniques so that the scales can be measured as a function of wave frequency.

With the experimental arrangement shown in Fig. 1 it is particularly easy to obtain the horizontal direction of wave propagation by examining the sign of $[\overline{v^2(\theta)} - \overline{v^2(-\theta)}]$. For example, Fig. 2 shows the simple case of a single plane internal gravity wave propagating in the $+x$ direction with downward phase velocity (upward group velocity) in the z direction. In the asymptotic limit, which often applies for gravity waves, the velocity perturbation v', is linear and lies along the phase fronts (Hines, 1960); it is apparent by inspection that larger Doppler velocities will be measured in the $+\theta$ beam than in the $-\theta$ beam. Consequently, the difference of the mean squared velocities will be positive for waves propagating in the $+x$ direction and negative for oppositely directed waves. In general, of course, the gravity wave motions will be elliptically polarized, but the principle still holds.

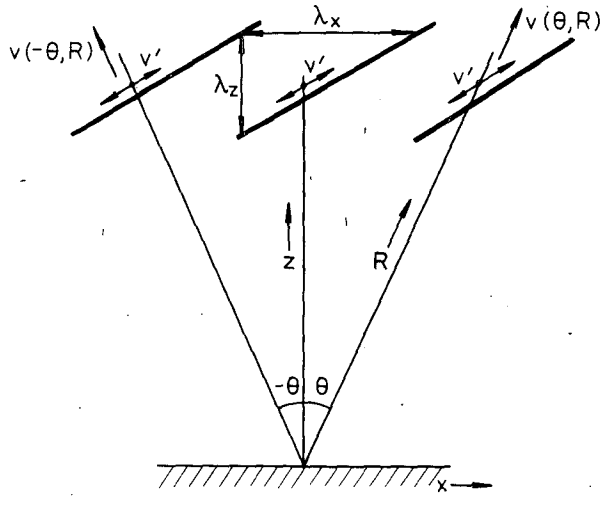

FIG. 2. Idealized situation in which a single plane gravity wave propagates in the $+x$ direction. The direction of propagation may be obtained from a comparison of v' for each of the beams. The heavy lines represent the gravity wave phase fronts, and v' the perturbation wind velocities.

Once the horizontal direction of motion has been established, the horizontal wavelength of the wave can be obtained from the phase of the cross spectrum between the two velocity components $v(\theta, R, t)$ and $v(-\theta, R, t)$ observed with the two beams. For example, if the perturbation velocities u' and w' are due to a single gravity wave of angular frequency ω_0, horizontal wavenumber k_x and vertical wavenumber k_z, then

$$v(\theta, R, t) = (w'_0 \cos\theta + u'_0 \sin\theta)e^{i(\omega_0 t - k_x l - k_z z)}, \quad (6)$$

where w'_0 and u'_0 are the peak vertical and horizontal perturbation velocities respectively and $l = R\sin\theta$ and $z = R\cos\theta$.

If the Fourier transform of $v(\theta, R, t)$ is $F(\theta, R, \omega)$ such that

$$F = \int_{-\infty}^{\infty} ve^{i\omega t}dt,$$

then

$$F(\theta, R, \omega) = (w'_0 \cos\theta + u'_0 \sin\theta)e^{-i(k_x l + k_z z)}\delta(\omega - \omega_0), \quad (7)$$

where δ indicates the delta function. Similarly for the $-\theta$ beam

$$F(-\theta, R, \omega) = (w'_0 \cos\theta - u'_0 \sin\theta)e^{i(k_x l - k_z z)}\delta(\omega - \omega_0). \quad (8)$$

Using the so called "polarization relations" given by Hines (1960), which relate the vertical and horizontal perturbation velocities, we have

$$w'_0 = AZ = A\omega_0(\omega_0^2 - k_x^2 c^2),$$

$$u'_0 = AX = A\omega_0 k_x c^2[k_z - i(2 - \gamma)/2\gamma H],$$

where γ is the ratio of the specific heats, H the pressure scale height, A an arbitrary amplitude and c is the velocity of sound. The cross spectral power is given by

$$W(R, \omega) = F(-\theta, R, \omega)F^*(\theta, R, \omega),$$

where the asterisk indicates the complex conjugate. Thus, the phase of the cross spectrum is given by

$$\zeta = -2k_x l + \zeta',$$

where

$$\zeta' = \tan^{-1}\left[\frac{Z(X - X^*)\sin\theta\cos\theta}{Z^2\cos^2\theta + X^2\sin^2\theta}\right]. \quad (9)$$

This can be expanded in terms of k_x, ω_0 and k_z using the polarization relations such that

$$\zeta' = \tan^{-1}\left[\frac{-k_x(\omega_0^2 - k_x^2 c^2)Bc^2\sin 2\theta}{(\omega_0^2 - k_x^2 c^2)^2\cos^2\theta - k_x^2 c^4 k_z^2 \sin^2\theta}\right], \quad (10)$$

where $B = (2 - \gamma)/2\gamma H$. The expression (9) for ζ is easily evaluated for a given ω_0 and k_x. It is noteworthy that ζ is symmetrical in k_z and that ζ only changes sign if the horizontal direction of motion is reversed. In principle, then, the wavelength can be found for a wave of frequency ω_0 by comparing the measured cross spectral phase with the values ζ computed from Eq. (9) for different values of k_x. In practice, the situation is probably more complicated because a whole spectrum of waves is likely to be present and some criterion is required to establish the significance of the cross spectral phases. This point is taken up in Section 3c when observations are discussed.

The above discussion has ignored the effects of any background winds due to the prevailing winds and tides. If a "steady" component **u** is present then the Doppler shifted wave frequency given by

$$\Omega = \omega_0 - \mathbf{k} \cdot \mathbf{u},$$

must be substituted for ω_0 in the evaluation of the phase correction term ζ'. Consequently, measurements of longer period winds are required if the horizontal wavelengths of the gravity waves are to be properly evaluated.

b. Prevailing and tidal winds

Long period winds due to prevailing and tidal motions will have much longer scales than the horizontal separation of the beams. In these circumstances they can be estimated by a vector decomposition of the Doppler velocities averaged over suitable time intervals. If the mean radial Doppler velocities observed along the $+\theta$ and $-\theta$ directions at a particular range R are $\overline{V(\theta, R)}$ and $\overline{V(-\theta, R)}$ respectively, then the mean horizontal wind component in the x-direction is

$$\bar{u}(z) = \frac{\overline{V(\theta, R)} - \overline{V(-\theta, R)}}{2 \sin\theta}, \tag{11}$$

and the mean vertical component is

$$\bar{w}(z) = \frac{\overline{V(\theta, R)} + \overline{V(-\theta, R)}}{2 \cos\theta}. \tag{12}$$

These are special cases of the more general situation required for the analysis of Velocity–Azimuth Display (VAD) radars which measure the mean radial velocity at a fixed zenith angle over a full 360° rotation of the beam. It would also appear that expressions similar to that given in (5) have been used in VAD radar studies of turbulent momentum fluxes in the planetary boundary layer (Wilson and Miller, 1972).

3. Observations

Observations of mesospheric gravity wave momentum fluxes and horizontal wavelengths were made in the period 11–14 May 1981 using the Buckland Park antenna array located about 40 km north of Adelaide (35°S, 138°E). The array is ~1 km in diameter which means that beams with half power widths of ±4.5° are obtained at the fundamental operating frequency of 1.98 MHz. To measure the zonal components of momentum and wavelength, two beams were used with one beam offset eastward at an angle θ of 11.6° from the zenith and the other at a corresponding angle westward. An angle of 11.6° was chosen because it not only reduced the effects of any specular reflections from the vertical (Hocking, 1979) but was also expected on the basis of previous wind measurements at Adelaide to allow the weighted vertical ($w \cos\theta$) and horizontal ($u \sin\theta$) terms to contribute approximately equally to the line of sight Doppler velocities.

Pulse transmissions with a pulse length of 25 μs and peak power of 50 kW were made with a repetition frequency of 20 Hz and the returned echoes in each beam were coherently detected and sampled every 2 km over the range 70–98 km. The in-phase and quadrature components of the echoes were sampled, digitized and coherently integrated over eight consecutive pulses for each range, and the Doppler velocities calculated from 2 min of data. The velocities themselves were computed from the time derivative of the phase of the complex autocorrelation in a manner similar to that described by Woodman and Guillen (1974). The signal-to-noise ratios were usually high, and the estimated velocity standard deviation associated with each 2 min measurement was about ±0.7 m s^{-1}. To reduce this error further, consecutive observations were averaged in pairs to produce an overall sampling period of 4 min. Since the east and west beam receiving systems were completely separate, tests for systematic errors were made by pointing the two beams in the same direction and measuring the Doppler velocities independently. No significant differences in velocity were found.

In general, the quality of the data was high. If the signal-to-noise ratios were low or if the phase of the correlation function was poorly determined, the data were rejected and small gaps in the data interpolated over. With the exception of a complete loss of data in both beams during the period 1300–1500 LST on 13 May due to a solar flare, complete time series were obtained over the three days at all heights above 78 km. At heights below 78 km, echoes were only obtained during daytime. Furthermore, at heights below ~80 km the ionospheric scatter is often strongly anisotropic with strongest echoes coming from the zenith (Hocking 1979; Vincent and Belrose, 1979). Since we cannot be sure that echoes observed at heights below 80 km were due to scatter from irregularities located at a mean zenith angle of 11.6°, we have concentrated on the 80–94 km height region

where the irregularities are quasi-isotropic in their scattering characteristics.

Figs. 3a and b show the dual-beam Doppler velocity time series after they have been subject to low and high pass filters, respectively. The high pass data refers to periods in the range 8 min to 8 h, while the low pass data is for periods > 8 h. In each case velocity variations are evident with magnitudes significantly greater than the estimated error. Tidal oscillations with 12 and 24 h periods are clearly apparent in the low pass filtered data (Fig. 3a) although the oscillations in each beam are not completely antisymmetric, which would be the case if the tidal winds were purely horizontal (see below). There is a high degree of similarity between the data from the two beams for high-frequency velocity fluctuations shown in Fig. 3b; for example, enhanced fluctuations are visible on the morning of 13 May for both beams. This suggests that the velocity statistics are reasonably independent of position and that the momentum flux calculations using (5) can be applied.

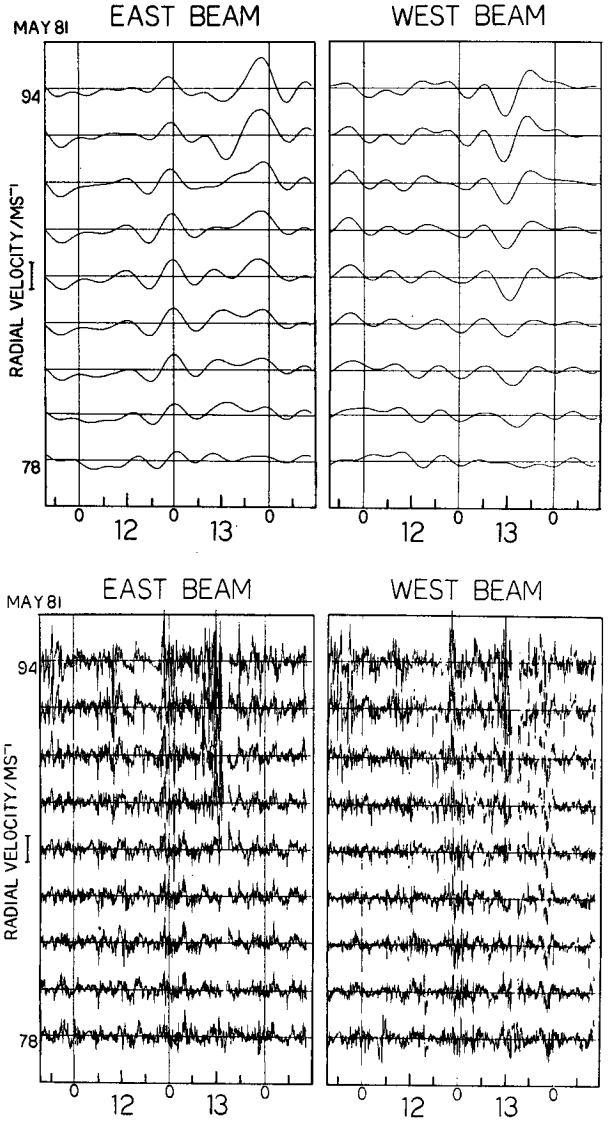

FIG. 3. The radial Doppler velocities for periods (a) greater than 8 h and (b) between 8 min and 8 h, measured by the east and west beams during the period 11–14 May 1981 at heights between 78 and 94 km. The bar on the left indicates a velocity of 8 m s^{-1}.

a. Prevailing and tidal winds

The prevailing and tidal wind velocities at a given height were calculated from time series of hourly-average Doppler radial velocities in the east and west beams. Then the hourly mean horizontal velocity is from (11),

$$\bar{u} = (\bar{V}_E - \bar{V}_W)/2 \sin\theta,$$

where $\bar{V}_E$ and $\bar{V}_W$ are the hourly average velocities. For $\theta = 11.6°$,

$$\bar{u} = 2.5(\bar{V}_E - \bar{V}_W). \quad (13)$$

The mean vertical velocity is given by (12), i.e.,

$$\bar{w} = (\bar{V}_E + \bar{V}_W)/2 \cos\theta$$
$$= 0.51(\bar{V}_E + \bar{V}_W), \quad (14)$$

and $\bar{u}$ and $\bar{w}$ are defined as positive eastward and upward, respectively. The time series of $\bar{u}$ and $\bar{w}$ were then analyzed harmonically in 24 h blocks to give the prevailing, 24, and 12 h tidal winds. Fig. 4 shows the prevailing winds and the tidal components in terms of their respective amplitudes and phases as averaged over the three days of observations.

The prevailing zonal wind is eastward decreasing with height above 90 km. This result is similar in direction, but somewhat smaller in magnitude, than other observations of the zonal wind made at Adelaide in early winter. An examination of the individual daily mean winds show, however, that there is a clear trend towards larger values with increasing time which suggests that the wind speeds may have been depressed by the passage of a long period disturbance. The zonal amplitudes of the 24 and 12 h tides are also rather small, but this is often a feature of early winter observations at Adelaide (Stubbs, 1976; Vincent and Ball, 1981).

The analysis of the vertical winds suggests that they are positive at heights below 86 km and negative above this height. The tidal amplitudes range between 0.1 and 0.15 m s^{-1} near 80 km to ~0.5 m s^{-1} near 90 km, but the reliability of these estimates is difficult to assess. Over the three days of observation, the prevailing vertical winds are not significantly different from zero if the rms day-to-day variations of ±0.3 m s^{-1} are taken into account. The tidal components are significantly larger (~5 times) than recent velocities calculated from theory. Forbes (1982a,b) gives values

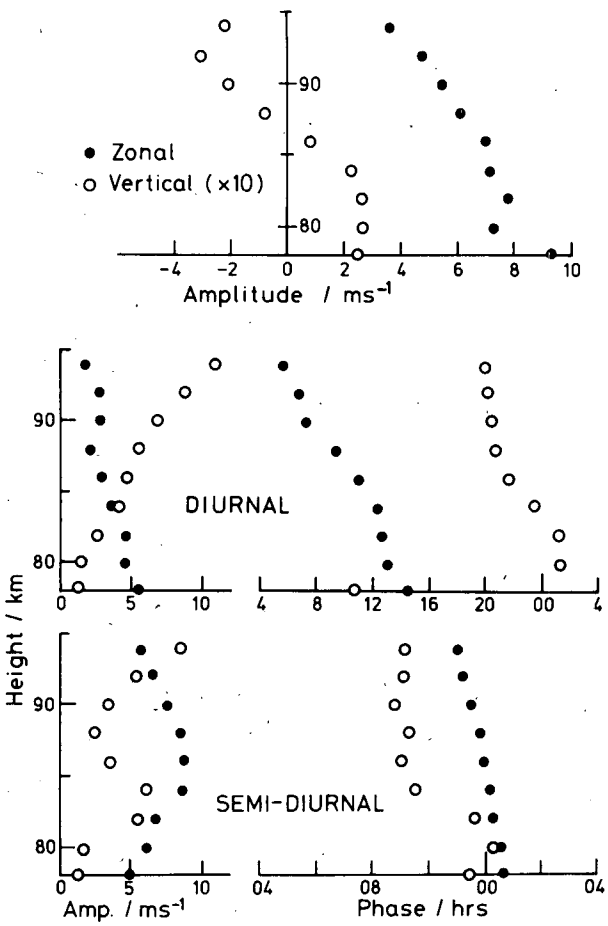

FIG. 4. The mean amplitudes (positive eastward and upward) and phases (times of maximum positive amplitude) of the zonal and vertical velocity 11–14 May 1981. The vertical amplitudes have been multiplied by 10.

of vertical velocity of ~0.1 m s^{-1} at 90 km for the diurnal and semidiurnal tides at the winter solstice. Walterscheid (private communication, 1982) states that his model for the semidiurnal tide gives vertical velocity amplitudes < 0.1 m s^{-1} at heights below 90 km.

Experimental determinations of vertical wind speeds are always complicated by their smallness relative to that of the horizontal wind. In the present case, any systematic tilt of the array axis from the horizontal will cause the beams to be displaced relative to the zenith and consequently the horizontal winds will not be fully removed from the vertical estimates. In the present case, any tilt of the array is due to slope in the ground plane of the array which is effectively the water table. Since the array is built on an extensive coastal plain, we do not expect the tilt of the water table to be significantly different from the tilt of the ground itself which is ~0.15° toward the southwest. A tilt of this magnitude would cause an error in w of $\sim 5 \times 10^{-3}\, u$, where u is the horizontal wind speed. Since mean horizontal winds in the present experiment were not much in excess of 10–20 m s^{-1} in any given hour, this implies systematic errors of less than 0.08 m s^{-1} in the mean vertical winds with similar values for the tidal amplitudes. Other sources of error in the vertical velocity involve systematic and random differences between the horizontal components of the Doppler velocities $\bar{V}_E$ and $\bar{V}_W$.

b. *Momentum fluxes*

The vertical flux of zonal momentum was evaluated at each height from the mean square Doppler velocities calculated from the filtered data (8 min–8 h) shown in Fig. 3b. The mean square velocities are shown in Fig. 5a, where it is apparent that the Doppler velocities measured in the westward beam are larger than those in the eastward beam at heights near 80 km but that the difference decreases with height until

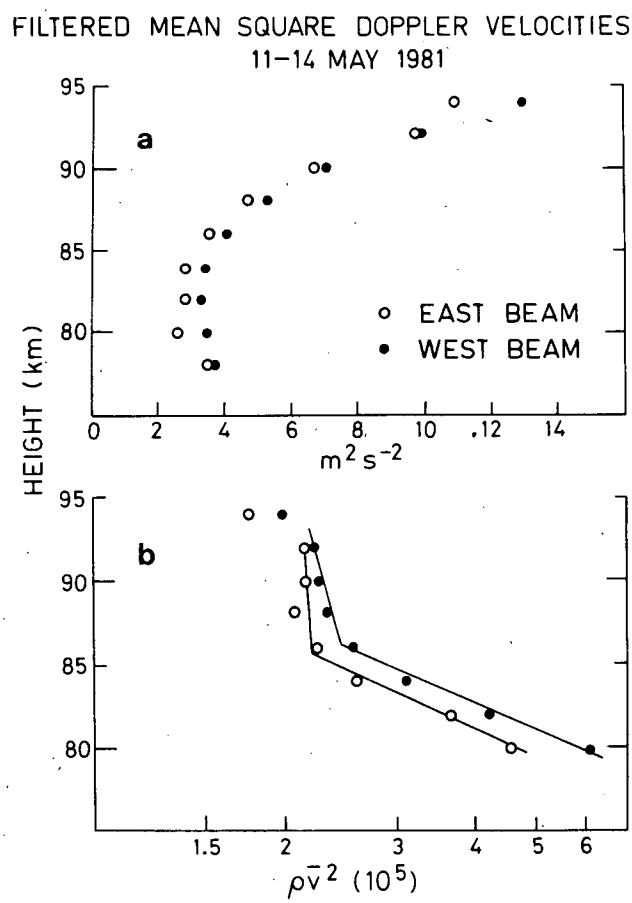

FIG. 5. (a) Height profiles of the mean square Doppler velocities 11–14 May 1981 for the period band 8 min–8 h for the east and west beams. (b) The $\rho\bar{v}^2$ products where ρ is the neutral density and $\bar{v}^2$ are the mean-square Doppler velocities.

the mean square velocities are nearly equal at 92 km. Velocity values are shown for the heights of 78 and 94 km, but it is probable that these values are not always reliable due to the presence of specular reflections from the zenith and we have not included these data in subsequent calculations.

The momentum flux at any given height is

$$\rho\overline{u'w'} = \rho(\bar{v}_E^2 - \bar{v}_W^2)/2 \sin 2\theta, \quad (15)$$

where $\theta = 11.6°$ so that

$$\rho\overline{u'w'} = 1.27\rho(\bar{v}_E^2 - \bar{v}_W^2), \quad (16)$$

and the net acceleration per unit mass is given by the flux convergence as

$$F = -\frac{1}{\rho}\frac{d}{dz}(\rho\overline{u'w'}). \quad (17)$$

The values of $\rho\bar{v}_E^2$ and $\rho\bar{v}_W^2$ are shown in Fig. 5b. In order to smooth them somewhat, functions proportional to $\exp(-z/h)$, where z is the height and h the height scale of ρv^2, were fitted to each of the height profiles. F is then given by

$$F = \left(\frac{\bar{v}_E^2}{h_E} - \frac{\bar{v}_W^2}{h_W}\right).$$

The height profile of $\overline{u'w'}$ shown in Fig. 6 shows that there was an upward flux of westward momentum at all heights of observation, but the flux became steadily more positive with increasing height implying a convergence of westward momentum. The calculated body force per unit mass F, expressed in m s^{-1} day^{-1}, is also shown in Fig. 6. Although somewhat variable with height, the implied accelerations are typically 10–20 m s^{-1} day^{-1}.

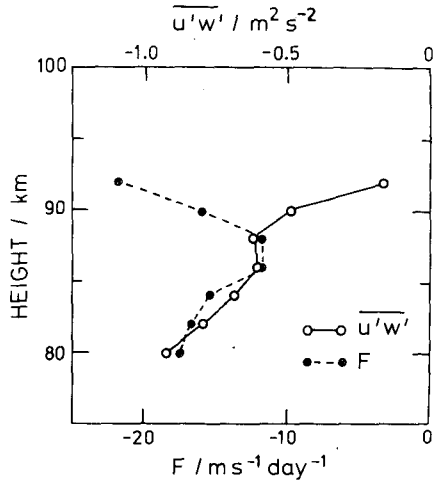

FIG. 6. Height profiles of the upward flux of zonal momentum ($\overline{u'w'}$) for the period 11–14 May 1981 (open circles) and the associated body force F (solid circles).

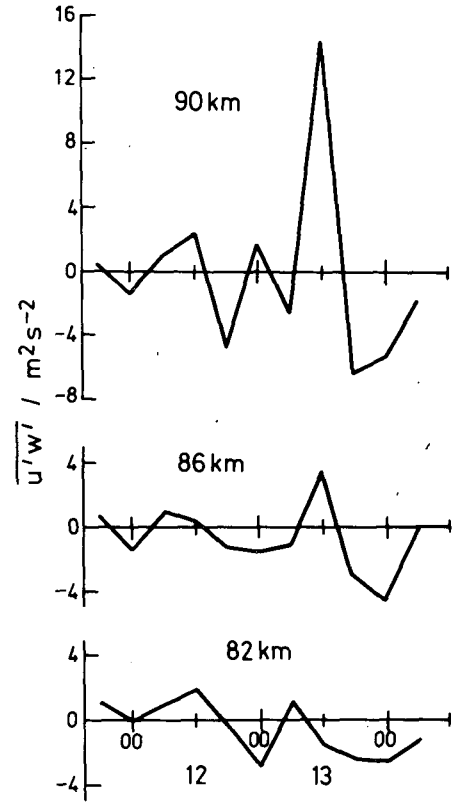

FIG. 7. Time series of the upward flux of zonal momentum for three representative heights. Each point corresponds to a value of $\overline{u'w'}$ calculated for a six hour data length and plotted at the center of each six-hour interval.

The momentum fluxes deduced above are values averaged over three days of observation. However, it might be expected that because of changes in the sources of the waves and/or in the transmissivity of the middle atmosphere, there could be significant short term changes in the flux. A search for systematic changes was made by analyzing the data in consecutive 6 h blocks; spectral analysis of the east and west beam data sets showed that, although the spectral energy could be enhanced at given frequency for one of the beams relative to the other, the overall spectra followed a power law of the form f^{-k}, where f is the frequency. Within statistical limits the spectral indices k were identical for the two beams for each block and thus satisfied the criterion that the data be statistically similar. Typically, k lay in the range 1.0–1.6. The time series of $\overline{u'w'}$ are shown in Fig. 7 for three representative heights (82, 86 and 90 km), and it is evident that significant time variations did occur. Strong upward fluxes of eastward momentum are especially evident during the enhanced wave activity observed in the period between 0000 and 1200 LST on 13 May.

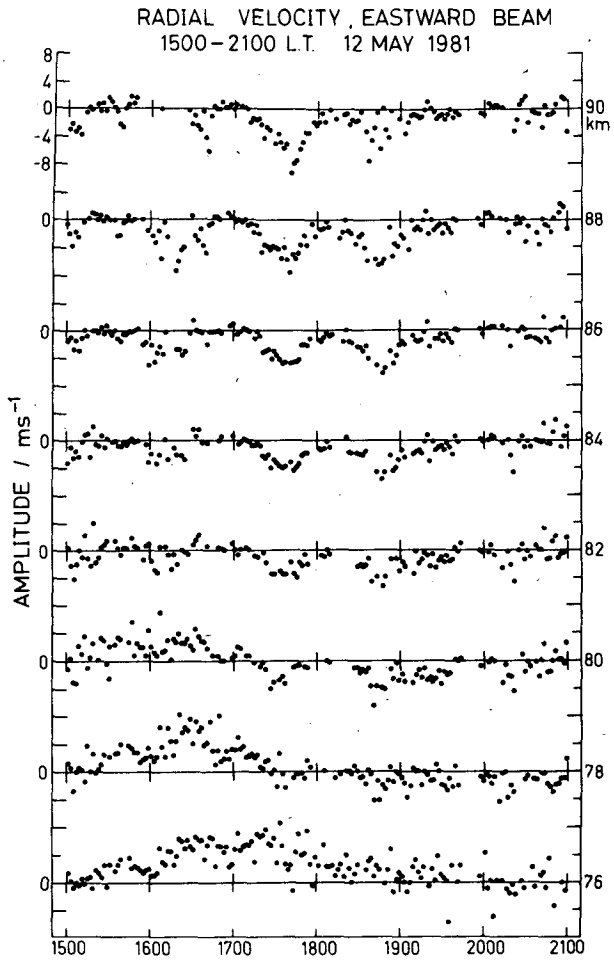

FIG. 8. Radial velocities measured by the eastward beam in the period 1500–2100 LST on 12 May 1981. Each point represents a 2 min observation.

c. *Phase velocities and wavelengths*

The Doppler velocities often showed systematic variations in time, apparently due to passage of discrete waves across the array. An example of a wave-like variation of approximately 1 h period in the east beam is shown in Fig. 8. The oscillations show decreasing phase with increasing height, indicating upward energy propagation with a rather long vertical wavelength. The wave was also clearly evident in the west beam so that there was high wave coherence in both the horizontal as well as the vertical.

Observations of this type are suitable for the cross-spectral analysis discussed in Section 2a. In our experimental situation, the mean horizontal spacing between the beams was $\sim 2l = 35$ km at heights near 85 km. This value, together with suitable values for the neutral temperature taken from the CIRA (1972) model atmosphere, were used in (9) to calculate the phase differences for eastward and westward traveling waves as a function of wavelength for several wave periods (Fig. 9).

To find the wavelengths, the power spectra of the velocity fluctuations for each beam and the cross spectra between the beams were computed from the Doppler velocity data for each height of observation. The cross spectrum was best represented by normalizing it with respect to the products of the powers $S_E(\omega)$ and $S_W(\omega)$ for the east and west beams, respectively, at a given frequency ω. The magnitude of the normalized cross spectrum is then the so-called coherence squared (coh^2) term which may be used to estimate the degree of similarity of the spatially separated observations at a given frequency. If the coh^2 value is significant then the phase of the cross spectrum can be used in conjunction with Fig. 9. to deduce the wavelength, provided the direction of propagation is known. This is conveniently obtained from the sign of $[S_E(\omega) - S_W(\omega)]$; positive and negative values indicating eastward and westward propagation respectively.

In order to obtain good resolution of the wave velocities as a function of time, it is desirable to use short length records. Otherwise, changes in the direction of waves of a given period will lead to "smearing" of the phase differences and a reduced coherence. However, for the purposes of good spectral resolution and significance, it is also desirable to use long records and average over a number of frequency bands. As a compromise, data lengths of 6 h duration were used with averaging of four adjacent frequency points to give 8 degrees of freedom for each estimate. The coherence squared (coh^2) values were used to estimate the degree of similarity of the spatially separated data at a given frequency (Julian, 1975). Values of coh^2 as low as 0.54 were on occasion accepted (nominally significant at the 90% level), but most of the accepted values had coh^2 greater than or equal to 0.68. For $\text{coh}^2 = 0.68$, the uncertainty in phase is ~ 0.45 rad (Jenkins and Watts, 1968). From Fig. 9, it is apparent that phase errors of this magnitude make estimates of wavelengths greater than 200 km very uncertain.

With the present experimental arrangement it was often easier to find the direction of wave propagation than to estimate the actual wavelength because wavelength estimates were complicated by the inherent 2π phase ambiguities which were sometimes encountered (see Fig. 9). For example, 20-min period waves of 30 and 120 km horizontal wavelength will have the same phase. In an effort to resolve these ambiguities the Doppler observations measured at different ranges in a given beam were compared to estimate the vertical wavelength of the particular oscillation in question. Since the vertical and horizontal wavelengths are related to the wave frequency by the gravity wave dispersion relation, this should give a means of choosing the correct horizontal wavelength. In

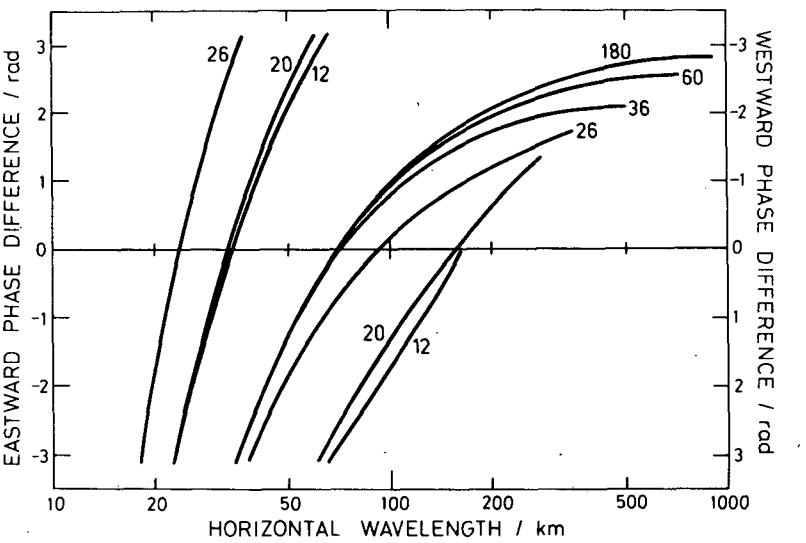

FIG. 9. Plot of the cross spectral phase in radians calculated from (9), plotted as a function of horizontal wavelength for different periods. The numbers against each curve give the wave period in minutes.

practice this method favored the selection of the longer wavelength estimate probably because the height resolution in the present system (~4 km) was not adequate to resolve the short vertical wavelengths associated with shorter scale waves. Consequently, some of the zonal wavelengths have probably been overestimated.

Figs. 10 and 11 show histograms of occurrence for the horizontal wavelength and phase velocities. Since no significant variations in wavelength were found as a function of height, all data in the 80–94 km height range have been included in Fig. 10. On the other hand, zonal velocities did show a change in

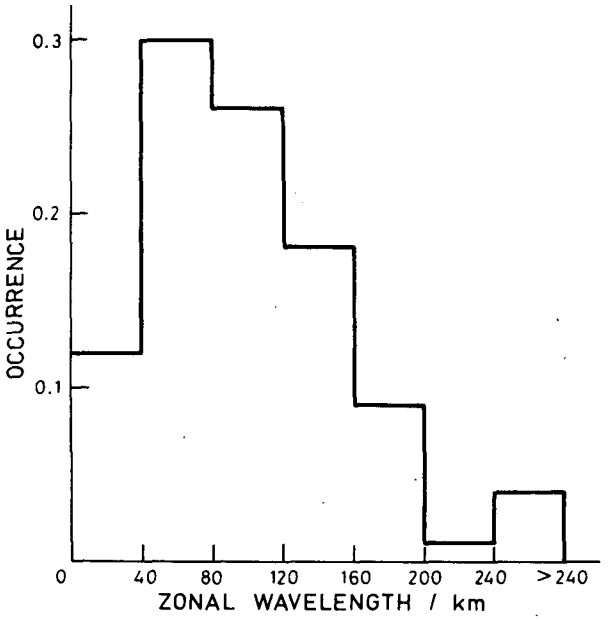

FIG. 10. Histograms of occurrence of zonal wavelength for heights between 80 and 94 km.

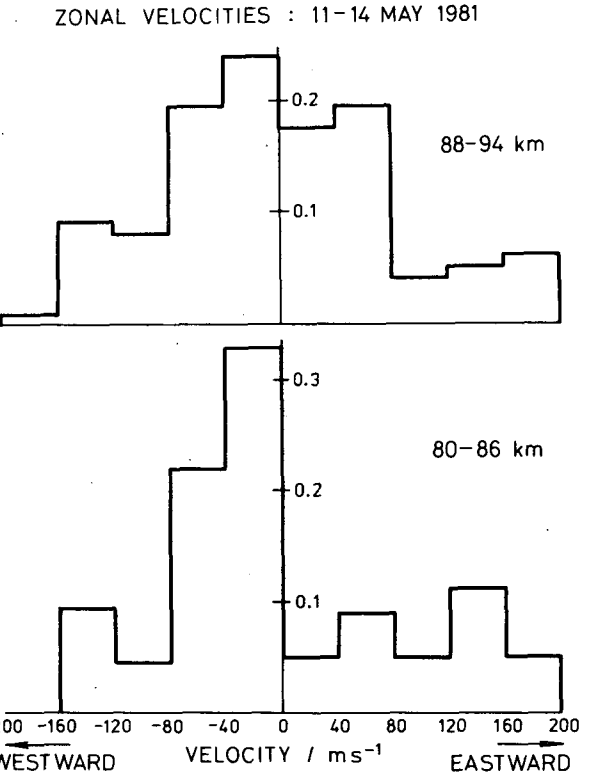

FIG. 11. Histograms of occurrence of zonal phase velocity for the height intervals 80–86 km and 88–94 km.

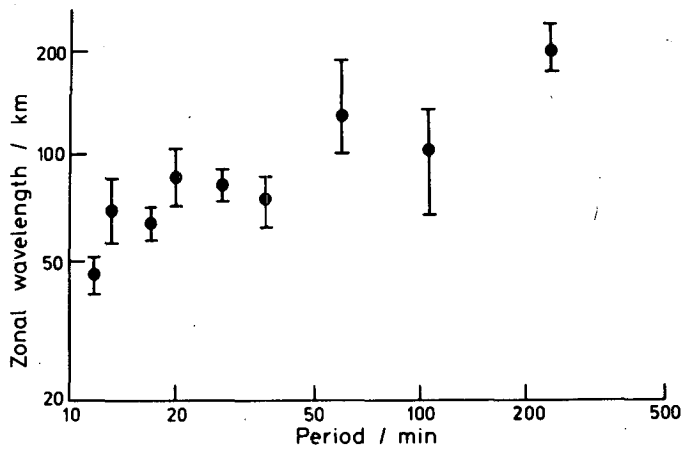

FIG. 12. The mean zonal wavelength plotted as a function of wave period.

direction with height so that results for the height ranges 80–86 and 88–94 km are shown separately in Fig. 11. In the lower range there was a clear bias towards westward propagating waves, but in the upper range eastward and westward waves were equally distributed.

It should be realized that the data shown in Figs. 10 and 11 are biased toward waves with periods < 1 h. This is because the data were analyzed principally in 6 h blocks with adjacent spectra averaged to improve reliability which resulted in a loss of resolution at the long periods. To partially overcome this lack of resolution, the data were re-analyzed in 24 h blocks with the emphasis on periods greater than 1 h. There did seem to be a systematic increase of wavelength with increasing period since at periods near 4 h, the mean estimated wavelength was ~200 km (Fig. 12). This is almost certainly an underestimate of the wavelengths at this period because of the poor resolution at these scales with the present beam separation. On the other hand, the wavelengths of shorter period waves have possibly been overestimated because of the wrong choice made when trying to resolve phase ambiguities.

The wavelengths and velocities shown in Figs. 10, 11 and 12 are of course all trace components and are therefore upper limits to the actual values. Observations of gravity-wave wind oscillations at Adelaide (Ball, 1981) show that they are approximately the same magnitude in the zonal and meridional planes which suggests that the gravity wave spectrum in the mesosphere is roughly isotropic in azimuth. If this is the case, the mean zonal wavelength (70 km) and phase velocity (70 m s^{-1}) are probably overestimates of the wavelength and velocity by a factor of $\sim\sqrt{2}$ *i.e.*, the actual values are closer to ~50 km and 50 m s^{-1}, respectively.

Finally, it should be noted that in the above analysis the effects of the background wind have been ignored. In the present case this does not appear to be a serious omission because the phase speeds appeared to be significantly larger than the zonal winds deduced from (11). Probably the easiest way to incorporate the wind effects in the analysis would be by an iterative approach whereby the phase velocity is estimated without including the wind and then the Doppler shifted wave period is calculated and the wavelength recalculated and so on. Tests on the present data show this method works well although, as suggested, the results do not differ significantly from the estimates made neglecting the wind.

4. Discussion

The results presented in section 3 show that multibeam Doppler radars can be used to study the vertical flux of horizontal momentum and related parameters of internal gravity waves in the mesosphere. In the present case a dual-beam HF radar was used to study the upward flux of zonal momentum in a three-day period in May 1981. Although there was considerable variability in the fluxes in both magnitude and direction with time, there was a net flux of westward momentum overall. The body force estimated from the vertical gradient of momentum gave a westward acceleration of ~15–20 m s^{-1} day^{-1} at heights near the mesopause.

It is probable that the momentum and the associated body force have been underestimated. One of the assumptions made in the calculations is that the Doppler velocities were measured along the beam axes, which, in our case, were pointed at angle of 11.6° from the zenith. However, the radar beams had significant width which means that if irregularities responsible for radiowave backscatter were not isotropic in their characteristics, then the effective ori-

entation would not be 11.6°. Observations of the angular scattering properties of the irregularities made at Adelaide show that in the 80–90 km height region the irregularities are somewhat anisotropic, tending to scatter preferentially from the zenith. Hocking (private communication, 1981) estimates an effective pointing angle of ~9.5–10° so that the fluxes and force calculated from (5) have been underestimated by ~15–20%. The corrected magnitude of the body force is ~17–25 m s^{-1} day^{-1}.

No measurements of the meridional wind were made in the present study but previous observations made at Adelaide show mean southward winds of between 2 and 15 m s^{-1} in the 80–90 km height region in May/June (Stubbs 1976; Vincent and Stubbs, 1977; Vincent and Ball, 1981). Coriolis torques due to this range of speeds would generate eastward zonal wind accelerations of between 15 and 100 m s^{-1} day^{-1} at a latitude of 35°. A westward body force of the same magnitude would be required to balance the momentum budget. Similar values of wave drag are required by the theoretical models of Matsuno (1982) and Holton (1982). While our observed values of the body force to the waves appear to be somewhat small in magnitude, they are certainly in the correct sense. Taking into account the short duration of the observations, the observed variability of the momentum fluxes and the fact that the observations were made at only one location, it would appear that gravity waves can contribute significantly to the mesospheric momentum budget. Longer term measurements and observations at more than one location are desirable since there is probably a large spatial variation in gravity wave fluxes. Australia is a low topography continent surrounded by a large ocean, and the wave fluxes might be expected to be smaller in this region than at locations downwind of large mountain ranges for example; taking into account the land/sea asymmetries between the Northern and Southern Hemispheres, there is possibly a large difference in the fluxes for each hemisphere.

The observed non-steady nature of the wave fluxes shown in Fig. 7 is also of some significance since they could be expected to lead to short term changes in the body force and hence the wind. The curves show short term fluctuations superimposed on a longer term trend towards more negative values of $\overline{u'w'}$. In Section 3 it was noted that the prevailing eastward wind increased with time and it can be expected that the larger eastward zonal wind at lower heights would act to remove a larger fraction of the eastward travelling waves through critical layer interactions. Tidal winds can also be expected to modulate the wave flux (Walterscheid, 1981). Our findings add support to Walterscheid's suggestions that time varying fluxes will generate quasi-random wind variations on tidal time scales, which could partially account for the day-to-day variability of the tides that is often observed in the upper atmosphere.

As noted previously, the enhanced positive values of $\overline{u'w'}$ evident on 13 May were associated with enhanced wave activity. Careful examination of the raw data suggest that on this occasion the enhancements were not due to discrete events or wave packets but rather to a general increase in wave flux over a range of frequencies. Spectral analysis does show, however, that the largest increases occurred in the 20 min to 1 h period range. The cross spectral analyses show that there were neither significant differences in the number of coherent events between adjacent blocks nor in the wavelengths and trace velocities deduced from the analysis.

Although the results show that gravity waves are capable of providing a significant body force on the atmosphere, they do not indicate if any particular part of the spectrum was contributing preferentially. To resolve this question the Doppler data were reanalyzed by filtering them into two period bands, for periods greater and less than 60 min respectively. In the 80–86 km region it was found that both long and short period waves had mean values of $\overline{u'w'}$ of ~ -0.4 m^2 s^{-2}, but in the 88–92 km region the corresponding values were about $+0.15$ m^2 s^{-2} for the short period band and ~ -0.5 m^2 s^{-2} for longer periods. Since the flux for short periods changed sign from negative to positive with increasing height, it would appear that approximately two thirds of the body force was caused by the preferential absorption of the shorter period (<60 min) westward propagating waves.

The cross spectral analysis of the dual-beam data showed that waves with periods less than 60 min had mean zonal wavelengths and phase speeds of the order of 70 km and 70 m s^{-1}, respectively. However, it is emphasized that these results should be treated with caution for a number of reasons. First, ambiguities occurred in the horizontal wavelength determination which may not have been successfully resolved; it is possible that the wavelengths and velocities have been overestimated. Second, the effects of the background winds have been ignored although, in the present case, this is not believed to be a serious omission. Third and perhaps most importantly, the "high coherence" events accounted for only ~25% of the spectra which means that for any given spectrum there was a substantial range of frequencies for which the cross spectral analysis could not be applied. It is possible that at these frequencies, the coherences may have been reduced because of the randomizing influence of turbulence or because there was a broad spectrum of waves present in any given frequency band, the different frequency components propagating in different directions with different velocities.

Whatever the reasons, the observations which

could be successfully analyzed may not be fully representative of the overall spectrum of waves. Nevertheless, the wavelengths deduced here are in reasonable agreement with the scales found for internal gravity waves observed in noctilucent clouds. European and North American sightings, summarized by Haurwitz and Fogel (1969), gave horizontal wavelengths in the range 10–70 km.

In future experiments of the type described here, it would be desirable to have as many beams available as possible; the optimum situation would be obtained if a single beam could be scanned as a function of azimuth as in VAD radars. In the present case, this arrangement is not possible, but because signal-to-noise ratios are so large it will be possible to split the powers and generate up to four independent beams. With the addition of more beams it will be possible to determine additional parameters of the wind field. Experiments which are planned include the simultaneous measurements of both zonal and meridional winds ($\bar{u}$ and $\bar{v}$) and the corresponding momentum fluxes ($\overline{u'w'}$ and $\overline{v'w'}$). Measurements made with different zenith angles θ will enable the spatial coherence of the wave motions to be investigated as a function of angle. It is noted that if (3) and (4) are summed, then

$$\overline{v^2(\theta, R)} + \overline{v^2(-\theta, R)} = 2(\overline{w'^2}\cos^2\theta + \overline{u'^2}\sin^2\theta),$$

so that observations at different angles will allow the variations in wave kinetic energy given by $(\overline{u'^2} + \overline{w'^2})/2$ to be studied as a function of height.

5. Conclusions

A method has been presented by which ground based radars can study the vertical flux of horizontal momentum due to gravity waves and turbulence in the middle atmosphere. The method requires the measurement of the radial Doppler velocities measured with pairs of narrow radar beams lying in a vertical plane and offset from the vertical. Provided the atmospheric motions are horizontally homogeneous, the momentum flux is proportional to the difference of the variances of the Doppler velocities.

The technique has been applied to observations of the upper mesosphere made with a HF radar located near Adelaide, Australia. Measurements were made in May 1981 with two beams offset in the east–west plane so that the vertical flux of zonal momentum $\overline{u'w'}$, was obtained. The zonal and vertical wind components of the prevailing and tidal winds were also derived from the Doppler measurements and show that the zonal winds were typical of an early winter situation. The vertical velocities, however, appear to be large in comparison with theoretical estimates.

The flux measurements show that $\overline{u'w'}$ can change significantly in sense and magnitude over time scales of the order of hours. Nevertheless, when the results are averaged over the three days of observation there was a net flux of westward momentum. From the observed flux convergence, a body force equivalent to a westward acceleration of $\sim$20 m s^{-1} day^{-1} was deduced near the mesopause. This value compares reasonably well with recent theoretical estimates of the wave drag required to balance the zonal accelerations due to Coriolis torques imposed by the mean meridional circulation. Much of the body force appeared to be due to absorption of waves with periods less than one hour.

Cross-spectral analyses of the Doppler velocities show that at some periods the motions measured with the displaced beams could be highly coherent. This coherence was interpreted as being due to the passage of internal gravity waves with well defined directions of propagation. The zonal direction of propagation and the associated horizontal wavelengths and phase velocities were deduced from the measured cross spectral phases. At periods of less than one hour, the mean zonal wavelength and phase velocity was 70 km and 70 m s^{-1}. However, these measurements were subject to some uncertainties which have yet to be resolved.

Dual beam radar measurements of the type discussed here should be generally applicable to the MST radars now coming into operation at various locations (Balsley, 1981). It is hoped that the spatial and temporal variability of the momentum fluxes and gravity wave motions, in general, will soon be better understood.

Acknowledgments. We wish to thank Dr. B. H. Briggs, Dr. W. G. Elford, Dr. W. K. Hocking, Dr. R. A. Plumb and Dr. R. L. Walterscheid for their many helpful comments. This work was supported by the Australian Research Grants Scheme and the Radio Research Board.

REFERENCES

Ball, S. M., 1981: Upper atmosphere tides and gravity waves at mid- and low-latitudes. Ph.D. thesis, University of Adelaide, South Australia, 322 pp.

Balsley, B. B., 1981: The MST technique—A brief review. *J. Atmos. Terr. Phys.*, **43**, 495–509.

CIRA, 1972: *International Reference Atmosphere.* Akadamie-Verlag, 450 pp.

Elford, W. G., 1979: Momentum transport due to atmospheric tides. *J. Geophys. Res.*, **84**, 4432–4440.

Forbes, J. M., 1982a: Atmospheric tides I. Model description and results for the solar diurnal component. *J. Geophys. Res.*, **87**, 5222–5240.

——, 1982b: Atmospheric tides II. The solar and lunar semidiurnal components, *J. Geophys. Res.*, **87**, 5241–5252.

Haurwitz, B., and B. Fogle, 1969: Wave forms in noctilucent clouds. *Deep Sea Res.*, **16**, 85–95.

Heath, D. F., E. Hilsenrath, A. J. Krueger, W. Nordberg, C. Prabhakara and J. S. Theon, 1974: Observations of the global structure of the stratosphere and mesosphere with sounding rockets

and with remote sensing techniques from satellites. *Structure and Dynamics of the Upper Atmosphere,* Vol. I, F. Verniani, Ed., Elsevier, 131–203.

Hines, C. O., 1960: Internal atmospheric gravity waves at ionospheric heights, *Can. J. Phys.*, **38,** 1441–1481.

Hocking, W. K., 1979: Angular and temporal characteristics of partial reflection from the D-region of the ionosphere. *J. Geophys. Res.*, **84,** 845–851.

Holton, J. R., 1982: The role of gravity wave induced drag and diffusion in the momentum budget of the mesosphere. *J. Atmos. Sci.*, **39,** 791–799.

Houghton, J. T., 1978: The stratosphere and mesosphere. *Quart. J. Roy. Meteor. Soc.*, **104,** 1–29.

Jenkins, G. M., and D. G. Watts, 1968: *Spectral Analysis and Its Applications.* Holden-Day, 525 pp.

Julian, P. R., 1975: Comments on the determination of significance levels of the coherence statistic. *J. Atmos. Sci.*, **32,** 836–837.

Lindzen, R. S., 1981: Turbulence and stress due to gravity wave and tidal breakdown. *J. Geophys. Res.*, **86,** 9707–9714.

Matsuno, T., 1982: A quasi-one-dimensional model of the middle atmosphere circulation interacting with internal gravity waves. *J. Meteor. Soc. Japan.*, **60,** 215–226.

Miyahara, S., 1980: Solar diurnal tides and the induced zonal mean flows. *J. Meteor. Soc. Japan.* **58,** 302–306.

Moreels, G., and H. Herse, 1977: Photographic evidence of waves around the 85 km level. *Planet. Space Sci.*, **25,** 265–273.

Plumb, R. A., 1982: The circulation of the middle atmosphere. *Aust. Meteor. Mag.*, **30,** 107–121.

Rastogi, P. K., and S. A. Bowhill, 1976: Gravity waves in the equatorial mesosphere. *J. Atmos. Terr. Phys.*, **38,** 51–60.

Stubbs, T., 1976: Mean and periodic components of ionospheric drifts in the D-region at 35°S during 1972. *J. Atmos. Terr. Phys.*, **38,** 979–990.

Vincent, R. A., and T. Stubbs, 1977: A study of the motions in the winter mesosphere using the partial reflection drift techniques. *Planet. Space Sci.*, **25,** 441–455.

——, and J. S. Belrose, 1979: The angular distribution of radio waves partially reflected from the lower ionosphere. *J. Atmos. Terr. Phys.*, **40,** 35–47.

——, and S. M. Ball, 1981: Mesospheric winds at low- and mid-latitudes in the Southern Hemisphere. *J. Geophys. Res.*, **86,** 9159–9169.

Walterscheid, R. L., 1981: Inertio-gravity wave induced accelerations of mean flow having an imposed periodic component: Implications for tidal observations in the meteor region. *J. Geophys. Res.*, **86,** 9698–9706.

Wilson, D. A., and L. J. Miller, 1972: Atmospheric motion by Doppler radar. *Remote Sensing of the Troposphere,* V. E. Derr, Ed., NOAA and University of Colorado, 13-1 to 13-4.

Woodman, R. F., and A. Guillen, 1974: Radar observations of winds and turbulence in the stratosphere and mesosphere. *J. Atmos. Sci.*, **31,** 493–505.